

PROCEEDINGS OF SIOEL'98

Bucharest, Romania



1998

CSP 98 - 1038

Contract F61775-98-WE022

SIOEL'98

Fifth Symposium on Optoelectronics

23-25 September 1998
Bucharest, Romania

Teodor NECSOIU
CHAIRMAN

19990413 081

Sponsored by:

Ministry of Research and Technology
Romanian Academy
Ministry of Education
Ministry of National Defence
European Office of Aerospace Research and Development (EOARD)
European Optical Society

Reproduced From
Best Available Copy

AAF 99-07-1281

ISBN 973-0-00813-2

All rights reserved.

No part of this publication may be reproduced, stored in a retrieval system or transmitted in any form or by any means, electronic, mechanical, photocopying, recording or otherwise, without the written permission of the Publishing Board.

Edited, printed and published by



IOEL-S.A. – Institute of Optoelectronics

P.O. BOX MG-22, MAGURELE
1 ATOMISTILOR str., 76900 BUCHAREST, ROMANIA

Phone: (401) 780.66.40

Fax: (401) 423.25.32

REPORT DOCUMENTATION PAGE

Form Approved OMB No. 0704-0188

Public reporting burden for this collection of information is estimated to average 1 hour per response, including the time for reviewing instructions, searching existing data sources, gathering and maintaining the data needed, and completing and reviewing the collection of information. Send comments regarding this burden estimate or any other aspect of this collection of information, including suggestions for reducing this burden to Washington Headquarters Services, Directorate for Information Operations and Reports, 1215 Jefferson Davis Highway, Suite 1204, Arlington, VA 22202-4302, and to the Office of Management and Budget, Paperwork Reduction Project (0704-0188), Washington, DC 20503.

1. AGENCY USE ONLY (Leave blank)		2. REPORT DATE 1999	3. REPORT TYPE AND DATES COVERED Conference Proceedings	
4. TITLE AND SUBTITLE Fifth Symposium on Optoelectronics			5. FUNDING NUMBERS F617089	
6. AUTHOR(S) Conference Committee				
7. PERFORMING ORGANIZATION NAME(S) AND ADDRESS(ES) Institute of Optoelectronics P.O. Box MG-22 Bucharest - Magurele 76900 Romania			8. PERFORMING ORGANIZATION REPORT NUMBER N/A	
9. SPONSORING/MONITORING AGENCY NAME(S) AND ADDRESS(ES) EOARD PSC 802 BOX 14 FPO 09499-0200			10. SPONSORING/MONITORING AGENCY REPORT NUMBER CSP 98-1038	
11. SUPPLEMENTARY NOTES				
12a. DISTRIBUTION/AVAILABILITY STATEMENT Approved for public release; distribution is unlimited.			12b. DISTRIBUTION CODE A	
13. ABSTRACT (Maximum 200 words) The Final Proceedings for The 5th Symposium on Optoelectronics, 23 September 1998 - 25 September 1998 This is an interdisciplinary conference. Topics include materials and components for optoelectronics, new components, analysis and control methods for fabrication of optoelectronic devices and materials, and optoelectronic applications.				
14. SUBJECT TERMS EOARD, Optoelectronic materials, Optoelectronic components, Diode lasers, Optoelectronic applications			15. NUMBER OF PAGES 279	
			16. PRICE CODE N/A	
17. SECURITY CLASSIFICATION OF REPORT UNCLASSIFIED	18. SECURITY CLASSIFICATION OF THIS PAGE UNCLASSIFIED	19. SECURITY CLASSIFICATION OF ABSTRACT UNCLASSIFIED	20. LIMITATION OF ABSTRACT UL	

NSN 7540-01-280-5500

Standard Form 298 (Rev. 2-89)
Prescribed by ANSI Std. Z39-18
298-102

Contents

xi Symposium Committee

xiii Introduction

- Plenary session 1 Electro-optic crystals for EOS applications**
S. Miyazawa, USHIO Research Institute of Technology (URIT) Inc., USHIO INC. (Japan)
- 10 Some techniques for improving the confidentiality in coherence modulation systems**
B. Wacogne, A. Mokhenache, H. Porte, P. Mollier, Laboratoire d'Optique P.M. Duffieux, Institut des Microtechniques de Franche-Comté, Université de Franche-Comté (France); D. A. Jackson, Physics Department, University of Kent at Canterbury (UK)

SESSION A1 MATERIALS FOR OPTOELECTRONICS AND RELATED FIELDS

- 19 Optical limiting in porous silicon films**
I. Cojocaru, V. Pasat, V. Chumash, Centre of Optoelectronics, Institute of Applied Physics of the Academy of Sciences (Moldova); V. Karavanskii, Institute of General Physics, Russian Academy of Sciences (Russia).
- 23 Anomalous behavior of drift mobilities during field-assisted migration of ions in optical glass**
A. Lupascu, C. P. Cristescu, I. M. Popescu, Physics Department, University "Politehnica" (Romania); A. Kevorkian, GeeO, Institut National Polytechnique (France)
- 28 Cathodoluminescence from optoelectronic materials**
T. A. Nazarova, M. V. Nazarov, Technical University of Moldova, Kishinev (Moldova)
- 33 Modification of plastic and brittle properties of InP single crystals by ion implantation**
D.Z. Grabko, N.A. Palistrant, M.I. Medinskaya, N.B. Pyshnaya, Institute of Applied Physics, Academy of Sciences (Moldova)
- 37 The influence of the annealing temperature on the interface layer in metal/ferroelectric/semiconductor heterostructures**
I. Boerasu, L. Pintilie National Institut of Materials Physics (Romania); M. Alexe, Max - planck Institut fur Mikrostrukturphysik (Germany)
- 42 About the nature of deformation anisotropy of the InP:Zn crystals**
D. Grabko, N. Palistrant, M. Dyntu, M. Medinschi, E. Rusu, Institute of Applied Physics of Academy of Sciences (Moldova)

- 46 **New Invar alloys for high-frequency devices**
H. Chiriac, M. Lozovan, Fl. V. Rusu, National Institute of Research & Development for Technical Physics (Romania)
- 49 **On Ni content influence on hall effect in (Ni alloy)-SiO₂ granular thin films**
H. Chiriac, F. Rusu, M. Lozovan, National Institute of R & D for Technical Physics (Romania)
- 52 **Hot pressed zinc sulphide for ir optical windows. Microstructure and purity influence on optical properties.**
C. Onose, S. Jinga – MATPUR (Romania)
- 55 **Structural and dielectric characterization of chemically derived (Pb, La) (Ti, Mn)O₃**
L. Păcurar, E.J. Popovici, M. Vădan, Institute of Chemistry "Raluca Ripan" (Romania)
- 58 **Optical Properties in Aluminophosphate Semiconductor - Doped Glasses**
R. Rogojan, M. Elisa, MATPUR S.A. (Romania); P. Sterian, University "Politehnica" (Romania)
- 61 **Domain instabilities and dynamical scattering mode in new synthesised 4,4'-bis-(4-chloro)-benzyloxy-azoxybenzene liquid crystal**
C. Sarpe-Tudoran, M. Socaciu, D. Mustaza, C. Uncheselu, University of Craiova, Faculty of Sciences (Romania)
- 64 **Study of the absorption spectra changing with temperature for new synthesized liquid crystals**
M. Socaciu, C. S. Tudoran, G. Iacobescu, C. Sarpe-Tudoran, University of Craiova, Department of Physics (Romania); J. Neamtu, University of Medicine and Pharmacy (Romania)
- 67 **Doped and undoped meta-dinitrobenzene thin films growth and characterization**
A. Stanculescu, F. Stanculescu, MATPUR, (Romania)
- 71 **Uniformity of magnetron sputtered aluminium nitride layers**
M. Tanase, L. Tugulea, Faculty of Physics-University of Bucharest (Romania); V. Dumitru, C. Morosanu, National Institute of Materials Physics (Romania); D. Nicolae, National Institute of R&D for Optoelectronics (Romania)
- 75 **Tribological properties of rf-PECVD deposited a-C:H films**
N. Tomozeiu, University of Bucharest, Faculty of Physics (Romania)
- 80 **Study on the synthesis of rare earth activated calcium tungstate phosphors**
Flavia Forgaciu, Elisabeth-Jeanne Popovici, "Raluca Ripan" Institute of Chemistry (Romania); Marilena Vasilescu, "I.G. Murgulescu" Institute of Physical Chemistry of the Romanian Academy (Romania)

SESSION A2 LASERS AND APPLICATIONS

- 85 Donor-acceptor systems on the base of carbazolyalcylmetacrylat's copolymers for registration optical information (invited paper)**
V.V.Bivol, A.M.Prisacari, Centre of Optoelectronics, Academy of Sciences (Moldova); S.V.Robu, N.A.Barba, G.A.Dragalina, L.A.Vlad, I.V.Dementiev, State University of Moldova (Moldova)
- 91 Cesium source for atomic fountain**
C. Mandache, M.Bengulescu, T.Acsente, M.Ungureanu, National Institute for Laser, Plasma and Radiation Devices, Nuclear Fusion and Plasma Physics Laboratory (Romania)
- 94 Calculation method of smith-purcell radiation power in 1-30 MeV electron energies range**
F. Scarlat, M. Facina, National Institute for Laser, Plasma and Radiation Physics (Romania); V. Manu, National Institute for Nuclear Physics and Engineering "Horia Hulubei" (Romania)
- 99 Termographic analysis of water precipitation in α -berlinite monocrystals hydrothermally obtained**
I. Grozescu, D. Irimia, D. Rata, National Institute of Electrochemistry and Condensed Matter Research (Romania)
- 103 Invariance principles for the nonlinear equations of evolution as linear stochastic equations**
V. Babin, M. Grigore, S. Ersen, A. Moldovan, National Institute of Research & Development for Optoelectronics - INOE-2000 (Romania)
- 108 A study about the action laser radiation on the evolution of "in vitro" grapevine crop**
D. Giosanu, S. Anghel, I. I. Siman, Faculty of Sciences, University of Pitesti (Romania)
- 111 Holographic solar concentrators recorded on spherical surfaces with acrylic photopolymers**
Silvia Nicolau-Rebigan, National Institute of Lasers, Plasma and Radiations Physics (Romania); St. Levai, B. Nicolae, Roxana Rebigan, University of Bucharest, Faculty of Physics, (Romania)
- 115 New photopolymers laser obtained and their applications**
Silvia Nicolau-Rebigan, M. Ristici, Doina Mitea, National Institute of Lasers, Plasma and Radiations Physics, (Romania) St. Levai, Roxana Rebigan, B. Nicolae, University of Bucharest, Faculty of Physics, (Romania)

SESSION A3 OPTOELECTRONIC COMPONENTS. ANALYSIS AND CONTROL METHODS

- 123 Influence of structural defects upon the parameters of III-V p-i-n photodiodes (invited paper)**
V.Dorogan, V.Coseac, T.Vieru, Technical University of Moldova, Laboratory of Microelectronics (Moldova)
- 131 Modeling the optical amplification of $\text{Er}^{3+}:\text{Ti:LiNbO}_3$ curved waveguide amplifiers**
N. N. Puscas, A. Ducariu, I. M. Popescu, Physics Department, University "Politehnica" Bucharest (Romania); B. Wacogne, B. Grappe, Laboratoire d'Optique P. M. Duffieux, Sciences et Techniques Université de Franche-Comté (France)
- 135 High frequency transmission in a dispersive fiber using a multi longitudinal mode laser diode**
P. Mollier, H. Porte, J.P. Goedgebuer, GTL-CNRS TELECOM, Laboratoire d'Optique P.M. Duffieux (France); B. S. Rinza, C. G. Martinez, INAOE - Coordination de Optica Puebla Puerto (Mexico)
- 139 Liquid crystals refractive index measurements by interferometric method**
Cristina S. Tudoran, M. Ursache, L. Socaciu, V. Calian, C. S. Tudoran, University of Craiova, Department of Physics (Romania)
- 144 The determination of the refractive-index profile from near field and effective refractive-index measurements**
D. Pîrcalaboiu, Optoelectronic Department, University "Politehnica" Bucharest (Romania); G. Perrone, Dipartimento Elettronica, Politecnico Torino (Italy); N. N. Puscas, Physics Department, University "Politehnica" Bucharest (Romania)
- 147 On the IR reflectivity of $\text{Bi}_{12}\text{SiO}_{20}$ crystal in the ionic plasma frequency range**
A. Ioanid, Department of Solid State Physics, Faculty of Physics, University of Bucharest, National Center of Physics (Romania)
- 150 New type of soliton quantization**
V.Calian, M.Ursache, University of Craiova, Dept. of Physics (Romania)
- 153 Spectral response simulation for solar cells**
G.Stoenescu, V.Calian, University of Craiova, Dept.of Physics (Romania); N.Baltateanu Institute of Atomic Physics (Romania)
- 156 Variable $\lambda/2$ retardation plate**
A. M. Beldiceanu, S.C. PRO OPTICA S.A (Romania)
- 160 Astigmatic output beam of double-heterostructure lasers**
F. Jitescu, O. Novac, M. Serghie, Military Equipment and Technologies Research Agency (Romania)

- 163 Silicon integrated electro-optical modulators for 1.3 μm fiber-optics**
G. Paunescu, V. Cimpoca, D. Cengher, R. Ghita, National Institute for Materials Physics (Romania); N. Olariu, C. Oros, Valahia University, Targoviste (Romania); M. Cimpoca, National Institute for Microtechnologies, Bucharest, (Romania)
- 167 Application of finite elements method to avalanche photodiode**
P. Schiopu, Electronic Department of the University "Politehnica" (Romania); E. Lakatos, V. Degeratu, S.C.Baneasa S.A. (Romania); S. Ivan, University of Bucharest, Faculty of Physics (Romania)
- 173 Influence of electron-beam recording conditions on properties of diffraction gratings of submicron period**
S.A. Sergeev and S.D. Shutov, Center of Optoelectronics, Institute of Applied Physics of the Academy of Sciences (Moldova)
- 177 Acoustic waves detection system for closed areas with the help of acousto-optical sensors**
V.Bivol, A.Prisacari Center of Optoelectronics of Academy of Science, (Moldova Republic); Ghe. Paun, Institute of Optoelectronics (Romania)

SESSION A4 & B6 TECHNOLOGIES IN OPTOELECTRONICS AND ENVIRONMENT

- 181 Interferometric devices for integrated optics remote sensor systems**
H. Porte, W. Elflein, J. P. Goedgebuer, Laboratoire d'Optique P.M.Duffieux, Université de Franche-Comté, Institut des Microtechniques (France)
- 192 Particle reflection from rough surface in binary collision model**
V.I.R.Niculescu, National Institute for Laser, Plasma and Radiation Physics, Electron Accelerators Laboratory (Romania); A.O.R. Cavaleru, Institute of Optoelectronics (Romania); R. Candea, Semanatoarea S.A. (Romania)
- 195 Plasma parameters determination in a pulsed duopigatron ion source**
V. Braic, C.N. Zoita, A. Kiss, M. Braic, National Institute for Optoelectronics (Romania)
- 199 Optimisation of wavelength selectivity in resonant microcavities for C^3SL , VCSEL and RCE photodetectors**
C. Cotîrlan, B. Bălăsoiu, Institute of Optoelectronics, (Romania)
- 206 Experimental tests for the characterization of ultrasonic probes utilized for non destructive examinations in the industrial field**
Claudio Cantore, Isotest, via Roma, (Italy); Maria Robu, Institute of Optoelectronics, (Romania)

- 211 Radar Systems for Intelligent Cruise Control of Road Vehicles**
A. Stoica, A. Caramizoiu, D. Jianu, Institute of Optoelectronics, (Romania)

**SESSION B5 & B7 OPTOELECTRONICS DEVICES AND COMPUTERS IN
OPTOELECTRONIC RESEARCH**

- 219 The "3eyes" active vision system for metrological applications**
D. Cojoc, University "Politehnica" of Bucharest (Romania); P. Grattoni, G. Pettiti, Centro di Studio per la Televisione – CNR (Italy); R. Nerino, Istituto Elettrotecnico Nazionale Galileo Ferraris (Italy)
- 226 Optical fiber methane sensor**
S. Miclos, T. Zisu, B. Robea, I. Munteanu, National Institute of Research and Development for Optoelectronics (Romania)
- 230 Enhanced optical fiber remote explosion starter**
I. Munteanu, T. Zisu, S. Miclos, B. Robea, National Institute of R&D for Optoelectronics - INOE 2000 (Romania)
- 233 Impact of the night vision devices on the ocular physiology**
L. Iorga, Psychological Examination Army Department (Romania); C. Iliuta, C. Ispasoiu, Institute of Medicine for Air-Force (Romania); R. Copot, Institute of Optoelectronics (Romania)
- 236 Modular miniaturized power supply for repetitive medium power solid state lasers**
S. Sârbu, Carmen Radu, Silvia Radu, N. Mincu, National Institute of Research and Development for Optoelectronics, Bucharest (Romania); I. Pricop, Institute of Optoelectronics, Bucharest (Romania)

**SESSION B8 & B9 OPTOELECTRONICS IN ANALYTICAL INSTRUMENTATION
AND MEDICINE**

- 241 Combined scanning ophthalmoscope and optical coherence tomographic system for ocular studies (invited paper)**
D. A. Jackson A. Gh. Podoleanu, School of Physical Sciences, University of Kent (UK)
- 247 Results of on-site monitoring of phenol and related chemicals, using an intensity modulated fiber optic sensor**
M. Vladescu, Electromagnetica GoldStar Ltd., (Romania); M. Guina, "Politehnica" University of Bucharest, Faculty of Electronics and Telecommunications (Romania)
- 252 The study of the fractal structure of colloidal and smoke aggregates by light scattering**
T. Nicula, G. Costache, Military Chemistry Application School (Romania)

- 255 **Self-organization processes in low-pressure plasmas**
B. Oprescu, M. Sanduloviciu, Faculty of Science, University of Pitesti,
(Romania)
- 258 **Considerations about the vibratory states of piezoelectric structures by a
finite element method**
I. Chilibon, National Institute of Research and Development for
Optoelectronics, INOE-2000, Bucharest (Romania)
- 262 **Laser biostimulation used in the treatment of hair loss**
C. Chelarescu, Private consulting room (Romania); D.Chelarescu, Ministerul
de Interne Tg-Mures (Romania)
- 265 **Low energy laser treatment in lichen planus and fingers pulpits**
T. Ciuchiță, Military Hospital, Pitesti (Romania); S. Anghel, C. Stănescu,
Faculty of Sciences, University of Pitesti (Romania); C. Antipa, Coltea Clinical
Hospital Bucharest (Romania); A.Nicolescu, "N.G.Lupu" Clinical Hospital
Bucharest (Romania); M. Uşurelu, Military Hospital Cluj-Napoca (Romania)
- 269 **Low acoustical sensitivity pyroelectric laser energymeter**
E.Smeu, N.Puscas, I.M.Popescu, "Politehnica" University of Bucharest, Physics
Department (Romania)
- 273 **On the photodynamic therapy of carcinoma in buccal cavity**
Evantya Ungureanu-Coles, Faculty of Medicine, (Romania); Silvia Nicolau,
M. Ristici, Institute of Atomic Physics, (Romania)

278 *Author index*

Symposium Committees

Symposium Chairman

Teodor Necsoiu, Institute of Optoelectronics (Romania)

PROGRAMME COMMITTEE

V.Bivol (Moldova)
V.Braic (Romania)
A.Cavaleru (Romania)
V.Ciumas (Moldova)
E.Cordos (Romania)
D.Dumitras (Romania)
V.Grecu (Romania)
I.Iova (Romania)
C.Ispas (Romania)
N.Irimie (Romania)
I.Jelev (Romania)
M.Kopica (Poland)
St.Levai (Romania)
M.Mihaita (Romania)
I.Munteanu (Romania)
T.Necsoiu (Romania)
N.Nedev (Romania)
D.Oancea (Romania)
N.Plaviciosu (Romania)
I.M.Popescu (Romania)
M.Puscă (Romania)
M.Robu (Romania)
P. Sterian (Romania)
A. Stoica (Romania)
Fl.Tanasescu (Romania)

SCIENTIFIC COMMITTEE

A.Andries (Moldova)
A.Balaban (Romania)
M.Bertolotti (Italy)
D.Botez (U.S.A.)
K.D.Bouzakis (Greece)
J.P.Chaminade (France)
E.Curatu (Canada)
K.L.Dickson (U.S.A.)
S.Miyazawa (Japan)
B.Molinas (Italy)
M.Peculea (Romania)
K.B.Radev (Romania)
A.Rigas (Greece)
E.T.Sarris (Greece)
A.Sandulescu (Romania)
A.Simaschievici (Moldova)
M.Strzelec (Poland)
V.I.Topa (Romania)
V.Vlad (Romania)

TECHNICAL COMMITTEE

M.Robu (Romania)
M.Nedelcu (Romania)
C.Radu (Romania)
S.Radu (Romania)
Gh.Oprisan (Romania)
C.Dragomirescu (Romania)

SYMPOSIUM SECRETARIAT

M.Nedelcu (Romania)
T.Popescu (Romania)
G.Botea (Romania)
S.Voicu (Romania)
R.Stefan (Romania)
A.Caramizoiu (Romania)
O.Curcan (Romania)
M.Iliescu (Romania)
M.Valceanu (Romania)

Organized by



Institute of Optoelectronics



National Institute of Research & Development for Optoelectronics

“Politehnica” University of Bucharest

University of Bucharest (Faculty of Physics)



Romanian Physics Society



SPIE – RO

Co-sponsoring institutions

Romanian Ministry of Research and Technology



Romanian Academy

Romanian Ministry of Education

Romanian Ministry of National Defence



European Office of Aerospace Research and Development (EOARD)



European Optical Society (EOS)

**We wish to thank the following for their contribution to the success of this
symposium: United States Air Force European Office of Aerospace Research
and Development**

Introduction

The Optoelectronics Symposium "SIOEL '98" held in Bucharest every year is at its fifth edition. It brings together specialists in optoelectronics from throughout Romania and abroad for an exciting three-day exchange of experience, and sharing of research results, etc.

The aim is to create a large forum of debate in the fast growing field of optoelectronics. The Symposium covers a wide range of topics, from lasers and their applications in the science of materials, to remote sensing and metrology.

The organization of The Optoelectronics Symposium has been possible through the joint action and support of several Romanian and international institutions, such as: The Institute of Optoelectronics - S.A., The National Institute of Development and Research of Optoelectronics - INOE-2000, University "Politehnica-Bucharest", University Bucharest - Faculty of Physics, Romanian Society for Physics, SPIE - RO.

I thank them all !

I want to express my deep gratitude to the co-sponsoring institutions for their sage counsel and their contribution to the success of this symposium, namely to the European Office of Aerospace Research and Development (EOARD), the Romanian Ministry of Research and Technology, ROMENERGO-S.A., the Military Technical Academy.

I acknowledge the efforts of the Scientific and Standing Committees which have selected for presentation a number of 134 papers from 12 countries. Plenary sessions and 16 invited lectures have also been scheduled.

I would like to address my thanks to the Organizing Committee, to colleagues and members of various Committees and to the Secretariat for their time, energy and creativity invested in this endeavor. We owe them a debt of gratitude and appreciation. I also acknowledge the referees, the invited professors and all participants at this important event for their outstanding contribution to the success of this edition of the symposium.

I do hope that the participants to the fifth "Optoelectronics Symposium" will appreciate the scientific sessions and will enjoy Romania's points of interest and cultural attractions.

On behalf on the Organizing Institutions, I would like to extend my warmest welcome to all participants of the fifth Optoelectronics Symposium and I do hope that this meeting will be a very successful one.

Teodor NECSOIU

ELECTRO-OPTIC CRYSTALS FOR EOS APPLICATIONS

Shintaro Miyazawa

USHIO Research Institute of Technology (URIT) Inc.,
1-90 Komakado, Gotemba-shi, Shizuoka 412-0038, Japan
Tel: +81 550 87 5880, Fax: +81 550 87 5887, E-mail: miyazasn@mail.ushio.co.jp

ABSTRACT

A high-impedance EOS (Electro-Optic Sampling) probe has become a standard tool in testing and measuring the fast electrical signals in printed circuits, multi-chip modules and ultrafast optical devices, and its system is now in a stage of improvement for practical uses. EOS probe is an optoelectronic device, consisting of ultrafast pulse laser, optical components and electro-optic (EO) crystals. EO crystal $\text{Bi}_{12}\text{TiO}_{20}$ (BTO) has survived as a practical crystal for a novel handy-type, high-impedance EOS probe head. An improvement in the voltage sensitivity of a handy-type, high-impedance EOS probe system is demonstrated, as compared to $\text{Bi}_{12}\text{SiO}_{20}$ (BSO).

The reproducibility of a top-seeded solution growth (TSSG) pulling growth of BTO single crystals was evaluated experimentally by establishing a substantial phase relation of the Bi_2O_3 - TiO_2 binary system in the region close to the stoichiometric BTO. It was emphasised that a starting solution, with a 10.0 ~ 10.1 mol% TiO_2 concentration, results in large single crystals with a highly homogeneous lattice constant within $\pm 1 \times 10^{-4}$ Å.

1. INTRODUCTION

Recent advances of ultrahigh speed electronics and optoelectronics devices and ICs operating at frequencies over 10 Gb/s in applications of high-speed communication network systems have outpaced the capability of conventional measuring and testing instruments. Instruments capable of measuring internal-node signals noninvasively are important in diagnosing ICs, to reduce developmental cost and time. Ultrafast pulse laser and optoelectronics technologies have spawned a variety of novel measurement technique whose potential bandwidth approaches the THz regime. Various types of probing techniques, such as electronic sampling using FET probe, E-beam probing, and electro-optic sampling (EOS), have been developed¹⁾, among which a high-impedance EOS probe has already become a standard tool in testing ultrafast optical devices and integrated microelectronic circuits^{1,2)}. Moreover, EOS systems are in a stage of improvement for practical application in measuring the fast electrical signals in printed circuits and multi-chip modules now being applied to mobile communication and data transmission. Thus, EOS probe is an optoelectronic device consisting of ultrafast pulse laser, optical components, and electro-optic crystals.

This paper introduces the principle of EOS, (primarily handy-type EOS probe are useful for multi-GHz signal measurement of on-board circuits), and focuses on the new electro-optic crystal $\text{Bi}_{12}\text{TiO}_{20}$ (BTO) as a new sensitive probe head. Reproducible growth of BTO single crystals using the TSSG method is established by the re-examination of the phase relation of Bi_2O_3 - TiO_2 binary system. Finally, EOS characteristics are demonstrated by comparison to the conventionally used $\text{Bi}_{12}\text{SiO}_{20}$ (BSO) crystal.

2. PRINCIPLE OF EOS PROBING

The Electro-optic (EO) effect is now widely used in ultrafast optoelectronics devices, such as light intensity modulators/deflectors. The refractive index of EO crystals changes when an electric field is applied to the crystal, and the polarization of the optical beam passing the EO crystal then changes according to the strength of the applied electric field through electro-optic coefficient. The change in polarization can be easily converted into an intensity change of the electric field using crossed polarizers. Combining this EO phenomenon with ultrashort pulse lasers makes EOS possible.

To apply EOS technique for measuring actual circuits, external non-contact probing configurations are shown in Fig.1 schematically.

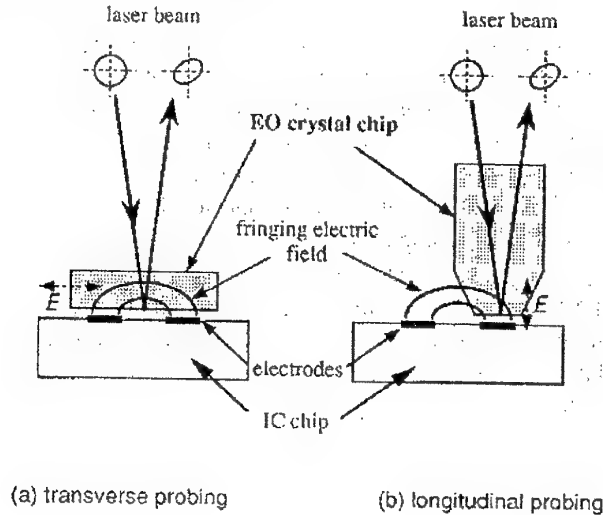


Fig.1 External non-contact probing configuration

Here, the EO crystal is used as a proximity electric-field sensor placed over the IC to detect the fringing field from the interconnections, that is so-called a *high impedance probing*. Transverse probing (a) relies on local field components parallel to the circuit surface, while the longitudinal probing (b) senses the normal components of the electric field. For dense integrated circuits, longitudinal probing crystals are favourable to minimize crosstalk problems.

More recently, a novel handy-type, high-impedance probing system consisting of an electro-optic $\text{Bi}_{12}\text{SiO}_{20}$ (BSO) crystal was developed for measuring multi-GHz signals³. A few of the features of this handy-type prober are: a 10-GHz bandwidth measurement with only one-point contact, ultrahigh input impedance ($> 100 \text{ M}\Omega$ and $< 0.2 \text{ pF}$), and immunity to electrostatic discharge. The probe head is briefly illustrated in Fig.2, showing how electric signals in ICs can be detected through an electro-optic crystal installed in the module³. A probe head consisting of an electro-optic crystal and a metal needle tip senses longitudinal electric fields by which the refractive indicatrix of a EO crystal chip changes through the electro-optic effect, i.e., $\Delta(1/n^2) = rE$, where n is the refractive index, r is the electro-optic constant and E is the evanescent electric field. The polarization of the input laser is then modulated in proportion to the intensity of the input laser light is then modulated in proportion to the intensity of the electric fringing fields, which enables us to measure the propagating signal in an integrated circuit by detecting a change in the polarization of light reflected through the head.

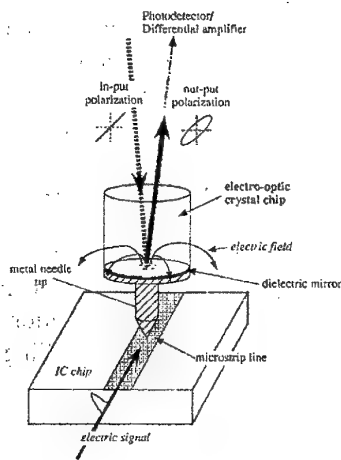


Fig.2 Schematic drawing showing how an electric signal in a strip line can be detected by a longitudinal EOS probing

3. ELECTRO-OPTIC CRYSTALS FOR EOS

The most important issues in selecting EO crystals suitable for external EOS system are sensitivity, the crystal symmetry related to the direction of the electric field that can be efficiently sensed, and transparency at the laser wavelengths used. Table I summarizes typical EO crystals quite suitable for the external EOS application. The shot-noise-limited expression for the minimum detectable voltage V_{\min} in the EOS technique¹⁾ is expressed as

$$V_{\min} = 4 V_{\pi} / \pi \cdot \sqrt{q} / i_{\text{avg}}, \quad (1)$$

where V_{π} is the half-wave voltage of the electro-optic crystal, q is the electron charge, and i_{avg} is the average photocurrent of the system's photodetector. Because V_{π} is inversely proportional to n^3r , the product of electro-optic constant r and refractive index n , the sensitivity can be transformed to n^3r/ϵ , the figure of merit of sensitivity. The intensity change is proportional to n^3r , but the amount of the fringing field coupled to the crystal increases as ϵ decreases.

Table I. Electro-optic crystals for external EOS

crystal	symmetry	n	r (ij)	ϵ	n^3r/ϵ	probing mode
LiNbO ₃	3m	2.23	30.8 (33)	32	11.7	T (L*)
LiTaO ₃	3m	2.18	30.8 (33)	43	7.3	T
KDP	2m	1.51	10.6 (63)	48	1.7	L
KTiOPO ₄	mm2	1.83	35	15.4	14.6	L
KTiOAsO ₄	mm2	1.8	40 (33)	18	13.0	T (L**)
Bi ₁₂ SiO ₂₀	23	2.5	5.0 (41)	56	1.4	L
Bi ₄ Ge ₃ O ₁₂	43m	2.1	1.0	16	0.6	L
GaAs	43m	3.5	1.2 (12)	12	3.9	L
ZnTe	43m	3.1	4.3 (12)	10	12.8	L
CdTe	43m	2.8	6.8 (12)	9.4	15.8	L
Bi ₁₂ TiO ₂₀	23	2.56	5.75 (41)	(~50)		L

T and L denote, respectively, transverse and longitudinal sensing, L*:55° cut, L**: z-cut

A high-impedance, handy-type EOS probe sensing the longitudinal probing was first developed for multi-GHz signal measurement of on-board ICs by using a typical sillenite Bi₁₂SiO₂₀ (BSO) single crystal³⁾. Among commercially available materials for a longitudinal probing, BSO crystal has a

relatively high optical/crystalline quality, as compared to KTP and ZnTe. However, for this handy-prober to be a practical reality, its voltage sensitivity must be further improved, because it consists of a very expensive fibber amplifier. Then, the author turned his attention to $\text{Bi}_{12}\text{SiO}_{20}$ (BTO) single crystal for use in EOS probe head, because it has the largest electro-optic constants r_{41} among sillenites so far reported in available literatures⁴⁾, a refractive index larger than that of BSO⁵⁾ and ϵ smaller than that of BSO.

4. CRYSTAL GROWTH OF BTO

According to the phase diagram of the Bi_2O_3 - TiO_2 binary system reported by Bruton⁶⁾, BTO melts incongruently at $873\sim 875^\circ\text{C}$, decomposing into liquid and $\text{Bi}_4\text{Ti}_3\text{O}_{12}$ associated with a peritectic reaction; the single phase BTO does not have any solid solution. Therefore, BTO single crystals are usually grown using the top-seeded solution growth (TSSG) pulling method from Bi_2O_3 - rich solution of less than about 12 mol% TiO_2 , far from the stoichiometric BTO (14.28₆ mol% TiO_2 composition)^{7,8,9,10,11)}. However, a standard method for growing BTO single crystals has not been established yet. For this purpose, the phase diagram reported earlier⁶⁾ was renewed experimentally.

4.1 Experiments

Ultra-high purity raw materials of Bi_2O_3 (99.995%) were used throughout this work. In establishing a substantial phase diagram close to the stoichiometric BTO (14.28₆mol% TiO_2), a differential thermal analysis (DTA) of binary compounds with different TiO_2 concentrations close to the stoichiometric composition was carried out in order to re-examine the peritectic reaction and eutectic temperatures. To clarify the peritectic composition experimentally, TSSG pulling was carried out with solution which varied between 10.25 and 11.25 mol% TiO_2 .

Single crystals of BTO were grown using a TSSG technique from off-stoichiometric solutions with various starting compositions of TiO_2 mol%. Growth apparatus has been reported elsewhere¹¹⁾, where about 350 gr total amount charged in a 40 cc Pt crucible. Three to five single crystals, typically 15~20 mm in diameter and about 25 mm in length, typically weighing about ~40 gr, were grown in succession from one starting solution. For successive growth from the initial solution, calcined stoichiometric BTO ceramics, equal in weight to the previously grown crystal, were added to the residual solution. The grown crystals were characterized by their lattice constants estimated with X-ray powder diffractometry using $\text{K}\alpha_1$ at room temperature with Si powder as a reference by means of the Nelson-Riley approximation method. Measurement accuracy was estimated to be less than $1 \times 10^{-4}\text{\AA}$. Samples were prepared from the first crystallized part immediately below the seed crystal. Further growth experiments of relatively long single crystals were carried out with 9.0 and 10.0 mol% TiO_2 solution to examine the change in lattice constants along the crystal. The change is discussed using the substantial phase diagram renewed here.

4.2 Results and Discussion

A. Phase diagram

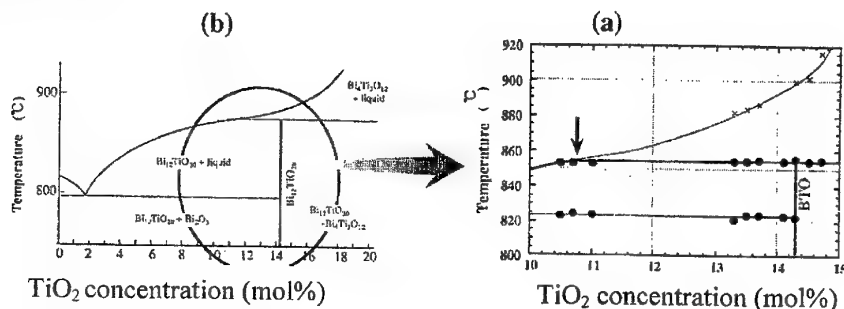


Fig.3 (a) Substantial phase diagram obtained by DTA (see text), and (b) the phase diagram reported by Bruton⁵⁾

Figure 3(a) shows the determined peritectic and eutectic reaction temperatures were determined to be $823 \pm 3^\circ\text{C}$ and $855 \pm 2^\circ\text{C}$, respectively. Surprisingly, the temperatures corresponding to the eutectic reaction were lower than those reported by Bruton⁶⁾ as shown in Fig.3(b). Since clear peaks corresponding to the liquidus temperature close to the peritectic composition could not be obtained on DTA curves, TSSG pulling was carried out with 10.25 to 11.25 mol% TiO_2 solution in order to verify the peritectic composition. Polycrystalline boules consisting of Bi_2O_3 , BTO and $\text{Bi}_4\text{Ti}_3\text{O}_{12}$ were obtained from 11.00 mol% TiO_2 solutions, while single phase BTO crystals were obtained from 10.50 mol% TiO_2 solutions. The boule grown from a 10.75 mol% TiO_2 solution looked polycrystalline (dominantly $\text{Bi}_4\text{Ti}_3\text{O}_{12}$), but the inside more than 95% of the lower half part was recognized to be a monocristalline BTO phase with a lattice constant of 10.1743\AA . This leads to the conclusion that the substantial peritectic composition must lie close to a 10.75 mol% TiO_2 concentration or less to some degree, different from Bruton's phase relation.

B. Lattice constant of the $\text{Bi}_{12}\text{TiO}_{20}$ single crystals

Figure 4 shows the estimated lattice constants of BTO single crystals grown in succession from each starting solution in mol% TiO_2 , where one point data of the crystals grown from 10.10 and 10.75 mol% TiO_2 solutions are added to the early result¹²⁾. The lattice constant decreased monotonously with an increased TiO_2 concentration, but those of crystals grown from a 9.0 mol% TiO_2 solution show the minimum. Noticeably, the lattice constants of crystals grown from 8.0 and 10.25 mol% TiO_2 solutions are larger than grown from a 9.0 mol% TiO_2 solution and are almost the same. This means that the crystal compositions grown from 8.0 and 10.25 mol% TiO_2 solutions must be very close to each other, regardless of point defects, such as anticitates and/or oxygen deficiency, and this strongly suggests that a solidus curve must be retrograde.

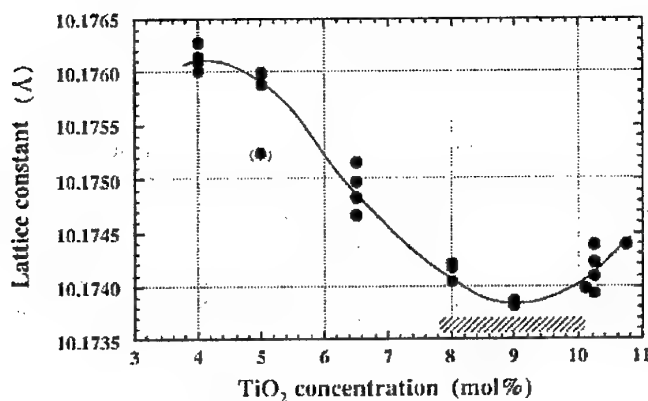


Fig.4 Lattice constant of single crystals against TiO_2 concentration in solution. This stoichiometry dependence is a proof of the retrograde solidus curve

C. Renewed phase relation of the solid solution

The standard deviation of calculated lattice constants of the single crystals grown from each solution was taken into account in drawing the solidus line of a solid solution. This is because the composition of the primarily crystallized phase corresponds predominantly to the solidus line in phase equilibrium. The deviation of lattice constants of the crystals grown from the 9.0 mol% TiO_2 solution showed a minimum value of $2.6 \times 10^{-5}\text{\AA}$. This means that the corresponding solidus line changes its slope (dT/dC_s , where T is the temperature and C_s is the TiO_2 concentration) from a positive to a negative one. On the other hand, the lattice constant deviation of other crystals became larger to some degree, which implies a gentle slope of the solidus line, especially that from a 10.25 mol% TiO_2 is relatively large.

Therefore, it can be said that the crystal composition grown from a 9.0 mol% TiO_2 solution must correspond to the turning point of a retrograde solidus curve, even when the starting solution composition changes to some degree by the successive adding of a stoichiometric compound equal in weight to that of the previously grown crystal. This proves the minimum deviation of lattice constants of the crystals grown from the 9.0 mol% TiO_2 solution.

Together with experimental results and the expected considerations described above, it is possible to draw the relevant part of the phase diagram in the hypo-peritectic region close to the stoichiometric composition of a BTO (14.28 mol% TiO_2).

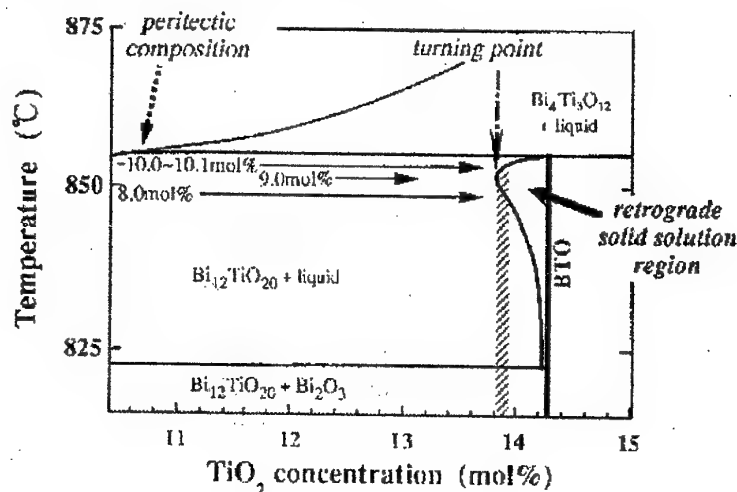


Fig.5 Substantial Bi_2O_3 - TiO_2 binary phase relation for growing BTO crystals

Figure 5 shows a renewed, substantial phase diagram with a plausible retrograde solid solution close to the stoichiometric BTO. We can consider that the turning point of the retrograde solidus curve lies around 13.80~13.85 mol% TiO_2 , based on the stoichiometry dependence on lattice constant of BTO phase in calcined ceramics. This retrograde characteristic is very similar to that in the solid solution regime of congruently melting $\text{Bi}_{12}\text{SiO}_{20}$ ¹³⁾, and clarified in the next section D.

The renewed phase relation implies that a very high reproducibility of the crystal composition from the 9 mol% TiO_2 solution is to be expected. We achieved reproducible growth of high quality BTO single crystals (relatively the same lattice constant) by adding stoichiometric ceramics equal in weight to that of the previously grown crystal, as shown in Fig.6.

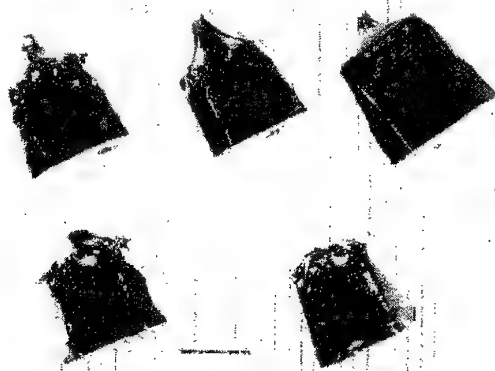


Fig.6 Successively grown BTO single crystals grown from a 9.0 mol% TiO_2 solution by adding stoichiometric ceramics

Because the stoichiometric of these crystals should be poorer in TiO_2 concentration than in stoichiometric BTO ones, we are now investigating the crystal chemistry of off-stoichiometric BTO single crystals grown from different starting solutions.

D. Growth of long single crystals

In the case of TSSG pulling, the starting solution composition changes gradually along the liquidus line as crystal grows up. The variation of the lattice constant along the crystal length was investigated by growing long single crystals. An about 53 mm long and 123.9 gr weighed single crystal was grown from a 10.0 mol% TiO_2 solution.

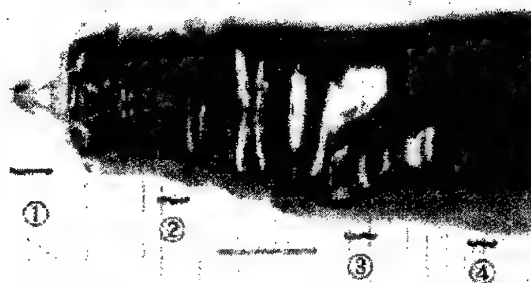


Fig.7 Long single crystal grown from a 10.0 mol% TiO_2 solution from which lattice constants at (1), (2), (3) and (4) were measured (see text)

Figure 7 shows the as-grown crystal, where the lattice constants of (1) the first crystallized part, (2) the upper part of the boule, (3) the lower part of the boule, and (4) the bottom part were evaluated to be 10.1741 \AA , 10.1739 \AA , 10.1745 \AA , and 10.1752 \AA , respectively. This change in lattice constants along the growth axis follows the retrograde solidus line shown in Fig.5 reasonably well. The lattice constants of the parts (1), (2), (3), and (4) correspond to crystals grown from 10.00~10.1 mol%, ~9.8 or 8.6 mol%, ~7.1 mol%, and ~6.1 mol% TiO_2 solutions, respectively, as results from Fig.4.

The single crystal grown from the 10.0 mol% TiO_2 solution had a solidified fraction of 49.7%, since the total amount of solution was which a BTO crystallizes 249.2 gr in weight. In referring to Fig.4, single crystals grown from solutions with TiO_2 concentrations of between ~7.5 and ~10.0 mol% have a lattice constant deviation of less than $\sim 1.0 \times 10^{-4} \text{\AA}$. Consequently, it can be said that a starting solution with a 10.0~10.10 mol% TiO_2 is very practical for growing relatively homogeneous single crystals whose lattice constants lie within $\pm 1 \times 10^{-4} \text{\AA}$ over the whole crystals boule, as indicated by the shadow bar in Fig.5, when a solidified fraction is at least less than 45% for this purpose.

5. EOS CHARACTERISTICS OF BTO

Fig. 8 shows examples of a BTO head prepared from the single crystals grown from a 9.0 mol% TiO_2 solution as shown in Fig.5. A high-reflective dielectric mirror was coated on one endface. These chips were mounted on a probe head, as illustrated in Fig.2, instead of the BSO chip, and the voltage sensitivity was measured. The voltage sensitivity was measured with a 1 V, 100 MHz sinusoidal signal on a standard micro-strip line³⁾. A handy-type EOS system with a probe head made of a BTO crystal has 1.5 times higher voltage sensitivity than one made with a BSO crystal¹⁴⁾.

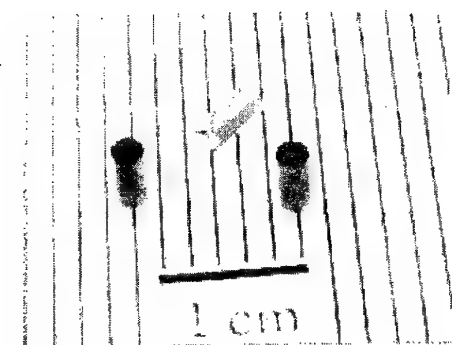


Fig.8 Samples of an EOS probe heads

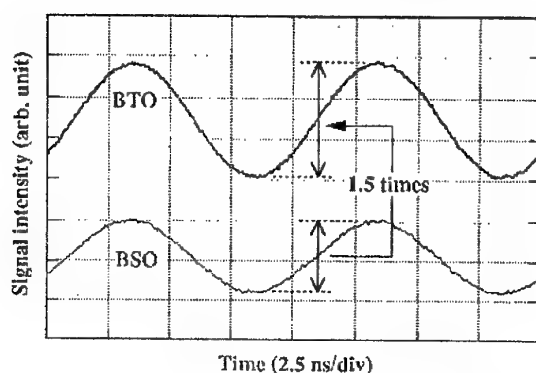


Fig.9 The improvement of voltage sensitivity using a BTO crystal head, as compared with using a BSO

Fig.9 shows the measured result and illustrates an improvement in voltage sensitivity of more than 1.5 times higher than that of a BSO head with precise manipulation. Since the shot-noise-limited expression for a minimum detectable voltage V_{\min} is given by Eq.(1) where V_{π} is inversely proportional to n^3r , the increase in sensitivity can be analyzed semi-quantitatively as follows, even though there is a lack of accurate values; r_{41} of a BTO is 1.15 ~ 1.4 times larger⁴⁾ and n is about 1.04 times larger than that of a BSO¹⁴⁾, that yields a 1.3 times larger n^3r_{41} than that of a BSO. By taking into account the difference in dielectric constants, a 1.5 times improvement in voltage sensitivity is reasonable.

More recently, Shinagawa et al.¹⁵⁾ succeeded in improving the total sensitivity of an EOS probe system up to 3.6 times higher than the earlier developed system made of a BSO probe using (a) a BTO probe head, (b) 1.3 μm laser diode and (c) by increasing the sampling rate. In this advanced and practical system, the use of a BTO crystal as a probe head was one of the key elements contributing to the improvement of voltage sensitivity.

6. SUMMARY

This paper presents the new application area of optoelectronics used electro-optic crystals, namely a handy-type EOS prober sensing high-speed electric signals in ICs. For that purpose, quadratic electro-optic crystal BTO was focused as a new, high sensitive probe head. For reproducible growth of the single crystals, the phase relation was re-examined and it strongly proved the existence of a solid solution region with a retrograde solidus curve whose turning point lies around 10.80 ~ 10.85 mol% TiO_2 , corresponding to an about 9.0 mol% TiO_2 solution. A starting solution with a 10.0~10.1 mol%

TiO₂ concentration and the solidified fraction of the crystal of less than about 45% will result in a relatively homogeneous single crystal whose lattice constant deviation is less than 1×10^{-4} Å.

The improvement in voltage sensitivity in the handy-type EOS system by replacing a BSO with a BTO for a probe head was verified, because the product n^3r of a BTO was estimated to be about 1.3 times larger than that of BSO. So the reproducible growth of the single crystal described in this paper is very effective for practical uses as an EOS probe head and is indispensable to reducing the total cost of the system.

Performances of optoelectronics devices/systems are strongly dependent on materials and crystal growth technology is key.

ACKNOWLEDGEMENTS

This paper was prepared while the author was in NTT System Electronics Labs., till March, 1998. The author wishes to express his thanks to T.Tabata, NTT Advanced Technology Corp. for his crystal growth experiments and lattice constant measurements, and to Drs.M.Shinagawa, T.Nagatsuma, and Y.Kato, NTT System Electronics Labs., for their EOS measurements. He is also indebted to Dr.M.Mukaida, Yamagata Univ., for his valuable comments and suggestions on lattice constant measurements.

7. REFERENCES

- [1]. Weingarten, K.J., Rodwell, M.J., and Bloom, D.M.; IEEE J.Quant.Electron, **QE 24**, p.198 (1988)
- [2]. Shinagawa, M. and Nagatsuma, T.; IEEE Trans.Instr.& Meas., **43**, p.843 (1994)
- [3]. Shinagaawa, M. and Nagatsuma, T.; IEEE Trans.Instr.& Meas., **45**, p.575 (1996)
- [4]. Wilde, J.P., Hesselink, L., McCarhon, S.W., Klein, M.B., Rytz, D., and Wechsler, B.A.; J.Appl.Phys., **67**, p.2245 (1990)
- [5]. Miyazawa, S. and Tabata, T.; NTT REVIEW, **10**, p.62 (1998)
- [6]. Burton, T.M. J.Sol.Sta.Chem., **9**, p.173 (1974)
- [7]. Burton, T.M., Brice, J.C., Hill, O.F., and Whiffin, P.A.C.; J.Cryst.Growth, **23**, p.21 (1974)
- [8]. Rytz, D., Wechsler, B.A., Nelson, C.C., and Kirby, K.W.; J.Cryst.Growth, **99**, p.864 (1990)
- [9]. Okano, Y., Wada, H., and Miyazawa, S.; Jpn.J.Appl.Phys., **30**, p.L1307 (1991)
- [10]. Miyazawa, S.; Opt.Mat., **4**, p.192 (1995)
- [11]. Miyazawa, S.; J.Cryst.Growth, **167**, p.638 (1996)
- [12]. Miyazawa, S. and Tabata, T.; J.Cryst.Growth, **191**, p.512 (1998)
- [13]. Brice, J.C., Hight, M.J., Hill, O.F., and Whiffin, P.A.C.; Philips Tech.Rev., **37**, p.250 (1977)
- [14]. Aldrich, R.E., Hou, S.L., and Harvill, M.L.; J.Appl.Phys., **42**, p.493 (1971)
- [15]. Shinagawa, M. and Nagatsuma, T.; Proc.of 1997 IEEE Instr.& Meas.Tech.Conf. (19~21 May, 1997, Ottawa, Canada), T34-2 (Shinagawa, M., Nagatsuma, T., and Miyazawa, S.; to be published in IEEE J.Quant.Electron., 1998)

SOME TECHNIQUES FOR IMPROVING THE CONFIDENTIALITY IN COHERENCE MODULATION SYSTEMS

B. Wacogne, A. Mokhenache, H. Porte, P. Mollier, D. A. Jackson*

Laboratoire d'Optique P.M. Duffieux, UMR 6603, Institut des Microtechniques de Franche-Comté, FR 0067, CNRS, Université de Franche-Comté, 25030 Besançon cedex, France. Tel.

Tel. (33) 1 81 66 65 63. Fax: (33) 1 81 66 64 23. E-mail: bruno.wacogne@univ-fcomte.fr.

*Physics Department, University of Kent at Canterbury, Canterbury CT2 7NR, United Kingdom

ABSTRACT

This paper, presents the research carried out in our Laboratory on the secure coherence modulation systems. Different techniques, based on the corruption of the transmitted signal are discussed in this manuscript. They consist in applying a key modulation to the emitter, in such a way that any eavesdropper detects a meaningless message. At the reception stage, the authorised receiver applies the right key to its decoder in order to restore the signal. Keying methods using delay lines and polarisation are proposed while experimental results are discussed in this paper.

1. INTRODUCTION

Over the last few years, considerable interest has been shown to secure transmissions. Among the different optical telecommunication systems, transmission techniques which are not based on the direct modulation of light can potentially be adapted for secure communications. Various properties of the light have been exploited to design confidential transmission demonstrators [1-5].

However, the focus of this paper is on coherence modulation (CM), also termed Optical Path Difference (OPD) modulation [6-8]. The scheme employs two interferometers in tandem, whose OPDs are larger than the coherence length of the source. One is used at the emission stage (hereafter the encoder), while the second at the reception stage (the decoder). Interference fringes are observed at the decoder output only when its OPD closely matches that of the encoder. This allows a signal to be transmitted. The scheme was thought to be secure since apparently, a perfectly matched decoding interferometer is required to restore the signal [8]. However, we recently showed that this is not the case since a simple chromatic filter enables any eavesdropper to tap the signal [9]. Different techniques have been proposed in order to enhance the security of the scheme [10-13].

The purpose of this paper is to describe new methods, which were first investigated at the University of Kent, United Kingdom, and are now developed in our Laboratory. The basic idea is to modulate both the encoder and the decoder with a dynamic key parameter. Any eavesdropper, who does not know the key parameter and/or the modulation applied onto it, detects a meaningless message composed of a combination of the signal to be transmitted with the modulation of the key parameter. At the reception stage, the authorised user applies the right modulation on the right parameter, and restores the signal efficiently. Please refer to part 2 for the classical coherence modulation scheme, and the explanation of how it is possible to tap the signal without the need for a specialised decoder. A scheme based on OPD scrambling, which is currently in demonstration at the Laboratory is presented in part 3. Part 4 is devoted to a technique using polarisation scrambling to encode the signal, which is also under investigation. Our conclusions are summarised in part 5.

2. CONVENTIONAL COHERENCE MODULATION: SECURITY VULNERABILITY

This section deals with the basics of CM and shows how it is possible to tap the signal without any specialised decoder. Consider figure 1, where the classical coherence modulation scheme is presented. The broadband source emits wave-packets denoted $s(t)$. Since the coherence length of the source is much smaller than the encoder's OPD, this initial wave-packet is split into two secondary

packets: $s_1(t) = s(t)/2$ and $s_2(t) = s(t - \tau_e)/2$, where τ_e is the differential time delay introduced by the encoder. By hypothesis, these packets do not overlap, and no interference is observed in the transmission link, where the intensity is therefore constant. This constitutes the first step toward security.

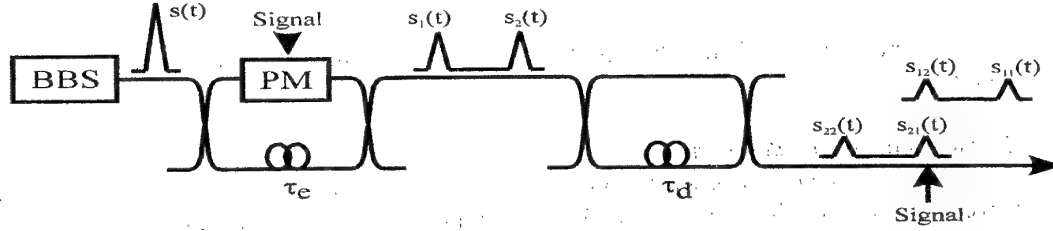


Fig. 1 Schematic diagram of the classical coherence modulation scheme. BBS: broadband source, PM: phase modulator

These twin packets, $s_1(t)$ and $s_2(t)$, propagate in the optical link and through the decoder whose differential time delay is τ_d . Again, they are split into four secondary packets. If the differential time delays of both the encoder and the decoder are matched, only $s_{12}(t)$ and $s_{21}(t)$ are overlapping and are producing interference's. The intensity, at the output of such a system is given by:

$$I_{det}(t) = \frac{P_0}{4} \left\{ 1 + \frac{1}{2} \cos \left(\pi \frac{d(t)}{V_\pi} - \frac{\pi}{2} \right) \right\} \quad (1)$$

where P_0 is the incident optical power, V_π the phase modulator half-wave voltage, and $d(t)$ the voltage applied to the phase modulator corresponding to the signal to be transmitted. Apparently, the system is secure because a perfectly matched decoder is required in order to decode the signal. However, we showed that this is not the case since a simple chromatic filter enables any eavesdropper to tap the signal [9]. To understand this, we refer to Fig.2, and we consider what happens in the spectral domain.

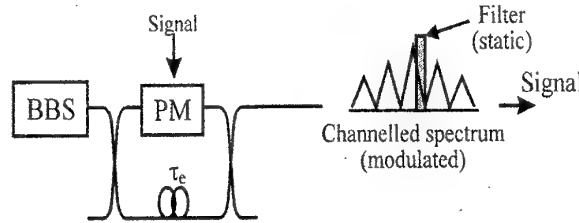


Fig. 2 Situation where a static chromatic filter is used to tap the signal. As the OPD of the encoder is larger than the coherence length of the source, a channelled spectrum exists in the transmission link. The peaks of the spectrum are modulated according to the signal, which allows an eavesdropper to tap the signal

Since the OPD of the encoder is much larger than the coherence length of the source, a channelled spectrum exists in the transmission link. The positions of its peaks are modulated according to the signal applied to the phase modulator. Therefore, a static chromatic filter with a bandwidth roughly matching the width of a channelled spectrum peak, enables an eavesdropper to tap the signal. However, although it is less convenient to use than a fibre Bragg grating, a scanning Michelson interferometer tuned to the correct OPD also reject the signal. So, the weakness in security of the initial CM scheme arises first, because it is easy to scan a Michelson interferometer until the coherence between the interfering wave-packets is found, and second, because of the existence of a channelled spectrum which is modulated only with the signal to be transmitted.

We are currently working on different techniques to enhance the security of coherence modulation. The first technique we propose has been demonstrated recently [14,15] and it consists of coding the interferometers OPD with a key applied simultaneously to their phase modulators.

3. OPTICAL PATH DIFFERENCE SCRAMBLING

The OPD scrambling method is briefly described below, while a complete presentation can be found in references [10,14,15].

3.1 Theoretical considerations

The method is based on the assumption that CM requires two interferometers exhibiting the same OPD. However, this is still valid when the OPDs are varying in time, under the condition that they are both subject to the same time dependent variations. Fig.3 gives a schematic diagram of the technique.

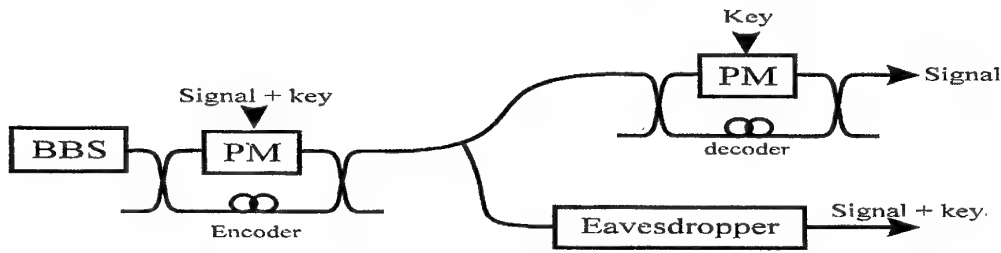


Fig. 3 Schematic diagram of secure coherence modulation by OPD scrambling

Since the OPDs of both interferometers can be subject to the same time dependent variation, we modulate the encoder not only with the signal to be transmitted, but also with a key. Consider first what happens at the reception stage when the correct key is applied. Since both OPDs are subject to the same time dependent variation, the operating point of the system is fixed and given by the factor $\pi/2$ in equation (1). Therefore, the interference signal only depends on the signal to be transmitted $d(t)$, and the message is correctly decoded. However, this is not the case for the eavesdropper whose OPD is not modulated. In this case, the operating point is determined by the key applied to the encoder. The interference signal is therefore given by the addition of the signal to be transmitted plus the key:

$$I_{eav}(t) = \frac{P_0}{4} \left\{ 1 + \frac{1}{2} \cos \left(\pi \frac{d(t) + k(t)}{V_\pi} - \frac{\pi}{2} \right) \right\} \quad (2)$$

where $k(t)$ represents the encoding key. Equation (2) shows that the message tapped by the eavesdropper is blurred by the encoding key.

3.2 Experimental confirmations

The method described above has been initially demonstrated at the University of Kent. The optical source was an Er Doped Fibre Amplifier, and the interferometers were built with single mode optical fibres. PZT cylinders were employed as phase modulators. The driving frequencies were therefore relatively low, but a first experiment was demonstrated. Later on, we demonstrated the OPD scrambling system in our Laboratory by using integrated optics Mach-Zehnder interferometers. In Fig. 4, we present an example of secure transmission at about 20 Mb/s, but higher data rate can be obtained by means of travelling wave electrodes [16] modulators. Also, when using integrated optics components, a particular care must be taken with the polarisation state of the light entering the modulator. However, the use of polarisation independent coherence modulators should overcome this problem [17].

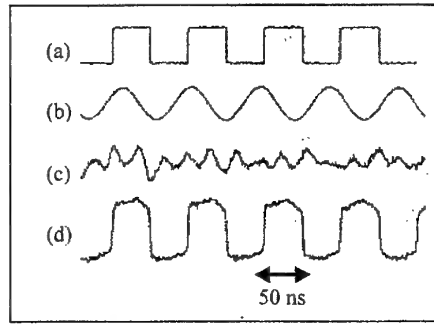


Fig. 4 Example of secure transmission at higher bit rate by means of integrated optics Mach-Zehnder interferometers. (a) Signal to be transmitted. (b) Key used to corrupt the signal. (c) Signal tapped by the eavesdropper when the key is applied. (d) Signal restored at the decoder output. In this example, the data rate is 20 Mb/s

The technique we have presented that can be used to enhance the security aspect of coherence modulation. A demonstrator of this technique is operating on a routine basis in our Laboratory. Presently, we are developing a second technique based the polarisation properties of the wave-packets propagating in the transmission link, presented below.

4. POLARISATION SCRAMBLING

In the method presented in part 3, the OPD of the interferometers were coded with a key. In the technique described hereafter, the idea is to dynamically code the state of polarisation of a wave packet propagating in one arm of the encoder. Consider an eavesdropper tapping the signal with a chromatic filter. If the polarisation of one wave-packet ($s_1(t)$ for example) is modulated, the visibility of the channelled spectrum is modulated accordingly. Therefore, the eavesdropper detects a meaningless intensity variation due not only to the signal itself, but also to the visibility variation caused by the polarisation modulation. At the decoder stage, the authorised receiver applies the same polarisation modulation. This makes the visibility of the interference signal constant, and the signal can efficiently be restored.

4.1 Theoretical considerations

The scalar description of the wave-packets propagating in the system has to be transposed to a vectorial form, X and Y being the axes orthogonal to the propagation of the light. The incident wave-packet $s(t)$ is supposed to be polarised along the X direction. The polarisation transformation is performed in one arm of the interferometers. We call M_e the Jones matrix representing the polarisation transformation in one arm of the encoder. It is given by:

$$M_e = \begin{pmatrix} A_e'(t) & B_e(t) \\ -B_e^*(t) & A_e^*(t) \end{pmatrix} \quad (3)$$

where * denotes the complex conjugate. The same notations, with the subscript "d" are used for the matrix M_d attached to the decoder. Consider an eavesdropper tapping the signal with an apparatus which does not include a polarisation scrambler. For him, $A_d(t) = A_d^*(t) = 1$, and $B_d(t) = B_d^*(t) = 0$. It can be shown that the intensity detected by the eavesdropper is given by:

$$I_{\text{av}}(t) = \frac{P_0}{4} \left\{ 1 + \frac{1}{2} \text{Re}(A_e(t)) \cos \left(\pi \frac{d(t)}{V_\pi} - \frac{\pi}{2} \right) \right\} \quad (4)$$

where Re denotes the real part. Equation (11) shows that the visibility of the tapped signal is modulated by the real part of the time dependent variable $A_e(t)$. Therefore, the modulation of the polarisation state can be used to code the signal.

At the reception stage, the signal detected by a receiver using the same polarisation scrambler as the one used in the encoder, i.e. $A_e(t) = A_d(t) = A(t)$ and $B_e(t) = B_d(t) = B(t)$ detects a signal given by :

$$I_{\text{det}}(t) = \frac{P_0}{16} \left\{ 3 + \left(|A(t)|^2 + |B(t)|^2 \right)^2 + 2 \left(|A(t)|^2 + |B(t)|^2 \right) \cos \left(\pi \frac{d(t)}{V_\pi} - \frac{\pi}{2} \right) \right\} \quad (5)$$

In the case of a lossless propagation medium, Jones matrices are unitary, which implies that $|A(t)|^2 + |B(t)|^2 = 1$. Therefore, equation (5) is reduced to equation (1), which shows that the signal is efficiently restored.

4.2 Early experimental results

This technique of polarisation scrambling is currently under experimental investigation. We have chosen two different approaches. First, we demonstrate the visibility modulation using a bulk Michelson interferometer with a polarisation scrambler inserted in one arm. Second, we consider the fabrication of integrated optics Mach-Zehnder interferometers including a polarisation rotator in one arm.

Visibility modulation in bulk optics

A bulk Michelson interferometer is illuminated with a broadband source at a central wavelength of 1.3 μm . The incident beam is vertically polarised. In one arm, we used a nematic liquid crystals cell oriented at 45° of the incident polarisation. The phase difference induced by the cell between its axes varies from 0 to 2π for driving voltages between 0 and 10 Volts. Therefore, a tunable elliptical polarisation state can be obtained in this arm. In the other arm, we inserted a second liquid crystal cell with one axis parallel to the incident polarisation in order to equalise the optical losses in both arms, and to enhance the visibility of the interferences. In Fig. 5, we show the evolution of the visibility of the channelled spectrum for different applied voltages. It can be seen that for 1.35 Volts, the visibility is zero. Here, the phase difference is equal to π and the interfering beams are orthogonal.

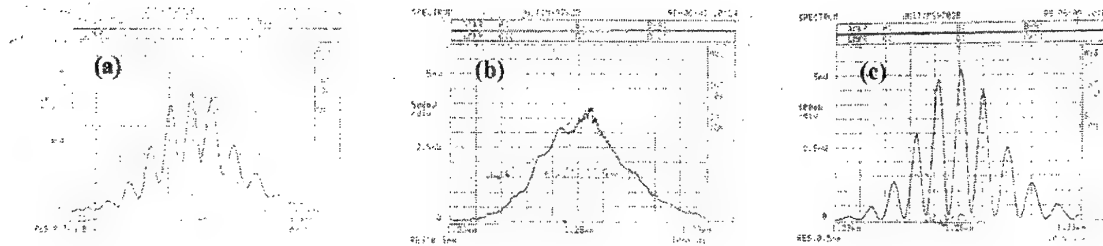


Fig. 5 Visibility of the channelled spectrum for: (a) 1.1 Volts, (b) 1.35 Volts, and (c) 10 Volts

Integrated Mach-Zehnder with a polarisation rotator

We are currently fabricating an integrated Mach-Zehnder interferometer, which includes a polarisation rotator in one arm. Fig. 6 shows the structure of the interferometer. A bent arm is used in order to obtain an OPD of about 100 μm , while a set of four electrodes is used to achieve a phase modulation in the bent arm and a polarisation rotation in the straight arm. The polarisation rotation is based on the coupling between the TE and TM modes that propagate in the straight waveguide. If

suitable sinusoidal electric fields are applied along the X and Y directions of the crystal, it is possible to rotate the polarisation state at the electric fields frequency (see Fig. 7). The voltages to be applied are given by:

$$V_x = V_{MC} \cos(\Omega t) \quad (6)$$

$$V_y = V_{\pi} \sin(\Omega t) + V_{PM}$$

where V_{MC} , V_{PM} , V_{π} , are the mode coupling, phase matching, and half-wave voltages, and Ω is the driving frequency. Therefore, a linearly polarised beam propagating through the rotator see its azimuth of polarisation rotating at a frequency Ω . An intensity modulation at a frequency 2Ω is observed, when the output of the rotator is seen through a polariser. We achieved such a polarisation rotator in our Laboratory a few years ago. Figure 8 gives an example of a polarisation rotation obtained with this rotator. Upper traces shows the two applied voltages in quadrature, while the lower trace presents the signal observed through a polariser, at twice the driving frequency.

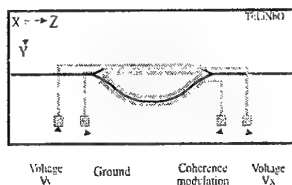


Fig. 6 Design of an integrated Mach-Zehnder interferometer including a polarisation rotator

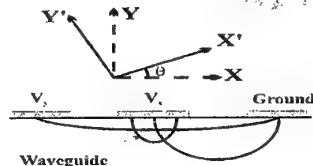


Fig. 7 Rotation of the principle axes by application of two orthogonal electric fields

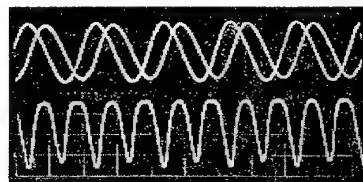


Fig. 8 Output of a polarisation rotator. Upper curves: driving voltages. Lower trace: signal transmitted

We are currently fabricating and testing an integrated interferometer including a polarisation rotator in one arm. Secure transmission results should be available soon.

5. CONCLUSION

In this paper, we have presented some techniques, initially investigated in the Physics Department, University of Kent, and currently developed in our Laboratory, in the field of secure coherence modulation. The methods are based on a dynamic coding of one optical parameter of the interferometers employed to transmit the signal. Of course, there is still to solve the difficult problem of synchronisation between the keys applied to both encoder and decoder, although the use of commercial broadcasts as a unique source for the key may be an issue. However, this problem is, in itself, a subject of intense research. This should be one of our focus points in the near future.

ACKNOWLEDGEMENTS

The authors would like to acknowledge the support of the EPSRC and the British Council.

6. REFERENCES

- [1] Bennett CH, Bessette F, Brassard G, Salvail L, and Smolin J, J. of Cryptology, Vol. 5, pp. 3-28, (1992)
- [2] Goedgebuer JP, Larger L, and Porte H, Phys. Rev. Lett., Vol. 80, No 10, pp.2249-2251, (1998)
- [3] Wacogne B, Jackson MD, Fisher NE, Podoleanu A, and Jackson DA, J. of Light. Tech., Vol. 14, No 5, pp.665-670, (1996)
- [4] Sampson DD, and Jackson DA, Opt.Lett., Vol. 15, No 10, pp. 585-587, (1990)
- [5] Mahric ME, and Yang YL, Elec. Lett., Vol. 25, No 22, pp. 1535-1536, (1989)

- [6] Porte H, Goedgebuer JP, and Ferriere R, J. of Light. Tech., Vol. 10, No 6, pp. 760-766, (1992)
- [7] Goedgebuer JP, Porte H, Hamel A, J. Quant. Elect., Vol. 23, No 7, pp. 1135-1144, (1987)
- [8] Yao SK, and Asawa CK, 7th Euro. Conf. Opt. Comm., Copenhagen, Denmark, Paper P29-1, (1981)
- [9] Wacogne B, and Jackson DA, Photon. Tech. Lett., Vol. 8, No 3, pp. 470-472, (1996)
- [10] Wells W, Stone R, and Miles E, J. of Selected Areas in Comm., Vol. 11, No 5, pp. 770-776, (1993)
- [11] Griffin RA, Sampson DD, and Jackson DA, J. of Light. Tech., Vol. 13, No 9, pp. 1826-1837, (1995)
- [12] Mazurenko YT, Giust R, and Goedgebuer JP, Opt. Comm., Vol. 133, pp. 87-92, (1997)
- [13] Karafolas N, Gupta GC, and Uttamchandani, Opt. Comm., Vol. 123, pp. 11-18, (1996)
- [14] Wacogne B, and Jackson DA, Photon. Tech. Letters, Vol. 8, No 7, pp. 947-949, (1996)
- [15] Wacogne B, Elflein W, Pieralli C, Mollier P, Porte H, and Jackson DA, Opt. Comm., Vol. 154, No 5,6, pp. 350-358, (1998)
- [16] Gutierrez-Martinez C, Porte H, and Goedgebuer JP, Microwave and Opt. Tech. Lett., Vol. 10, pp. 66-70, (1995)
- [17] Hauden J, Porte H, Goedgebuer JP, Gibassier C, Abiven J, and Gutierrez-Martinez C, J. of Light. Tech., Vol. 14, No 7, pp.1630-1638, (1996).

Session A1

**MATERIALS FOR OPTOELECTRONICS
AND RELATED FIELDS**

OPTICAL LIMITING IN POROUS SILICON FILMS

I. Cojocaru, V. Karavanskii*, V. Pasat, and V. Chumash

Centre of Optoelectronics, Institute of Applied Physics of the Academy of Sciences, 1 Academiei St., Chişinău, MD-2028, Moldova. Phone: (373-2)723481, Fax: (373-2)739805, E-mail: chumash@cc.acad.md, cojocaru@as.md.

* Institute of General Physics, Russian Academy of Sciences, 38 Vavilov St., Moscow, 117942, Russia. Phone: 007-(095)-1328226, Fax: 007-(095)-1328173, E-mail: karavan@kapella.gpi.ru

ABSTRACT

The peculiarities of the nonlinear interaction of strong laser pulses with free-standing porous silicon thin films have been studied at room temperature, showing that porous silicon is an interesting material for optical limiting devices. The mechanism of nonlinear light absorption in PS, taking into account the interaction with nonequilibrium phonons and localized on the structure inhomogeneities vibrational modes have been suggested as an explanation.

1. INTRODUCTION

The constant interest for porous silicon (PS) in the past years has been connected to the potential applications of this material in Si-based optoelectronics. Assuming quantum confinement effect and the possibility of optical band gap control, PS becomes a very attractive material for visible Si optoelectronic devices, including active ones.

The non-linear light transmission in PS is studied in a large temporal range, but most of the papers deal with millisecond [3] and picosecond/femtosecond [3-5] time scales. The ultrafast nonlinear phenomena are important for all-optical switchers, while the slow optical nonlinear effects are suggested for parallel operations [6]. Equally interesting is PS application for optical limiting or noise reduction [7].

Our paper presents the peculiarities of optical power limiting during the nonlinear propagation of strong laser pulses in free-standing PS thin films.

2. PS SAMPLES PREPARATION AND CHARACTERISTICS

The PS films (thickness $d=16 - 25 \mu\text{m}$) were prepared by anodization in the dark from bulk commercial Si substrates (KES 0.01), $0.01 \Omega\text{-cm}$, (111) cut orientation. After that, for free-standing film separation the current density was switched sharply to $j = 70 \text{ mA/cm}^2$. Free-standing PS films were rinsed by ethanol and dried in air stream. PS samples prepared in this way have very low visible photoluminescence efficiency under Ar laser excitation ($\lambda = 488 \text{ nm}$) and weak dark red photoluminescence under UV line excitation of He-Cd laser ($\lambda = 325 \text{ nm}$).

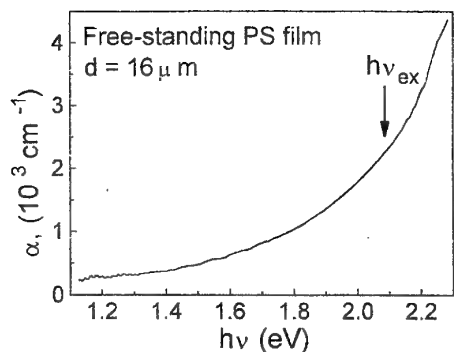


Fig. 1 Optical absorption spectra of free-standing PS film. Arrow - laser wavelength position

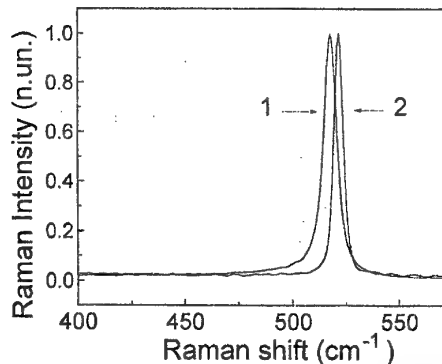


Fig. 2 Raman spectra of free-standing PS film (1) and initial Si substrate (2)

The used PS thin films are optical homogeneous. Fig. 1 shows the optical absorption spectrum for measured PS film with $0.16 \mu\text{m}$ thickness. Information about PS samples can be obtained from the Raman spectra (Fig. 2). Thus, one can see that the free-standing PS has a low-frequency shifting of the Raman peak (517.5 cm^{-1}) with a small broadening in comparison with the Raman peak of initial bulk crystal substrate (521.5 cm^{-1}). This is a typical Raman picture behavior for PS samples, determined by the phonon confinement and by the strains owing to huge specific surface area. Analysis of the Raman peak form point at good crystallinity of porous layers and the contribution of amorphous phase is estimated to be less than 2%.

3. EXPERIMENT

The experiments were done in a single-beam transmission or reflection setup, which has allowed to measure synchronously the fluence of incident (E_0), transmitted (E_t) or reflected (E_r) pulses. The measurements were carried out using a rhodamine 6G flash-lamp pumped dye laser ($h\nu_{\text{ex}} = 2.09 \text{ eV}$, pulse duration (FWHM) $\tau_{\text{ex}} \approx 0.9 \mu\text{s}$, bandwidth $\Delta\lambda_{\text{ex}} \approx 0.1 \text{ nm}$). The wavelength of the dye laser generation was over the range of the strong light absorption of the material (where the absorption coefficient α was more than $2 \cdot 10^3 \text{ cm}^{-1}$, Fig. 1). Both input and output/reflected laser pulses were registered by coaxial vacuum photodetectors (time resolution $< 10^{-9} \text{ s}$) and an oscilloscope. In order to avoid the effect of the light fluence decreasing due to the photodetector size limitation (or induced light scattering), vacuum photodetectors with large diameter of photocathode ($\sim 5.5 \text{ cm}$), situated no far from the sample, were used. The spot diameter of the focus on the sample laser beam was $\sim 0.2 - 0.3 \text{ mm}$, and an input fluence up to 1 J/cm^2 was achieved. All experiments were done at room temperature.

4. RESULTS AND DISCUSSION

Fig. 3 shows the transmitted through PS sample pulse fluence as a function of the input fluence. At input fluences higher than the threshold value $E_{\text{th}} \approx 0.08 - 0.1 \text{ J/cm}^2$, an increase of the light absorption in PS was detected, leading to sublinear dependence of the output fluence from the input one. PS film seems to work like a power limiter for strong laser pulses. Thus, for example, at $E_0 = 0.3 \text{ J/cm}^2$ (lower than the pulse fluence E_d , where damaging of the sample surface may occur), the transmission of PS film (with $16 \mu\text{m}$ thickness) decreases by a factor of about 2. The measured nonlinear absorption changes are reversible up to E_d (Fig. 3), and no residual effects are detected (within experimental errors $\sim 20 \%$). This was tested by measurements performed with increasing and decreasing incident fluence on the same place of the sample.

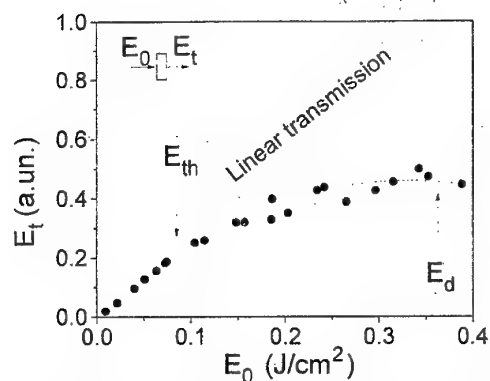


Fig. 3 Pulse fluence transmission of PS sample (thickness 16 μm) versus the input one

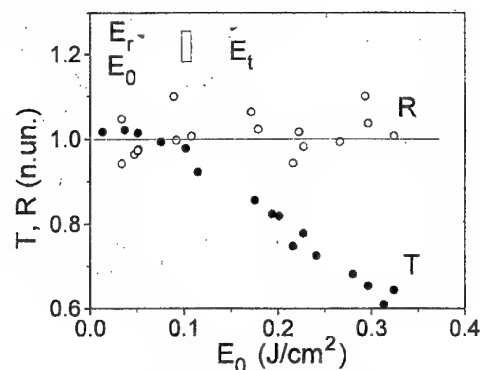


Fig. 4 Normalised transmission (T) and reflection (R) from the PS film vs. pulse input fluence. Beam incident angle $\sim 20^\circ$

In order to elucidate the physical mechanisms which contribute to nonlinear laser pulse absorption in PS, the behaviour of light reflected from the surface of the sample in a regime of laser pulse nonlinear transmission was also measured. Fig. 4 shows the reflection and transmission of PS film of the normalised laser pulse energy versus laser input fluence. Up to $\sim 0.3 \text{ J/cm}^2$ no increase is detected in the reflected light. This points to a real increase of the PS light absorption that can not be related to a carrier concentration increase in the excited region, or to the melting of the material on the region's surface.

The induced light absorption in PS films was investigated in [3, 8-13]. Under the ultrashort pulse excitation a very large nonlinear light absorption in free-standing PS were detected. The initial induced light absorption peak is assigned to free carrier absorption or two-photon absorption in Si microcrystals [12]. The decay of this nonlinear absorption has two components: fast and slow. The fast (picosecond) recovery is attributed to rapid thermalization of the photoexcited carriers to the surface states [3, 8, 12, 13] or to bimolecular radiative recombination [9-11]. The slow response nonlinearity in PS (from nanosecond [11] to millisecond [3, 9]) is connected to the carrier localization on the surface states of Si microcrystals. The thermal effects due to laser heating may also play a significant role, since PS has an extremely low thermal conductivity [3]. As mentioned in [3], the results of time-resolved transmission measurements suggest that PS acts as an indirect band gap semiconductor or disordered semiconductor and Si nanocrystalline core state has indirect gap properties [3, 8-13]. The investigations of carrier dynamics in PS, a-Si:H, c-Si and GaAs samples performed under identical conditions by femtosecond time-resolved spectroscopy confirm the indirect band gap structure of PS [12].

Transitions with a simultaneous participation of light quanta and phonons play a considerable role in the interband light absorption of the indirect band gap semiconductors [1,2]. PS possesses a large specific surface and consequently a large concentration of structure inhomogeneities of crystalline silicon in nanometric scale, which lead to some spatial localization of the phonon vibrational modes, and as a result contributes to nonequilibrium state formation at a high level of laser excitation. The capture of nonequilibrium phonons by such inhomogeneities increases their effective lifetime [14]. This, in its turn, leads to a change of the light absorption coefficient as a result of the appearance (or disappearance) of additional optical transition channels between the earlier forbidden (or less probable) band states. Analogous nonlinear photoinduced absorption was measured in typical indirect gap semiconductor (noncrystalline semiconductors, including a-Si:H films [1,2] and c-Si [14]).

We suggest that the mechanism of nonlinear light absorption, taking into account the interaction with nonequilibrium phonons and localized vibrational modes [1,2] can be applied in case of high excitation of PS samples.

5. REFERENCES

- [1]. V.Chumash, I.Cojocar, E.Fazio, F.Michelotti, M.Bertolotti. Progress in Optics 36, 1 (1996).
- [2]. A.Andriesh, V.Chumash. Pure Appl. Opt. 7, 351 (1998).

- [3]. Y.Kanemitsu. Phys.Reports 263, 1 (1995).
- [4]. V.I.Klimov, V.S.Dneprovskii, V.A.Karavanskii. Appl.Phys.Lett. 64, 2691 (1994).
- [5]. V.Klimov, D.McBranch, V.Karavanskii. Phys.Rev.B 52, R16989 (1995).
- [6]. H.M.Gibbs. Optical Bistability: Controlling Light with Light. Academic Press, 1985.
- [7]. S.D.Smith. Applied Optics 25, 1550 (1986).
- [8]. T.Matsumoto, O.B.Wright, T.Futagi, H.Mimura, Y.Kanemitsu. Journ Non-Cryst.Sol. 164-166, 953 (1993).
- [9]. P.Maly, F.Trojanek, J.Kudrna, A.Hospodkova, S.Banas, V.Kohlova, J.Valenta, I.Pelant. Phys.Rev.B 54, 7929 (1996).
- [10]. P.Maly, J.Kudrna, F.Trojanek, A.Hospodcova. Thin Solid Films 276, 84 (1996).
- [11]. F.Trojanek, P.Maly, I.Pelant, A.Hospodcova, V.Kohlova, J.Valenta. Thin Solid Films 255, 77 (1995).
- [12]. J. von Behren, Y.Kostoulas, K.Burak Ucer, P.M.Fauchet. Journ.Non-Cryst.Sol. 198-200, 957 (1996).
- [13]. J.C.Owrutsky, J.K.Rice, S.Guha, P.Steiner, W.Lang. Appl.Phys.Lett. 67, 1966 (1995).
- [14]. R. Orbach. J. Non-Cryst. Sol. 164-166, 917 (1993).

ANOMALOUS BEHAVIOR OF DRIFT MOBILITIES DURING FIELD-ASSISTED MIGRATION OF IONS IN OPTICAL GLASS

A. Lupascu, C. P. Cristescu, A. Kevorkian*, I. M. Popescu

Physics Department, University "Politehnica", 313 Spl. Independentei, 77206 Bucharest, Romania,

Phone : (401)-410 45 85/102, e-mail: cripoco@physics2.physics.pub.ro

* GeeO, Institut National Polytechnique, 42 Av. Félix Viallet, 38031 Grenoble Cedex, France,

Phone: (33)-0-476 57 47 95, Fax: (33)-0-476 57 45 84, e-mail: Antoine.Kevorkian@inpg.fr

ABSTRACT

During field-assisted migration of Ag^+ ions in Na^+ containing glasses we have observed that drift mobilities and diffusion coefficients do not follow the Nernst-Einstein relationship the diffusion coefficients vary almost 15 times with ionic concentrations, whereas mobility variations are only about 20%. This effect is a consequence of a local space charge build up at concentrations of incoming ions greater than the transition concentration, defined as the concentration for which the diffusion coefficients of the ionic species are equal. The resulting model applies to all profiles of Ag^+ - Na^+ inter-diffusion in silicate glasses.

1. INTRODUCTION

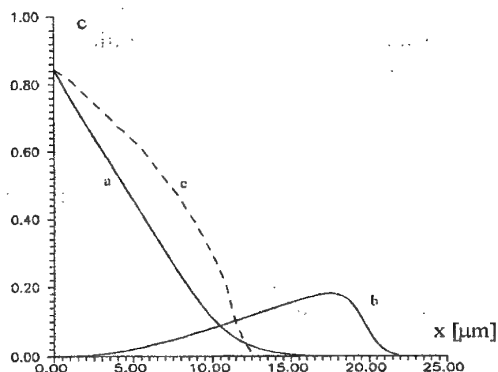


Fig. 1 One of the methods used in the elaboration of integrated optical circuits is ion exchange in glass

We shall investigate only ionic exchanges between glass and a molten salt. The glass containing the host monovalent cation b is immersed in a fused salt bath containing the foreign ions a , chosen so as to locally increase the refractive index. Usually a two-step process is used:

- a pure thermal diffusion introduces foreign ions into the glass and a surface guide results (curve a, Fig. 1)
- a field-assisted diffusion in a bath containing the host ions b buries the waveguide (curve b, Fig. 1)

Another possibility would be to use from the beginning an electric field. The process is called field-assisted migration (FAM). The resulting profile is steeper (curve c, Fig. 1).

In a recent paper [1], we have presented a thorough modeling of ionic inter-diffusion in glass, which takes into account the concentration dependence of diffusion coefficients and mobilities. The model rests upon a series of assumptions, the most important being listed below:

- i) Only mono-valent cations participate to the diffusion processes;
- ii) Mechanical stress may be neglected. This is true e. g. for the Ag^+ - Na^+ exchanges;

iii) Local neutrality is respected all over the glass, during all fabrication steps; iv) The mechanisms of thermal diffusion and of field assisted drift are similar. This assumption allows the use of the Nernst-Einstein relationship between diffusion coefficients and mobilities :

$$\mu_i(c_i, T) = \frac{eD_i(c_i, T)}{HkT}, \quad i=a, b \quad (1)$$

where: e -electronic charge, k -Boltzmann constant, H -Haven ratio, T -temperature. Index a refers to incoming ions, e. g. Ag^+ , index b to host ions, such as Na^+ .

Let us introduce the usual notations: c_0 - the initial, constant concentration of host ions, $c = c_a/c_0$ - the reduced concentration of incoming ions, $J_0 = J_a + J_b$ - the density of the total ionic flux, which is non-zero only when an external electric field is applied. Define the quantity

$$\alpha(c) = 1 - \frac{D_a(c)}{D_b(c)} \quad (2)$$

The concentration dependence for a typical silicate glass was found in [1] to be of the type:

$$D_a(c, T) = D_{oa}(T) \exp[ac^2] \quad D_b(c, T) = D_{ob}(T) \exp[b(1-c)^2] \quad (3)$$

where $D_{oi}(T)$ are Arrhenius-type functions, while the local neutrality was assumed.

Nernst-Einstein relation (1) suggests that the mobilities should obey the same exponential law. The law is true indeed for all thermal, as well as for buried profiles (curves a and b in Figure 1). However, this turns out to be false for FAM. The objective of our study is to set forth this anomalous behavior of drift mobilities and to propose an explanation for it.

2. LOCAL ELECTRIC EFFECTS DURING FIELD-ASSISTED IONIC EXCHANGES

The assumption of local electric neutrality is quite inexact. A local space charge ρ appears whenever an electric current, be it constant, flows through an inhomogeneous material. Indeed, Gauss equation and Ohm's law give :

$$\nabla(\varepsilon \mathbf{E}_0) = \nabla \left(\varepsilon \frac{\mathbf{J}_0}{\sigma} \right) = \mathbf{J}_0 \nabla \left(\frac{\varepsilon}{\sigma} \right) = \rho \quad (4)$$

The charge is zero during pure thermal exchange ($\mathbf{J}_0 = 0$) and has negligible effects in burying processes [2]. The approximation of zero space charge is written $c_a(\mathbf{r}, t) + c_b(\mathbf{r}, t) = c_0$ and allows to compute an expression for the local electric field (see e. g. [3]) :

$$\mathbf{E}_0 = \frac{Hk_B T}{e} \frac{\mathbf{J}_0}{c_0 D_b} \frac{1}{1 - \alpha(c)c} - \frac{Hk_B T}{e} \frac{\alpha(c) \nabla c}{1 - \alpha(c)c} = \mathbf{E}_{\text{ext}} + \mathbf{E}_{\text{diff}} \quad (5)$$

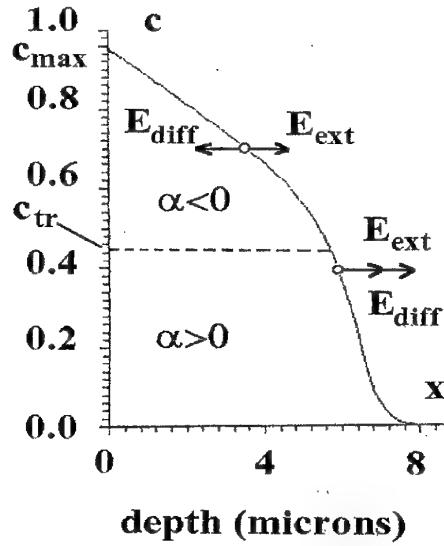


Fig. 2 The above relation was used only for constant diffusion coefficients

Taking into account that concentration dependence of relevant quantities leads to a new phenomenon, namely the coexistence, in the same diffusion profile, of two cases, the stable, as well as the unstable one, introduced by Cooper and Abou-El-Leil in [4]. Indeed, let us define the transition concentration c_{tr} as the concentration for which the diffusion coefficients are equal :

$$D_a(c_{tr}) = D_b(c_{tr}), \quad \text{hence} \quad \alpha(c_{tr}) = 0 \quad (6)$$

From Eq. (5) one sees that the term E_{diff} changes its sign around c_{tr} , the situation being sketched in Figure 2. At concentrations higher than c_{tr} , E_{diff} opposes to the main ionic flux, i. e. it points towards the glass surface. This phenomenon helps to build up a space charge, the net effect of which is to make the drift mobility almost constant.

3. DRIFT MOBILITY DURING FIELD-ASSISTED MIGRATIONS

We have studied the dependence of the mobilities on the concentration using different FAM profiles. Our method is a generalization of the usual Boltzmann method used to obtain $D(c)$ from the experimental profile of a pure thermal process $c(x)$. The Boltzmann method begins with the diffusion equation written in one dimension :

$$\frac{\partial c}{\partial t} = \frac{\partial}{\partial x} \left(\tilde{D}_a(c) \frac{\partial c}{\partial x} \right), \quad \text{where} \quad \tilde{D}_a(c, T) = \frac{D_a(c, T)}{1 - \alpha(c, T)c} \quad (7), (8)$$

Using the new variable $y = xt^{-1/2}$, and integrating Eq. (7), after a little algebra one finds the inter diffusion coefficient $\tilde{D}_a(c)$ (see e. g. [5]) :

$$\tilde{D}_a(c) = -\frac{1}{2t_1} \frac{dx}{dc} \int_0^c x(c') dc' \quad (9)$$

with t_1 the duration of the thermal diffusion. Field-assisted processes are described by the following equation (index M indicates migration, the inter-mobility $\tilde{\mu}_a$ is defined analogous to $\tilde{D}_a(c)$):

$$\frac{\partial c_M}{\partial t} = \frac{\partial}{\partial x} \left(\tilde{D}(c_M) \frac{\partial c_M}{\partial x} \right) - \frac{\partial}{\partial x} (c_M \tilde{\mu}_a(c_M) E_0) \quad (10)$$

A generalization of the procedure going from Eq. (7) to Eq. (9) leads to the desired result :

$$c_M \tilde{\mu}_a(c_M) E_0 = \tilde{D}_a(c_M) \frac{dc_M}{dx} + \frac{1}{2t_2} \int_0^c x(c'_M) dc'_M \quad (11)$$

with t_2 the duration of the FAM. Inserting in (11) the function $\tilde{D}_a(c)$ computed from a pure thermal diffusion, one obtains the inter-mobility $\tilde{\mu}_a(c_M)$. The two curves are shown together in Figure 3.

They ought to be proportional, if the Nernst-Einstein relations (1) were true. Instead, we observe that $\tilde{D}_a(c_M)$ grows 15 times, whereas $\tilde{\mu}_a(c_M)$ remains almost constant (if fact it decreases by 20%). *This anomalous behavior contradicts Nernst-Einstein relations.* However, we believe these relations remain valid even for FAM.

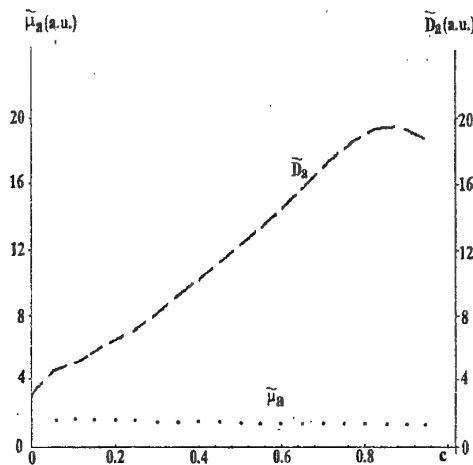


Fig. 3

We explain the apparent constant value of the drift inter-mobility as an effect of the aforementioned manifestation of a local space charge, high enough to have appreciable effects. This happens at concentrations higher than c_{lr} , because at such high concentration levels the diffusion term of the electric field, E_{diff} , changes its sign and opposes to the ionic flux. As a result, in the region where $c > c_{lr}$, ions are slowed down and accumulate. This piling up would eventually prevent some of the ions to participate to the drift.

To test our hypothesis, we have performed a fit of FAM profiles using for the mobility the following compound function :

$$\tilde{\mu}_a(c_M) = \begin{cases} \frac{e\tilde{D}_a(c_M)}{HkT} & \text{for } c_M < c_{tr} \\ \frac{e\tilde{D}_a(c_{tr})}{HkT} = \text{const} & \text{for } c_M > c_{tr} \end{cases} \quad (12)$$

We have succeeded to accurately model all the ionic inter-diffusion profiles, be them pure thermal, buried, or FAM. *Very dissimilar curves, as those from Figure 1, may be described with exactly the same five parameters, D_{oa}, D_{ob}, a, b, H . But in order to do this, the inter-mobility must be kept constant for concentrations higher than c_{tr} .*

4. DISCUSSIONS

Why the anomalous behavior of mobilities is not present during thermal diffusion, or field-assisted burying? With regard to pure thermal processes, only a small part of their profile lies above the transition concentration. Moreover, as in this situation the total ionic flux J_0 is certainly zero, the space charge given by Eq. (4) is zero too.

As for the field assisted burying, the entire final profile remains below the transition concentration. In the first moments of the current set-up, it seems that the effects of the space charge should be perceptible. However, this is prevented by the particular way the burying takes place. Indeed, the burying begins with a process of glass heating in the oven, without any contact with the salt bath. During this period, an important re-diffusion takes place. When the electric current begins to flow through the glass, the concentration of incoming ions is below c_{tr} in all points.

We have found a departure from the Nernst-Einstein relation (1) in all the FAM studied so far. This anomalous behavior may be explained by a space charge build up at high concentrations of foreign ions and by an associated supplementary electric field. These two effects can not be discriminated by optical studies, because the term responsible for both contains the product $c\tilde{\mu}_a(c)E_0$.

All the deviations from a simple proportionality between diffusion coefficients and mobilities become important at concentrations above c_{tr} . Therefore we believe this transition concentration is an important quantity in ionic inter-diffusion.

5. REFERENCES

- [1]. Lupascu A., Kevorkian A., Boudet T., Saint-André F., Persegol D., Levy M, Opt. Eng., vol. 35, pp. 1603-1610, (1996)
- [2]. Ramaswami R. V., Srivastava R., J. Lightwave Technol., vol. 6, pp. 984-1002, (1988)
- [3]. Albert J., Lit J. W. Y., Appl. Opt. Vol. 29, pp. 2798-2804, (1990)
- [4]. Abou-El-Leil M., Cooper A. R., J. Am. Ceram. Soc., vol. 62, pp. 390-395, (1979)
- [5]. Crank J., "The mathematics of diffusion", Clarendon Press, Oxford, 1956.

CATHODOLUMINESCENCE FROM OPTOELECTRONIC MATERIALS

T. A. Nazarova, M. V. Nazarov

Technical University of Moldova, Kishinev, MD-2012, Moldova
e-mail: nazarov@phys.moldova.su

ABSTRACT

Various measurement methods based on the phenomena connected with electron penetration into solids materials are presented below. Particular attention is paid to colour cathodoluminescence in scanning electron microscopy (CCL-SEM). The possibilities of these methods are illustrated by micro-characterisation of such optoelectronic crystals as BGO ($\text{Bi}_4[\text{GeO}_4]_3$), MgO, ZnS, ZnSe and thin crystal layers, formed by different diffusion doping. The methods allow to reveal spatial distributions of impurities and other point defects, which are of prime importance for the optoelectronic device industry.

Keywords: cathodoluminescence, point defects, annealing, BGO, MgO, ZnS, ZnSe.

1. INTRODUCTION

Recently it had been celebrated a century of electrons. During this short historical period, the phenomena induced by the electron-beam in different materials have changed our life cardinally: they have given us modern television and computers' display and continue to provide science and industry with the most powerful tools such as electron microscopy, electron probe microanalysis, electron beam microrecording, electron holography and others.

We all depend on our previous history. Even a crystal, presenting a system of the highest order no exception to this rule. For example, grown conditions, doping, annealing and mechanical damage can dramatically change optical characteristics of crystals and create a lot of difficulties to manufacturers of optoelectronic materials. The major issue is how to characterise the quality of performed material with maximal volume of information and minimal negative influence of the applied measurement methods.

We present below various measurement methods, based on the colour cathodoluminescence (CCL) in scanning electron microscopy (SEM), as well as combinations of CCL-SEM with backscattered electron (BSE) mode and computer graphics.

2. METHODS

2.1 Possibilities of SEM in materials science

SEM characterisation of semiconductor and dielectric crystals is based on local electron beam induced injection of electrons and holes. These carriers, once created, can undergo several processes. They can be removed from a particular region of the sample by an internal or external field, they can be trapped, or they can produce photons or phonons. These processes are the physical fundamentals of such techniques as electron beam induced current (EBIC), scanning deep level transition spectroscopy (SDLTS), cathodoluminescence (CL) and others. The interdependent character of these processes can be very helpful in approaching the challenging task of quantifying the SEM analysis of crystals, in particular the analysis of defects in these materials. There are several problems to be solved in this respect. One of them stems from the fact that the defect-related contrast in any of the techniques mentioned is a complex multi-parameter function of the physical properties of the defect and of the material. This makes the quantitative analysis very difficult, and one possible way is a combined utilisation of various techniques. In fact, such an approach is used today when combining different SEM modes to analyse the same object.

In recent years the SEM has moved largely from a picture-taking instrument, providing qualitative photographic information, to more of a quantitative instrument useful in many scientific disciplines, as well as in industrial applications. Therefore, better understanding of the derivation of the

signals being viewed and measured in the SEM is necessary. The possibilities of SEM techniques for the measurement of local properties of semiconductor structures and for revealing the physical property inhomogeneities in microelectronic structures are discussed. We have chosen some traditional and some original modes and image processing to illustrate these possibilities. The results of experimental investigations of some semiconductor and dielectric materials by conventional techniques (such as backscattered electrons) as well as by new techniques (such as colour cathodoluminescence defectoscopy and others) are presented.

2.2 CCL methods

CL means the electron beam-induced light emission from organic or inorganic materials exhibiting an electronic band structure with a band gap energy from about 6 down to 0.6 eV. In such materials the electron beam creates electron hole pairs which can recombine radiatively to emit light in the wavelength range from the ultraviolet to the near infrared (200-2000 nm). The recombination processes result not only from transitions between the band edges, but can also involve additional energy levels within the band gap which can be created by vacancies, impurities, dopants or other defects. Therefore, CL spectral analysis can also yield material specific information. The electronic transitions between the conduction band and valence band gap can be detected by CL measurements. Most semiconductors and insulators show local changes in the energy gap structure due to the presence of defects. Hence, investigation of defect distribution in such materials can be successfully performed using CL measurements.

Our proposed method is based on the application of the CL modes in the SEM for both the spectral and spatial characterisations of the material of interest. It provides recognition of impurities and a structural defect induced by thermal treatment itself as well as by diffusion doping of the crystal's subsurface layers. In our work the CL examinations were carried out using a modified SEM "Stereoscan" with a special attachment for CCL (1,2) and a solid state barrier counter for measurement of BSE current, integrated with a CCL-light collector. The BSE-detector was located near the specimens under parabolic mirror. Undistorted CCL- and BSE- signals were detected simultaneously during electron beam scanning.

3. RESULTS AND DISCUSSION

3.1 Magnesium Oxide, MgO

MgO yields only to diamond in its high hardness, melting point, and resistance to chemical attack and, of course, in price. These features make it widely used in industry and advanced technology. Besides, MgO is a traditional object for fundamental studies of structural defects, occurring by nature and design in real crystals. Hence, it is of interest to find a sensitive method for examining this stable material under extreme conditions.

Generally, composites, try to take advantage of the properties of two or more materials to create a structure whose properties are better than each of the constituents. In our work we used Al as the doping element with an ion radius less than the radius of Mg. We intended obtain not only the precipitate of Al, but also the filling of cation vacancies, as well as the appearance of interstitials. We have also chosen Al because it is widespread in nature and plays an important role in defects creation in A^2B^6 compounds as uncontrolled impurity. By putting together aluminium and magnesium oxide, we should be able to create a material with new physical properties.

Images of MgO crystals after annealing in Al melt at 1420 K for 150 h are presented in Fig.1. By using CCL mode, variations in optical properties of MgO:Al are shown in zones created by Al diffusion (red emission). Cardinal changes of both the intensity and spectra of luminescence from these layers were revealed. Applying CL spectral analysis we have also found the correlation between the intensities of luminescent band centred at 480 nm and the concentration of Al in MgO:Al samples.

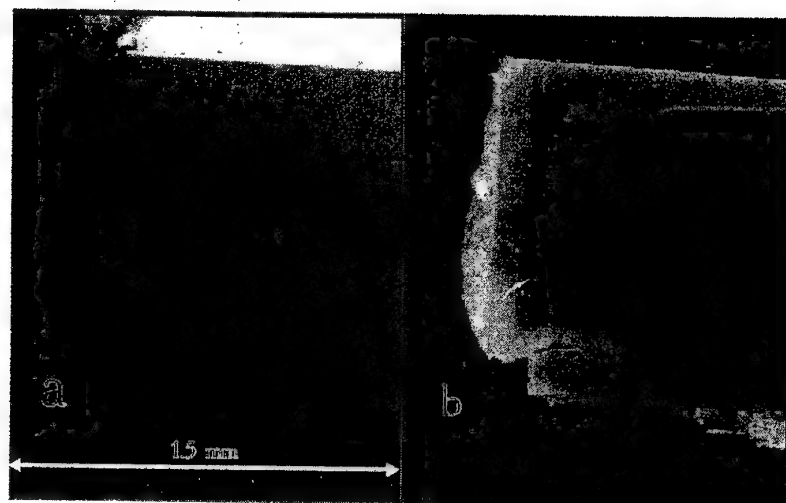


Fig.1 Section of MgO crystal annealed in Al melt in BSE mode (a) and CCL (b). H.F.W.=1.5 mm

3.2 Zinc sulphide, ZnS

Among wide-band-gap A^2B^6 materials, ZnS has an increasing number of applications as a host crystal for doping to create luminescence in the blue spectral range.

Lately, new results have been reported using Bi as a dopant in Si and GaAs. We also used Bi in ZnS and ZnSe host crystals despite the bigger atomic radius of Bi compared to the radius of both the Zn and S.

Single crystals of low resistivity ($\rho \approx 100$ ohm per cm) ZnS:Al were annealed in a melt of Bi and Bi +0.2 % BiCl₃ for 100 h at 1200 K with a subsequent tempering in air. The volume of the melts was 10 times greater than that of ZnS:Al.

Differences in the luminescent topography of the cleavages subjected to various heat treatments were observed by using the high sensitive CCL mode. It was established that the annealing in the above mentioned melts changes the impurity-defects composition. We observed the appearance of the blue band about 500 μ m width near the edge of the sample (Fig.2). An advantage of applied composite CCL+BSE contrast in Fig.2 (c) is obvious. The CCL-SEM technique may be used for topographical and spectral examination of specimens. Information on the spatial distribution and spectral features of light emissive centres can be noticed simultaneously.

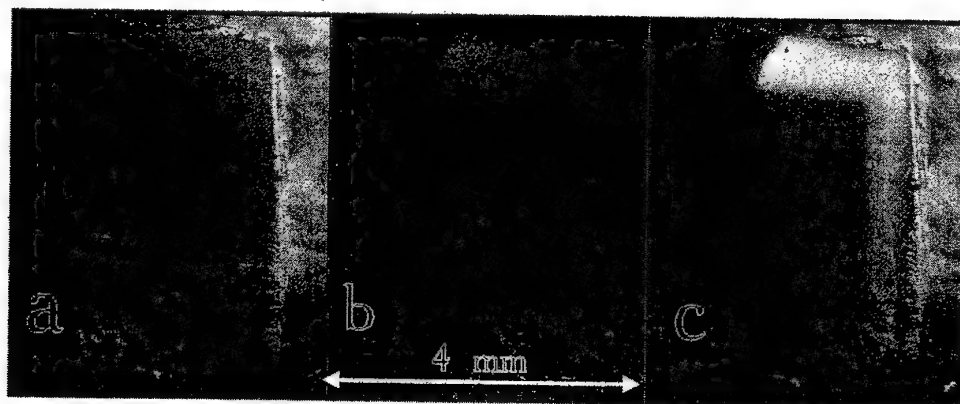


Fig. 2 ZnS:Al images after annealing in Bi melt in different SEM modes: a) BSE, b) CCL, c) composite BSE+CCL. H.F.W.=4 mm

The most interesting results were obtained at the annealing ZnS:Al in Bi +0.2 % BiCl₃ melt (Fig.3). Three characteristic zones with different CL intensities and spectral compositions are revealed. In particular, the first zone ($\approx 200 \mu\text{m}$), localised in the vicinity of the doped surface, shows a decay in the luminosity owing to a high density of structural defects. The second zone ($\approx 500 \mu\text{m}$) has an intensive blue emission attributed to Bi-doping in the subsurface layer. This luminescent band has a composite structure. It consists of different colours: violet, blue, orange and bright green separated from one another. The third zone is the undoped crystal volume giving a green emission. The CCL image reveals in general a good correlation with the CL and PL spectra recorded in different points of sample. However, we found a distinguishing feature: the local CL spectra taken from all the characteristic zones at 77 K differs from the corresponding PL spectra. This difference could be related to changes in excitation conditions for the luminescence centres at the laser beam excitation, when $h\nu < E_g$, and at the electron beam excitation, when $E_{\text{exc}} > E_g$.

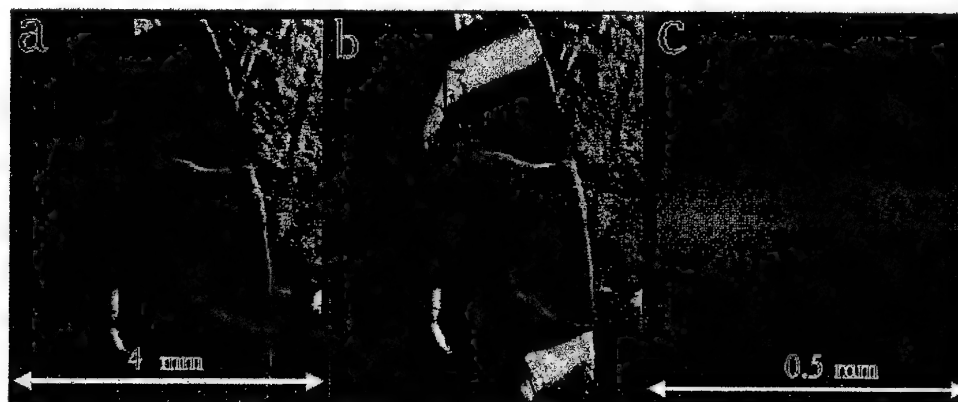


Fig.3 ZnS:Al images after annealing in Bi+BiCl₃ melt in different SEM modes: a) BSE, b) composite BSE+CCL, c) Fragment of bright band in CCL. H.F.W. (a, b)=4 mm, H.F.W.(c)=0.5 mm

3.3 Zinc selenide, ZnSe

On the host ZnSe sample one can see the bright blue radiation from the whole surface, so CL emission has a uniform spectral composition. This agrees with CL and PL spectra recorded in different points. Only one blue band with the maximum close to 466 nm (2.66 eV) and the half width of 0.09 eV was fixed. Moreover, in CCL examinations we observed a change in both the intensity and wavelength of CL depending on the external influence and the injected charge. These changes in the CL spectra are irreversible. This makes it possible to employ such crystals as carriers of information recorded by a fine electron beam with a density of 10^8 bit/cm^2 .

3.4 Bi₄[GeO₄]₃ crystals

The BGO single crystals are widely used for the x-ray and position detector and also have been applied as a solid-state laser host and to nonlinear optics. They are used for the reversible optical memories, phase conjugation, coherent light modulation and amplification and other purposes. However, as shown in our CCL investigations, BGO applications are limited because photons and particles induce a decrease of the luminescence output. Fig.4 presents a CCL-SEM image of the indentation region on (001) of the undoped BGO. The additional luminescent centres, providing the CL in a wider spectral band can be induced by the gliding of the edge components of dislocation loops in the primary slip system. One can see the decay of CL in the centre of the indentation, owing to a high concentration of point and linear defects in the form of dislocation networks created by microindentation. The extrinsic CL from BGO depends on the doped impurities and dislocation configuration. A significant increasing of CL intensity and broadening of spectral band were found in the dislocation zones, created around microindentations on doped BGO:Fe and BGO:Yb crystals.

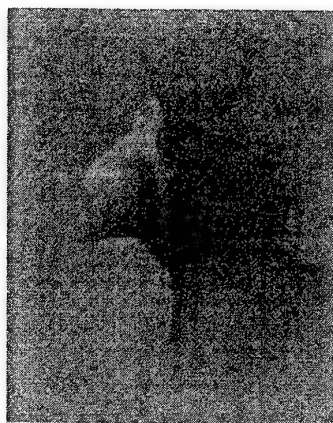


Fig.4 CCL image of the indentation region ($P=200$ g.f., $T=300$ K) on (001) of the undoped BGO. H.F.W. ≈ 160 μm

4. CONCLUSIONS

Composite CCL+BSE contrast in the scanning microscopy is a new type of SEM mode which is a prospective tool for the investigation of luminescent materials. The (CCL+BSE)-SEM-images with both fine structure and colour informations are able to simplify the observation, interpretation and analysis of different specimens. The proposed method can be used both for checking of the substance state and studying the characteristics of dislocations and point defects. The present results show that the CCL technique in the SEM is very sensitive to detect the variations in mechanical, optical and luminescence properties of crystals subjected to thermal treatments. The analysis of optical and diffusion characteristics is of great importance for the future development of new optoelectronic structures and devices.

ACKNOWLEDGEMENT

The authors thank Dr. Sushkevich K.D. (State University of Moldova) for the ZnS and ZnSe specimens, Dr. Topa V. (Institute of physics and technology of materials, Bucharest, Romania) for the BGO crystals and Dr. Saporin G.V. and Dr. Obyden S.K. (Moscow State University) for providing assistance with the SEM equipment.

5. REFERENCES

- [1]. Saporin G.V., Obyden S.K.: Colour display of video information in scanning electron microscopy. Principles and applications to physics, geology, soil science, biology and medicine. Scanning, 10, 87-106, (1988)
- [2]. Saporin G.V., Obyden S.K.: Colour in the Microworld: Real Colour Cathodoluminescence Mode in Scanning Electron Microscopy. European Microscopy and analysis. 7-9, March (1993)
- [3]. Nazarova T.A., Nazarov M.V. Analysis of cathodoluminescence from indented MgO crystals subjected to thermal environments. Philosophical Magazine (UK), A, 74, 1311-1318, (1996)
- [4]. Nazarova T.A., Saporin G.V., Obyden S.K., Ivannikov P.I. Colour cathodoluminescence study of oxides subjected to thermal environments. Scanning, 19, 48-54, (1997).

MODIFICATION OF PLASTIC AND BRITTLE PROPERTIES OF InP SINGLE CRYSTALS BY ION IMPLANTATION

Daria Grabco, Natalia Palistrant, Maria Medinskaya, Natalia Pyshnaya

Institute of Applied Physics of Moldavian Academy of Sciences,
Academy str. 5, MD-2028, Chisinau, Moldova

ABSTRACT

The influence of the third group ions (B^+ , Al^+ , Ga^+) implantation on some mechanical properties of undoped (n-InP) and Fe-doped InP single crystals is investigated in this work. It is shown that the inversion of conductivity type takes no place in this case, however, it is observed the modification of mechanical characteristics (H , σ , γ). The peculiarities of these parameters change evidence in favour of mechanism of implanted ions entrance in the In lattice sites for both n-InP and InP:Fe crystals.

1. INTRODUCTION

The implantation of different ions into semiconductor materials is usually directed to the modification of their electrical and optical parameters. But at the time inevitable variation of other crystal properties (in particular, plastic and brittle) takes place. This fact obligatory is to be taken into account to predict the quality and duration of design functioning.

Along with this it is of interest the examination of mechanical parameters of semiconductors by their implantation to elucidate the issue connected with physics of this process. Since the electrical and optical properties of materials as well as the mechanical ones are structurally sensitive characteristics and its changes may be caused by identical transformations in the crystals structure. With allowance of above mentioned, the influence of the third group ions (B^+ , Al^+ , Ga^+) implantation on some mechanical properties of undoped (n-InP) and Fe-doped InP single crystals is investigated in this work.

2. EXPERIMENTAL PROCEDURE

An ions implantation was performed into chemically polished (001) plane at room temperature and beam energies from 300keV to 1MeV and doses from $3 \times 10^{13} \text{ cm}^{-2}$ to $3 \times 10^{15} \text{ cm}^{-2}$ to obtain a plate concentration profile of ions distribution. After 15 minutes annealing at 700°C for damaged layer restoration the last had following parameters: the holes concentration $p = 3 \times 10^{15} \text{ cm}^{-3}$, depth of implanted ions distribution $d \approx 0,6 \text{ m}$.

After that the implanted (001) plane of the crystals was deformed at room temperature by concentrated load. Micromechanical properties (microhardness (H), microdurability (σ), and microbrittleness (γ)) were investigated. Indentations were made by Vickers diamond pyramid. The indentation diagonals (d) were parallel to the $\langle 100 \rangle$ directions. Measurements of microhardness were performed with microhardness tester PMT-3.

The mechanical parameters were calculated using the usual formulae [1,2]; the indenter loads P were equal to 0,2 and 1N. Using of the first load ($P=0,2\text{N}$) permitted to obtain the indentations with depth less than 0,6 μm , i.e. to determine the microhardness of region under implanted zone was estimated. The same refers to others studied mechanical characteristics. The free charge-bearers concentration and Hall coefficient were determined as electrical parameters.

3. RESULTS AND DISCUSSION

The third group elements (B^+ , Al^+ , and Ga^+) implantation had been taken up to introduce the In .. type structural defects. Such defects are found to reflect in the indium phosphide crystals as the acceptors, and their presence must lead to the conductivity type change [3-5].

However, the measuring of electrical parameters shown that the implantation of enumerated ions didn't lead to the expected inversion. This result may point out that implanted ions don't occupy the phosphor vacancies and another mechanism of implanted ions localization takes place in this case. Three alternative versions of implanted ions penetration into indium phosphide crystal lattice are possible (into In lattice points; into P lattice points and into interstitial places). But only the first and the second mechanism seem to be real, as the acceptor centres of InP type hadn't been revealed by the electrical measurements.

For the verification of the more preferable mechanism one can refer to the experimental results of mechanical parameters determination. The values of microhardness, microdurability and microbrittleness for the n-InP crystals implanted by B^+ , Al^+ , and Ga^+ ions are presented in table 1 (Concentration of unmonitored, uncompensated donor centres in undoped n-InP crystals amounts to $2 \times 10^{16} \text{ cm}^{-3}$).

Table 1 Modification of mechanical parameters (H , σ and γ) third group ions implantation of InP crystals. $P=0,2N$

Nr.	Crystal	Atomic radius of element, r, A	$\Delta r_1 = r_{In} - r_{I.e.}^*$	$\Delta r_2 = r_p - r_{I.e.}$	H, MPa	σ, MPa	γ
1.1	n-InP	In-1,62	-	-	3600	-	-
1.2	n-InP $^+Al^+$	Al-1,43	0,19	-0,25	3290	330	4,4
1.3	n-InP $^+Ga^+$	Ga-1,39	0,23	-0,21	3150	303	4,7
1.4	n-InP $^+B^+$	B-0,91	0,71	0,27	3060	235	6,0

*) $r_{I.e.}$ - atomic radius of implanted elements.

As it is seen from table 1, the clearly regularity in the change of mechanical parameters in dependence of atomic radius of implanted elements in row Al-Ga-B is observed. One can notice, that H and σ values decrease, and γ values increase when passing from Al^+ to B^+ . And the difference in microhardness value $\Delta H = H_{n-InP} - H_{n-InP+M}$, for example, is the greater the bigger the difference of atomic radius values is $\Delta r_1 = r_{In} - r_{I.e.}$.

It is fair to think, that the decreasing of microhardness values in the investigated crystals range has to note about the plasticity rise by the indium phosphide implantation. However, the pattern of the σ and γ values change points out another. Indeed, the material plastification, as it is known, must be accompanied by microdurability increase (i.e. by rise of the resistance to crack formation) and by microbrittleness decrease. But in our case we have an opposite effect-the σ decreases and γ increases with Δr_1 growth. Therefore, it may be concluded, that the H decrease is not caused by improving of plastical properties of materials, and it is bound by the growth of tendency to the fragile destruction. The failure appearing by the indendor penetration brings about the supplementary indentation growth and, as consequence, the microhardness value diminution.

Another effect is noticed by implantation of the InP:Fe crystals (table 2).

Table 2 Modification of mechanical parameters (H , σ and γ) by third group ions implantation of InP:Fe crystals. $P=1N$

Nr.	Crystal	Atomic radius of element, r, A	$\Delta r_1 = r_{In} - r_{I.e.}^*$	$\Delta r_3 = r_{Fe} - r_{I.e.}$	H, MPa	σ, MPa	γ
2.1	InP :Fe	In-1,62 Fe-1,24	-	-	3000	211	6,5
2.2	InP :Fe $^+Al^+$	Al-1,43	0,19	-0,19	3140	278	5,0
2.3	InP :Fe $^+Ga^+$	Ga-1,39	0,23	-0,15	2950	296	
2.4	InP :Fe $^+B^+$	B-0,91	0,71	+0,33	3165	310	4,5

Here, the H dependence versus implanted atom is not very clearly, but as a whole it may be marked the tendency to the hardening of implanted samples against the unimplanted ones. This tendency is well looked through in the modification on other (σ and γ) characteristics too. And we can see that the hardening is concerned with microdurability increase and microbrittleness diminution.

The regularities, marked by use of small loads ($P=0,2N$), are confirmed by application to the indenter of more high ones ($P=1N$) too (table 3 and 4). This result indicate that the structural transformations, occurring in thin implanted layer, also influence on the more deep ones.

As it was noted, three possible variants of implanted atoms entrance in the InP lattice can be expected: in the interstitial places, in the phosphorus and indium lattice points. We can discuss in favour of which of them speak the data of micromechanical parameters measurements.

It is naturally to expect that the samples brittleness will be the less the smaller r_{ie} is, if it is supposed that the implanted ions in n-InP crystals are located in the interstitial sites. The experiment shows the opposite effect. The possibility of second mechanism realization should have to reveal the correlation of mechanical parameters modification with Δr_2 , what is missing at the experiments too.

In the same time the regular interconnection between the change of mechanical characteristics and Δr_1 is seen from the tables 1-4. This result allows to assume that the ions of implanted elements preferencely hold the place in the lattice sites. And it will be understood that bigger value of Δr_1 leads to more strong lattice distortion that causes the mechanical parameters to be modified.

Table3 Modification of mechanical parameter (H, σ and γ) by third group ions implantation of n-InP crystals $P=1N$

Nr.	Crystal	H, MPa	σ , MPa	γ
1.1	n-InP	3800	-	-
1.2	n-InP+Al ⁺	3350	218	7,3
1.3	n-P+Ga ⁺	3170	198	7,6
1.4	n-InP+B ⁺	3390	185	8,9

Table 4 Modification of mechanical parameters (H, σ and γ) by third group ions implantation of InP:Fe crystals. $P=1N$

Nr.	Crystal	H, MPa	σ , MPa	γ
2.1	InP:Fe	3270	-	-
2.2	InP:Fe+Al ⁺	3166	183	8,35
2.3	InP:Fe+Ga ⁺	3320	204	7,80
2.4	InP:Fe+B ⁺	3220	214	7,10

Somewhat other situation is created in the case of InP:Fe crystals implantation. The iron doped atoms, may be, exert the damping affect on the structural modification by implantation, and thereby reducing the tendency of crystals to the frail destruction.

4. CONCLUSIONS

1. As the electrical measuring results show, the inversion of conductivity type take no place by implantation of the n-InP and InP:Fe crystals with third group elements. That indicates the missing of the In... type defect structure formation.
2. The n-InP and InP:Fe crystals implantation is accompanied by modification of their mechanical characteristics (H, σ and γ).
3. It is observed the brittleness increase for the n-InP crystals and rise of plasticity for the InP:Fe ones in the row of (Al⁺-Ga⁺-B⁺) implanted ions.
4. The modification of mechanical parameters by InP crystals implantation evidences in favour of mechanism of implanted ions entrance in the In lattice points for both n-InP and InP:Fe crystals.

5. REFERENCES

- [1]. Boyarskaya Yu.S., Grabko D.Z., Kats M.S. "Physics of Microindentation Processes", Kishinev, Stiinta, 294, (1986).
- [2]. Berdikov V.F., Bogomolov N.I., Babanin A.V. et al. "News in Microhardness Tests", Moscow, Nauka, 119, (1974).
- [3]. Corshunov F.P., Radautsan S.I., Sobolev V.A. FTP, 23,9,1581, (1989).

- [4]. Pyshnaya N.B., Spitsyn A.V., Tighineanu I.M. et al. Coll. of V Unional Conf. "Ternary semiconductors and their application", Kishinev, 169.
- [5]. Verner B.D., Pshenichnyi A.A., Radaustan G.I. et al. "Ternary semiconductors and their application", Kishinev, 175, (1983).

THE INFLUENCE OF THE ANNEALING TEMPERATURE ON THE INTERFACE LAYER IN METAL/FERROELECTRIC/SEMICONDUCTOR HETEROSTRUCTURES

I.Boerasu, L.Pintilie, M.Alexe*

National Institute of Materials Physics, Bucharest-Magurele
P.O.Box MG - 27, Romania; E-mail:boerasu@alpha1.infm.ro

*Max - Planck Institut fur Mikrostrukturphysik, Weinberg 2, Germany

ABSTRACT

Lead titanate thin film were deposited on p type Si substrates, with and without native SiO_2 , using the sol-gel method. The SEM figures show the appearance of an interface layer, between the silicon substrate and the ferroelectric thin film. The XRD study revealed an amorphous structure for this new layer in case of PbTiO_3 film deposited on Si substrate after SiO_2 is removed, and a PbSiO_4 structure (polycrystalline) for the deposited on native SiO_2 film. The thickness of the interface layer depend on the annealing temperature and on the existence of the native SiO_2 film too. Unfortunately, this layer has a negative influence on the ferroelectric thin film properties in the MFS heterostructure.

1. EXPERIMENTAL

The PbTiO_3 thin films were obtained by the sol-gel method. More details about the deposition technique can be found in a previous paper ⁽¹⁾. The crystallisation of the PbTiO_3 thin film was made by thermal annealing. Two type samples were prepared: 1) PbTiO_3 was directly deposited on the p type silicon substrate (the native SiO_2 film was removed from the substrate by chemical etching with HF 10%); 2) PbTiO_3 deposited on the native SiO_2 film existent on the surface silicon substrate. These samples were annealed by conventional thermal annealing (CTA), in air, at 550°C, 600°C and 650°C for 30 min.

The MFS heterostructures were obtained by deposition of metallic electrodes: aluminium electrodes of about 2000 Å thick on the silicon substrate and gold electrodes of about 600 Å thick on the PbTiO_3 surface. The gold electrodes were shaped into rectangles of 1.25 x 1.5 mm² by evaporation through a metallic mask. The final geometry of the heterostructure is presented in Figure 1.

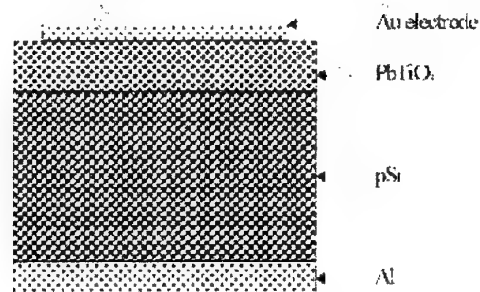


Fig. 1 The MFS heterostructure

2. RESULTS AND DISCUSSIONS

First, the structure of the annealed PbTiO_3 films was investigated by x-ray diffraction (XRD), Atomic Force Microscopy (AFM) and Scattering Electron Microscopy (SEM). X-ray diffraction (XRD)

patterns were taken on a 0 - 20 diffractometer using $\text{CuK}\alpha$ radiation, and a flat graphite monochromator placed before the NaI(Tl) scintillation counter.

Figure 3 shows the diffraction patterns for the PbTiO_3 deposited on silicon substrate. As noticed for all samples, the diffraction patterns show the existence of a single, PbTiO_3 with perovskite structure, and a good and complete crystallisation.

Figure 3 also shows that the diffraction peaks increased in amplitude and their full width at half maximum (FWHM) decreased with increasing of the annealing temperature. This suggests that the crystallite dimensions increase with increasing the annealing temperature.

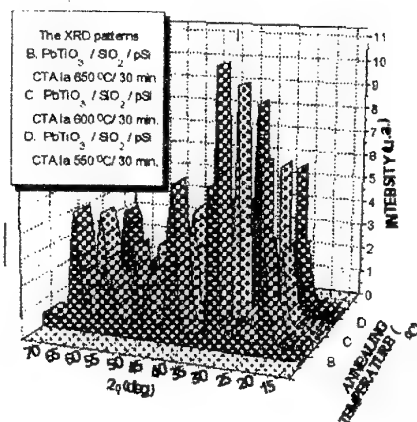


Fig. 3 The XRD patterns for MFS heterostructure

Figure 4 shows the AFM pictures performed on a Jeol 6300A scanning electron. This analysis revealed a good crystalline structure for all samples and a medium crystallite size of about $40 \div 75$ nm, depending on the annealing temperature.

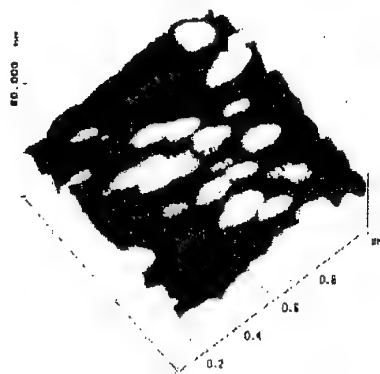


Fig. 4 The AFM picture of MFS heterostructure crystallised at 600°C by CTA for 30 min

The SEM study was also performed on a Jeol 6300A scanning electron microscope. The micrographs, shows in figure 5, indicate a thickness of about $0,6 \mu\text{m}$ for the deposited film and the presence of a new phase at the ferroelectric - semiconductor interface probably PbTiO_4 . The new phase PbSiO_4 is polycrystalline for PbTiO_3 deposited on the p type silicon substrate with native SiO_2 film, and is amorphous for a PbTiO_3 film deposited on the p-type silicon with native SiO_2 film removed. The SEM

micrographs show an increase of the interface film thickness with increasing the annealing temperature (the dependence on annealing temperature is shown in Fig. 2).

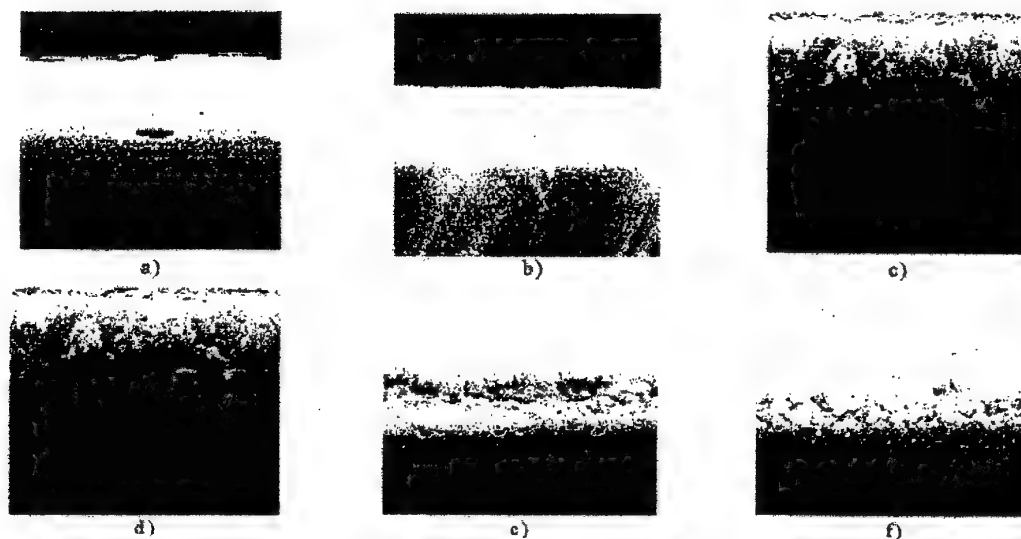


Fig. 5 The SEM picture for the $\text{PbTiO}_3/\text{pSi}$ and CTA at a) 550°C; b) 600°C; c) 650°C respectively for the $\text{PbTiO}_3/\text{SiO}_2/\text{pSi}$ and CTA at d) 550°C; e) 600°C; f) 650°C

The dependence of the interface layer thickness with the annealing temperature is shown in Fig.2. This Figure shows that the thickness of the new amorphous film is increasing more rapidly with the annealing temperature increase of a direct deposition on p type substrate. The samples obtained using spin-on solution and metalorganic decomposition for PT on the native SiO_2 film show a polycrystalline interface layer, with a small thickness. Unfortunately, the films show caves, but the caves are disappearing as the annealing temperature increases. Most probably, these caves occur due to the different dilatation coefficients and due to the accumulation of gases.

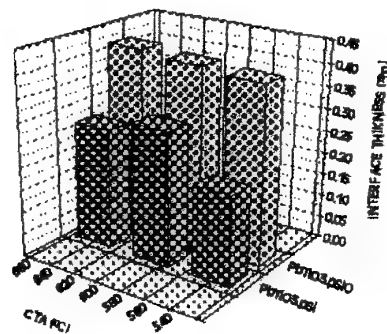


Fig. 2 The interface thickness dependence vs.CTA for $\text{PbTiO}_3/\text{SiO}_2/\text{pSi}$ and $\text{PbTiO}_3/\text{pSi}$

The electrical characterisation of PbTiO_3 films consists in capacitance - voltage characteristics (C-V)⁽²⁾. The measurements were performed using a HP 4194A Impedance - Gain Analyser. The frequency of the test signal was 100 kHz, and the results are presented in Figure 6.

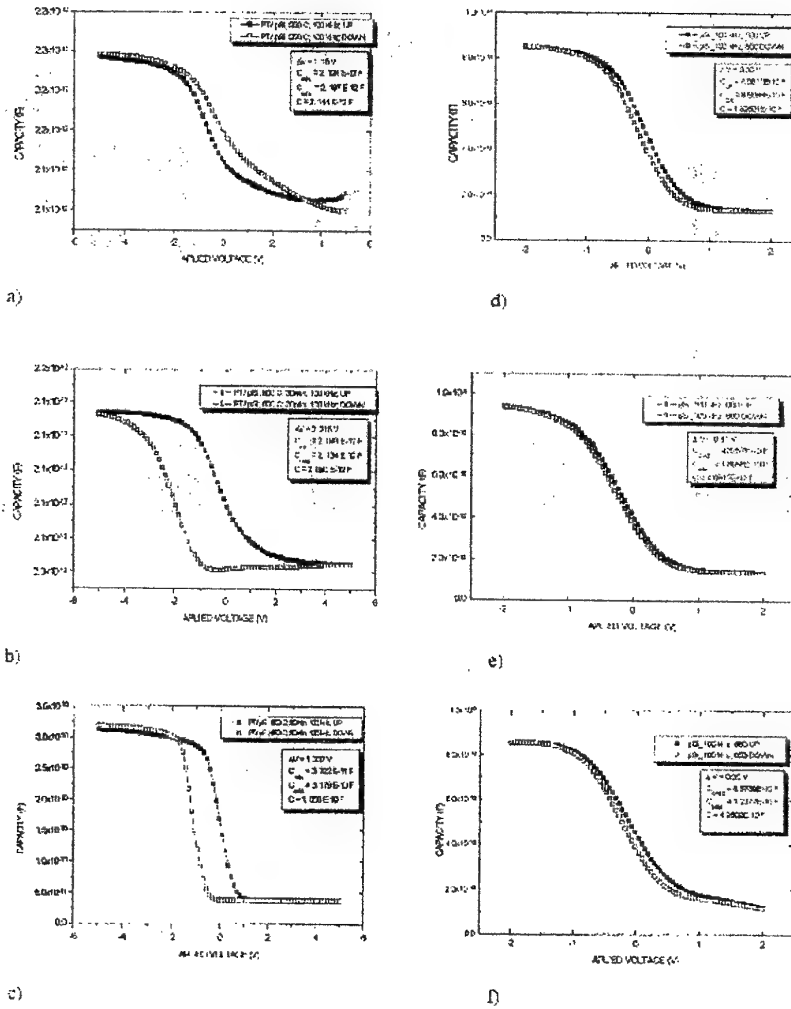


Fig. 6 The C - V characteristics for PbTiO₃/SiO₂/pSi and CTA at a) 550°C; b) 600°C; c) 650°C respectively for PbTiO₃/pSi and CTA at d) 550°C; e) 600°C; f) 650°C

The C-V characteristics reflect all the elements of a MOS characteristic⁽³⁾ and they reveal the appearance of a hysteresis loop⁽⁴⁾ due to the existence of the spontaneous polarisation in the ferroelectric film. It also reveals critical increases for the capacitance values in case of sample PbTiO₃ films obtained by direct deposition on the p type silicon substrate, comparing to the known values from literature⁽⁵⁾. This is a result of the stronger interface layer influence. The capacitance versus annealing temperature is shown in Figure 7.

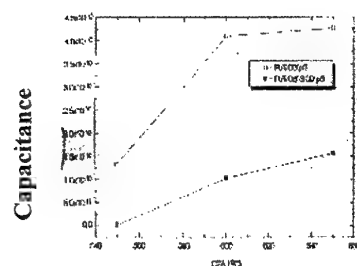


Fig. 7 The capacitance dependence vs.CTA

The memory windows⁽⁶⁾ is decreasing with increasing annealing temperature (Figure 8). For the Au/PbTiO₃/pSi, the memory windows have small values comparing to the Au/PbTiO₃/SiO₂/pSi memory windows values, as a normal consequence of the capacitance growing⁽⁷⁾.

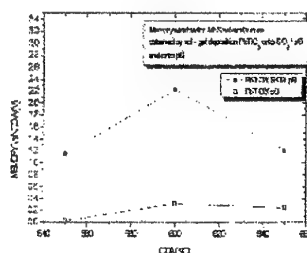


Fig. 8 Memory window vs.CTA

3. CONCLUSIONS

Using spin-on solutions and metalorganic decompositions, PbTiO₃ thin films were deposited in two cases: either directly onto p type silicon substrates, or onto native SiO₂ film from the p type silicon. The SEM analysis revealed the appearance of a new layer, at the ferroelectric - semiconductor interface. This layer is amorphous for directly deposited films, and polycrystalline for the films deposited on the native SiO₂. The thickness of the new layer is increasing with the annealing temperature for all samples obtained by direct deposition on the p-type Si, and for this reason the electrical properties of the MFS are negatively influenced.

4. REFERENCES

- [1]. I.Boerasu, L.Pintilie, V.Dragoi and M.Alexe - Anualele Universitatii Bucuresti; XLVI - 1997, pp.331.
- [2]. M.Alexe, M.Popescu, V.Dragoi and C.Tanasoiu - Proc.of 18th Annual Semicond. Conf., Sinaia, Romania, 1995, pp.725.
- [3]. P.Richmann; MOS Field Effect Transistors and Circuits; John Wiley & Sons; N.Y., 1973
- [4]. J.K.Park and W.W.Grannemann; Ferroelectrics 10; 1976; pp.217.
- [5]. D.L.Polla; Science and Technology of Electronic Thin Film; Kluwer Academic Publishers; 1995; pp.413.
- [6]. K.Aizawa and H.Ishiwara; Jpn.J.Appl.Phys.33; 1994; pp.5178.
- [7]. M.Alexe; Proc.of 17th Annual Semicond.Conf. Sinaia, Romania, 1994, pp.713

ABOUT THE NATURE OF DEFORMATION ANISOTROPY OF THE InP:Zn CRYSTALS

Daria Grabko, Natalia Palistrant, Maria Dyntu, Maria Medinschi, E. Rusu

Inst.of Appl.Phys. of Academy of Sciences,
Academy str.5, 2028, Kishinau, Moldova

ABSTRACT

The regularities of plastic deformation under the action of concentrated load in two crystallographic directions $\langle 100 \rangle$ and $\langle 110 \rangle$ of InP crystals doped with zinc, have been investigated. The study revealed that the crystal deformation in $\langle 110 \rangle$ direction is more sensible to the distribution of growth dislocations than in $\langle 100 \rangle$ one. The hypothesis about the nature of the observed anisotropy of plastic properties by indentation and by indenter motion is advanced.

1. INTRODUCTION

The InP crystal is a material widely used in semiconductor electronics. It is known that doping of a given compound with different impurities is the way to obtain materials with programmed electrophysical properties. The structure perfection, in particular, the density and distribution of growth dislocations play an important role. The question about the correlation between growth dislocation density and both mechanical and electrophysical properties has been little studied [1-3]. There is also no information about the mechanism of plastic deformation of InP crystals [3-5]. Therefore, the purpose of this paper is to investigate the regularities of the InP crystal deformation in connection to the growth dislocation distribution.

2. EXPERIMENTAL PROCEDURE

The InP crystals were grown using the liquid-encapsulated Czochralski (LEC) technique. The investigations were performed on the (001) face. The Vickers diamond pyramid was used for the crystal deformation (the indentation and scratching methods). Microhardness by indentation (H) and by scratching (H_s) was calculated using the usual formulas [6]. The microhardness measurements were produced in two orientations: 1) the indenter's diagonals d II $\langle 100 \rangle$ and 2) d II $\langle 110 \rangle$.

3. RESULTS AND DISCUSSION

The data shown below in the table reveals some interconnection among the parameters.

Table Relationship different physical parameters N, H, n, μ in pure and doped with Zn InP crystals

Crystal	N, cm^{-2}	H, kg/mm^2	n, cm^{-3}	μ , cm^2/BC
n-InP	$(2 \div 3) \times 10^4$	360	$4,1 \times 10^{16}$	3900
p-InP:Zn	5×10^4	375	$2,7 \times 10^{18}$	50
p-InP:Zn	$2,1 \times 10^5$	410		

There is some clear correlation between the change of the growth dislocation density (N) and other properties of InP crystals (microhardness (H), concentration of bearers (n), electron mobility (μ). Please note that average values for N and H are mentioned in the table. However, it is known that the density of growth dislocations is spreads nonhomogeneously in the table. But it is known that the density

of growth dislocations is spreads nonhomogeneously in the diameter (D) of a crystal ingot. Therefore it is important to follow the change of these parameters inside of the ingot. To this purpose some sections on the (001) plane were cut out from the big ingot (fig.1a). The density of dislocations and respectively the microhardness H and H_s for $\langle 100 \rangle$ and $\langle 110 \rangle$ directions were evaluated on them. Received results are given in the fig.1,2. As it is seen from fig.1b, the curve of the dislocation density (N) has a concave form: the minimum N is in the center of piece, the maximum - on the edge of the surface.

Also a change of the Vickers and scratching microhardness (fig.2).

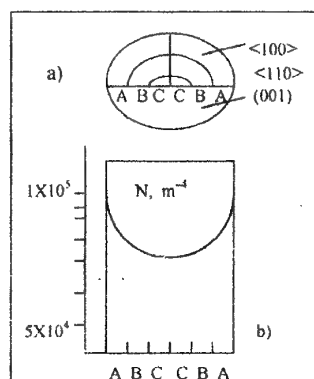


Fig.1 a) Schematic image of investigated regions of surface with D=20 mm; b) The distribution of the dislocation density on the (001) of the InP:Zn piece

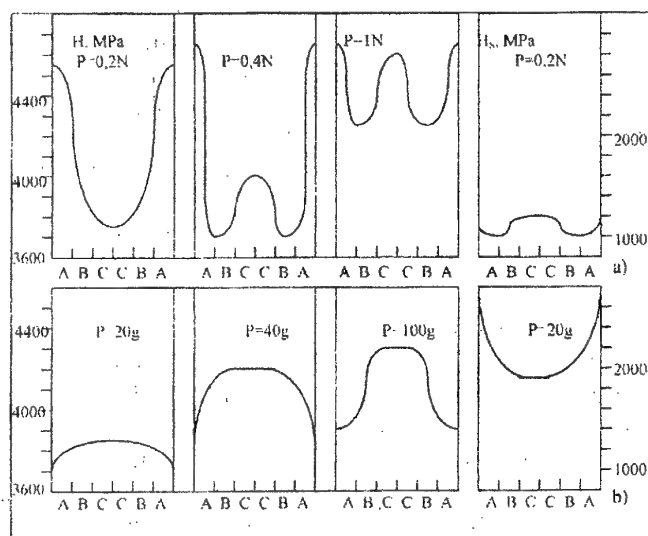


Fig.2 Microhardness change on the (001) plane of InP:Zn crystals by indentation (H) and by indenter motion (H_s) for two orientations $\langle 100 \rangle$ (a) and $\langle 110 \rangle$ (b) at measured removal from the cut center

It is important that curves have a complicated shape for both directions. As observed, the curves $H(D)$ ($dH/\langle 100 \rangle$) have in general a concave form and the best correlation with $N(D)$ takes place at $P = 20$ g; the curve $H_s(D)$ has slightly a convex shape.

A contrary situation occurs in the $\langle 110 \rangle$ direction: $H_s(D)$ has a clearly concave form, analogous to the dependence $N(D)$. The curves $H(D)$, on the contrary, have a convex shape and the convexity increases with the growth of the indenter load.

The interconnection between the mechanical properties change and the dislocation distribution is also clearly followed by a change in the anisotropy coefficient K ($K = (H_{\max} - H_{\min}) / H_{\min}$, %), fig.3.

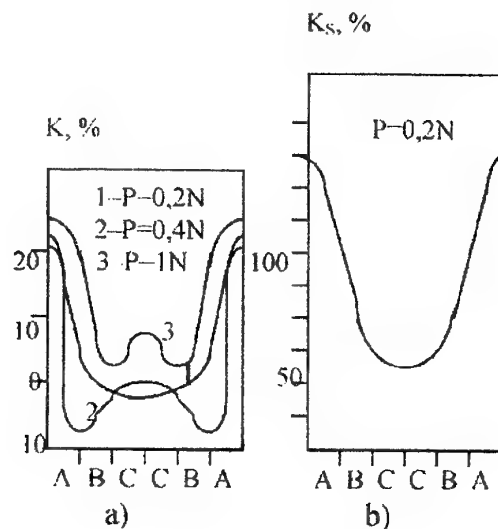


Fig.3 InP:Zn, plane (001). The change of anisotropy coefficient at indentation (a) and at indenter motion (b). Curves: $K = (H_{\langle 100 \rangle} - H_{\langle 110 \rangle} / H_{\langle 110 \rangle})$ %, $K_s = (H_{s\langle 110 \rangle} - H_{s\langle 100 \rangle} / H_{s\langle 100 \rangle})$ %

One can see that the curves $K(D)$ and $K_s(D)$, have generally a concave shape i.e. the anisotropy degree increases with the growth of the dislocation density (fig.3 and fig.1b).

It is known that one of the main causes of the dislocation production in crystals obtained from melt are the thermoelastic strains which appear due to non-uniform cooling [6]. The regions of most dislocation production (in our case characterised by parameter N) indicate high internal stresses present in the crystal. A regular radial increase of the growth dislocation density, the change of the microhardness and of the coefficient of microhardness anisotropy are obviously due to a like cause, and confirm the increase of the internal stress concentration in the periphery parts of the cut versus in its central one.

The above data also specify that microhardness in the $\langle 100 \rangle$ (fig.2a) and $\langle 110 \rangle$ (fig.2b) directions changes inadequately by the radial removal from the cut centre. The curves $H_{s\langle 110 \rangle}(D)$ and $H_{\langle 100 \rangle}(D)$ in general are synchronously changed with $N(D)$, i.e. by deformation along these directions the material undergoes the hardening in the regions with high concentration of internal stresses. The curves $H_{s\langle 100 \rangle}(D)$ and $H_{\langle 110 \rangle}(D)$ are in contrast to this.

The inadequate behaviour of curves $H_{s\langle 100 \rangle}$ and $H_{s\langle 110 \rangle}$ at high temperature deformation ($T > 300K$) was explained in the work [5] by different contributions of two mechanisms of plastic deformation - sliding and twinning in the process of deformation by the indenter motion along $\langle 110 \rangle$ and $\langle 100 \rangle$ directions. It was shown that the sliding process brings more contribution in the first case, but the twinning - in second one.

If these factors play a certain role in the deformation of InP crystals at room temperature, then the $\langle 110 \rangle$ scratching direction must be more sensible to the internal stress change versus $\langle 100 \rangle$ direction, because the dislocations arising at indentation will meet by sliding the bigger resistance in regions with more high stress concentration. The twinning process of the contrary will be lightened in the overstressed region [7]. This is really noticed in the experiment (fig.2, $H_{s\langle 110 \rangle}$ and $H_{s\langle 100 \rangle}$).

A contrary situation takes place in the case of the indentation - with the $N(D)$ change better correlates $\langle 100 \rangle$ direction. It is known that the deformation maximum takes place in the center of Vickers indentation sides [6, 7]: namely for $d \parallel \langle 100 \rangle$ maximum of plastic deformation noticed along $\langle 110 \rangle$ direction, but for $d \parallel \langle 110 \rangle$ - along $\langle 100 \rangle$ one. Comparing these results, one may conclude, that the twinning process is responsible in case of indentation at $d \parallel \langle 110 \rangle$ and sliding one - in case of

indentation at $d \parallel \langle 100 \rangle$. It is necessary to note that the above two factors, are not the only ones in the deformation of the InP crystals. However these factors will act in the region of high temperatures. However, at low temperatures in covalent crystals the dislocation mobility is small and the deformation at $T < 0,4 T_{\text{melt}}$ (for InP $T_{\text{melt}} = 1346 \text{ K}$) cannot be stipulated for the only dislocation mechanism. The mechanism of interstitial plasticity, i.e. mass transfer by the motion of point defects can play some role at relatively low temperatures [6, 8, 9]. The curves in fig.2 confirm this idea. Indeed the pointed out correlation between $H(D)$ and $N(D)$ exists only in general outline. In reality the situation is more complicated. There are maximum on the curves which are more pronounced by the increase of the indenter load. Presence of maximum in fig.2 curves indicates that the deformation of the InP single crystals at the room temperature is determined not only by the mentioned mechanisms - sliding and twinning. Probably a third mechanism - interstitial plasticity also exists. The contribution degree of this mechanism is the aim of a separate investigations.

4. CONCLUSIONS

1. The regularities of plastic deformation by indentation for two directions $\langle 100 \rangle$ and $\langle 110 \rangle$ ((RT) in dependence of growth dislocation density were studied.
2. It was noticed that the deformation along $\langle 110 \rangle$ directions is more sensible to the N change than along $\langle 100 \rangle$.
3. The observed microhardness anisotropy was explained as a result of two deformation mechanisms - sliding and twinning.
4. The third mechanism probably, interstitial plasticity, takes place by indentation of the InP single crystals at room temperature as well as marked above two ones. Its role will be investigated in the future.

5. REFERENCES

- [1]. M.G. Milvidskii, B.V.Osvenskii. The structure defects in semiconductor materials M.,: Metallurgia, (1984).
- [2]. E.V.Rusu, N.B.Pysnaia, I. Muscutariu, T. Dragos. Some characteristics of the InP single crystals obtained by Chochralskii method. Abstracts of the Vth National Conference in Physics and technology of the crystalline and amorphous materials, Iasi, p.143. (1996).
- [3]. I.Yonenaga, K.Sumino. Effects of dopants on dynamic behaviour of dislocations and mechanical strength in InP, J.Appl. Phys., 74 (2), 15, p.917, (1993).
- [4]. S.G.Simasko, N.V.Bejan, V.D.Martinenko, Some mechanical properties of InP FTT, 19, p.1619, (1977).
- [5]. Yu.S.Boyarskaya, D.Z.Grabko, M.I.Medinskii, N.A.Palistrant. Mechanical properties of the pure and doped InP crystals, elucidated by the concentrated load FTP 1997, v.31, N2, p.179-182.
- [6]. Yu.S.Boyarskaya, D.Z.Grabko, M.S.Kats, Physics of the microindentation processes, Kishinev, Stiintsa, (1986).
- [7]. Process of the real crystals growth, N.Nauko, (1977).
- [8]. M.V.Klassen-Neklindova, Mechanical twinning of crystals, (1960).
- [9]. B.V.Mott. The hardness testing by microindentation. M.:Metallurgizdat, (1960).

NEW INVAR ALLOYS FOR HIGH-FREQUENCY DEVICES

H. Chiriac, M. Lozovan, Fl. V. Rusu

National Institute of Research & Development for Technical Physics
47 Mangeron Blvd., 6600 Iasi 3, Romania, phone: 032 135144, fax: 032 231132,
e-mail: mlozovan@mail.dntis.ro

ABSTRACT

This paper studies the influence of thermal treatments on the expansion of some Fe-Ni Invar alloys with addition. The $\Delta\alpha$ effect was made evident in case of the studied alloys. Small amounts of Mn and Si do not change essentially their Invar characteristics, although the mechanical workability is improved. The obtained results are discussed considering the dimensional, thermal and time stability of the high frequency devices.

1. INTRODUCTION

There are many types of ferromagnetic alloys and compounds that present Invar properties, and the Invar issue has recently become important, since the Invar effects are closely connected to the origin of the ferromagnetism in the transition metals and alloys.

The Fe-Ni alloys containing 30 to 50 wt. % of Ni, as well as some Fe-Ni alloys including Co, Cr, or Mn additions shows anomalies in their physical properties (known as Invar anomalies).

Except for their low thermal expansion coefficient, the Fe-Ni binary alloys or the (Fe-Ni)-Co pseudobinary alloys show unusual physical properties, namely a very high forced volume magnetostriction, large pressure effects on the Curie point, a sudden decrease of the magnetization when the alloy composition changes [1].

We studied the influence of 0.3-0.4 wt.% Mn and 0.1-0.15 wt.% Si on the thermal expansion of some Fe-Ni Invar alloys and the Fe-Ni-Co Superinvar alloy.

As previously mentioned small amounts of Mn and Si added to the basic alloy lead to better workability [2]. Consequently we studied the mechanical properties of some Invar alloys having technical utilization. In addition, the influence of thermal treatments on the thermal expansion of the alloys is analyzed.

2. EXPERIMENTAL METHODS

The influence of composition on the thermal expansion of Invar alloys was studied in previous works [2-4].

By using as starting materials electrolytic Ni, Co, Mn as well as Fe with 0.03%C and chemically pure Si, three alloys were achieved by melting and casting in a vacuum blast furnace at a pressure of 0.133N/m². The chemical composition of the alloys namely I1, I2, I3 are given in Table 1.

The alloys were forged in 8x8 mm square section from ingots and then annealed in H₂ atmosphere at 1200°C for 10 hours. This thermal treatment ensures homogenization, desulphurization and decarburization of the alloys [2]. The 5mm diameter and 35 mm long samples were cooled together in furnace down to 250°C at a rate of 250°C/hour.

The thermal expansion coefficient was measured with a vertical extensometer equipped with a Hottinger inductive displacement transducer 0-1mm and an electronic gauge type N23, the heating rate during the measurements being of 30C/minute. The extensometer accuracy was 10-8 m. In order to avoid the sample oxidization at the high temperatures, the studies were performed in argon atmosphere. Negative temperatures down to -53°C were obtained by using a mixture of dry ice in 87.5% ethanol. The chemical analysis of the samples was performed by atomical absorption spectrophotometry.

The experiments have followed the elaboration of an alloy with a small coefficient of expansion within the temperature range of -50°C to $+50^{\circ}\text{C}$, meant to be used in applications requiring a high stability of the thermal expansion coefficient.

Fig. 1 presents the specific elongation versus temperature for alloys I1, I2 and I3.

The I2 alloy has its smallest specific elongation $\Delta l/l$, between -50°C and 50°C . It has been experimentally proved that a deviation of more than 0.5% wt. in the Ni content, as compared to the above mentioned compositions results in the variation of the thermal expansion coefficient of the alloy beyond the proposed limits.

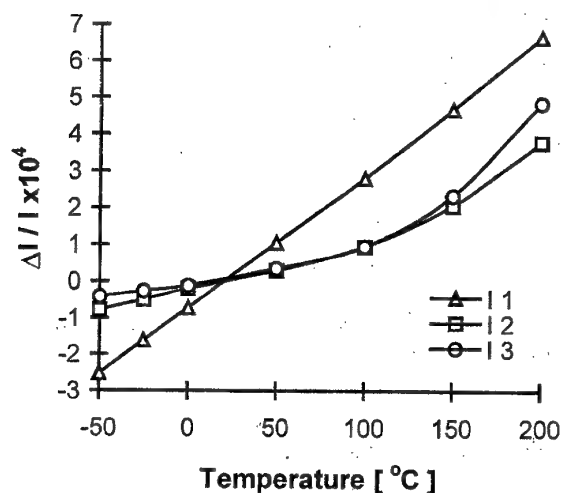


Fig. 1 Temperature dependence of specific elongation for the studied alloys

Table 1 presents the values of the coefficients of thermal expansion at different temperatures for the studied alloys which, prior to measurements, have been subjected to the following thermal treatment: heating up to 1000°C + water cooling + 1 h at 315°C + air cooling.

Table 1

Alloy	Chemical composition (wt.)	Mean thermal expansion coefficient $\times 10^{-7}/^{\circ}\text{C}$ between 20°C and:					
		-50°C	50°C	100°C	200°C	300°C	400°C
I 1	40.05Ni, 0.39Mn, 0.15Si, rest Fe	-36	35	35	37	36	47
I 2	36.21Ni, 0.35Mn, 0.12Si, rest Fe	-11	10	12	21	47	76
I 3	31.85Ni, 0.41Mn, 0.11Si, 4.03Co, rest Fe	-6	5	12	27	63	92

One can notice that the Fe-Ni-Co alloy has the smallest coefficient of expansion near room temperature, its value being $5 \times 10^{-7}/^{\circ}\text{C}$. Chicazumi et al [5] found $\alpha = 0$ for the Fe-Ni-Co Superinvar alloys without impurities.

Given the phase transitions that can occur in the Invar alloys as a result of different temperature modifications, it is expected that the thermal treatments will lead to modifications of the thermal expansion coefficients. Therefore, the effect of thermal treatments on the thermal expansion coefficient was studied in case of alloys I1, I2 and I3. The thermal treatments performed on these alloys and the obtained results are given in Table 2.

Table 2

Alloy	Chemical composition (wt.%)	Mean thermal expansion coefficient $\times 10^{-7}/^{\circ}\text{C}$ between 20°C and:				
		50°C	100°C	200°C	300°C	400°C
I 1	1000°C+water quenching	8	10	18	45	73
	1000°C+water quenching +1 hr at 315°C+air cooling	10	12	21	47	76
	1000°C+water quenching +1 hr at 315°C+air cooling +50 hr at 100°C +very slow cooling	7	7	17	47.5	75
I 2	1000°C+water quenching	33	33	35	34	46
	1000°C+water quenching +1 hr at 315°C+air cooling	35	35	37	36	47
I 3	1000°C+water quenching	5	7	23	60	85
	1000°C+water quenching +1 hr at 315°C+air cooling	5	12	27	63	92

As a result of cooling from 1000°C, a decrease of the thermal expansion coefficient is noticed. A slow cooling results in the increase of the expansion coefficient, which can be attributed to short range atomic ordering of FeNi₃ type [6].

The stabilization treatment at 100°C performed for a long time results in the decrease of the expansion coefficient of the alloy and in time stability (preserving its value in time). The measurements performed after about 4 months have shown the same values of the expansion coefficients, within the limits of the experimental errors.

3. CONCLUSIONS

The analysis of the results obtained leads to the following conclusions:

The Invar alloys with 36.7% wt. Ni and 31.8% wt. Ni+4%wt. Co with low expansion coefficients are adequate for manufacturing high frequency devices while the Invar alloy with 40% wt. Ni is indicated to be used for metal-glass seals (weldable with Pyrom glass).

The manufacturing procedure and the stress stabilization thermal treatments result in a good time stability of the thermal expansion coefficient and in repeated heating-cooling cycles, which enable the use of these alloys at the achievement of precise metrological and high frequency devices.

4. REFERENCES

- [1]. Bozorth R. M., Ferromagnetism, D. Van Nostrand Co. Inc., p. 108, (1951)
- [2]. Chiriac H, Lozovan M., Neagu M., Rom. Reports in Physics, Vol. 46, Nos. 2-3, p. 215, (1994)
- [3]. Chiriac H, Lozovan M., Buletinul Institutului Politehnic din Iasi, Tom XLII (XLVI), Fasc 3-4, Sectia IX, p.85, (1996)
- [4]. Chiriac H, Lozovan M., Buletinul Institutului Politehnic din Iasi, Tom XLII (XLVI), Fasc 3-4, Sectia IX, p.91, (1996)
- [5]. Chicazumi S., Mizoguchi N., Yamaguchi J., J. Appl. Phys., 19, p. 939, (1968)
- [6]. Chiriac H, Lozovan M., Buletinul Institutului Politehnic din Iasi, Tom XLI (XLIV), Fasc 1-2, Sectia IX, p.108, (1994)

ON Ni CONTENT INFLUENCE ON HALL EFFECT IN (Ni ALLOY)-SiO₂ GRANULAR THIN FILMS

H. Chiriac, F. Rusu, M. Lozovan

National Institute of R & D for Technical Physics, 47 Mangeron Blvd., 6600 Iasi 3, Romania
Tel. +40 32 130 680; Fax +40 32 231 132; E-mail: mlozovan@mail.dntis.ro

ABSTRACT

We present below some results of our studies on the electrical transport and Hall effect of (NiFe)_x-(SiO₂)_{1-x} nanocomposite thin films and their possible applications. We deposited (NiFe)_x-(SiO₂)_{1-x} thin films with metal content values near the percolation threshold (e.g. between 40% and 60%) and with different fractions of Ni in the NiFe alloy. We determined the influence of the Ni content in the Ni alloys on the intensity of the Hall effect in (NiFe)_x-(SiO₂)_{1-x} thin films.

1. INTRODUCTION

Granular metal thin films consisting in nanometric-size metal grains embedded in an insulator matrix have lately aroused an increasing scientific and technological interest [1-4], due to their unique microstructure, depending on particle size, volume fraction of components, preparation techniques and subsequent thermal treatments. In this paper we present some results concerning the electrical transport and Hall effect in (NiFe)_x-(SiO₂)_{1-x} granular nanocomposite thin films (x is the atomic fraction of metal in films), in view of using them for thin films miniature electrical and/or magnetic sensors. We used NiFe alloys with different Ni contents (Ni₈₀Fe₂₀, Ni₃₆Fe₆₄) as metallic component of the composite films and we investigated the influence of the Ni content on the physical properties of the composite films.

2. EXPERIMENTAL

We deposited (NiFe)_x-(SiO₂)_{1-x} thin films on glass substrates at room temperature during the deposition, by r.f sputtering in an argon atmosphere, at $p \sim 10^{-2}$ mbar. The microstructure of the samples was investigated by X-ray diffraction, using a Bragg-Brentano arrangement and the monochromatized Mo-K α radiation. In order to study the effect of the thermal treatments on the (NiFe)_x-(SiO₂)_{1-x} samples microstructure, we had them thermally treated in vacuum, at 250°C, 350°C and 450°C respectively for 2h each step. The resistivity of the samples was determined by the standard four point probes method, in air at room temperature. The Hall voltage measurements were also performed in air, at room temperature, for magnetic field induction values up to 2T.

3. RESULTS AND DISCUSSION

Figure 1 presents the dependence of the resistivity of the (NiFe)_x-(SiO₂)_{1-x} films on the metal content in films, before and after the thermal treatment at 450°C. The resistivity of these films is strongly dependent on the microstructure and the metal content in films.

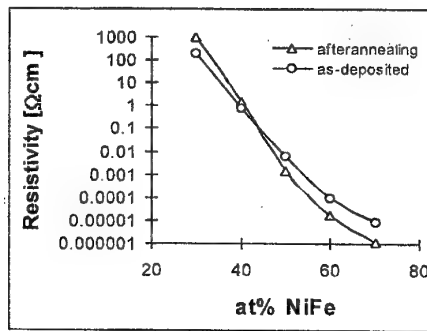


Fig. 1 The dependence of the electrical resistivity of as-deposited and annealed NiFe-SiO₂ thin films on the metal content in films

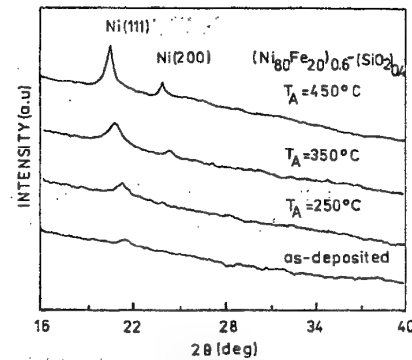


Fig.2 X-ray diffraction patterns for (Ni80Fe20)_{0.6}-(SiO₂)_{0.4} thin films

At the sample with metal content higher than 60%, for all the investigated NiFe alloys, we determined values of the sheet resistivity of about $10 \Omega/\square$, which for the 300 nm thickness of the $(\text{NiFe})_x(\text{SiO}_2)_{1-x}$ films means a resistivity value of about $3 \times 10^{-6} \Omega \text{ m}$. The $(\text{NiFe})_x(\text{SiO}_2)_{1-x}$ thin films with a metal content lower or equal to 50%, present sheet resistivity values of about $300 \text{ k}\Omega/\square$ or higher, which means that the electrical resistivity values are of the order of $30 \Omega \text{ m}$. The thermal treatments at 250°C and 350°C determined neither structural nor electrical resistivity value changes. The samples' resistivity presents a small change in value only after the thermal treatment of the samples at 450°C . This increase in the electrical resistivity values after the thermal treatment at 450°C , for the samples with metal content lower than 50%, is due to local agglomeration of metal in the films. This determinates breaks of the filamentar clusters that still exist in the films having such metal concentration values. The decrease of the electrical resistivity after the thermal treatment at 450°C , at the samples with NiFe content higher than 50% is due to an increase of the metallic grains dimension, because of the recrystallization phenomena.

The X-ray diffraction patterns of the as-deposited and thermally treated $(\text{NiFe})_x(\text{SiO}_2)_{1-x}$ samples suggest that the metallic phase is present in the system as nanocrystalline, while the insulating phase is amorphous. In Figure 2 we present the annealing temperature influence on the $(\text{Ni80Fe20})_{0.6}(\text{SiO}_2)_{0.4}$ thin films' microstructure. There are no microstructure changes after the thermal treatment at 450°C , when the peaks start to sharp and grow in height, suggesting an increase in size of the crystalline grains. From the Hall voltage measurements in $(\text{NiFe})_x(\text{SiO}_2)_{1-x}$ films, one may also note that there is a decrease in the Hall sensitivity with the decrease of the percentage of Ni in the NiFe alloy. The most important results are presented in Figure 3-a, b: Figure 3-a presents the results of Hall voltage measurements for the thin films sample $(\text{Ni36Fe64})_{0.6}(\text{SiO}_2)_{0.4}$, and for the sample biasing current values of 2, 3, 4 and 5 mA.

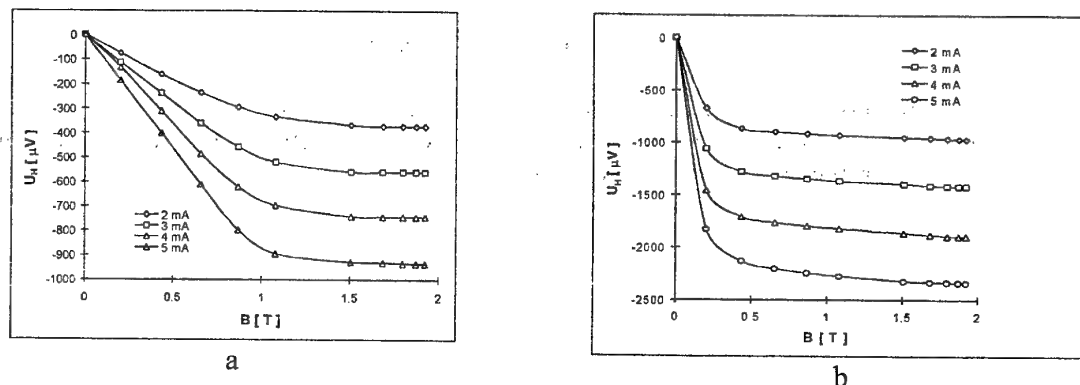


Fig. 3 Hall voltage dependence on the magnetic induction in $(\text{NiFe})_{0.6}(\text{SiO}_2)_{0.4}$ thin films samples: a - Ni36Fe64; b - Ni80Fe20

We determined Hall sensitivity values up to 0.9 mV/T for the 5 mA value of the biasing current and for magnetic induction values up to 1 T. Figure 3-b illustrates the results of Hall voltage measurements for the thin film sample $(\text{Ni}_{80}\text{Fe}_{20})_{0.6}-(\text{SiO}_2)_{0.4}$ and for the sample biasing current values of 2, 3, 4 and 5 mA. We determined Hall sensitivity values up to 8 mV/T for magnetic induction values up to 0.25 T.

4. CONCLUSIONS

We may conclude that the electrical transport properties of the $(\text{NiFe})_x-(\text{SiO}_2)_{1-x}$ films are strongly dependent on their microstructure and on the metal fraction in films, on the deposition conditions and on the subsequent thermal annealing. The electrical conduction and Hall effect in thin films of $(\text{NiFe})_x-(\text{SiO}_2)_{1-x}$ reflect the percolation threshold at about 60at% of metal in films. This fact is suggested by the strong increase of the Hall voltage values measured for $(\text{Ni}_{80}\text{Fe}_{20})_{0.6}-(\text{SiO}_2)_{0.4}$ films, as compared to the values determined for the films with lower metal content and for the metallic samples. The decrease of the Ni content in films determines a decrease in the Hall sensitivity of the investigated films. The value of the Hall coefficient for the $(\text{Ni}_{80}\text{Fe}_{20})_{0.6}-(\text{SiO}_2)_{0.4}$ nanocomposite thin films may be interesting in the field of magnetic field miniature sensors.

5. REFERENCES

- [1]. P.Sheng, Philosophical Magazine B, **65**, 357-384 (1992).
- [2]. A.Heinrich, J.Schumann, H.Vinzelberg, U.Brustel, C.Gladun, Thin Solid Films, **223**, 311-319, (1993).
- [3]. A.Devenyi, R.Manaila and C.Rusu, Thin Solid Films, **41**,143-150 (1977).
- [4]. P.Sheng, J.Klafter, Phys. Rev. B, **27**, 2583-2586, (1983).

HOT PRESSED ZINC SULPHIDE FOR IR OPTICAL WINDOWS. MICROSTRUCTURE AND PURITY INFLUENCE ON OPTICAL PROPERTIES

C.Onose, S.Jinga

MATPUR, Sos.Garii Catelu, nr.5, 73611, Bucharest
Phone: 401.255.69.00/132; Fax:401.255.01.48; E-mail: cristi@prima.matpur.ro

ABSTRACT

The high purity powders synthesis and the hot-pressing technology for optical ceramic materials based on ZnS was studied. Optimal conditions for optical windows manufacturing were established. The influences of material purity, particle size distribution and processing conditions on the optical parameters have been established.

1. INTRODUCTION

The optical ceramic obtained by hot-pressing is currently used for optical instruments and IR radiation technique, because of its interesting properties, such as: chemical inertia; low refraction; good mechanical processing. The thermal and mechanical properties of the window material must be near optimum if the windows are to survive environmental conditions. IR windows should therefore meet the following requirements for optimum thermal, mechanical and optical properties, namely: high melting point, low coefficient of thermal expansion, large band gap, good transmission into the infrared, high hardness, and good strength. Generally, materials with strong chemical bonds exhibit good thermo-mechanical properties but poor infrared transmission, while materials that transmit very well possess weaker chemical bonds and poor thermal and mechanical properties.

The starting powders should meet the following qualitative characteristics: high purity, submicronic particle size distribution (monodispersal powder), spherical shape of particle, weak tendency of agglomeration.

2. EXPERIMENTS

Our target was to obtain with this type of material high purity powders synthesis, hot-pressing technology and to study the material and technological parameters influence on the optical and mechanical properties of the IR windows.

We have studied the forming process of the liquid phase and its influence during the hot-pressing process. Polycrystalline ZnS with a transmission range of 0.57–14.70 μ m was studied. The optical windows from polycrystalline zinc sulphide was obtained in the following conditions: high purity materials (5-6N); pressure (1-3t/cm²); powder particle size distribution (0.1-1 μ m); heat treatment duration and heat treatment curve shape (between 15-60min); controlled work atmosphere.

We have ensured optimal conditions to all samples, in order to obtain increased optical transmissions and mechanical resistance. The purity analysis was made with an Induced Coupled Plasma Spectrophotometer. The optical ceramic material was characterised by VIS and IR transmission, using Specord M42 and Perkin-Elmer spectrophotometers. The particle size distribution was measured on a Laser Granulometric Analyser for the powder and with an optical microscope for the optical ceramic.

3. RESULTS

We have studied the influences of the work conditions on the parameters of the optical ceramic materials. As revealed by the following table, time and pressure have a drastic influence on the IR transmission parameter. We also noticed an increase of the particle size during the heat treatment. This had an important influence on the IR transmission parameters.

Table 1 Influence of time and pressure on IR transmission level.

Sample	Diameter (mm)	Force (kgf)	Temperature (°C)	Time (min)	Transmission (%)
1	20	5500	1000	15	29
2	20	5500	1000	30	26
3	20	5500	1000	45	33
4	20	5500	1000	60	29
5	20	5500	1000	25	37
6	20	6000	1000	45	40
7	20	2100	1500	50	19
8	20	2200	1500	50	43
9	20	2200	1500	30	20
10	45	8000	1500	50	17

We have also studied the purity influence on the transmission parameters. We noticed that any kind of impurity promoted the crystal growth by increasing the liquid phase quantum, guiding the process on the phenomenon of recrystallization.

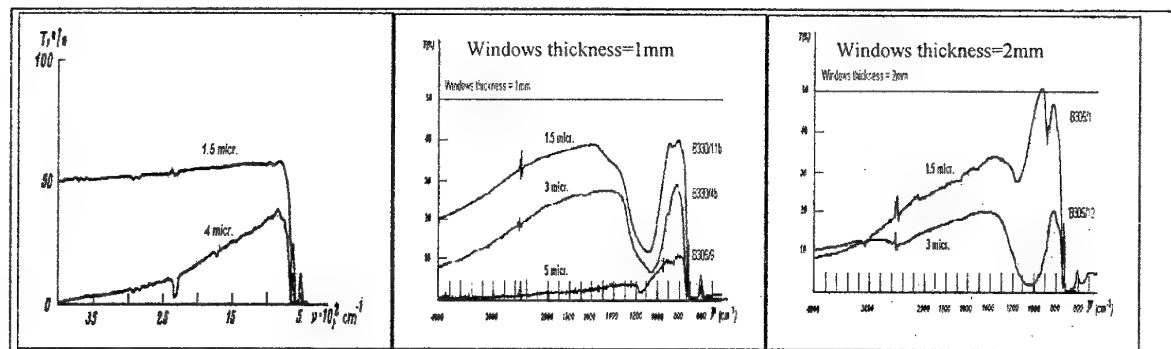


Figure 1. The dependence of the IR optical transmission on the ceramic particle size distribution and windows thickness

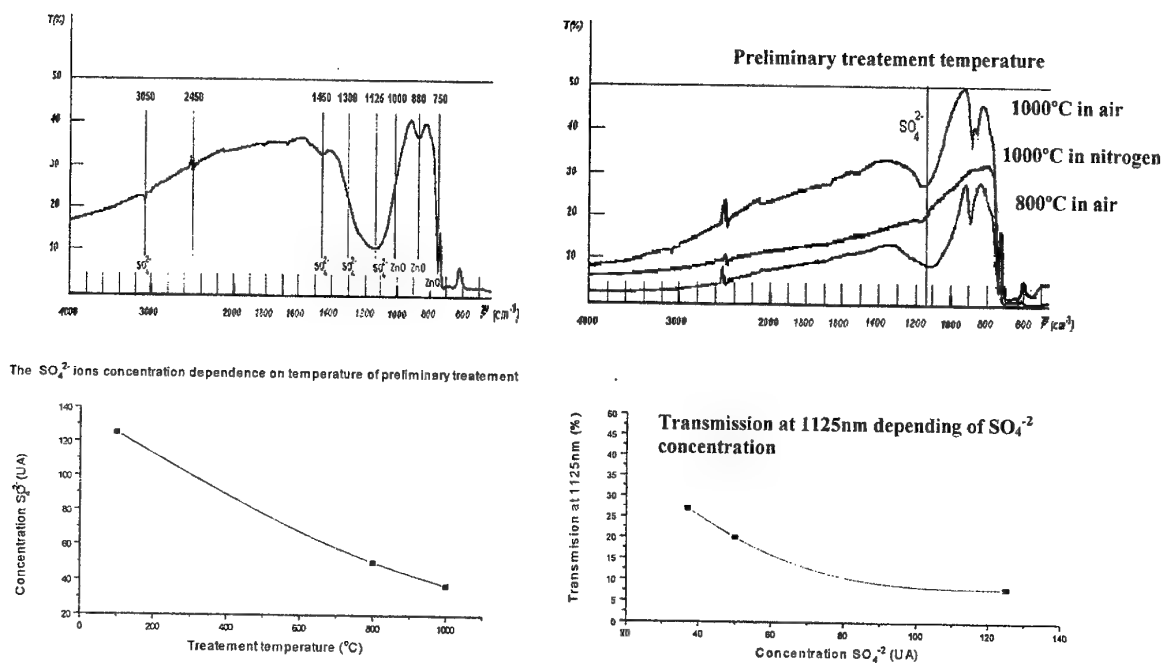


Fig. 2 The dependence of the optical transmission on the impurities contents (HO^+ , H_2O , SO_4^{2-})

4. REFERENCES

- [1]. *****, "Effect of grain growth on hot-pressed optical magnesium fluoride", *J. Am. Cer. Soc.*, Vol.71(3)C, pp.136-137, (1988).
- [2]. *****, "Sintering of magnesium fluoride", *J. Am. Cer. Soc.*, Vol. 42 (12), pp.1149-1153, (1967).
- [3]. Liang A, Xue and Rishi Raj, "Effect of diamond dispersion on the superplastic rheology of zinc sulphide", *J. Am. Cer. Soc.*, Vol.73(8), pp. 2213-16, (1990).
- [4]. *****, "Fracture and stiffness characteristics of particulate composite of diamond in zinc sulphide", *J. Am. Cer. Soc.*, Vol. 73(10), pp.3074-80, (1990).
- [5]. *****, - *J. Am. Cer. Soc.*, 73(10), 3074-80, (1990).
- [6]. *****, - *Neorganicheskie Material*, vol. 24, nr. 12, (1988).
- [7]. *****, - *J. Am. Cer. Soc.*, 71(3)C, 136-137, (1988).
- [8]. A.Smakula, J.Kalnajs, M.J.Redman, "Optical Materials and Their Preparation", *Applied Optics*, Vol.3, nr.3, p.323-328, (1964).
- [9]. F.K.Volinet, "Spasobi izgotovleniya, struktura i fiziko-himicheskie svoystva opticeskoi keramiki", *OMP*, nr.9, p.48-60, (1973).
- [10]. F.K.Volinet, "Opticeskie svoystva i oblasti primeneniya opticeskoi keramiki", *OMP*, nr.10, p.47-57, (1973).
- [11]. R.Sharma & Y.Chang - *J.of Crystal Growth*, p.88193-204, (1988).

STRUCTURAL AND DIELECTRIC CHARACTERIZATION OF CHEMICALLY DERIVED (Pb, La) (Ti, Mn)O₃

Lucia Păcurar, Elisabeth-Jeanne Popovici, Maria Vădan

Institute of Chemistry "Raluca Ripan" 3400 Cluj-Napoca,
str.Fântânele 30, c.p.702, of.5, tel.064-180165, fax.40.64.42.04.41
E-mail: pacurar@icrr.org.soros cj.ro

ABSTRACT

The synthesis of high purity fine grains PbTiO₃ (PT) by using chemical solution technique, in the presence of H₂O₂, at different pH ranges was undertaken. The as precipitated powders were characterized by TG-DTA and XRD. The resulted powders were doped with La₂O₃ and MnO₂ and the dielectric constants of the ceramics were measured.

1. INTRODUCTION

The PbTiO₃ powder prepared by the solution technique has a high reactivity and homogeneity. From this compound, ceramics with desirable combinations of properties have been achieved lately [1,2]. Previous studies [3,4] suggests that the H₂O₂ addition to the starting solutions of TiCl₄ and Pb(NO₃)₂ avoids the hydrolysis of Ti⁴⁺ ions and the formation of basic lead carbonate compounds. The ionic equilibrium present in the system is controlled by the pH of the precipitation. The hydrous oxide of titanium forms over a wide range of basic pH, but the amount of lead may be lost if the pH is not maintained close to the solubility minimum of PbO and Pb(OH)₂ at about 9.50 [5]. In order to obtain stoichiometric PbTiO₃, the precipitation pH should be kept near this value. Otherwise, the occurrence of PbO-deficiency is expected to appear in the resulting perovskite structure.

The aim of this paper is to present the effects of pH on the characteristics of PbTiO₃ powders and on La and Mn doped ceramics.

2. EXPERIMENTAL

The PbTiO₃ samples were made using TiCl₄, Pb(NO₃)₂, H₂O₂ (25%) and (NH₄Cl+NH₄OH) buffer solutions of high purity, as starting materials. H₂O₂ in a molar ratio 1:1 was added to 1000 ml water diluted TiCl₄ solution (0,05 M), and then a stoichiometric amount of lead nitrate solution was introduced finally. Small quantities of lead chloride are formed after several minutes, but they can be dissolved by dilution and heating. The precipitation took place at 42°C, adjusting the pH to the desired value by adding NH₄OH solution. Four samples were prepared (pH = 7.5 - 8.0, a; 8.0 - 8.5, b; 9.0 - 9.5, c and 10.0 - 10.3, d). The filtered and washed precipitates were then dried at 80°C for 24 hrs and calcined at 600°C for 5 hrs.

While the as precipitated precursor powders were characterized by thermogravimetric analysis, the heat treated powders were analyzed by X-Ray diffraction. The PbTiO₃ ceramic specimen with 0.965 PbTiO₃ + 0.025 La₂O₃ and 0.01 MnO₂ composition was prepared from all the calcinated samples. The oxide mixture were ground and calcined at 850°C for 2 hrs. The fired materials were thoroughly reground and then pressed into disks at 1400 kgf/cm². Sintering was performed in air, at 1140°C for 2 hrs. For dielectric measurements the samples were silver electroded by vacuum evaporation.

3. RESULTS AND DISCUSSIONS

The prepared TiCl₄ and H₂O₂ solution is strongly acidic and the formation of complex species is observed [6, 7]. In the 7.0 - 8.5 pH range, yellow species consisting of one peroxy group for each

titanium atoms is formed, with the possible formula of $\text{TiO}_3 \cdot \text{H}_2\text{O}_2$. At pH values greater than 10, colourless species are observed, with proposed formula of either $[\text{Ti}(\text{O}_2)_2(\text{OH})_2]^{2-}$ or $[\text{Ti}(\text{O})(\text{O}_2)_2(\text{OH})_2]^{2-}$.

Lead oxide presents a catalytic activity in decomposition reaction of H_2O_2 , but the way H_2O_2 affects the coprecipitation process at different pH values is unknown [5]. It is assumed that the change of the pH of the solution during the coprecipitation process leads to changes in the composition and structure of the peroxidic compounds of Ti^{4+} .

The *thermogravimetric analysis* of the dried precipitates at different pH values is shown in figure 1. The powders obtained at pH = 7.5 - 8.0 and 8.0 - 8.5 show a weight loss in two stages, ranging from 80 to 365°C and 560 to 720°C, respectively. The TG curve of the powder formed at pH = 9.0 - 9.5 is similarly developed, but in this case the weight loss is relatively much lower. Sample obtained at pH = 10.0-10.3 shows a weight loss of only 9.65% in one stage. The DTA curves for all samples present endothermic peaks corresponding to the weight losses and three exothermic effects at 250, 280 and 465°C. The first two correspond to the formation of Pb_3O_4 and PbO_x ($1.58 < x < 1.41$) [8] and the peak at 465°C can be attributed to PT crystallization. From the shape of TG-DTA curves of the powders one can conclude that there is a different thermal behaviour between the samples obtained at low and high pH values. Although it is known that below pH=9.5 lead becomes soluble as Pb^{2+} ions and at higher pH values the soluble lead specie is the plumbate ion HPbO_2^- [5], one cannot predict the type of precipitate generated in solution in each of pH ranges. From the intensity of the exothermic peaks at 250 and 280°C, corresponding to the formation of Pb_3O_4 and PbO_x , one can assume that the process is more intense in the samples corresponding to pH values far from the solubility minimum.

X-Ray diffraction spectra of the as-precipitated powders of the heat treated samples (600°C, 5 hrs) are shown in figure 2. The dried samples have amorphous structure with a few slightly intense and relatively flat maxima. These maxima are to be found at the same values of the diffraction angles as the main lines of corresponding PbTiO_3 obtained by powder calcination. All the calcined samples show X-Ray diffraction spectra corresponding to the crystalline structure of tetragonal lead titanate, PbTiO_3 . Nevertheless, a diffraction peak ($d = 2.93 \text{ \AA}$) with poor and variable intensity appears in calcined powders. This second phase may be assigned to a lead deficient lead titanate, PbTi_3O_7 , which decomposes to PbTiO_3 and TiO_2 at temperatures higher than 700°C [8]. The quantity of this phase increases with the corresponding decrease of the pH values bellow 9.5. This statement is in good agreement with the TG data. Thus, the appearance of the PbTi_3O_7 phases is clearly controlled by pH.

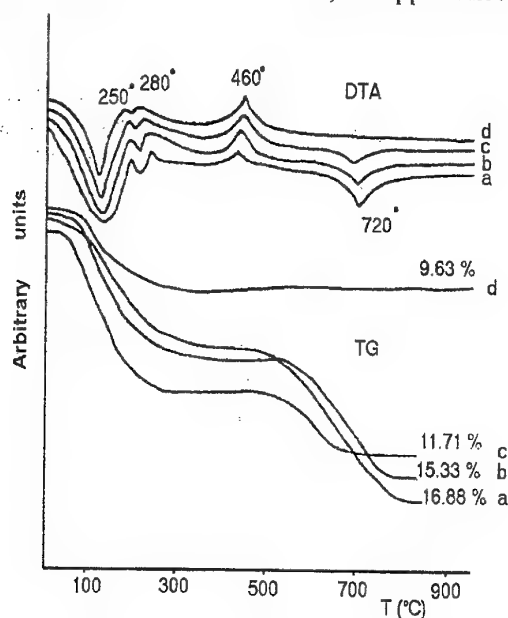


Fig. 1 TG-DTA analysis of powders precipitated at different pH values

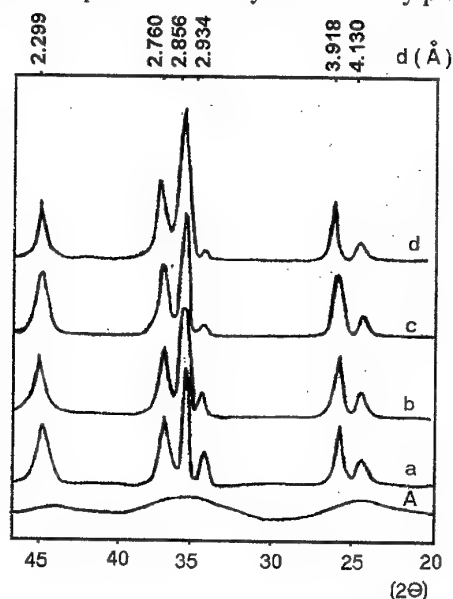


Fig. 2 X-ray diffraction spectra of heat treated (600°C, 5 hrs) samples

Preliminary particle size analysis (Coulter-Counter method) shows that the granulometric distribution of the dried powders lies from 0.7 μm to 25 μm . Powders precipitated at higher pH values consist of smaller particles than those prepared at lower pH values.

Figure 3 presents the temperature dependence on the *dielectric constant* for sintered ceramic samples. One can see that T_C for all La and Mn doped samples is lower ($T_C = 460^\circ\text{C}$) than that for pure PbTiO_3 ($T_C = 495^\circ\text{C}$). The dielectric constant values at T_C (at 1 KHz field) decreases with the decrease of the pH, phenomenon which can be explained by the increase of densification at higher pH values.

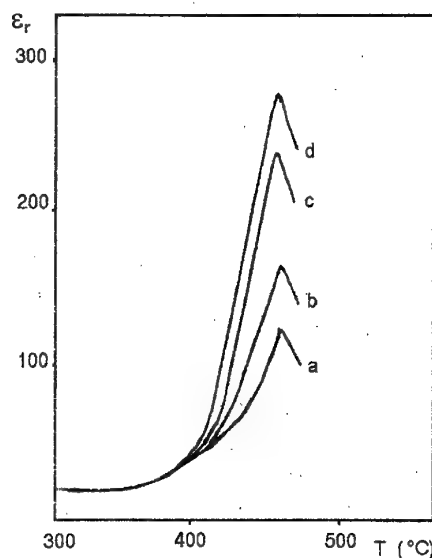


Figure 3. The temperature dependence on dielectric constants

4. REFERENCES

- [1]. Faure S.P., Barboux P., Gaucher P. and Gaune J.P., *Ferroelectrics*, 128, 19-24 (1992).
- [2]. Wolny W.W. and Pederson L., *Ferroelectrics*, 93, 145-149 (1989).
- [3]. Murata M. and Wakino K., *Mater.Res.Bull.* 11, 323 (1976).
- [4]. Schwartz R.W., Eichorst D.J. and Payne D.A., *Mater. Res. Society Symp. Proc.* 73, 123 (1986).
- [5]. Ripan R. and Ceteanu I., "Chimia Metalelor" vol.1, Ed.Didactică si Pedagogică, Bucuresti, 1967.
- [6]. Connor J.A. and Elsworth, E.A.V., *Inorg. Chem.and Radiochem.*, vol.6, Ed. by Emelens H.J. and Sharpe A.G., Academic Press, New York, 1967.
- [7]. Cotton F.A. and Wilkinson G., *Adv. Inorg. Chemistry*, 2nd edition, J.Wiley & Sons, N.Y, 1967.
- [8]. Calzada M.L., De Frutos J., *J.Mat.Sci.Materials in Electronics*, 5, 13-16 (1994).

OPTICAL PROPERTIES IN ALUMINOPHOSPHATE SEMICONDUCTOR – DOPED GLASSES

Rodica Rogojan, P. Sterian*, M. Elisa

MATPUR S.A. Sos.Garii Catelu nr.5, 73611 Bucharest, ROMANIA,
E-mail: rodica@prima.matpur.ro

*University "Politehnica" Bucharest, ROMANIA

ABSTRACT

Semiconductor doped glasses are commercially available as sharp cut - off, high - pass filters; they have been among the first nonlinear optical materials investigated, their absorption saturation being reported as early as 1964. Greater attention started to be paid to these materials after that a fast - subnanosecond - and large third order susceptibility $\chi^{(3)}$, ranging from 10^{-12} esu (as in CdS_2) to 10^{-9} esu (n_2 of the order 10^{-14} m^2/W) was reported in quantum confinement effects; thus, microcrystallites of semiconductors or metallic microparticles in a glass matrix can represent an effective and relatively simple way of realising Quantum Dots Structures. In the present paper we present the fabrication of aluminophosphate semiconductor - doped glasses, their transmission and absorption spectra in uv, vis and ir range and some of their nonlinear properties as well.

1. INTRODUCTION

Semiconductor doped glasses have recently drawn the attention due to their relevant non-linear optical properties. This paper presents the obtaining process of semiconductor doped glasses, which manifest non-linear optical properties, glasses applied to the fabrication of integrated optical structures, optical circuits with fast switching time (below 10^{-14} s) and planar channel wave guides¹.

Besides semiconductors, crystals and organic materials, an increased attention is paid to $\text{CdS}_x\text{Se}_{1-x}$ semiconductor glasses². All studies so far have been applied on semiconductor glasses, in which a microcrystalline phase was grown in silicate vitreous matrix.

The present paper presents our studies directed on the growth of $\text{CdS}_x\text{Se}_{1-x}$ microcrystallites into the aluminophosphatic vitreous matrix. Consequently, the vitreous matrix composition was modified by adding small amounts of Na_2CO_3 (NaOH), SiO_2 and ZnO , which can retain S, Se and Cd at high temperatures. Then, at low temperature, these elements are liberated in order to grow microcrystalline phase.

2. GLASS FABRICATION

Two semiconductor glass compositions were experimented:

- SD1.1. which belongs to the system : $\text{Li}_2\text{O} - \text{P}_2\text{O}_5 - \text{Al}_2\text{O}_3 - \text{BaO} - \text{SiO}_2 - \text{La}_2\text{O}_3$, in which 1% (weight percent) $\text{CdS}_{0.5}\text{Se}_{0.5}$ and 1% (w. p.) ZnO are added;
- SD2.1. which belong to the system: $\text{Li}_2\text{O} - \text{Na}_2\text{O} - \text{P}_2\text{O}_5 - \text{Al}_2\text{O}_3 - \text{BaO} - \text{SiO}_2 - \text{La}_2\text{O}_3$, in which 1% (w. p.) $\text{CdS}_{0.5}\text{Se}_{0.5}$ and 1% (w. p.) ZnO are added.

It can be observed that the second composition contains some percentages of Na_2O , so that we emphasise the doped - semiconductor glass composition influence on the semiconductor and optical properties. A brief description of the technological process is presented bellow. The weighing of raw materials according to the glass molecular formula, the damp homogenisation, the chemical reactions of lithium, natrium, barium and aluminium phosphate occur simultaneously at about 200°C . Then, the drying process and the preliminary heat treatment occur among $100 - 800^\circ\text{C}$, in order to obtain homogeneous phosphates. Melting process takes place at about 1200°C followed by the cleaning up of

the molten glass during several hours, process that has the goal of obtaining a homogeneous glass without defects (gases and fibrous inclusions, etc.).

After all these treatments, stoichiometric amounts of Cd, S and Se are added (for $x=0.5$) paying attention to introduce a supplementary amount of each element, in order to counteract the loss by volatilisation. After the casting process the colourless and transparent glass samples are treated at 425°C, 450°C and 475°C for 2h, 4h, 6h, heat treatments which bring about colouring of SD1.1. and SD2.1. glass samples. The formation and estimation of the microcrystallite stoichiometry is further complicated by the presence of zinc³. There is some concern that zinc, which is present in all these glasses, may substitute to a small degree for cadmium, decreasing the average lattice constant. Because of this it would usually be better to deal with a four component system $Zn_yCd_{1-y}S_xSe_{1-x}$ instead of the three-component system CdS_xSe_{1-x} . Research on this issue has been carried out by Borelli et al. and by Potter et al.^{4,5}

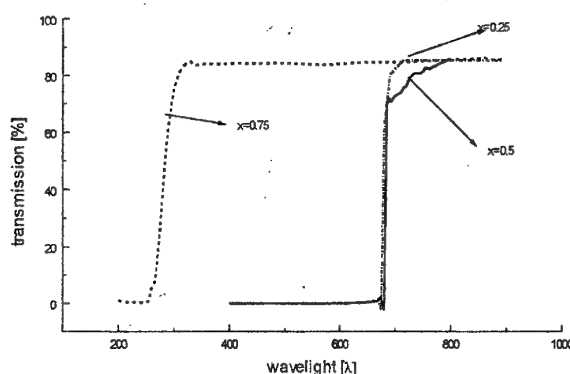


Fig. 1

3. RESULTS

Figures 1 show the behaviour of the absorption edge for SD2.1. glass samples, connecting to the shift of absorption edge to red, for three values of nanocrystallite's composition ($x = 0.25, 0.5$ and 0.75) and 4 hours of heat treatment at 475°C.

SD2.1. glass samples, figure 2, present a short shift of absorption edge (10-40 nm) to red, for all temperatures and all times of heat treatment, so that in this case, even at 425°C, the absorption edge is placed at about 600 nm. This fact can be explained by the growing process of the semiconductor particles, which takes place even before the heat treatment, namely after Cd, Se, S addition and the clearing up of the molten glass.

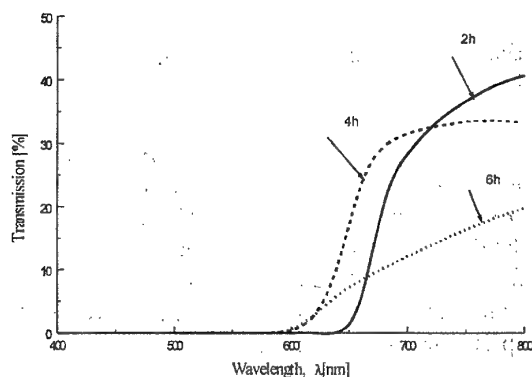


Fig. 2

To characterise the glasses we also measured fluorescence spectra. Using SD2.1. glass sample and the striking process mentioned above we obtained the following results (Figure 3). Samples SD2.1. that were striked at 425°C for 2, 4 and 6 hours shows a peak with a maximum at 578 nm. Decreasing the time of heat treatment causes a decrease in the intensity of the maximum.

The samples were excited with a common xenon lamp using several filters. The wavelength region of excitation was located between 300 and 400 nm.

4. CONCLUSIONS

It would be of great interest to establish a correlation between "x" values (micro crystallites' composition) and several parameters such as: vitreous matrix nature, temperature and time of heat treatment, etc.). We consider important to carry out some X-ray scattering experiments in order to determine the quantitative and qualitative glass compositions: However, we could not achieve high resolution microscopy measurements for estimating the semiconductor micro crystallite's sizes.

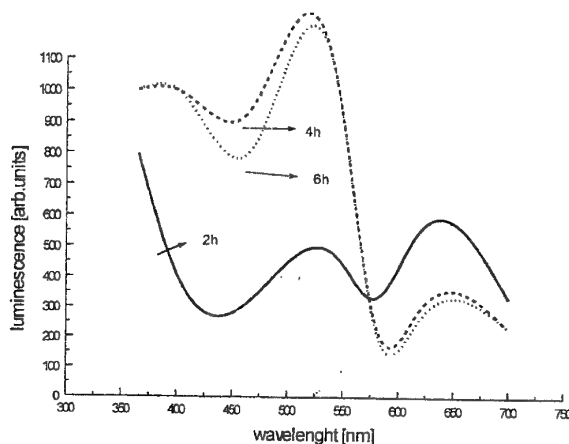


Fig. 3

In the future, it is necessary to continue the experiments in order to emphasise the non-linear optical properties of these glasses and to estimate semiconductor micro crystallite's electron microscopy, small angle X- ray scattering, small angle neutron scattering, low frequency inelastic scattering of light, etc. We consider that aluminophosphate doped-glasses offers good opportunities as a non-linear material.

5. REFERENCES

- [1]. G.C. Righini, G.P. Banfi, V. Degiorgio, F. Nicoletti, S. Pelli, "Semiconductor doped glasses: structural and waveguide characterization", *Materials-Science and Engineering*, Vol. B9, pp.397-403, (1991).
- [2]. L. G. Zimin, *Materials-Science and Engineering*, Vol. B9, pp.405-412, (1991).
- [3]. K. E. Remitz, N. Neuroth, B. Speit, "Semiconductor-doped glasses as a nonlinear material", *Materials-Science and Engineering*, Vol. B9, pp. 413-416, (1991).
- [4]. N. F. Borrelli, D. W. Hall, H. J. Holland, D. W. Smith, "Growth study concerning Cd(S,Se) nanocrystals", *J. Appl. Phys.*, Vol. 61(12), pp.5399-5406, (1987).
- [5]. B.G. Potter and J.H. Simmons, "High resolution transmission electron microscopy", *Phys. Rev. B*, Vol. 37 (18), pp.10 838 -10957, (1988).

DOMAIN INSTABILITIES AND DYNAMICAL SCATTERING MODE IN NEW SYNTHESISED 4,4'-BIS-(4-CHLORO)-BENZYLOXY-AZOXYBENZENE LIQUID CRYSTAL

C.Sarpe-Tudoran, Margareta Socaciu, D.Mustaza, Cornelia Uncheselu

University of Craiova, Faculty of Sciences 13 A.I.Cuza,
1100, Craiova, Romania

ABSTRACT

We present our experimental investigation of the dynamical scattering mode electro-optic effect identified on the new synthesised 4,4'-bis-(4-chloro)-benzyloxy-azoxybenzene liquid crystal.

The presence of smectic B, smectic A and nematic type mesophases in this compound was proven both at heating and cooling by microstructural analysis and differential thermal analysis [1]. This compound has a negative dielectric anisotropy and a low electric resistivity, conduction-induced fluid flow occurring when a DC or AC electric field is applied. The domains induced by electrohydrodynamic instabilities which appear in these conditions lead to a visible pattern modification. Moreover, a dynamical scattering mode electrooptic effect was identified.

1. INTRODUCTION

When a DC or low frequency AC field is applied to a nematic liquid crystal-cell, the anisotropy of the electrical conductivity induces electrohydrodynamic flow. This flow is coupled to the molecular alignment via the viscosity coefficients of the nematic fluid. In these conditions, due to the strong optical anisotropy, the liquid crystal becomes turbulent and scatters light strongly. This effect has received considerable attention due to its applications in displays. The dynamic scattering mode has the advantage that it does not require a polarizer to modulate the light and has been used in displays and light valves in the early stage of liquid crystal device development.

We present our experimental investigations of dynamical scattering mode electrooptic effect identified on the new synthesised 4,4'-bis-(4-chloro)-benzyloxy-azoxybenzene liquid crystal [2].

In order to identify the polymorphism of this compound, we have used the microstructural analysis in polarized light and differential thermal analysis. As a result of these studies, we have identified the presence of S_B , S_A and nematic mesophases, both at heating and cooling.

Due to the symmetrical shape of the molecule of this liquid crystal and to the presence of the azoxy-moiety were found a negative dielectric anisotropy and a low electrical resistivity [1].

In these conditions, domain instabilities and dynamical scattering mode are expected when a DC or low frequency AC electric field is applied on the liquid crystal cell.

2. EXPERIMENTAL RESULTS AND DISCUSSION

In order to investigate this electro-optic effect the liquid crystal sample was encapsulated by capillarity in a sandwich type thickness liquid crystal cell with In_2O_3 electric electrodes. In order to impose a planar alignment of the molecules to the cell walls, a mechano-chemical treatment was realised using polyvinilic alcohol. The cell was thermostated using a computer-controlled microscope hot stage, a stability around $\pm 0.5^\circ\text{C}$ being obtained by a phase controlled device with a numerical PID algorithm [3].

The electro-optic effect appearance was determined by recording the dependence of the transmitted light intensity through the liquid crystal cell as a function of the applied electric voltage. The

light intensity was measured with a Si photodetector placed inside one of the oculars of a IOR MC5A microscope and recorded on a computer through a Keithley Metrabyte DAS 1601 data acquisition board.

The presence of a DC or low frequency AC field induce Williams domains or matriceal texture formation if the applied voltage is greater than a threshold value. If the applied field intensity increases, a dynamical scattering mode electro-optic effect occurs and the transmitted light intensity strongly decreases.

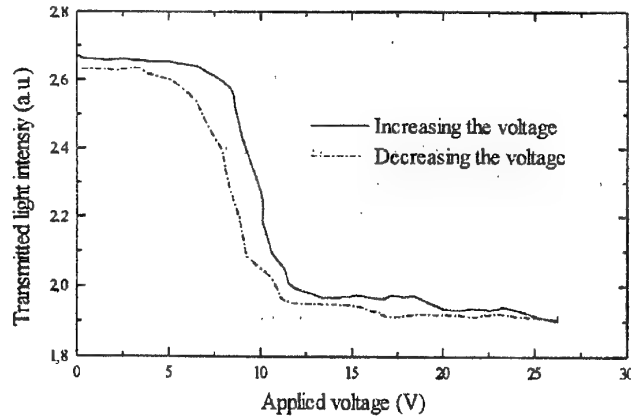


Fig.1 Transmitted light intensity through liquid crystal cell as function of applied alternative voltage (50 Hz). The William domains apparition at 6,9 V and dynamical scattering mode at 12.7 V

This behaviour is presented in Fig.1 at increasing and decreasing of the voltage respectively. From these plots it can be seen that a hysteresis phenomena is present.

The switch-on and switch-off times of the dynamical scattering mode electro-optic effects were determined by recording the transmitted light intensity through the liquid crystal cell under a pulsatory electric field. For a good measurement of these parameters, a semiconductor laser (670 nm) and a high speed photodiode amplifier connected to the computer by the interface in DMA mode were used. The values so obtained are: $\tau_{on} = 182$ ms and $\tau_{off} = 246$ ms respectively (at 15 V applied voltage).

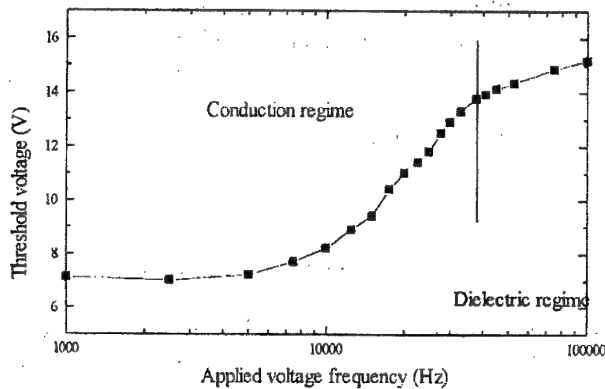


Fig.2. The dependence of the threshold value for Williams domains apparition as a function of the frequency. The dielectric regime apparition at 33 kHz

For high frequency AC fields, the pattern changes to chevrone-like domains or snake-like regions. The dependence of the threshold voltage on the occurrence of the Williams domains or

chevrone-like domains on the frequency in plotted in fig.2 where one can see the cut-off value (33 kHz) at which the transition from conduction to dielectric behaviour of the liquid crystal layer arises.

3. REFERENCES

- [1] Sarpe-Tudoran Cristian, Margareta Socaciu, George Bratulescu, presented in Romanian Conference on Advanced Materials, ROCAM 97, Bucuresti.
- [2] Radu S., Sarpe-Tudoran C., Jianu Anca, Rau Gabriela, accepted for publication in Revue Roumaine de Chimie, (1998).
- [3] Hall B.D., "Physics Experiments using Pcs", Springer-Verlag, Berlin, 1993.
- [4] Barall E.M., Vogel M.J., Thermochem Acta, 1, 127, (1970).
- [5] Sarpe-Tudoran C., M.Socaciu, M.Ursache, J.Neamtu, G.Bratulescu, S.radu, accepted for publication in Proceeding SPIE series, (1998).
- [6] S.Radu, Sarpe-Tudoran C., Afinidad, 474, 125-129, (1998).

STUDY OF THE ABSORPTION SPECTRA CHANGING WITH TEMPERATURE FOR NEW SYNTHESIZED LIQUID CRYSTALS

Margareta Socaciu, C. Sarpe-Tudoran, J. Neamtu*,
Gabriela Iacobescu, Cristina Sarpe-Tudoran

University of Craiova, Department of Physics, 13 A.I. Cuza, Craiova, 1100

*University of Medicine and Pharmacy, Craiova

ABSTRACT

This paper summarises some experimental results obtained on new synthesized liquid crystals, derivatives of 4,4'-dihydroxyazoxybenzene obtained by optical absorption spectroscopy. The dependence of these spectra on liquid crystal temperature is investigated. These data complete the results correlated with mesomorphism performed by other methods.

1. INTRODUCTION

The absorption of liquid crystals in the off-resonance region has several important bearings on liquid devices. First, in the electro-optic modulation of high power laser beams, the absorbed laser energy is transferred to heat and subsequently warms up the molecules. Consequently, the order parameter, the viscosity elastic constant, and the dielectric anisotropy are reduced. These changes influence the devices performances in unpredictable manners. Second, the absorption-induced thermal leasing effect may interfere with other optical field-induced effects. Third, the absorption of short wavelength photons may trigger some inter-molecular chemical reactions leading to degradation and shortening of the devices lifetime. The spectroscopic method was suggested as a way to determinate the temperature dependence of optical transmission in the visible and ultraviolet domains for liquid crystals with different mesophases.

We have investigated by optical absorption spectroscopy three aromatic azoxybisethers with liquid crystals behaviour[1,2]. The general chemical structure of these compounds is presented in figure 1, with R=F, Cl, Br.

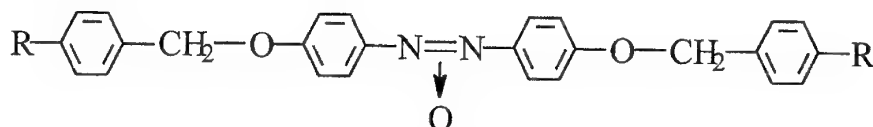


Fig. 1 Structure of the azoxyderivatives liquid crystals

Using the microstructural analysis in polarised light, smectic B, smectic A and nematic type mesophases were identified, both at heating and cooling. For a high precision determination of the phase transition temperatures, the differential thermal analysis was also used (the values are presented in table 1).

Table 1 Phase transition temperatures of the new synthesized azoxyderivatives
at heating (up) and cooling (down)

Radical R in general formula	K-S _B transition temperature	S _B -S _A transition temperature	S _A -N transition temperature	N-I transition temperature
F	123121	153136	185.6185.6	223.5223.5
Cl	120119	156.8135	179178	233.2233.2
Br	152150.3	177167	207.2206	251250

2. EXPERIMENTAL METHOD AND RESULTS

In order to study the dependence of the optical absorption spectra on temperature, a fiber optic spectrophotometer equipped with a 600 grooves/mm holographic grating and a 1024 points linear array CCD was used. The sample was conventionally prepared namely, the substance was encapsulated by capillarity in thick sandwich type cells. The cells were thermostated using a microscope hot stage allowing simultaneous microstructural observations. Using an optical device, the light beam was focused on a 1mm - diameter optical fiber and was transmitted to the spectrophotometer. The detector output was connected to the computer through a DAS 1601 interface in direct memory access mode for a high speed data acquisition. The signal was also monitored on a scope. The exposure time was established externally by a pulse generator in the range 1ms-10s. The spectrum of the empty cell was excluded and the spectral sensibility of the CCD detector was taken into account.

Using this experimental set-up, we have recorded optical transmission spectra in the range of 400-800nm, as function of the sample temperature, corresponding to different mesophases. In figure 2-4 there are presented the results obtained at heating for 4,4'-bis(4-fluor)benzyloxyazoxybenzene, 4,4'-bis(4-chlor)benzyloxyazoxybenzene, respectively. The shape of the spectra is identically reproduced at heating and cooling, for the same mesophases.

From the spectra presented in figure 2 it can be seen that for the azoxy- derivative compound with fluor in terminal position of the general chemical formula, there are narrow bands at 400nm and 735nm in solid and smectic phases, and one single band at 400nm in nematic and isotropic phases. For the compound with chlore in terminal position, the spectra shape (fig. 3) is similar, with only the difference that at high temperatures (nematic and isotropic phases) an absorption band at 778nm is also present.

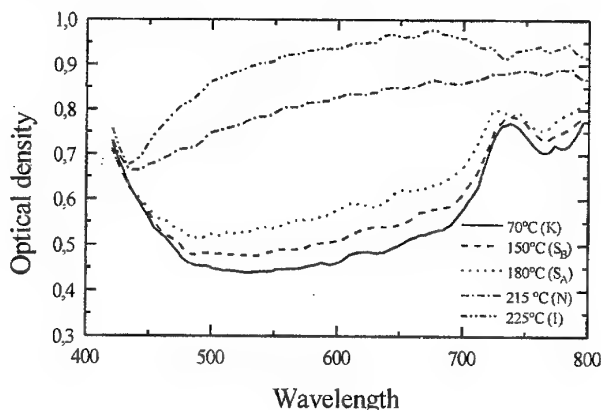


Fig. 2 Absorption spectra for 4,4'-bis(4-fluor)benzyl-oxyazoxybenzene

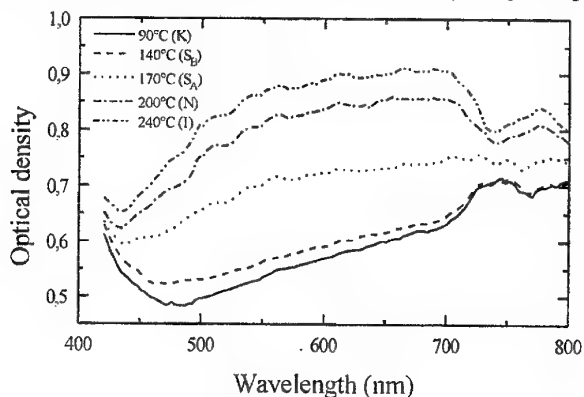


Fig. 3 Absorption spectra for 4,4'-bis(4-chlor)benzyl-oxyazoxybenzene

The spectra shapes for 4,4'-bis(4-brom)benzyloxy-azoxy- benzene (fig. 4) are different for the other two compounds in solid and smectic B phases, and are similar in nematic and isotropic phases.

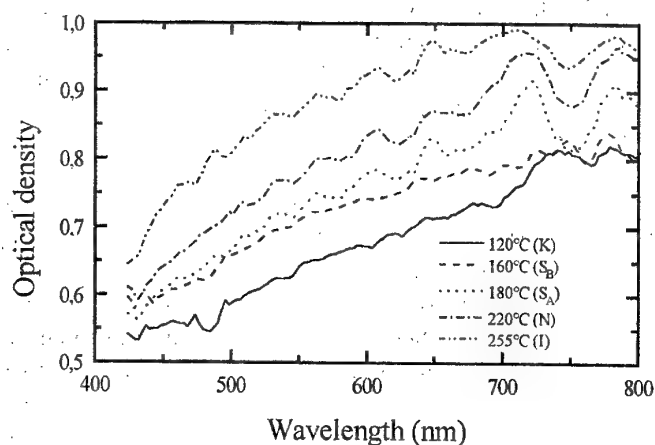


Fig. 4 Absorption spectra for 4,4'-bis(4-brom)benzyl-oxyazoxybenzene

3. REFERENCES

- [1] Radu S., Sarpe-Tudoran C., *Afinidad*, 474, 125-129, (1998)
- [2] Radu S., Sarpe-Tudoran C., Jianu Anca, Rau Gabriela, accepted for publication in *Revue Roumaine de Chimie*, (1998)
- [3] Sarpe-Tudoran Cristian, Margareta Socaciu, George Bratulescu, presented in Romanian Conference on Advanced Materials, ROCAM 97, Bucuresti
- [4] Sarpe-Tudoran C., Socaciu Margareta, Ursache Marcela, Neamtu J., Bratulescu G., Radu S., accepted for publication in *Proceeding SPIE series*, (1998).

DOPED AND UNDOPED META-DINITROBENZENE THIN FILMS GROWTH AND CHARACTERIZATION

Anca Stanculescu, F. Stanculescu,

MATPUR, Sos. Garii Catelu nr.5, 73611, Bucharest, ROMANIA
fax: +401-2550148, e-mail: anca@prima.matpur.ro

ABSTRACT

This paper presents a study on the thin films growth process of a disubstitute derivate of benzene of very high purity used as optical material. As dopants we have used oxine (8 hydroxy-quinoline) and resorcinol (1.3 dihydroxybenzene). The thin film growth process consists of two stages: 1. synthesis of pure and doped meta-dinitrobenzene ingots; 2. growth films of different thickness, between two glass/quartz plates. The thin films have been characterized by UV-VIS Transmission Spectroscopy. The influence of the dopant on the optical properties of meta-dinitrobenzene and their effect on the band gap energy of the material and on the absorption mechanism near the absorption edge have been analysed.

1. INTRODUCTION

The disubstituted derivative of benzene presents strong second order nonlinear optical effects. Any substituent group can disturb the symmetry of the electronic cloud, the optical nonlinear susceptibilities being usually measured by average interaction dipole momentum between substituent group and electronic cloud. This interaction is stronger for noncentrosymmetric crystalline class of compounds.

Meta-dinitrobenzene is a promising optical material because it can be synthetized relatively easily and it shows transparency between UV and IR. The quality of the material structure can be reduced and it is possible to use the organic material as crystalline thin films and not as bulk crystal.

This paper presents a study on the thin films growth process and characterization of a disubstituted derivate of benzene used as optical material.

2. EXPERIMENTAL METHOD

The starting material was meta-dinitrobenzene of very high purity synthetized from very pure components by a nitration reaction of the aromatic compound with a mixture of sulphuric and nitric acids. This material was then purified successively by chemical and physical methods. The impurities content was reduced by vacuum distillation under 10^{-4} torr and by directional freezing in two steps [1].

This material was used to obtained organic crystals by a Bridgman-Stockbarger modified method with a steeper thermal gradient at the growing interface ($\sim 8-9^\circ\text{C}$), a special geometry of the ampoule and a slow moving speed (~ 1 mm/h). We have used as dopants 0.006 g of 8 hydroxy-quinoline (oxine) for a charge of 0.6 of meta-dinitrobenzene, and 0.02 g 1.3 dihydroxybenzene (resorcinol) for a charge of 0.20 g of meta-dinitrobenzene. The growth process of meta-dinitrobenzene crystal doped with oxine is characterized by: a temperature gradient at the interface of 5°C and an interface speed of 1 mm/h [2]. Meta-dinitrobenzene crystal doped with resorcinol was obtained in a quartz ampoule under vacuum and agitation to assure the homogeneity of the material.

Crystalline fragments from pure and doped crystals of meta-dinitrobenzene have been used to grow crystalline organic thin films between two glass/quartz plates in the conditions of the dendritic growth. We have obtained films with a columnar structure in their plane because of the high growth anisotropy. Optical properties of the films and the influence of the dopant were investigated by UV-VIS transmission spectroscopy.

The fitting of the spectral data with function: $\alpha(E)=A+B(E-E_g)^n$ gives us the band gap energy of every type of material and the dominant absorption mechanism near the absorption edge. Comparing these results we can deduce the influence of the dopant on the properties of organic compound.

3. RESULTS

Transmission spectra of pure m-DNB and m-DNB doped with oxine and resorcinol are presented in Figure 1 and respectively in Figure 3. The influence of film crystalline quality and thickness are illustrated in Figure 1. The influence of the dopant on the transmission spectra depends of the quality (purity, crystallinity) of the starting fragments used to grow thin films and the dopant concentration. Experimental data processing of m-DNB near the absorption edge (Figure 2) gave a band gap energy, E_g ; 2.95-2.97 eV and a power coefficient n ; 1.31-1.42, suggesting a direct forbidden band to band transition. The presence of dopant can strongly affect the band gap energy (m-DNB doped with resorcinol, $E_g=2.52$ eV, Figure 5), or practically have a little influence on it (m-DNB doped with oxine, $E_g=2.96$ eV, Figure 4). The absorption mechanism remains the same: $n=1.60$ for m-DNB doped with oxine and $n=1.64$ for m-DNB doped with resorcinol.

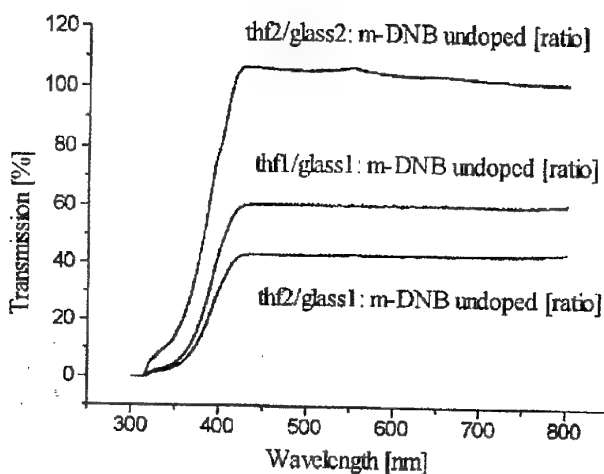


Fig. 1 Thin films transmission spectra on undoped meta-dinitrobenzene (m-DNB) of different thickness and crystalline quality

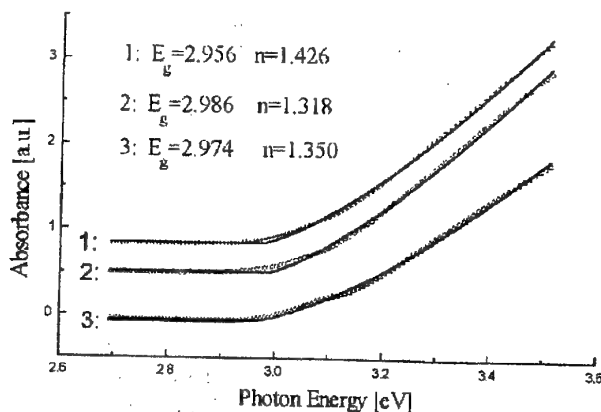


Fig. 2 Power function fitting on experimental data of undoped meta-dinitrobenzene thin films

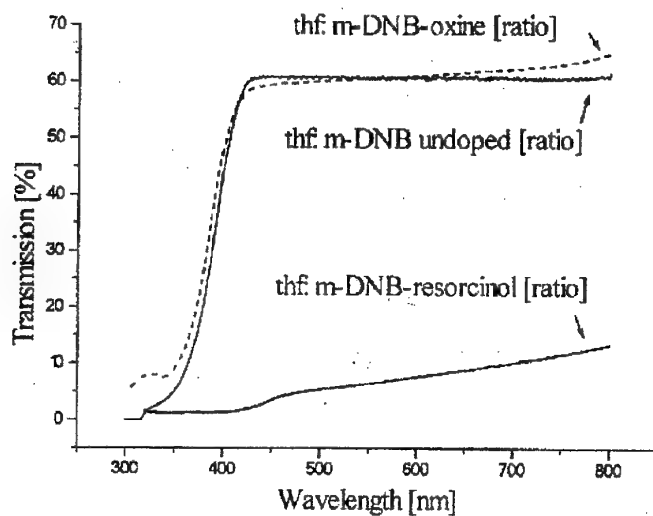


Fig. 3 The influence of the dopant (oxine, resorcinol) on the transmission spectra of meta-dinitrobenzene

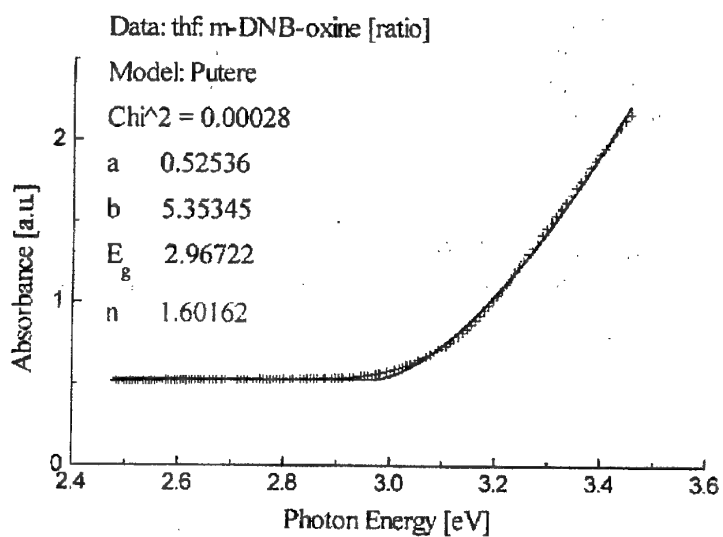


Fig. 4 Power function fitting on experimental data of meta-dinitrobenzene doped with oxine thin film

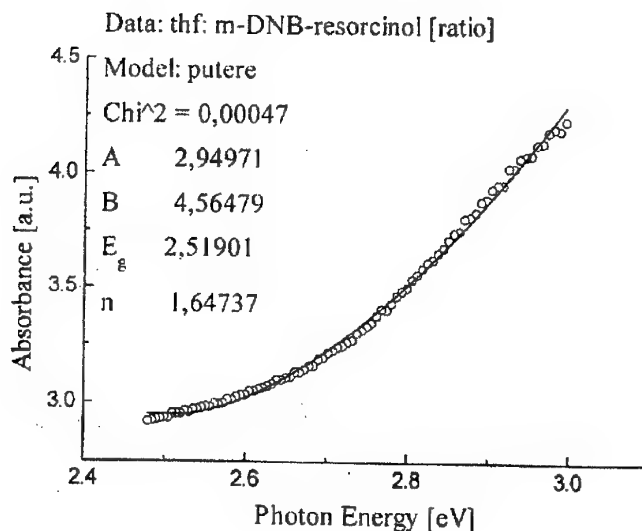


Fig. 5 Power function fitting on experimental data of meta-dinitrobenzene doped with resorcinol thin film

4. CONCLUSIONS

We have obtained organic doped and undoped thin films by a dendritic growth process between two substrates of glass or quartz. The presence of dopant affects the optical properties of organic crystalline thin films. The influence on band gap energy and absorption mechanism have been investigated. The most important parameters are: the dopant concentration, the quality (purity, crystallinity) of the material used for thin films growth and the films' thickness.

5. REFERENCES

- [1] Stanculescu, Anca, Popina, Al., SPIE Vol. 2700, 93(1993);
- [2] Stanculescu, Anca, Stanculescu, F., Alexandru, H., J. Crystal Growth, To be published (1998).

UNIFORMITY OF MAGNETRON SPUTTERED ALUMINIUM NITRIDE LAYERS

Mihaela Tanase, V.Dumitru*, C.Morosanu*, Laura Tugulea, Doina Nicolae**

Faculty of Physics-University of Bucharest, Magurele-Bucharest, P.O. Box MG 11

*National Institute of Materials Physics, P.O. Box Mg7, Magurele, Bucharest

**National Institute of R&D for Optoelectronics, P.O. Box MG-5, Magurele, Bucharest

ABSTRACT

Thickness uniformity of adherent, low stress aluminium nitride films were studied. A level of non-uniformity within a range of 2% on a 2 cm diameter region, and within a range of 10% on a 5 cm diameter region, for a 2.8 cm target-substrate distance was obtained. Better uniformities, like 13% on 8 cm diameter could be obtained detrimental to the decrease in deposition rate.

1. INTRODUCTION

Aluminium nitride has a wide direct band-gap (6.2 eV), a high value of refractive index in the visible range (>2.1), a good chemical and thermal stability, a very fast Rayleigh velocity and good dielectric properties. Due to the combination of these interesting properties, AlN thin films are promising for many applications.

The deposition conditions for obtaining, by magnetron sputtering of adherent and transparent AlN layers with various growth modes, from highly oriented to amorphous, have been previously studied [1,2].

The use of AlN films in different optical applications depends on a good thickness uniformity.

The aim of this paper is to study the dependence of the thickness uniformity of AlN layers deposited by magnetron sputtering on deposition conditions. We have also investigated the growth mode in the centre of the layers.

2. EXPERIMENTAL DETAILS

Films of AlN were obtained in a conventional DC, RF magnetron system using reactive sputtering method in argon and nitrogen. The experimental details have been previously reported [2]. We have deposited AlN layers on glass substrates at distances target-substrates between 2.8-20 cm, and in a pressure range of 2-6 mTorr. Optical transmission measurements were performed by means of a Perkin Elmer Lambda 2S spectrophotometer. We have estimated the thickness of the layers from the interference fringes in the visible range. Structure of the films was investigated by X-ray diffraction. A DRON-2 diffractometer provided with a copper target tube was used.

3. RESULTS AND DISCUSSIONS

It is known that for the magnetron sputtering deposition mode, the optimum target-substrate distance is approximately half of the discharge diameter ring. In our case, while the ring diameter is around 5.6 cm, we have chosen a 2.8 and 3.0 cm target-substrate distance in order to estimate the uniformity and its dependence of the deposition parameters.

The layers deposited in the range 2-2.5 mTorr pressure, at 30% ratio of nitrogen to total flow have been yielded in partially stress-damaged, which could be explained by high compressive stresses due to low pressure intense positive ions and neutral atoms bombardment [3]. We have succeeded to obtain well-adherent layers at this target-substrate distance by increasing the deposition pressure to 4 mTorr and 6 mTorr, which increases the scattering rate, and therefore the number of the particles to reach the film obliquely and with low energies. The decreasing of compressive stresses is due to this increase in pressure.

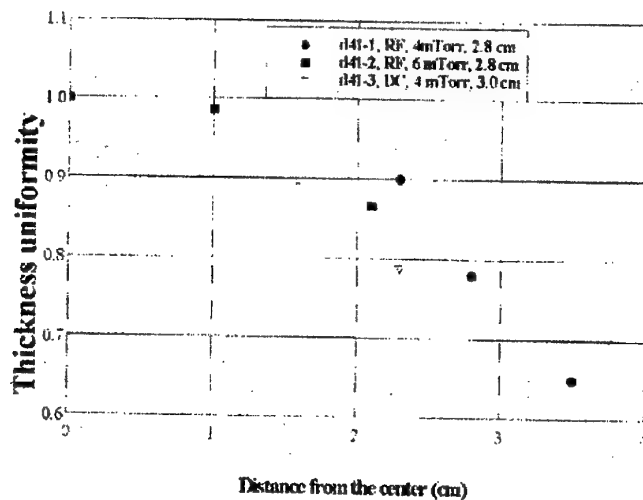


Fig. 1 Thickness uniformity of some layers deposited at a target-substrate distances of around 3.0 cm, in different depositions

Figure 1 shows the strong uniformity dependence on the deposition conditions for the well-adherent layers obtained at 2.8 and 3cm target-substrate distances. One can see that it was possible to obtain a level of non-uniformity within a range of 2% on 2cm diameter (sample D41/2) and within a range of 10% on 5cm-diameter region (sample D41/1).

When increasing the target substrate distance, the non-uniformity is growing first, but for distances as three-four times the discharge ring diameter, the uniformity is improving. Fig. 2 shows the increased thickness uniformity for a target-substrate distance of 15cm (D43/2) within a 13% range variation, on an 8cm diameter. For a distance of 2.8cm, such a variation is likely to appear on a 4cm diameter.

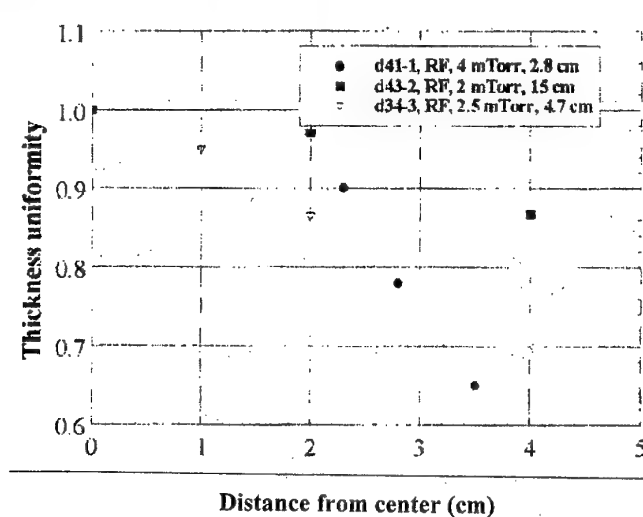


Fig. 2 Thickness uniformity of some layers deposited at a different target-substrate distances

Unfortunately this improvement in uniformity is accompanied by a decrease of deposition rate due to the greater target-substrate distance. Figure 3 shows the deposition rate vs. a set of target to substrate

distances. In the same deposition conditions (RF mode, 2 mTorr, 30% nitrogen/(nitrogen + argon)) it decreases dramatically, around 8.7 times, for an increase in distance from 4.7 to 20 cm.

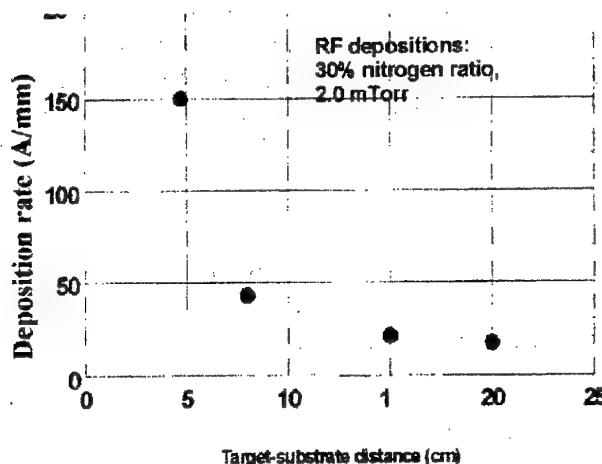


Fig. 3 Variation of deposition rate vs. target substance distance

For the layers in fig. 3, we have done X-ray diffraction measurements in order to investigate the influence of the target substrate deposition distance on the growth mode of the AlN layers.

The layers deposited at 4.7cm distance from the target were obtained high-oriented, with the c axis normal to the substrate (fig.4).

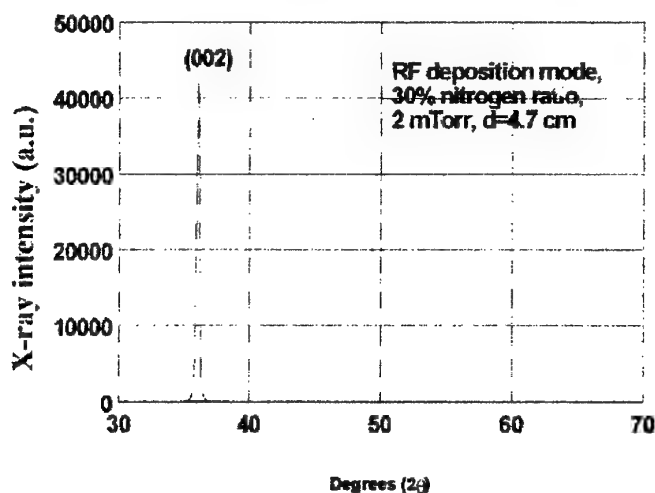


Fig. 4 X-ray diffraction pattern for a high oriented layer, obtained at a 4.7 cm target-substrate distance

A value of FWHM of 0.27° was estimated for the X-ray diffraction measurements. Increasing the distance target substrate to 8 cm, the ions bombardment upon the substrate decreases due to the scattering and the layers become amorphous. The same diffraction pattern, without any X-ray peaks, was obtained for the layers deposited at 15 and 20cm distance from the target.

4. CONCLUSIONS

The uniformity of the quality of aluminium nitride layers is an important parameter when applications on these layers are considered. A level of nonuniformity within a range of 2%, on a 2 cm diameter, and the high value of the refractive index [4], make these layers attractive for use in optical applications, such as antireflection layers for AlGaAs laser diodes. Besides, the amorphous and the high uniform layers (13% nonuniformity on a 8 cm diameter) are strongly recommended for chemical protective layers. The c-axis high oriented AlN films (FWHM= 0.27°) are suitable for use in GHz band surface acoustic wave devices.

5. REFERENCES

- [1]. H.Okano, Y.Takahashi, T.Tanaka, K. Shibata, S. Nakano, Jpn. J. Appl. Phys., Vol. 31 (1992), p. 3446-3451.
- [2]. C.Morosanu, V.Dumitru, E.Cimpoiasu, C.Nenu, NATO ARW "Wide Band Gap Electronic Materials", 20-21 june 1996, Russia, to be published in ASI Series.
- [3]. G. L. Huffman, D. E. Fahnline, R. Messier, L.J.Pioline, J. Vac. Sci. Technol. A 7(3) 1989.
- [4]. V. Dumitru, E. Cimpoiasu, C. Morosanu, C. Nenu, D. Necsoiu, Proceedings of 19th International Semic. Conf.(1996), Sinaia, Romania, Oct.12-14, pg. 641-644.

TRIBOLOGICAL PROPERTIES OF rf-PECVD DEPOSITED a-C:H FILMS

N. Tomozeiu

University of Bucharest, Faculty of Physics, P.O. Box 11Mg, 5600, Bucharest, ROMANIA

ABSTRACT

Amorphous hydrogenated carbon (a-C:H) thin films have been intensively studied in recent years due to their applications in various fields such as optical, wear and corrosion resistant coatings. These films may have properties similar to those of crystalline diamond, such as chemical inertness, hardness, optical transparency and high electrical resistivity.

The a-C:H thin films were deposited onto silicon and glass substrates using a rf-PECVD (Plasma Enhanced Chemical Vapor Deposition) process. The plasma was studied using optical emission spectroscopy (OES). The effect of the diluent gases inert (He) plus CH₄ on both the plasma parameters and the film properties are discussed. The tribological properties of the resulting films were evaluated for samples deposited. The most important observation is that He dilution (>90%) promotes enhanced adhesion with respect to both substrate materials studied.

1. INTRODUCTION

Carbon shows a variety of structures in its elemental state and a great diversity concerning the physico-chemical properties. In most chemical environments, carbon forms electronic states close to the sp³, sp² or sp¹ hybridization. In the crystalline states, the sp³ and sp² configurations are diamond and graphite, respectively. The amorphous state means the existence of an intermediate hybridization states because some of the atoms are in highly strained configurations. Generally the existence of the sp³ and sp² groups which form the a-C:H structure is assumed. The sp³/sp² ratio is a good parameter, which defines from structural point of view the a-C:H layer [1]. Many authors use this ratio related to the material properties of the carbon layer. The high surface smoothness and chemical inertness in combination with a low friction coefficient make the hydrogenated amorphous carbon with high sp³/sp² ratio (DLC layers) an ideal candidate for wear-protective applications.

A number of deposition techniques have been reported for the deposition of a-C:H films. These include ion beam, sputtering, laser ablation and a number of CVD methods. The rf-PECVD technique use standard plasma processing technology which requires low temperature and is relatively inexpensive and simple. The most important disadvantage of using this deposition technique is the fact that the resulting DLC films exhibit high compressive stress [2]. In order to minimize the stress values, Clay et al. [3] show that it is possible to obtain films of widely varying properties by influencing various deposition parameters, such as the substrate negative self-bias, pressure, flow rate, power, etc.

This paper analyzes the tribological properties of a-C:H layers obtained by rf PECVD process from mixtures of pure methane with helium (CH₄+He) or argon (CH₄+Ar).

2. EXPERIMENTAL DETAILS

2a. Sample preparation

The DLC films were deposited onto silicon substrates using a standard capacitively coupled parallel plate electrode reaction chamber, powered by a 13.56 MHz rf power source. Because the electrode radii are asymmetric and the electron and ion mobilities are different in the rf electric field, a negative dc self-bias was developed across the plasma sheath and driven electrode. The substrates were placed on the lower electrode which was maintained at 20°C. The pressure inside the reactor chamber was kept at the same value - 100mTorr - during all depositions. All samples were chemically pre-cleaned using an acid dip followed by a selection of solvent and deionised water in an ultrasonic bath. In order to

remove any oxide layer at the substrates surface, the substrates were putter cleaned in-situ using Ar plasma.

During deposition the reaction gasses (CH_4 and CH_4+He or CH_4+Ar respectively) are fragmented into ions, electrons and neutral species. Ions are accelerated to the negatively self-biased lower electrode by a constant electric field and this ion bombardment together with diffusion and neutral species through the plasma sheath leads to the film formation.

2b. Film Characterization

The thickness of deposited films was determined by ellipsometry and profilometric measurements. Deposition rate is related to the deposition parameters via plasma composition determined using Optical Emission Spectroscopy (OES) measurements. In order to obtain the OES spectra, a monochromator connected by an optical fiber to the quartz window of the reactor chamber was used.

Wear and friction coefficient were determined by a tribotester which is schematically presented in figure 1. The slider had a spherically shape diamond stylus of radius 5.7mm. During all measurements the speed of the slider was 20mm/s and the load 14.7N. For each sample, wear scars were obtained after 100, 500, 1000, 5000 and 10000 cycles and measured by profilometry.

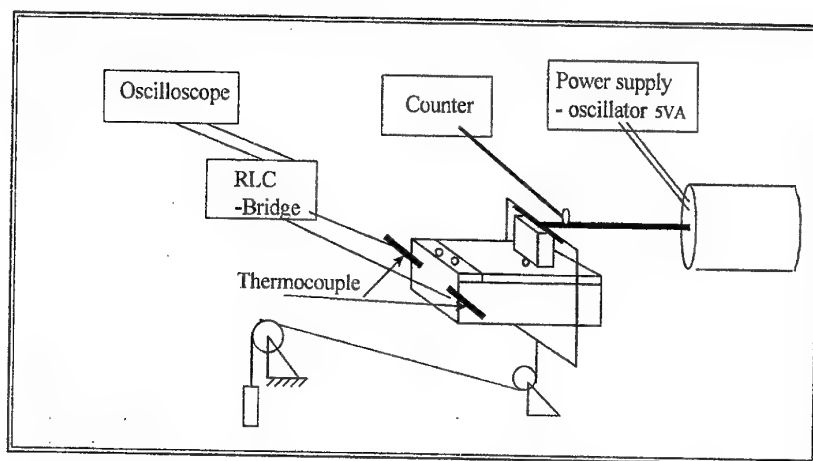


Fig. 1 A tribotester schema

3. RESULTS AND DISCUSSIONS

Optical emission spectra of the generated plasma between the electrodes are studied and the lines common to both plasma types - pure methane and mixture methane + helium- observed in the spectra, are shown in figure 2. The CH line was identified at 430nm and two lines of Balmer series of the atomic hydrogen were identified in the spectra as follows: H_β at 486nm and H_α at 656nm [4]. We highlight the helium influence on the CH and atomic H lines. From figure 2, we can observe that the hydrogen line - 656nm is smaller in intensity when helium is used, whereas the CH lines at 430nm are more intense with helium. This means that the excitation processes described by:



are more effective in CH_4 -He plasmas than in pure CH_4 plasmas.

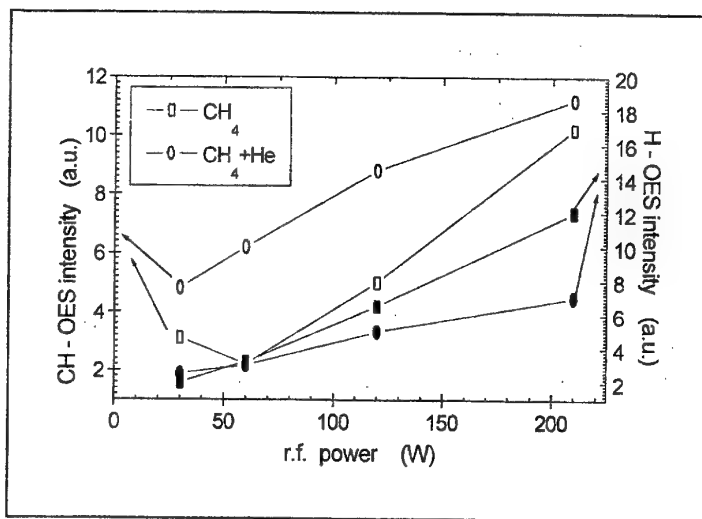


Fig.2 OES intensity lines for pure methane and methane + helium plasmas

Deposition rate as a function of rf power is shown in figure 3. It is known that during deposition process, there is a physical sputtering of the weakly bond species. Therefore, the deposition rate is the result of a deposition - etching equilibrium process. The difference between the CH₄ and CH₄+He films deposition rates may be due to the sputter yield of helium. With increasing the rf power, the deposition rate increases for both plasma types. It can be seen that the deposition rate of films grown from CH₄+He plasmas, although lower, follows the same trend as those grown from pure CH₄ plasmas.

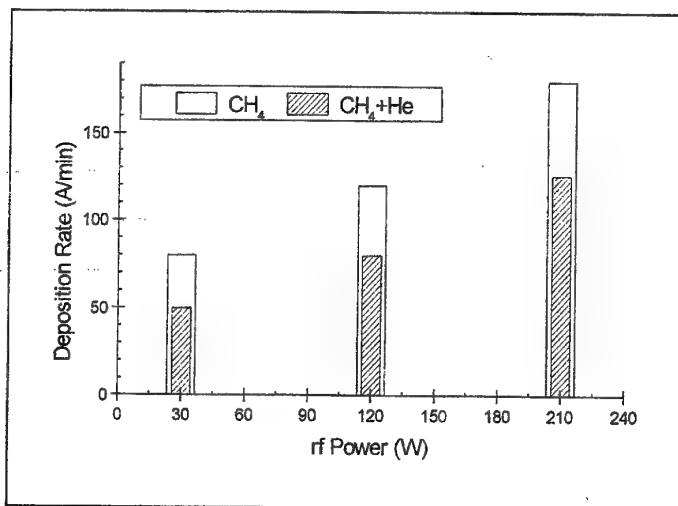


Fig.3 Deposition rate versus rf power applied

The adhesion of the a-C:H film to the substrate is a function of deposition conditions, substrate nature, gas diluent used. We observe that the deposited film adhesion to silicon wafer is better than to optical glass. Delamination was observed with increasing film thickness. Only from CH₄+He plasmas was possible to obtain films with thickness above 3000Å. The smallest adhesion was observed for samples deposited from pure methane.

Tribological measurements in order to test wear and friction coefficient were performed on samples deposited from CH₄+He and CH₄+Ar plasmas. The wear scar depth versus number of cycles is presented in figure 4a, for both types of samples in comparison to data for uncoated silicon substrate. It

can be observed that the a-C:H films assure a good protection from a wear point of view for silicon substrate. For 5000 cycles the wear depth scar is around 500Å for uncoated silicon and only 150Å for a-C:H layer. When the cycles number increases, the wear performances are higher: 1200Å for uncoated silicon in comparison to 400Å for a-C:H deposited from CH₄+He plasmas.

Friction coefficient values were calculated from the normal load N , and the frictional force F_f , using the well-known formula:

$$\mu = \frac{F_f}{N} \quad (2)$$

Figure 4a shows the coefficient of friction values obtained for various number of cycles. All values are below 0.1 and below the friction coefficient values for uncoated silicon. If for silicon wafer the measured friction coefficient is around 0.077, the a-C:H layers shows values around 0.065. This is due to the graphite-like carbon which exists in the structure of a-C:H films.

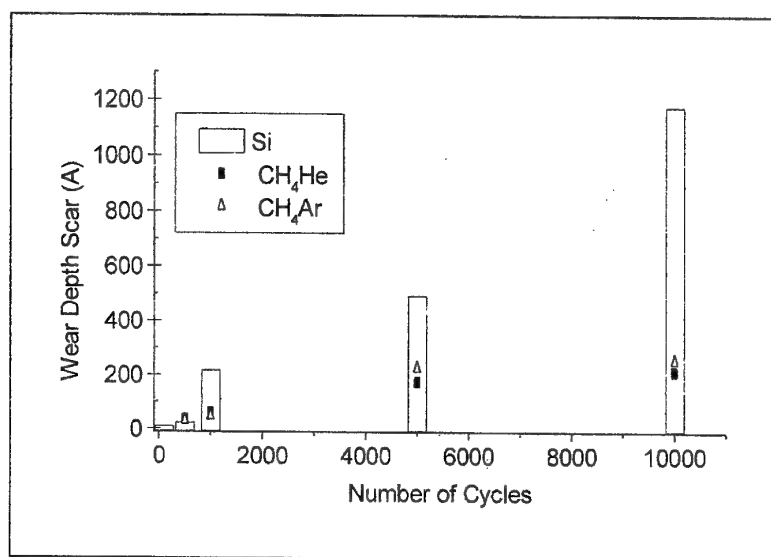


Fig. 4a. Wear scar depth as function on cycles number

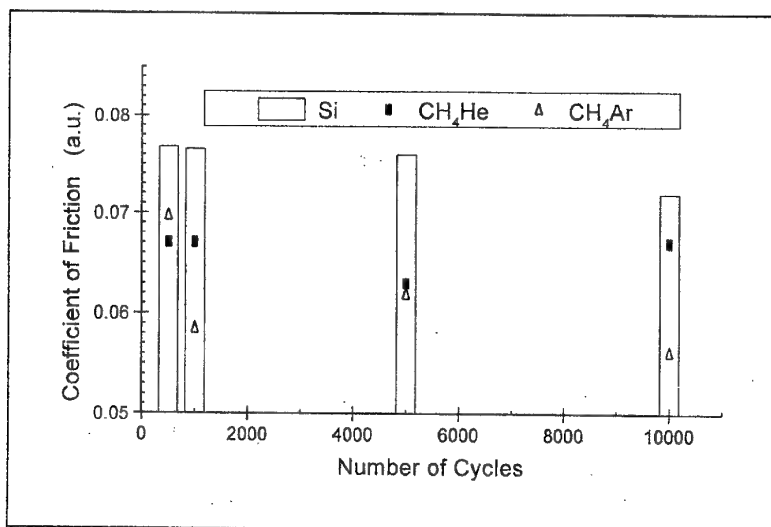


Fig.4b. Friction coefficient versus number of cycles

4. CONCLUSIONS

The results reported in this paper can be summarized as follows:

- i) helium dilution of the pure methane during deposition increases the CH - line intensity and decreases the H - lines intensity from OES spectra; it is expected that films deposited from this mixture to have a higher mass density and a smaller hydrogen content in comparison to those deposited from pure methane;
- ii) the differences in deposition rate is explained by He sputter yield;
- iii) adhesion of films deposited from CH₄+He plasmas is higher due to the higher ionization efficiency of He which lead to a higher sticking coefficient;
- iv) a-C:H films offer good tribological performances which recommend these material for wear - protective applications.

5. REFERENCES

- [1] J. Robertson, *Diamond and Related Materials*, 6 (1997) 212
- [2] J.W. Zou, K. Reichelt, K. Schmidt and B. Dischler, *J. Appl. Phys.*, 65 (1989) 3914.
- [3] K.J. Clay, S.P. Speakmann, N.A. Morrison, N. Tomozeiu, W.I. Milne - accepted to be published in *Diamond and Related Materials*
- [4] N. Tomozeiu, K.J. Clay, S.P. Speakman, W.I. Milne, to be published in *Diamond and Relat. Mater.*

STUDY ON THE SYNTHESIS OF RARE EARTH ACTIVATED CALCIUM TUNGSTATE PHOSPHORS

Flavia Forgaciu, Elisabeth-Jeanne Popovici, Marilena Vasilescu*

"Raluca Ripan" Institute of Chemistry, str. Fantanele 30, 3400-Cluj-Napoca,
Tel: 064-180165; Fax: 064-420441; E-mail: popovici@icrr.org.soroscj.ro

* "I.G.Murgulescu" Institute of Physical Chemistry of the Romanian Academy,
Spl. Independentei 202, Bucuresti, Romania

ABSTRACT

Polycrystalline Tb-activated CaWO_4 phosphors were prepared by high temperature calcination of the synthesis mixtures containing luminescent grade CaWO_4 and Na_2WO_4 (10%) as flux, and WO_3 and Tb_4O_7 as activating system. Phosphor samples were characterised by XRD-patterns and luminescence spectra. The influence of Tb-concentration on luminescent properties of $\text{CaWO}_4 : \text{Tb}$ phosphor was studied.

1. INTRODUCTION

Under UV or roentgen excitation, the self-activated calcium tungstate ($\text{CaWO}_4 : \text{W}$) phosphors exhibit blue luminescence that is related to some tetrahedral WO_4 -groups of scheelite host lattice (self-activated luminescence centres) [1]. The luminescence colour can be modified by using Eu- and Tb- ions as activators [2,3]. In this case, the characteristic luminescence is generated inside the RE^{3+} - luminescence centres. Depending on RE^{3+} - type and concentration, the apparent luminescence colour can be varied from blue to green to red.

Our previous works showed that, in Eu-activated CaWO_4 phosphors, both WO_4 and Eu- centres contribute to the apparent luminescence [4] and that the most efficient red-emitting phosphor was obtained with Na_2WO_4 as flux and 5 ÷ 7 mol % Eu [5]. The present paper reports some results referring to the synthesis and characterisation of terbium activated calcium tungstate ($\text{CaWO}_4 : \text{Tb}$), a phosphor with possible applications in optoelectronic device manufacture. Some aspects concerning terbium concentration effect on phosphor luminescent properties are discussed.

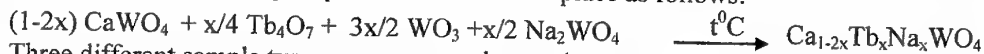
2. EXPERIMENTAL PART

Phosphor samples were synthesised from homogeneous mixtures containing luminescent grade CaWO_4 and Na_2WO_4 as flux (10%) and equivalent amounts of WO_3 and Tb_4O_7 (Johnson Matthey "Specpure") corresponding to $0.0025 \div 0.0050$ mol $\text{Tb}_2(\text{WO}_4)_3$ / mol phosphor. All luminescent grade substances were prepared in our laboratory, by original procedures. The thermal synthesis was conducted at 950°C , in covered alumina crucibles, for 2h. All samples were washed, dried and sieved.

Phosphor samples were characterised by crystalline structure (PW 1050 Philips Diffractometer) and luminescent properties (Perkin Elmer 204 Spectrofluorimeter). The excitation was performed with 254 nm radiation, while $\text{CaWO}_4 : \text{W}$ luminescent pigment (N61, Bad Liebestein) was taken as standard.

3. RESULTS AND DISCUSSION

Sodium tungstate used in phosphor synthesis acts as mineralising agent and also as source of compensating ions. As a result, phosphor formation takes place as follows:



Three different sample types were prepared, namely:

$\text{CaWO}_4 : \text{W}$ (Na_2WO_4) with no Tb addition (sample f59);

$\text{Ca}_{1-2x}\text{Tb}_x\text{Na}_x\text{WO}_4$ with 0.005; 0.10; 0.25; 0.050; 0.075 and 0.100 mol Tb/ mol phosphor (samples f54; f55; f56; f57; f58 and f60), respectively;

$\text{Ca}_{0.962}\text{Tb}_{0.025}\square_{0.013}\text{WO}_4$ with no Na_2WO_4 addition (sample f61).

All phosphor samples show relative intense luminescence under short UV excitation. Depending on Tb concentration, the apparent fluorescence colour changes from blue (f54) to blue-green (f56) to green-yellow (f58). The emission and excitation spectra of phosphors illustrate the contribution of different emission centres to the integral luminescence. $\text{CaWO}_4 : \text{W}$ phosphor shows the expected large self activated emission band ($\lambda_{\text{pk}} \sim 395$ nm, at 254 nm excitation) and correspondingly, the large excitation band ($\lambda_{\text{pk}} \sim 270$ nm, for the 400 nm emission). The terbium incorporation into the CaWO_4 lattice generates new emission bands at about 346; 378; 410; 433; 487 and 545 nm, the first four being superimposed over the large self-activated band due to WO_4 groups of the host lattice (Figure 1).

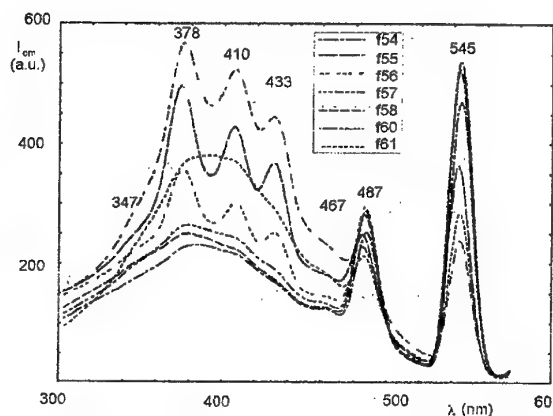


Fig.1 Emission spectra for $\text{Ca}_{1-2x}\text{Tb}_x\text{Na}_x\text{WO}_4$ samples ($\lambda_{\text{exc.}} = 254$ nm)

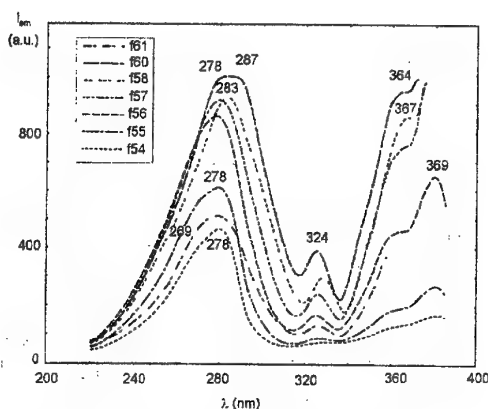


Fig.2 Excitation spectra for $\text{Ca}_{1-2x}\text{Tb}_x\text{Na}_x\text{WO}_4$ samples ($\lambda_{\text{em.}} = 545$ nm)

Excitation spectra consist also of many more or less intense bands. For the characteristic 545 nm green emission band of Tb-centres, some excitation peaks could be observed in the UV region at about 280; 290; 325; 365 and 370 nm (Figure 2). One can see that, whereas the luminescence of WO_4 groups is excited only by short UV radiation (below 300 nm), the luminescence of the Tb-centres could be excited by long UV radiation as well. Terbium incorporation determines the increase of UV excitability of tungstate phosphors.

Figure 3 presents the variation of peak intensities of different emission bands *versus* terbium concentrations; I_{395} of the standard phosphor was considered 100%. The increase of Tb-concentration brings about the continuous decrease of the main blue emission bands (378; 410 and 433 nm) and the simultaneous increase of the two Tb-green bands (485 and 545 nm) toward a maximum value. The green emission is more intense for $5.0 \div 7.5$ mol % Tb concentration. At higher values, the concentration quenching could be noticed.

The variation of excitability of the specific Tb-green band (545 nm) increases continuously with Tb-concentration, especially in the 280-290 nm domain (Figure 4).

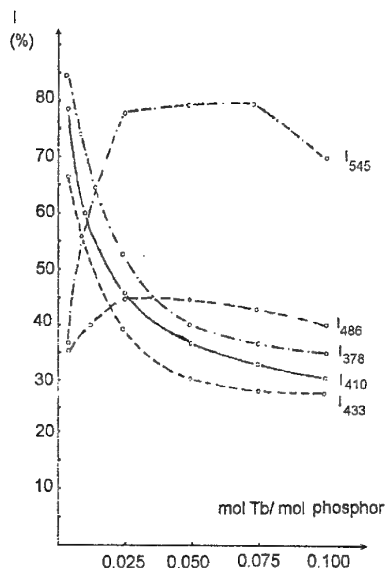


Fig.3 Relative intensity for some emission bands
versus terbium concentration ($\lambda_{ex} = 254$ nm)

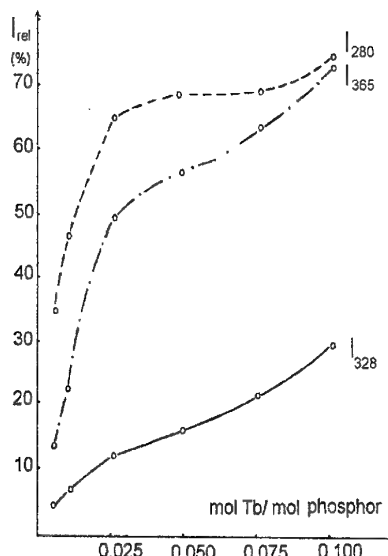


Fig.4 Relative intensity for some excitation bands
versus terbium concentration ($\lambda_{em} = 545$ nm)

Emission spectra and XRD - patterns reveal that, the use of Na_2WO_4 as mineralising agent ensures an uniform Tb-distribution into the well formed scheelite structure (tetr.- CaWO_4) of all terbium activated tungstates phosphors.

4. CONCLUSIONS

Efficient Tb-activated CaWO_4 phosphor with different emission colours could be prepared in the presence of Na_2WO_4 as flux, and with different activator concentration. Tb-optimum concentration for the green emission is $5.0 \div 7.5$ mol %. The UV excitability of phosphors increases with Tb-concentration. Whereas self activated tungstate can be excited only by short UV-radiation, Tb-activated tungstates became also excitable with UV radiation, this property being of practical interest.

5. REFERENCES

- [1]. Butler K.W., Fluorescent Lamp Phosphors, Technology and Theory, Penn. State, Univ, Press, (1980)
- [2]. Blasse G. and Grabmayer B.C., Luminescent Materials, Springer Verlag, Berlin, (1994);
- [3]. Uitert L.G. and Soden R.R., J. Chem. Phys., 32(6), 1687-1689, (1960);
- [4]. Popovici E.J., Forgaciu F., Nemes M., Ursu V. and Macarovici D., Rom. J. Optoelectronics, 5(1), 85-88, (1997);
- [5]. Popovici E.J., Forgaciu F., Nemes M. and Ursu V., SPIE Proceedings Series, (Bellington), vol 3405, 292-296, (1998).

Session A2

LASERS AND APPLICATIONS

DONOR-ACCEPTOR SYSTEMS ON THE BASE IS OF CARBAZOLYLALCYLMETACRYLATE'S COPOLYMERS FOR OPTICAL INFORMATION REGISTRATION

V.V.Bivol, *S.V.Robu, *N.A.Barba, *G.A.Dragalina, *L.A.Vlad, *I.V.Dementiev, A.M.Prisacari

Centre of Optoelectronics of Academy of Sciences of Moldova Republic

1 Academiei Str., MD-2028, Kishinev, Moldova Republic

Tel/Fax: (3732) 739805, E-mail: bivol@as.md

* State University of Moldova

ABSTRACT

This paper investigates a number of donor-acceptor systems from carbazoyl containing polymers, particularly from carbazoyl-ethylmethacrylates (CEM) with octylmethacrylates (OMA) [1,2] and polyepoxypropylcarbazoyl (PEPC) copolymers sensitized by 5-20 % of threinitrofluorenone (TNF) derivatives and additives of photochromical substances from a indolynspiropyrans row. It is established that donor-acceptor systems as photoplastic (PP) layers put on a conducting basis have a photosensitivity of $10^{-3} - 10^{-4}$ J/cm². The introduction in PP layers of 6-10 % photochromium additives increases the photosensitivity of donor-acceptor systems by 2-3 times. The essential growth in photosensitivity is observed in the blue-green area of a spectrum. The greatest sensitization effect has 8'-nitro-1, 3, 3-three methylindolynspiropyrans. The occurrence of the absorption band (500-600 nm) in seen area of the spectrum testifies the amplification of concentration of donor-acceptor groups in PP layers, and thus an appreciable increase in photosensitivity.

The appreciable sensitization effect is reached at drawing of PP layers on an injection substrates from chalcogenide vitreous semiconductors (CVS), such as As₂Se₃. Developed on the basis of photopolymer CEM:OMA donor-acceptor systems have a photosensitivity of 10^{-6} J/sm² at 80-85° C, which is 2-3 times higher than in usual donor-acceptor systems.

1. INTRODUCTION

Recently, in literature more attention is paid to organic photothermoplastic carriers of information (usually donor-acceptor systems [3,4]). As a rule the donor is made of carbazoyl or other polymer containing π -electronic systems – carbazoyl nucleus, while the acceptor consists of various low molecule connections containing an electron-acceptor groups, forming with carbazoyl nucleuses of polymer a complex with carry of a charge (CCC).

Carbazoyl nucleus have large potentials of ionization. Thus, the optical absorption inside photoeffect and photoconductivity of carbazoyl films is observed in UV-area of a spectrum. At introduction of electrons in carbazoyl acceptor, the part of a molecule forms with carbazoyl nucleuses binary associates-complexes with carry of a charge with specific covalent connection. It results in the occurrence in carbazoyl layers of a new band of absorption, and the internal photoeffect is seen and near IR-areas of a spectrum, as provides registration of the holograms.

These donor-acceptor systems are applied in engineering in the registration of reliefographic images and holograms; however, they are characterized by low photographic sensitivity ($10^{-3} - 10^{-4}$ J/sm²). In order to identify higher sensitive systems we have investigated the opportunity of further sensitizing the PP layers by photochromium additives and injection underlayers.

2. EXPERIMENTAL RESULTS AND DISCUSSION

In the creation of new donor-acceptor systems we used copolymers CEM:OMA of composition 60:40 mol % known as N-polyepoxypropylcarbazoyl. The sensitization of the photoplastic layers was made using a number of sensitizers in the range of polynitrofluorenone, particularly 2,4,7-

threenytrifluorenone (TNF), N-fenilamino-2,4,7-threenytrifluorenone (FTF) and ditianometylen -2,4,7-threenytrifluorenon (DTF) containing donor-acceptors groups.

For achievement of donor-acceptor photoplastical systems required a solution of photopolymers 10 % toluol concentration with 5-20 % additives of sensitizer and 0-12 % of photochromium on the weight of the photopolymer previously prepared. After complete dissolution of all components, the solution is carefully filtered and is used for drawing PP layers. The drawing of PP layers was carried out on flexible polyethylenetereftalat film on special watering installation, previously metallized by Al, Cr or SnO_2 thin layers, having a transparency 90-95%. After PP layers drying in air and in the drying chamber at 40 degrees within 3-5 hours, samples become suitable for the purpose of research. During the technological process of obtaining the PP layers, it is necessary to maintain the thickness at about 2,5 microns. The control of thickness is performed by interferometric microscope MII-4.

The measurement of electrophotographic sensitivity (EFS) is carried out by potential relaxation at illumination by coherent light with the 100 Lx strength on the frame. Charging the PP layers is made by a special crownig device. The spectral photosensitivity was measured using the contact method.

The research of electrophotosensitivity by potential relaxation of sensitizers concentration in photopolymer (Fig.1) and from temperature (Fig.2) has shown that the greatest photosensitivity is in PP layers sensitized by 12-14 % of TNF or DTF. At 14-15 % of sensitizer content in photopolymer the results is decrease of photosensitivity due to strong growth of darking conductivity of PP layers. At large sensitizers contents PP layers lose an optical transparency because of cristalization of sensitizer in a polymeric layer.

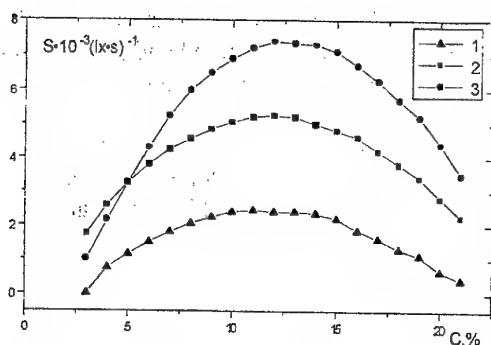


Fig.1 Dependence of electrophotosensitivity of CEM:OMA photopolymeric layers on concentration: 1 - FTF; 2 - TNF; 3 - DTF

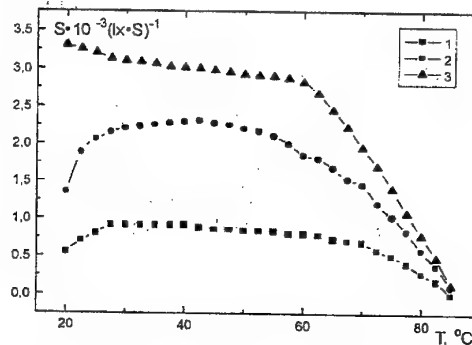


Fig.2 Dependence of electrophotosensitivity of photopolymeric layers containing 12 % of sensitizers on temperature: 1 - FTF; 2 - TNF; 3 - DTF

For all donor-acceptor systems the dependence of photosensitivity on temperature was studied. With the growth of temperature, the sensitivity of all PP layers gradually decreased. The strong recession of photosensitivity occurred in the transition field of the photopolymer from high elastic condition in fluid-viscous. As shown in Fig.2 the sharp recession of photosensitivity for PEPC layers occurs at $T \sim 55-60^\circ \text{C}$, and for CEM:OMA copolymers at temperature higher than 75°C .

By considering that the registration of images in a simultaneous mode is carried out at photopolymers softening temperature, where sensitivity is of the order $10^{-3} \text{ lx}^{-1} \cdot \text{s}^{-1}$, it is natural that the photographic sensitivity be very low, i.e. of $10^{-3} - 10^{-4} \text{ J/sm}^2$ at photographic contrast 0,5-0,6 units.

The research of spectral photosensitivity of PP layers has shown that the maximum of photosensitivity is revealed in blue-green area of the spectrum (Fig.3). As shown in the figure, the maximum photosensitivity belongs to PP layers sensitized by 12-14 % of TNF and DTF. The research of spectral photosensitivity from charge polarity of a PP-layer revealed maximal sensitivity at positive charging of a photopolymeric layer.

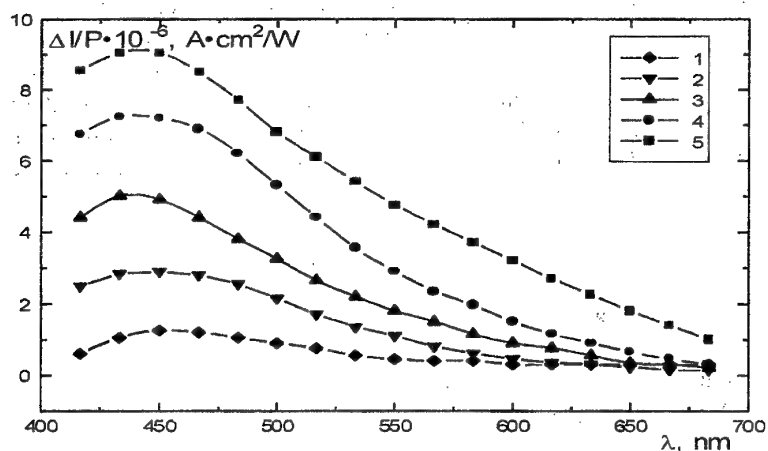


Fig.3 Curves of spectral photosensitivity of photopolymeric layers, sensitizing by TNF (1-3) and DTF (4-6): 1 - 8 %, 2 - 12 %, 3 - 15 %, 4 - 12 %, 5 - 15 %, 6 - 20 %

With the purpose of increasing PP layers photosensitivity, they were additionally sensitized by 4-12 % of photochromium (PC) additives from indoleniny's class. For sensitization, we used 1,3,3-threemethylindolynospiroantratsenopyran (PC-1), 6' and 8'-nytro-1,3,3-threemethylindolynospirobenzpyran (PC-2 and PC-3) and others. The PP layers thickness was of 2,5 microns.

The research of electrophotosensitivity dependence on temperature for PP layers with various contents of photochromium additives has shown that the optimal concentration is around 6-10 % of photopolymer weight (Fig.4). As resulting from the figure, PP layers additional sensitization, (in particular from PC-3) raises the level of sensitivity by 2-3 times. The greatest growth in sensitivity is observed in the range defined by room temperature and the photopolymer softening temperature. The best sensitization effect for PP PEPC layers is provided by photochromium 3 on a basis 8'-nytro-1,3,3-indolynospirobenzpyran as illustrated by the Fig. 5. The dependence of photosensitivity on temperature shows that at 60 degrees there is a sharp recession that is connected to transition of photopolymer from an high elastic condition to fluid-viscous.

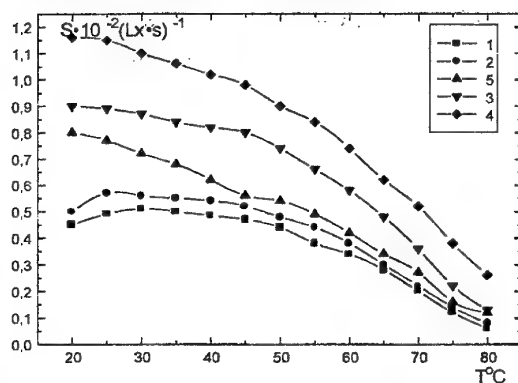


Fig.4 Dependence on temperature of electrophotosensitivity of PEPC photopolymeric layers with various PC-3 contents:
1 - 0 %, 2 - 3 %, 3 - 6 %, 4 - 8-10 %, 5 - 12%

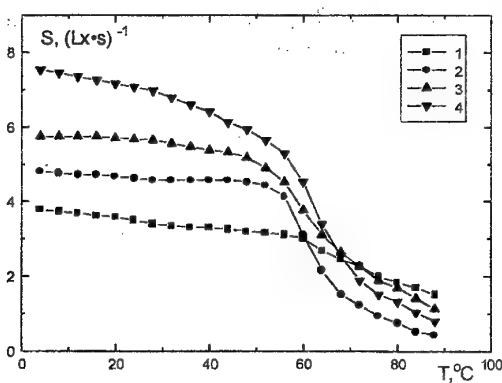


Fig.5 Dependence of electrophotosensitivity on temperature for PEPC photopolymeric layers without photochromium (1) and sensitizing by PC-1 (2), PC-2 (3) and PC-3 (4)

In order to define the power location of the localized states in the forbidden gap of the PEPC+TNF+PC-3 photopolymer, we used previous results on the optical spectrum of transmission (Fig.6) and on the photoconductivity spectrum (Fig.7). Fig.6 presents the characteristic dependence $T(\lambda)$

based on which factor of absorption α is counted and the dependence $\alpha(h\nu)$ is constructed. It is typical for the constructed characteristics to have three sections: 350-400 nm, 400-600 nm and 600-700 nm. The increase of concentration leads to a transmission decrease. As PEPC+TNF is sensitizing by photochromium, it is of interest to find the influence of UV-radiation on the photopolymers properties. To this purpose, we carried out an analysis of the transmission spectra before and after an irradiation by UV-light (Fig.6). The reduction of transmission factor T after an irradiation by UV-light and sharper deflection was observed in the field of 615 nm. However, in the field of 400-430 nm irradiated, samples are not transparent.

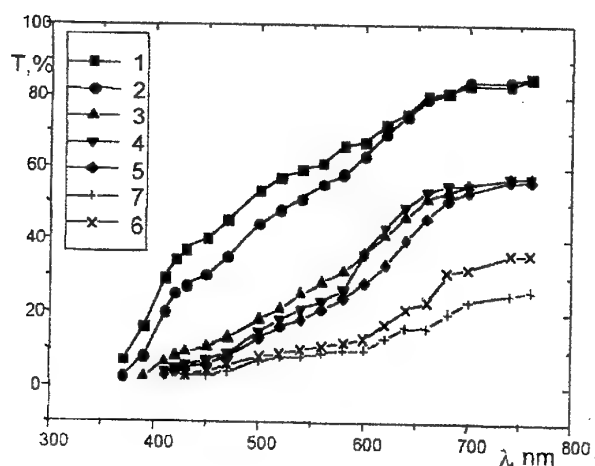


Fig.6 Spectrum of optical transmission of photopolymeric layers with various contents of photochromium additive from PC-3: 1 - 4 %, 2 - 6 %, 3 - 10 %, 4 - 15 %, 5 - 20 % - up to an irradiation; 6 - 20 %, 7 - 15 % - after irradiation

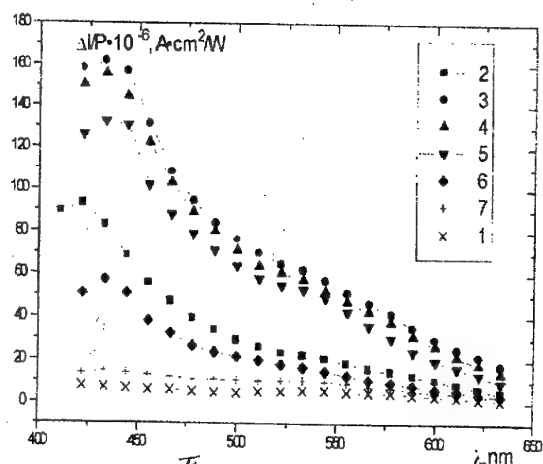


Fig.7 The photoconductivity spectrum of photopolymeric layers at various contents of the photochromium additive from PC-3: 1 - 0 %, 2 - 4 %, 3 - 8 %, 4 - 10 %, 5 - 12 %, 6 - 16 %, 7 - 20 %

The research of spectral photosensitivity of PP layers containing photochromium additive has confirmed the results on electrophotosensitivity. The maximal meanings of photosensitivity are when PP layers contain 6-10 % photochromium additive as illustrated in Fig. 7, PP layers additionally sensitized by PC-3 maintain a small photo-sensitivity even in the close IR-area of the spectrum up to 750 nm.

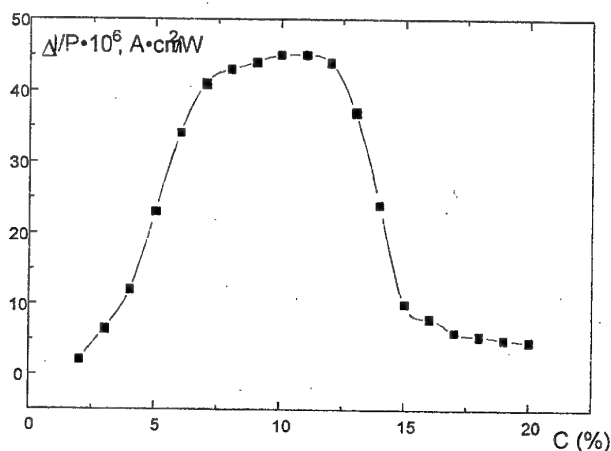


Fig.8 Dependence of sensitivity of photopolymeric PC-3 layers on the photochromium concentration at a 600 nm lengthwave

The integral curve of $\Delta I/P$ dependence on photochromium concentration in PP layers (Fig.8) confirms that the optimum concentration of photochromium is of 8-10%. The increase of the photochromium additive concentration above 10% results not only in the deterioration of electrophotosensitivity, but also in the deterioration of layer transparency due to partial crystalizing of photochromium.

In order to make an overall estimation of the photopolymers as registering media for photothermoplastic information carriers, the deformation characteristics of photoplastic layers in crowning discharge were investigated. We used the method on change of light intensity (i.e. dispersing ability R) passing through photoplastic layer. The registration of change in light intensity was carried out by means of a photo diode FD-7K, and the values thus obtained were automatically registered by a storage device. On a tangent of a declination corner of an characteristic curve initial site of the process "the deformation - relaxation" (Fig.9) is estimated speed of deformation, on which the photographic sensitivity of the information carrier depends, and also the dispersing ability, which correlates with the sizes of microdeformations on a surface of a photoplastic layer.

The contribution of photochromium addition to the deformation characteristic of photoplastic layers was further evaluated. The presence of photochromium in the photoplastic layers of a polymer improves the deformation characteristics as it results from the Fig. 10. This is connected to the photochromium plasticity. When the defined temperature on curves $V=f(T^0)$ and $R=f(T^0)$ is reached the maximum values are hit and after that the deterioration of the deformation characteristics occurs, as it is connected to the sharp growth in conductivity of photoplastic layers which are in of a fluid-viscous state.

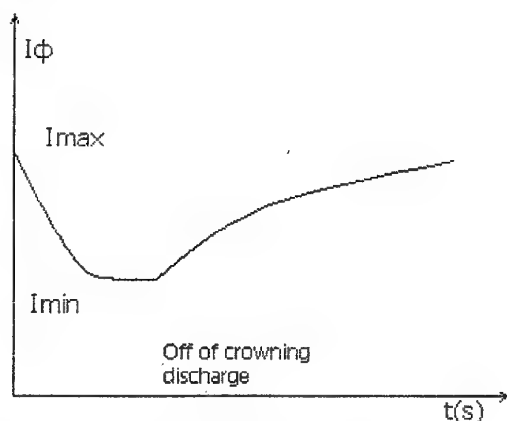


Fig.9 Characteristic curve of the "the deformation-relaxation" process

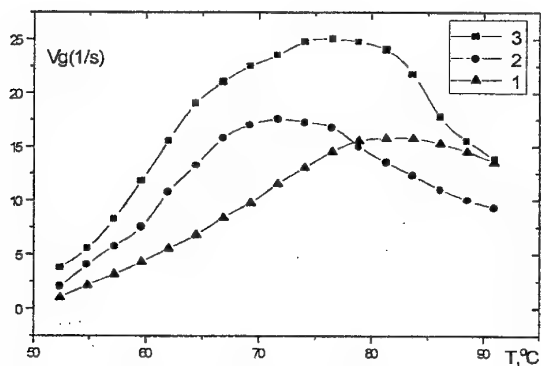


Fig.10 Dependence on the speed of deformation from temperature of a photopolymer layers without photochromium additives (1) and with a content of 6% of photochromium in PC-2 (2) and PC-3 (3)

The registration on photopolymers samples has confirmed improving photographic sensitivity. The photographic sensitivity of the containing photochromium sensitizer carrier is higher than the sensitivity of the usual medium and makes 10^{-5} J/sm² with photographic contrast 0,6 - 0,8 units. The resolving power of a photoplastic layers CEM:OMA is higher than 200 mm⁻¹.

To increase the photosensitivity, polymer layers were additionally sensitized by injecting sublayers made of CVS As₂S₃, As₂Se₃ with thickness of 0,3-0,5μm.

The evaluation of the electrophotosensitivity of photopolymers layers with injector and free of injector, was carried out by the potential relaxation method. It consists in recording the time required to decrease to one half the surface potential on the illuminated photopolymer layer, according to the relation of the sensitivity $S = (1/Et) (lx\ s)^{-1}$. Illumination on the layer was about 80 lx.

Experimental investigations on the photosensitivity (Fig.11) show that the photopolymer layers with injector substrates (3,4) in the range 20-100°C is 5-10 times higher than the photosensitivity of the films without injector (1,2). We suppose that the enhancement of the photosensitivity in the polymer with injection layers is due to the injection of the charge carriers from the chalcogenide layer. These layers are

characterised by an obvious growth of polyepoxypropylencarbazoly, that has a rich content of carbazoly nucleus.

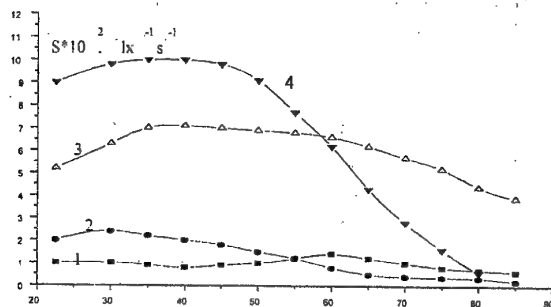


Fig.11 The temperature dependence of photosensitivity of photopolymers films without injection layer (1,2) and with injection layer (3,4)

The photothermoplastic film structures can be used for recording images, including holographic angles with the space frequency of 1000 mm^{-1} and with the diffraction efficiency of 8-10%. Its sensitivity for $\lambda = 0.5 \mu\text{m}$ is more than 10-15 times higher than the corresponding value for the structures without injection layer.

3. CONCLUSIONS

1. The research of electrophotosensitivity and spectral photosensitivity of photopolymer layers of carbazolyethylmetacrylat's and polyepoxylpropylcarbazoly's copolymers with sensitization by 2,4,7-threenytrifluorenones and ditsianometylen-2,4,7-threenytrifluorenone has shown a maximum photosensitivity of $\sim 10^{-4} \text{ J/cm}^2$.

2. By introducing 8-10 % of photochromium of the nytroindolynspirobenzpyran's class in a photopolymer layers, it was possible to increase the photosensitivity by 2-3 times. The presence of photochromium additives in polymer layers shifts the photosensitivity in the longer wavelength area of the spectrum.

3. By analysing the deformation characteristics of photoplastic layers, we concluded that the introduction of photochromium additives reduces the increase of both speed of deformation and sizes of microdeformations, which positively affect the photographic characteristics of the layers.

4. The plotting of photopolymer layers on injected sublayers from chalcogenide glass semiconductor As_2Se_3 reduces the increase of photosensitivity at 1-2 order, reaching values of $10^{-6} - 10^{-7} \text{ J/cm}^2$. On developed polymeric carriers, holographic images with holographic efficiency of 12-15 % and resolution up to 1000 mm^{-1} were registered.

4. REFERENCES

- [1]. Barba N.A., Dragalina G.A., Robu S.V. Coordinate and polymeric bonds. Synthesis. Investigations. Kishinev, "Stiinta", p.69, (1991).
- [2]. Robu S.V., Barba N.A. and other. Patent MD N.718. Photothermoplastic carrier. Published in BOPI (04.1997).
- [3]. Kuvshinskii N.G., Nahodkin N.G., Lamko I.N. Fundamentalnie osnovi opticheskoi pamiati i sredi. Kiev, v.18, p.15-34, (1987)
- [4]. Vannikov A.V., Grishina A.D. Fotochimia polimernih kompleksov. M., "Nauka", (1984).
- [5]. Nedujii S.A., Pavlov A.V., Tabotadze D.G., Celtsova T.V. Journal of Scientific and Applied Photography and Cinematography, p.404, (1982).

CESIUM SOURCE FOR ATOMIC FOUNTAIN

Cipriana Mandache, M.Bengulescu, T.Acsente, M.Ungureanu
National Institute for Laser, Plasma and Radiation Devices, Nuclear Fusion and Plasma Physics
Laboratory, R-76900, Bucharest, Magurele, P.O.Box MG-36, Romania,
phone number:7893865, e-mail: cipriana@alpha1.infim.ro

ABSTRACT

The goal of our work is to develop a cesium magneto-optical trap (MOT) and to realize an atomic clock using cesium cold atoms. Thermal, high velocity cesium atoms, which are to be stopped in MOT, are generated by a source located in the so called "cold-finger" configuration. The adjustment of thermal atoms' partial pressure in the trap, at a value which allows cooling, is achieved by varying the source temperature. To measure this partial pressure, a saturated absorbed experiment was used. The theoretical support of the method and its particularization in our trap geometry are presented below.

1. INTRODUCTION

The main source of uncertainty in classical time standards is related to atomic velocity. By reducing the velocity of atoms (cooling them) it is possible to eliminate the effect of Doppler shifts on the atomic transition. The cooling of atoms can be achieved by using six counterpropagation laser beams and a uniform gradient magnetic field, combination which is called magneto-optical trap (MOT). The collective of cold atoms obtained in a MOT is named optical molasses. Our MOT is represented schematically in fig.1, and it consists of three arms of fused silica with optical windows at every end allowing the access of laser radiation in the trap. A magnetic field with uniform gradient, oriented by Oz axis, is produced by two coils in anti Helmholtz configuration. The effective zone of trapping is at the intersection of lasers, where the magnetic field is zero. A cesium source, designed in the so called "cold finger" configuration, and an ionic pump are attached. To obtain cold atoms in a concentration of 10^7 - 10^8 atoms/cm³, the partial pressure of Cs thermal atoms in the trap must vary between 10^{-8} hPa and 10^{-7} hPa [1].

2. THEORETICAL CONSIDERATION

The dependence of Cs atoms concentration on temperature is described by the following empirical equations [2]:

$$\begin{aligned}\log n &= 35,531 - \frac{4150}{T} - 2,00 \log T, \text{ for } T < 302\text{K} \\ \log n &= 36,531 - \frac{4041}{T} - 2,35 \log T, \text{ for } T > 302\text{K}\end{aligned}\quad (1)$$

resulting that a partial pressure of 10^{-8} hPa corresponds to a temperature of -20°C . In reality, cesium source must be rather heated than cooled [1] to obtain the optimum partial pressure of cesium thermal atomic gas. This is explained by the adhesion of cesium atoms to the trap walls. In time the saturation of walls is reached and the temperature of cesium source may decrease, but the final temperature is not the one predicted by (1). We are not interested in the theoretical determination of the right value of the cesium source temperature, but rather in the determination of the proper concentration of thermal atoms in the trap. This task is accomplished by varying the temperature of the cold finger and by measuring the atoms concentration in the trap. For this, we have used a saturation absorbed experiment by sending a laser beam resonant with $F=4 \rightarrow F'=5$ transition of the cesium atom along Ox direction of the trap. The idea is to measure the transmission of the laser beam passing through the trap, and, from it to determine the value of partial pressure of cesium atoms.

A thermodynamically description of our system reveals an atomic reservoir containing cesium atoms (atomic trap), which has a temperature equal to the ambient, and coupled to a pressure source (cesium source) and a radiation source (laser field).

Starting from the Beer-Lambert law:

$$I/I_0 = \exp(-n\sigma L) \quad (2)$$

where I and I_0 are the intensities of laser radiation after and before passing the trap; n is the atomic cesium gas concentration in the trap, σ is the cross absorption section and L is the distance between two opposite optical windows, and taking into account Doppler effect and state degeneration, we obtain:

$$\frac{I}{I_0} = \exp\left(-n_0 \frac{\Gamma}{\sqrt{\pi}k\alpha} \sigma_{45} L\right) = \exp\left(-n_0 \frac{\Gamma}{\sqrt{\pi}k\alpha} 0.41 \frac{3\lambda^2}{2\pi} L\right) \quad (3)$$

where Γ is the natural width of transition; λ is the wavelength of cesium D2 line and k is the corresponding wave vector; α is the most probably velocity of cesium atoms, which at room temperature is $\alpha=194\text{m/s}$. Fig.2 shows I/I_0 as a function of thermal cesium atoms density in the trap, based on the last relation. A temperature of 300 K (trap temperature is the same with the ambient medium) is corresponding to an atomic concentration of $6,4 \cdot 10^{13}\text{atoms/m}^3$. In conclusion, to obtain proper conditions for cooling atoms in MOT it is necessary to fix the temperature of cesium source to a value where I/I_0 is greater than 85%. Assuming that concentration of atomic gas is the same in the source and in the trap (this is not the real situation due to adhesion to the trap walls), from (1) results that the temperature of atomic source must be -30°C . Due to this, the source is called "cold finger".

3. PRACTICAL DESIGN OF ATOMIC SOURCE

Due to the adhesion of cesium atoms to the trap walls, the temperature of cesium source must be greater than that theoretically predicted. Therefore, we designed a cesium source which allows us only to heat the atoms. Its elements are presented in fig.3. The heating element is a resistive wire wound around the glass tube of the cesium source, where the temperature sensor is located. The source temperature is electronically controlled in the range of $20^\circ\text{C} \dots 50^\circ\text{C}$.

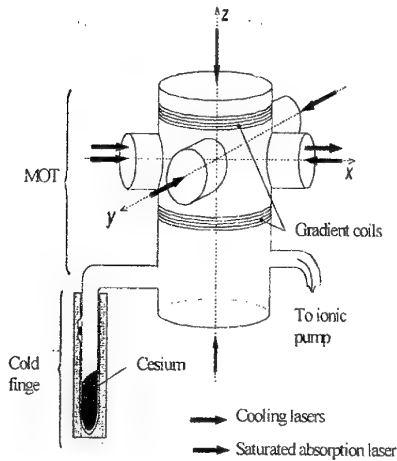


Fig.1 MOT and cesium source in "cold finger" configuration

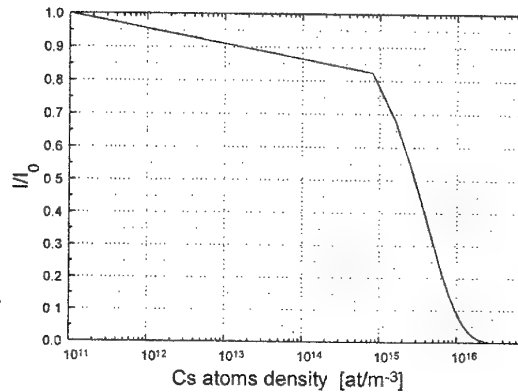


Fig.2 Transmission I/I_0 versus cesium thermal atoms. concentration in the trap

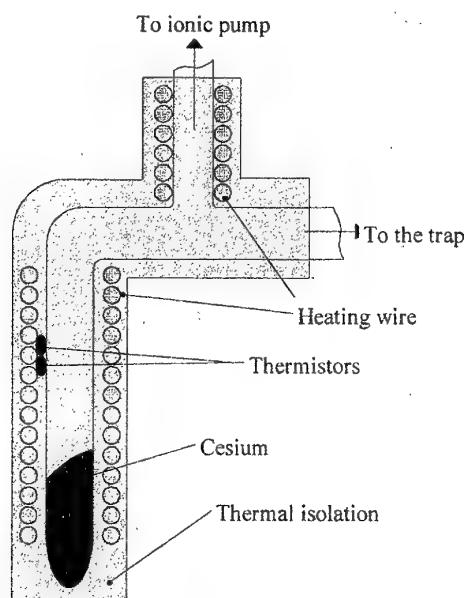


Fig. 3 Cesium source schematic

4. CONCLUSIONS

In this paper we described the design of a cesium source for a magneto-optical trap (MOT) and the modality to obtain a proper value for the thermal cesium atoms concentration in the trap, so that to obtain cold atoms.

5. REFERENCES

- [1]. Gregor Dudle, Contribution au developpement d'un etalon primaire de frequence a jet d'atomes ralents par laser, These, Neuchatel, (1996)
- [2]. Taylorand J.B., Langmuir L., Phys.Rev.51,753, (1937)

CALCULATION METHOD OF SMITH-PURCELL RADIATION POWER IN 1-30 MeV ELECTRON ENERGIES RANGE

F. Scarlat, M. Facina and V. Manu*

National Institute for Laser, Plasma and Radiation Physics, Bucharest, Romania

*National Institute for Nuclear Physics and Engineering "Horia Hulubei", Bucharest, Romania

ABSTRACT

Smith-Purcell (SP) radiation power emitted in order n by a electron beam per unit solid angle in the direction (η, ξ) depends on three factors. The first factor characterises the experimental setup and includes the current density, the size of the electron beam, the period of the grating and the order of diffraction that is observed. The second factor is a function of the electron energy and of the grating profile. The third factor is the so-called radiation factor which corresponds to the reflection coefficients in the classical diffraction problem of light. This paper presents the angular distribution of the emitted SP radiation power, calculated with the modal expansion method, for lamellar gratings and the first two orders of diffraction. The energies domain of the electron beam is 1-25 MeV, supplied by the 30 MeV INFLPR cyclic induction electron accelerator.

1. INTRODUCTION

An electron accelerated to the velocity $\beta = v/c$ which is moving very close and parallel to a metallic grating is emitting an outgoing light. This mechanism is called Smith-Purcell effect and it is equivalent to the Cherenkov effect. The diffraction of the Coulomb field of the electron, represents the SP effect, and the refraction of it represents the Cherenkov effect. In 1993, the experiments of Doucas et al. [1] demonstrated the possibility of using relativistic electron beams to produce the SP effect. The study of this phenomenon was carried out in view of applying it as a tunable electromagnetic source in particle acceleration or in a free-electron laser. The famous Smith-Purcell formula, established in 1953, gives the wavelength emitted by SP radiation in the n th order of diffraction:

$$\lambda_{sp} = \frac{\lambda_g}{|n|} (\beta^{-1} - \sin \eta). \quad (1)$$

The purpose of this paper is to present the preliminary results of the calculated SP radiation angular power distribution, using the modal expansion method for lamellar gratings and electron energies in the 1-25 MeV domain.

2. THE THEORY OF SP EFFECT

We consider that the electron is moving parallel to the surface of a grating along a trajectory $(x, y=0, z=z_0)$ which is transversal to the grooves. The top of the grating is in the (x, y) plane, and the grooves are parallel to y axis. The angles of observation are η and ξ . The angle η is taken between the wave vector associated to the incoming field and the (y, z) plane. The angle ξ is taken between the projection of the incoming wave vector on the (y, z) plane and z axis.

The energy lost by a single electron due to the emission of SP radiation with wavelength λ and wave vector $k_n(\alpha_n, k_y, \gamma_n)$ when traversing one period length λ_g of the grating at a distance z_0 above the surface of it, is given by[2]:

$$W = \frac{e^2}{\varepsilon_0 \lambda_g} \sum_n \int_{-\pi/2}^{\pi/2} \int_{-\pi/2}^{\pi/2} \frac{\cos^2 \eta \cos^2 \xi}{(\beta^{-1} - \sin \eta)^3} |R_n(\beta, \eta, \xi)|^2 \exp[z_0 / h_{\text{int},n}(\eta, \xi)] \cos \eta d\eta d\xi, \quad (2)$$

where e is the absolute value of the electric charge of the electron, and $h_{\text{int},n}(\eta, \xi)$ is given by:

$$h_{\text{int},n} = \frac{\lambda_g \cdot (\beta^{-1} - \sin \eta)}{4\pi \cdot (\beta^{-2} - 1 + \cos^2 \eta \sin^2 \xi)^{1/2}}. \quad (3)$$

$|R_n(\beta, \eta, \xi)|^2$ represents the radiation factor which is equivalent to the reflection coefficients in the classical diffraction problem of light. In equation (2), the summation is to be taken over all the propagative orders.

The total power of SP radiation emitted by an electron beam is obtained analytically integrating (2) over η and z_0 , i. e. over the beam profile. The power emitted in order n by the beam per unit solid angle in direction (η, ξ) is given by [2]:

$$\left(\frac{dP}{d\Omega}\right)_n = F \cdot G(\beta, \eta, \xi) \cdot |R_n(\beta, \eta, \xi)|^2 = F \cdot \frac{\cos^2 \eta \cos^2 \xi}{(\beta^{-1} - \sin \eta)^2 (\beta^{-2} - 1 + \cos^2 \eta \sin^2 \xi)^{1/2}} |R_n(\beta, \eta, \xi)|^2, \quad (4)$$

The first factor F characterizes the experimental setup and includes the electron beam parameters, the order of diffraction observed and the grating parameters. The second factor $G(\beta, \eta, \xi)$ is a function of the electron energy and the observation angles η and ξ . The third factor $|R_n(\beta, \eta, \xi)|^2$ is the radiation factor, and it depends on the grating profile parameters, the angles of observation and the electron energy.

3. METHOD OF CALCULATION

The wave vector of the incoming wave is $k_0(\alpha_0, k_{y0}, \gamma_0)$ and the wave vector of the diffracted wave in the n th order is $k_n(\alpha_n, k_y, \gamma_n)$. The grating is of lamellar type and its profile is described by the height h and the width a of the grooves.

In the (x, z) plane ($\xi = 0^\circ$) the SP mechanism is reduced to the study of the H-polarization diffraction because $\xi = 0^\circ$ implies $k_{y0} = 0$, for which the E-polarized contribution of the incoming waves vanishes.

The main problem in calculating the SP effect is to find a method which provides the truest value of the radiation factor. In the case of lamellar gratings and H-polarization we used the modal expansion method [2, 3]. With this method we obtained:

$$|R_n(\beta, \eta, 0)|^2 = \frac{4}{\varepsilon^2} \cdot \exp(2|\gamma_0|z_0) \cdot |U_{y,n}^r(\beta, k_y)|^2, \quad (5)$$

where $|U_{y,n}^r(\beta, k_y)|^2$ are obtained by solving the following linear infinite system of equations [3]:

$$\sum_{m=-\infty}^{+\infty} (\gamma_n \lambda_g \delta_{k,n} - V_{k,n}) \cdot U_{y,n}^r = C_k, \quad (6)$$

in which:

$$C_k = \frac{e}{2} \exp(i\gamma_0 z_0) \cdot (\gamma_0 \lambda_g \delta_{k,0} + \sum_{m=0}^{+\infty} \varepsilon_m \kappa_m \frac{\Gamma_m - 1}{\Gamma_m + 1} \Psi_{m,k} \Psi_{m,0}^*), \quad (7)$$

$$\varepsilon_m = 2 - \delta_{k,0}, \quad (8)$$

$$\kappa_m = [k_0^2 - (m\pi/a)^2]^{1/2}, \quad (9)$$

$$\Gamma_m = \exp(2i\kappa_m h), \quad (10)$$

$$\Psi_{m,n} = a^{-1} \int_0^a \cos(m\pi x/a) \exp(-i\alpha_n x) dx, \quad (11)$$

$$V_{k,n} = a \sum_{m=0}^{\infty} \varepsilon_m \kappa_m \frac{\Gamma_m - 1}{\Gamma_m + 1} \Psi_{m,k} \Psi_{m,n}^*, \quad (12)$$

$$\gamma_n = (k_0^2 - k_y^2 - \alpha_n^2), \alpha_n = \alpha_0 + 2\pi n / \lambda_g, \quad (13)$$

and $\delta_{k,n}$ being the Kronecker symbol. Knowing that $\text{Re}(\gamma_n) \geq 0$ and $\text{Im}(\gamma_n) \geq 0$, it results that the SP radiation is the sum of all the propagative waves, i. e., those waves for which $\text{Im}(\gamma_n) = 0$, and therefore only the negative orders n can contribute.

In order to find the unknown factors $U_{y,n}^r$ the infinite system of equations (6) is truncated and the order of truncation is increased until convergence is achieved.

For the first factor in equation (4) the below expression was used:

$$F = \frac{ei_0 L}{4\pi\varepsilon_0 \lambda_g |n| h_{\text{int},n}} \text{erf}(B/\sqrt{8}\sigma_y) \exp(c^2/4 - s_0)[1 - \text{erf}(c/2 - s_0/c)], \quad (14)$$

where B is the width of the grating and L is its length, σ_y and σ_z are the parameters of the Gaussian beam profile, $i_0 = J_0 2\pi\sigma_y\sigma_z$ is the total current of the beam, $c = \sqrt{2}\sigma_z/h_{\text{int},n}$, $s_0 = z_0/h_{\text{int},n}$ and $b = B/h_{\text{int},n}$.

4. RESULTS AND DISCUSSIONS

The infinite system of linear equations (6) was solved with the aid of a computer program. The calculations were performed considering that the ratios which characterise the grating profile are $a/\lambda_g = 0.5$ and $h/\lambda_g = 0.1$. The plane of observation of the SP radiation for which $\xi = 0^\circ$ was chosen. The length of the grating was $L = 100$ mm and its width $B = 50$ mm. The distance z_0 at which the beam is passed above the top of the grating was about 1 mm. The current density of the electron beam was considered $J_0 = 0.16$ A/mm² and the parameters $\sigma_y = 5$ mm and $\sigma_z = 2$ mm.

Figure 1 presents the results for the angular power distribution generated by an electron beam with the energy of 1 MeV, and the grating parameters presented above. Figure 2 presents the same results but for energies of 3 and 5 MeV. In both figures one can observe some peaks which are emitted in the forward direction, and that for the second order of diffraction, the intensities are decreasing with one or two orders.

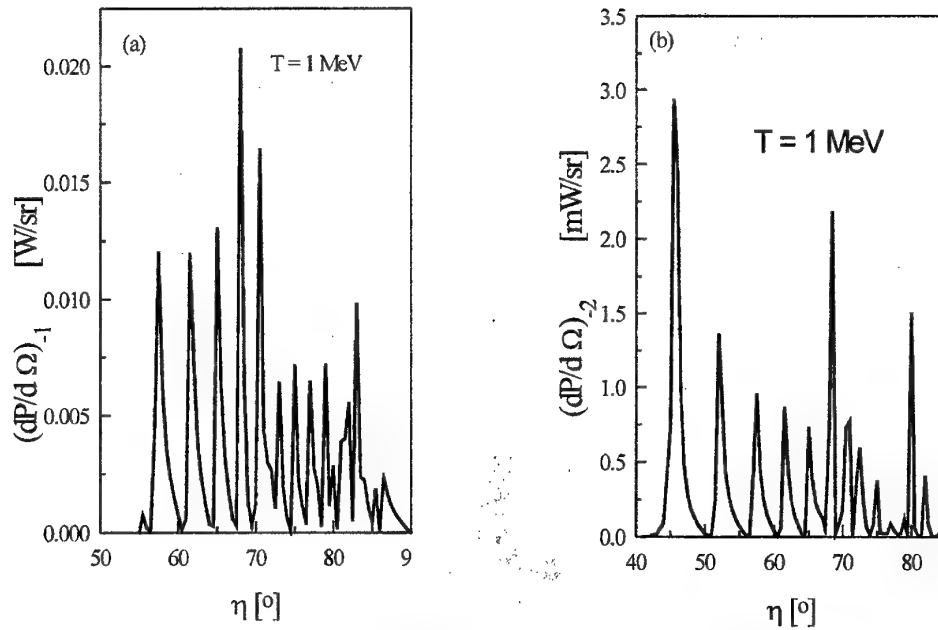


Fig. 1 The spectral angular power distribution of the SP radiation in the first negative order of diffraction (a), and the second negative order of diffraction (b) respectively, generated by electrons of 1 MeV energy and lamellar gratings with $a/\lambda_g = 0.5$ and $h/\lambda_g = 0.1$

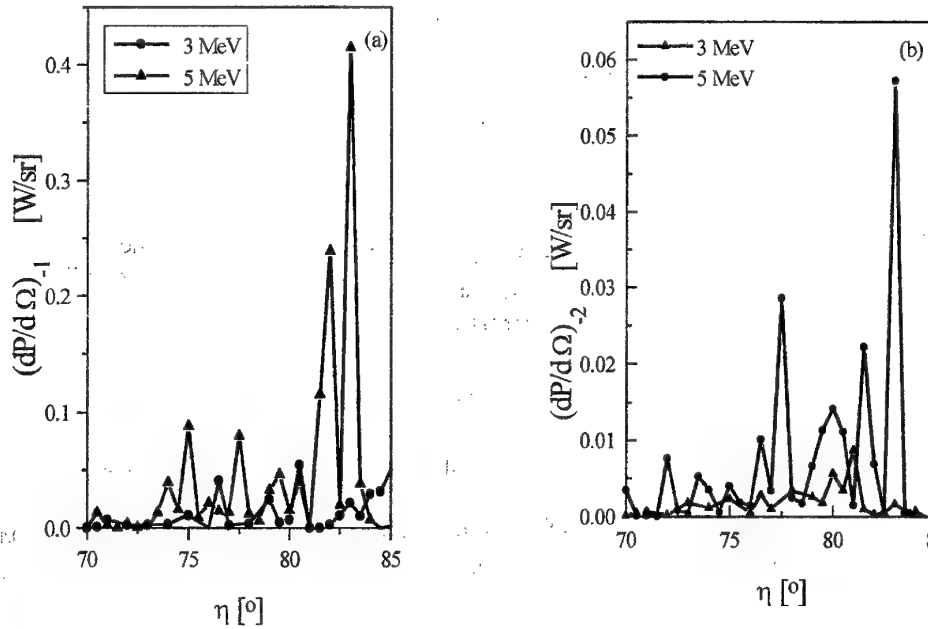


Fig. 2 The spectral angular power distribution of the SP radiation in the first negative order of diffraction (a), and the second negative order of diffraction (b) respectively, generated by electrons of 3 MeV and 5 MeV respectively, and lamellar gratings with $a/\lambda_g = 0.5$ and $h/\lambda_g = 0.1$

Figure 3 presents the calculation results for the angular power distribution of the SP radiation generated by electrons with energies of 10 MeV, and 25 MeV respectively, and for lamellar gratings.

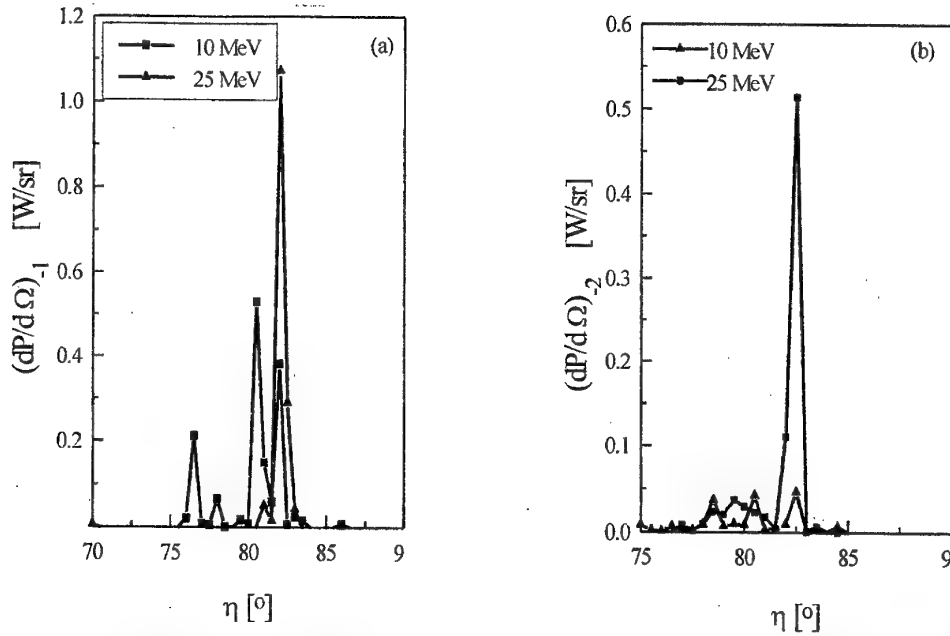


Fig. 3 The spectral angular power distribution of the SP radiation in the first negative order of diffraction (a), and the second negative order of diffraction (b) respectively, generated by electrons of 10 MeV and 25 MeV respectively, and lamellar gratings with $a/\lambda_g = 0.5$ and $h/\lambda_g = 0.1$

From the Figure 3 one can observe an important increase in intensity for SP radiation emitted in first negative order of diffraction by electron beams with the 25 MeV energy.

5. CONCLUSIONS

The results presented in this paper represent a data basis for the study of SP radiation power emitted in forward direction, using relativistic electron beams supplied by the INFLPR Betatron Accelerator. In view to performing the experimental study of SP effect, these results will be a guide in making a choice on the electron beam energy and the lamellar grating parameters

6. REFERENCES

- [1]. G.Doucas., J.H.Mulvey, M.Omori, J.Walsh, and M.F.Kimmit, Phys. Rev. Lett. **69**, 1761 (1992).
- [2]. O.Haeberle, P.Rullhusen, J.M.Salome, and N.Maene, Phys. Rev. E., **49**, 4, 3340 (1994).
- [3]. F.Scarlat, M.Facina, and V.Manu, Romanian J. of Optoelectronics, vol. 6, N° 2, April-June (1998).

TERMOGRAPHIC ANALYSIS OF WATER PRECIPITATION IN α -BERLINITE MONOCRYSTALS HYDROTHERMALLY OBTAINED

I. Grozescu, D. Irimia, Diana Rata

National Institute of Electrochemistry and Condensed Matter Research,
Tarnava str.1, 1900 Timisoara, ROMANIA, tel/fax 004 056 194413
E-mail: grozescu@icmct.uvt.ro

ABSTRACT

The analysis of differential thermogravimetric curve of different monocrystals hydrothermally growth shows that AlPO_4 monocrystalin present the same structural properties like nutrient, but in single crystals there was not a water elimination with mass decrease. That means, the quality of monocrystal hydrothermally growth is very good, with small bubble distribution in lattice. Powder obtaining by reaction between γ -alumina and phosphoric acid has a high humidity (about 5%), wherever aluminum phosphate obtaining is not a crystalohidrat.

1. INTRODUCTION

Aluminum orthophosphate, berlinite, AlPO_4 , is isostructural and isoelectronic with quartz [1]. The α -form (the stable form in standard condition) is stable below 584°C . Thus a solution growth technique is necessary. Flux growth might be considered, but taking into account that the highest growth temperature cannot exceed 584°C , a solution technique with an aqueous hydrothermal solvent is desirable [2-3].

Single AlPO_4 crystals are of particular interest as a piezoelectric material because they have a large electromechanical coupling constant and their resonant frequency is nearly independent of temperature for certain orientation. However, industrial application of α - AlPO_4 are not yet developed for two main reasons:

- a first difficulty arises in the preparation of large synthetic single crystals because of the negative temperature coefficient of AlPO_4 solubility in its usual solvents.
- although these synthetic crystals exhibit low dislocation density and no twins, their piezoelectric performances are rather poor and an irreversible behavior has been observed when resonators are heated.

This latter phenomenon is due to small amounts of water initially dissolved or finely dispersed in the crystal lattice. This water leads to appreciable electric losses and when crystals are heated, water precipitates in small bubbles visible by transmission electron microscopy [4-5]. Thus, growth conditions have to be changed in order to obtain dryer crystals with better performances.

2. EXPERIMENTAL PROCEDURE

2.1 Thermal differential analysis

Thermal differential analysis is a modern version of classical method used for phase transition investigation by time-temperature registering, during solid's uniform heating.

It is known that in usual condition almost are all solids substances, that are heating, suffer important chemical and physical transformations. In this case we are interested on discontinuous transformations, that are taking place in a reduced temperature range, as: thermal decomposition, polymorphous transformations, crystallization, melting, sublimation, etc.

All of these phenomena are taking place even with heat absorption even with its disengagement, both of them being noticed using a thermometer. So, it is possible to measure the sample temperature

along with a reference inert material that suffer no transformations over the whole temperature range, both sample being identically heated. At the phase transition sample - temperature will rise or decrease in comparison with reference's temperature. Using a differential installation having a null indicator these differences could be evidenced.

If between reference and sample there are no temperature differences, there will be no null indicator deviations. In the case of an endothermic phenomenon the null indicator will be deviated in a particular sense and if an exothermic effect is present the deviation will be produced in contrary sense. From the registered plots, precious information about temperature and transformations speed could be provided.

2.2 Thermogravimetric analysis

This analysis represents the classical gravimetric method development that consist in sample heating at different temperatures, a process followed by crystallization after each sequence. In this analysis the weight's sample is first determined continuously in time during its heating into a furnace with a constant heating speed. The sample's mass variation along with temperature $m = f(T)$ is automatically registered. This dependence gives indications upon the transformations that are accompanied by weigh lose during the heating process. Generally TG curves present horizontal constant levels for some temperature ranges but, when the weigh is varying, the curves present slopes of different angles that depend on heating speed.

2.3 Differential thermogravimetric analysis

The curve registered in our first analysis represent a mathematical conversion of $m=f(T)$ relation that characterized thermogravimetric analysis. In fact, it represent the achievement of differential curve of weigh variation which means that it is the graphic expression of mass derivative as a function of temperature. This curve has an aspect essentially different from the obtained TG curve, looking alike to ATD curve. If the ATD and GTD curves of the same substance are overlapping, the effects are overlapping too. It is obvious that only thermal effects that are caused by weigh looses are overlapping.

In order to study thermal degradation of nutrient material that is used for $AlPO_4$ monocrystals growth as well as of monocrystals obtained at I.N.C.E.M.C. Timisoara, it was used a type MOM-Budapesta derivatograph apparatus. This installation allows a simultaneous registering of T, ATD, GTD and GT curves.

Thermogrames were registered in static air atmosphere, with a heating speed of $10^{\circ}/\text{min}$ in a temperature range of $20-1000^{\circ}\text{C}$ (figure 1). Differential temperature and heating temperature have been measured using a Pt-PtRh thermocouple. The measurements were done on 150 ± 30 mg substance.

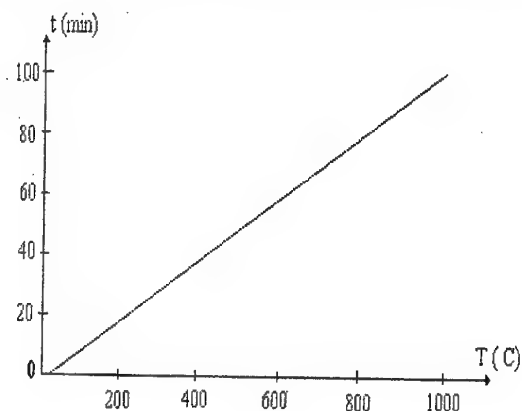


Fig. 1 The heating program

3. DERIVATOGRAMME'S INTERPRETATION

(maximum temperature = 1000°C, heating speed 10°C/min, samples weight = 0,1089 g, weight losses by heating = 0,026 g, weight's losses in percent: 23,8%)

Derivatogramme's analysis of AlPO_4 nutrient and the correlation of simultaneous variation of GT, GTD and ATD curves have been emphasized that in the region between room temperature and 120 °C the elimination of samples humidity takes place (figure 2). This effect is emphasized even by an endothermic small peak on ATD curve. This peak evidences the heat absorption in the investigated temperature range, an absorption that has a consequence the sample's humidity reduction.

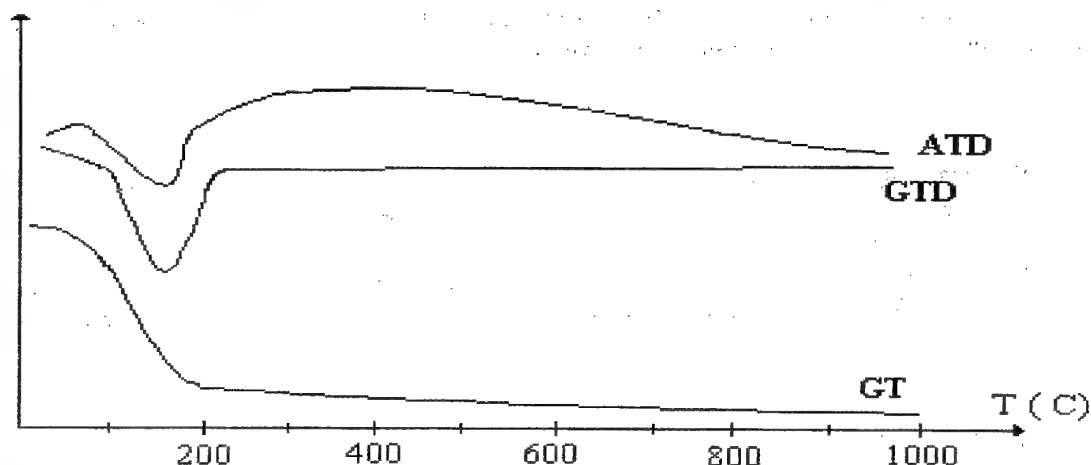


Fig. 2 ATD, GTD and GT curves of AlPO_4 powder

During the heating process at about 120 °C, GTD curve presents a shoulder. This shoulder shows a little weigh losses due to water's evaporation. As a consequence the most significant humidity reducing appears around 120 °C. So, 120 °C is the temperature of the evaporation of H_2O molecules that were crystallized in lattice of aluminum phosphate.

At 150 °C endothermic peak presents a pronounced maximum which means that the most significant dehydration and an overlapping of humidity reducing are realized at this temperature.

At 180 °C the dehydration process is completed, fact which is noticed by the reducing of the endothermic peak from ATD curve.

By heating the sample up to 420-425 °C it has observed that another exothermic and very weak peak appears on ATD curve. This peak is specific to a reaction that implies a heat disengagement, a phenomenon which characterizes a structural reorganizations of atoms in crystalline lattice.

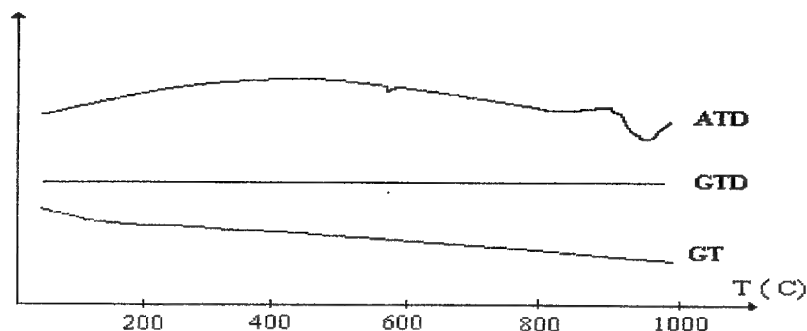
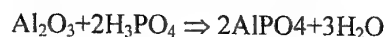


Fig. 3 ATD, GTD and GT curves of AlPO_4 monocrystals

The analysis of T, ATD, GTD and curves for aluminum phosphate single crystalline (maximum temperature = 1000°C, heating speed 10°C/min, samples weight = 0,1256 g) obtained from nutrient material by hydrothermal method emphasize a reduced water losses over whole temperature range, fact that is confirmed by the absence of the peaks from GTD and ATD curves respectively (figure 3). Thus, there are no present endothermic reactions, so, no water molecules are eliminated showing that AlPO₄ single crystal obtained by hydrothermal method has no water molecules into its crystalline lattice even if the nutrient material had water molecules from formation reactions:



γ-Aluminum ATD curves presents an exothermic peak at 458°C as a consequence of structural reorganization of atoms in monocystal lattice, with heat disengagement.

4. CONCLUSIONS

By analyzing thermogravimetric curve of as grown monocystals we concluded that monocrystalline AlPO₄ keeps structural properties of nutrient material but, because no water elimination, it results that by hydrothermal growth the AlPO₄ monocystal's quality is very good.

By reaction between γ-aluminum and phosphoric acid the obtained nutrient has an increasing humidity being, in fact, hydrate powder. But the obtained monocystal is not a crystallohydrate.

5. REFERENCES

- [1] L.E. Halliburton, L.. A. Kappers, A.. F. .Armington and J. Larkin, Ann. Freq.Control Symposium, 62, (1990);
- [2] Grozescu I., Muscutariu I., Irimia D., Tomuța Dana, Răță Diana, Romanian Journal in Physics, vol. 43, No. 1-2, p. 187, (1998);
- [3] Grozescu I., Novaconi Șt., Irimia D., Rață Diana, Romanian Journal of Physics, vol. 43, No. 1-2, p. 547, (1998);
- [4] J.C:Doukahan, B. Boulogne, P. Cordiec, E Philippet, J. Crystal Growth vol. 84, p. 167, (1987);
- [5] E.D. Kolb, R.H. Laudise, J. Crystal Growth., vol. 56, p. 83, (1982).

INVARIANCE PRINCIPLES FOR THE NONLINEAR EQUATIONS OF EVOLUTION AS LINEAR STOCHASTIC EQUATIONS

V. Babin, Maria Grigore, S. Ersen, A. Moldovan

National Institute of Research & Development for Optoelectronics INOE-2000

ABSTRACT

In this paper, we averaged the linear polistochastic equations and we obtained nonlinear deterministic equations of evolution. We used algebraic invariants associated to these nonlinear equations and identified the classes of equivalence for these systems of nonlinear equations. The analyze of the structure of these classes of equivalence revealed new evolution forms for the dynamic nonlinear systems. Thus, for the stimulated Brillouin scattering of the optical field, a gaussian polistochastic process it has been identified, which is superposed upon the classical scattering process. This fact was possible only as a consequence of the evaluation of the algebraic invariants. In this way, we identified dissipative systems with critical points separated and with ramification points.

1. INTRODUCTION

A lot of applications of nonlinear optics require systems of nonlinear equations of the following type:

$$\frac{dx}{d\xi} = \alpha_1 x + \beta_1 y + \varepsilon(\xi)[\alpha_2 x + \beta_2 y] \quad (1)$$

$$\frac{dy}{d\xi} = \gamma_1 x + \delta_1 y + \varepsilon(\xi)[\gamma_2 x + \delta_2 y]$$

where:

$\{x, y\} \Rightarrow$ dynamic variables: $\{x, y\} \in S_2$

$S_2 \Rightarrow$ bidimensional phase space $\{\alpha_1, \beta_1, \alpha_2, \beta_2, \gamma_1, \delta_1, \gamma_2, \delta_2\} \rightarrow$ physical constants

$\varepsilon(\xi) \Rightarrow$ random variable defined as:

$$\overline{\varepsilon(\xi)} \equiv \langle \varepsilon(\xi) \rangle = 0$$

$$\overline{\varepsilon(\xi) \cdot \varepsilon(\xi')} = \langle \varepsilon(\xi) \cdot \varepsilon(\xi') \rangle = 2\sigma^2 \cdot \delta(\xi - \xi')$$

The system (1) is known as a first-order nonlinear equations system with random parameters. Such systems can be solved using mathematical theory, by means of averaging the random variables. When these variables describe a complex random process (for example: a polistochastic process), the direct averaging of the system (1) is no more possible. Instead of this, the theory of polistochastic processes is used. This theory involves conditioned probabilities that describe features of the physical process illustrated in (1). Thus, it is possible to associate a system of nonlinear first-order differential equations with deterministic parameters with a system of linear first-order differential equations with random parameters.

The complexity of the polistochastic process is proportional to the nonlinearity degree of the nonlinear deterministic equations. Herein, we develop such a formalism, using the averaging technique of Liouville stochastic equations which lead to the Fokker-Planck-Einstein-Kolmogorov-equations¹. The solutions of these equations are the repartitions functions describing the polistochastic process. These repartition functions are classically used to obtain the moments of different degree for the parameters of interest. However, in our case these functions allow us to obtain the averaged nonlinear differential equations, which describe the physical process defined in (1).

2. THEORETICAL BACKGROUND

By dynamical averaging, using the Fokker-Planck equations, and the expressions:

$$\begin{aligned}\Phi_{\xi}(x, y) &= \iint x^{\lambda_1} \cdot y^{\lambda_2} \cdot P_{\xi}(x, y) dx dy \\ \frac{\partial P_{\xi}}{\partial \xi} &= -\hat{A} P_{\xi} + \sigma^2 \hat{B}^2 P_{\xi} \\ \hat{A} &= \frac{\partial}{\partial x} (\alpha_1 x + \beta_1 y) + \frac{\partial}{\partial y} (\gamma_1 x + \delta_1 y) \\ \hat{B} &= \frac{\partial}{\partial x} (\alpha_2 x + \beta_2 y) + \frac{\partial}{\partial y} (\gamma_2 x + \delta_2 y)\end{aligned}\quad (2)$$

we obtain the moment equation:

$$\frac{\partial \Phi_{\xi}}{\partial \xi} = - \iint x^{\lambda_1} \cdot y^{\lambda_2} \cdot \hat{A} P_{\xi} dx dy + \sigma^2 \iint x^{\lambda_1} \cdot y^{\lambda_2} \cdot [\hat{B}^2] P_{\xi} dx dy \quad (3)$$

The afin invariants, for a bidimensional system with quadratic nonlinearity, take the following form²:

$$\begin{aligned}I_1 &= a_{\alpha}^{\alpha}; \\ I_2 &= a_{\beta}^{\alpha} \cdot a_{\alpha}^{\beta}; \\ I_3 &= a_{\rho}^{\alpha} \cdot \sigma_{\alpha q}^{\beta} \cdot \sigma_{\beta \gamma}^{\gamma} \cdot \varepsilon^{pq}; \\ I_4 &= a_{\rho}^{\alpha} \cdot \sigma_{\beta q}^{\beta} \cdot \sigma_{\alpha \gamma}^{\gamma} \cdot \varepsilon^{pq}; \\ I_5 &= a_{\rho}^{\alpha} \cdot \sigma_{\gamma q}^{\beta} \cdot \sigma_{\alpha \beta}^{\gamma} \cdot \varepsilon^{pq}; \\ I_6 &= a_{\rho}^{\alpha} \cdot a_{\gamma}^{\beta} \cdot \sigma_{\alpha q}^{\gamma} \cdot \sigma_{\beta \delta}^{\delta} \cdot \varepsilon^{pq}; \\ I_7 &= \sigma_{\rho r}^{\alpha} \cdot \sigma_{\alpha q}^{\beta} \cdot \sigma_{\beta s}^{\gamma} \cdot \sigma_{\gamma \delta}^{\delta} \cdot \varepsilon^{pq} \cdot \varepsilon^{rs}; \\ I_8 &= \sigma_{\rho r}^{\alpha} \cdot \sigma_{\alpha q}^{\beta} \cdot \sigma_{\delta s}^{\gamma} \cdot \sigma_{\beta \gamma}^{\delta} \cdot \varepsilon^{pq} \cdot \varepsilon^{rs}; \\ I_9 &= \sigma_{\rho r}^{\alpha} \cdot \sigma_{\beta q}^{\beta} \cdot \sigma_{\alpha \delta}^{\delta} \cdot \varepsilon^{pq} \cdot \varepsilon^{rs}; \\ I_{10} &= a_{\rho}^{\alpha} \cdot a_{\delta}^{\beta} \cdot a_{\mu}^{\gamma} \cdot \sigma_{\alpha q}^{\delta} \cdot \sigma_{\beta \gamma}^{\mu} \cdot \varepsilon^{pq}; \\ I_{11} &= a_{\rho}^{\alpha} \cdot \sigma_{qr}^{\beta} \cdot \sigma_{\beta s}^{\gamma} \cdot \sigma_{\alpha \gamma}^{\delta} \cdot \sigma_{\delta \mu}^{\mu} \cdot \varepsilon^{pq} \cdot \varepsilon^{rs}; \\ I_{12} &= a_{\rho}^{\alpha} \cdot \sigma_{qr}^{\beta} \cdot \sigma_{\beta s}^{\gamma} \cdot \sigma_{\alpha \delta}^{\delta} \cdot \sigma_{\gamma \mu}^{\mu} \cdot \varepsilon^{pq} \cdot \varepsilon^{rs}; \\ I_{13} &= a_{\rho}^{\alpha} \cdot \sigma_{qr}^{\beta} \cdot \sigma_{\gamma s}^{\gamma} \cdot \sigma_{\alpha \beta}^{\delta} \cdot \sigma_{\delta \mu}^{\mu} \cdot \varepsilon^{pq} \cdot \varepsilon^{rs}; \\ I_{14} &= a_{\rho}^{\alpha} \cdot a_{\gamma}^{\beta} \cdot \sigma_{\alpha q}^{\gamma} \cdot \sigma_{\beta s}^{\delta} \cdot \sigma_{\gamma \delta}^{\mu} \cdot \sigma_{\mu \nu}^{\nu} \cdot \varepsilon^{pq} \cdot \varepsilon^{rs}; \\ I_{15} &= \sigma_{\rho r}^{\alpha} \cdot \sigma_{qk}^{\beta} \cdot \sigma_{\alpha s}^{\gamma} \cdot \sigma_{\delta l}^{\delta} \cdot \sigma_{\beta \gamma}^{\mu} \cdot \sigma_{\mu \nu}^{\nu} \cdot \varepsilon^{pq} \cdot \varepsilon^{rs} \cdot \varepsilon^{kl}; \\ I_{16} &= a_{\rho}^{\alpha} \cdot a_{\gamma}^{\beta} \cdot a_{\delta}^{\gamma} \cdot \sigma_{\alpha q}^{\delta} \cdot \sigma_{\beta s}^{\mu} \cdot \sigma_{\gamma \tau}^{\nu} \cdot \sigma_{\mu \nu}^{\tau} \cdot \varepsilon^{pq} \cdot \varepsilon^{rs}\end{aligned}\quad (4)$$

$I_1 \dots I_{16}$ form a fundamental polynomial base.

A polynomial base of K_{1+20} invariants taking the following form is also available:

$$\begin{aligned}
K_1 &= \sigma_{\alpha\beta}^\alpha \cdot X^\beta, \quad K_2 = a_\alpha^\rho \cdot X^\alpha X^q \cdot \varepsilon_{pq}, \quad K_3 = a_\beta^\alpha \cdot \sigma_{\alpha\gamma}^\beta \cdot X^\gamma, \quad K_4 = a_\gamma^\alpha \cdot \sigma_{\alpha\beta}^\beta \cdot X^\gamma \\
K_5 &= \sigma_{\alpha\beta}^\rho \cdot X^\alpha \cdot X^\beta \cdot X^q \cdot \varepsilon_{pq} \\
K_6 &= \sigma_{\alpha\beta}^\alpha \cdot \sigma_{\gamma\delta}^\beta \cdot X^\gamma \cdot X^\delta; \quad K_7 = \sigma_{\beta\gamma}^\alpha \cdot \sigma_{\alpha\delta}^\beta \cdot X^\gamma \cdot X^\delta; \quad K_8 = a_\gamma^\alpha \cdot a_\delta^\beta \cdot \sigma_{\alpha\beta}^\gamma \cdot X^\delta; \\
K_9 &= \sigma_{\alpha\rho}^\alpha \cdot \sigma_{\gamma q}^\beta \cdot \sigma_{\beta\delta}^\gamma \cdot X^\delta \cdot \varepsilon^{pq}; \quad K_{10} = \sigma_{\alpha\rho}^\alpha \cdot \sigma_{\delta q}^\beta \cdot \sigma_{\beta\gamma}^\gamma \cdot X^\delta \cdot \varepsilon^{pq}; \\
K_{11} &= a_\alpha^\rho \cdot \sigma_{\beta\gamma}^\alpha \cdot X^\beta \cdot X^\gamma \cdot X^q \cdot \varepsilon_{pq}; \quad K_{12} = a_\beta^\alpha \cdot \sigma_{\alpha\gamma}^\beta \cdot \sigma_{\delta\mu}^\gamma \cdot X^\delta \cdot X^\mu; \quad K_{13} = a_\gamma^\alpha \cdot \sigma_{\alpha\beta}^\beta \cdot \sigma_{\delta\mu}^\gamma \cdot X^\delta \cdot X^\mu \\
K_{14} &= a_\rho^\alpha \cdot \sigma_{\alpha q}^\beta \cdot \sigma_{\beta\delta}^\gamma \cdot \sigma_{\gamma\mu}^\delta \cdot X^\mu \cdot \varepsilon^{pq}; \quad K_{15} = a_\rho^\alpha \cdot \sigma_{\alpha q}^\beta \cdot \sigma_{\beta\mu}^\gamma \cdot \sigma_{\gamma\delta}^\delta \cdot X^\mu \cdot \varepsilon^{pq} \\
K_{16} &= a_\rho^\alpha \cdot \sigma_{\beta q}^\beta \cdot \sigma_{\alpha\mu}^\gamma \cdot \sigma_{\gamma\delta}^\delta \cdot X^\mu \cdot \varepsilon^{pq}; \quad K_{17} = \sigma_{\beta\gamma}^\alpha \cdot \sigma_{\alpha\gamma}^\beta \cdot \sigma_{\delta\mu}^\gamma \cdot X^\delta \cdot X^\mu \cdot X^\nu \\
K_{18} &= \sigma_{\mu\rho}^\alpha \cdot \sigma_{\alpha q}^\beta \cdot \sigma_{\beta\nu}^\gamma \cdot \sigma_{\gamma\delta}^\delta \cdot X^\mu \cdot X^\nu \cdot \varepsilon^{pq}; \quad K_{19} = a_\rho^\alpha \cdot a_\nu^\beta \cdot \sigma_{\alpha q}^\gamma \cdot \sigma_{\beta\mu}^\delta \cdot \sigma_{\gamma\delta}^\mu \cdot X^\nu \cdot \varepsilon^{pq}; \\
K_{20} &= \sigma_{\rho r}^\alpha \cdot \sigma_{\nu q}^\beta \cdot \sigma_{\alpha s}^\gamma \cdot \sigma_{\beta\gamma}^\delta \cdot \sigma_{\delta\mu}^\mu \cdot X^\nu \cdot \varepsilon^{pq} \cdot \varepsilon^{rs}
\end{aligned} \tag{5}$$

We present below the topological equivalent classes, assuming that:

$$I_1 = 0 \quad I_2 < 0 \quad I_6 = 0 \tag{6}$$

- The equivalence class (1):

$$\{I_4=0; \quad \alpha=0; \quad I_{16}=0; \quad I_{10}=0\}^{(1)} \equiv \{-\} \rightarrow \text{singular point classification "stable cycle"}$$

- The equivalence class (2):

$$\begin{aligned}
\{I_4=0; \alpha < 0\}^{(2)} &\equiv \{I_4=0; \alpha=0; I_{16}=0; I_{10} \neq 0\}^{(2)} \\
&\equiv \{I_4=0; \alpha > 0; I_8 < 0; I_{16} \neq 0\}^{(2)} \\
&\equiv \{I_4 \neq 0; I_{13}=0; \beta < 0; I_9 < 0; \gamma \leq 0\}^{(2)} \\
&\equiv \{I_4 \neq 0; I_{13}=0; \beta=0; \gamma < 0\}^{(2)} \\
&\equiv \{I_4 \neq 0; I_{13}=0; \beta=0; \gamma > 6\}^{(2)} \\
&\equiv \{I_4 \neq 0; I_{13}=0; \beta > 0; I_9 > 0; \gamma \geq 4\}^{(2)} \Rightarrow \text{stable cycle + SA, where SA is a critical point}
\end{aligned}$$

- The equivalence class (3):

$$\begin{aligned}
\{I_4=0; \alpha > 0; I_8 > 0; I_{16}=0\}^{(3)} &\equiv \\
&\equiv \{I_4 \neq 0; I_{13}=0; \beta < 0; I_9 > 0\}^{(3)} \quad \text{2 stable centers + 2 points SA} \\
&\equiv \{I_4 \neq 0; I_{13}=0; \beta > 0; I_9 < 0; \gamma < 0\}^{(3)} \rightarrow
\end{aligned}$$

- The equivalence class (4):

$$\{I_4=0; \alpha > 0; I_8 > 0; I_{16} \neq 0\} \rightarrow \text{2 stable cycles + 2 centers on the Poincare circle}$$

- The equivalence class (5):

$$\begin{aligned}
& \{I_4=0; \alpha>0; I_8=0; I_{16}=0\} \stackrel{(5)}{=} \\
& \stackrel{(5)}{=} \{I_4 \neq 0; I_{13}=0; \beta<0; I_9=0\} \stackrel{(5)}{=} \quad 1 \text{ stable cycle} + 2 \text{ SA points} + \text{center on the Poincare circle} \\
& \stackrel{(5)}{=} \{I_4 \neq 0; I_{13}=0; \beta>0; I_9=0; \gamma<0\} \rightarrow
\end{aligned}$$

- The equivalence class (6) :

$$\{I_4=0; \alpha>0; I_8=0; I_{16} \neq 0\} \stackrel{(6)}{=} \{-\} \rightarrow \quad 1 \text{ stable cycle} + 2 \text{ SA points} + \text{center on the Poincare circle}$$

Finally we present the form of invariants (I_{1+16}) defined in [6] and (K_{1+20}) defined in [7] for the S.B.S. system (the stationery regime case) with the parameters:

(α) normalized nonlinear losses of the optical field

$\sigma = g_B^e \cdot L_B \cdot I_0 \rightarrow$ normalized gain in the S.B.S. process

The (I_{1+16}) invariants take the form:

$$\begin{aligned}
I_1 &= -2\alpha \\
I_2 &= +2\alpha^2 \\
I_3 &= I_4 = I_5 = I_6 = 0 \\
I_7 &= I_8 = I_9 = -4\sigma^4 \\
I_{10} &= 0 \\
I_{11} &= I_{12} = I_{13} = -4\alpha \cdot \sigma^4 \\
I_{14} &= I_{15} = I_{16} = 0
\end{aligned} \tag{9}$$

The (K_{1+20}) invariants take the form²:

$$\begin{aligned}
K_1 &= \sigma(I_{LC} - I_S) & K_7 &= \sigma^2(I_{LC} - I_S)^2 \\
K_2 &= 0 & K_8 &= \alpha^2 \cdot \sigma(I_{LC} - I_S) \\
K_3 &= K_4 = -\alpha \sigma(I_{LC} - I_S) & K_9 &= 0 \\
K_5 &= -2\sigma(I_{LC} I_S)(I_{LC} + I_S) & K_{10} &= -2\sigma^3(I_{LC} - I_S) \\
K_6 &= -4\sigma^2(I_{LC} I_S) \\
K_{11} &= 2\alpha \sigma(I_{LC} I_S)(I_{LC} + I_S) & K_{17} &= -4\sigma^3(I_{LC} I_S)(I_{LC} - I_S) \\
K_{12} &= K_{13} = 4\alpha \sigma^2(I_{LC} I_S) & K_{18} &= -2\sigma^4(I_{LC} - I_S)^2 \\
K_{14} &= K_{15} = 0 & K_{19} &= 0 \\
K_{16} &= 2\alpha \sigma^3(I_{LC} - I_S) & K_{20} &= -4\sigma^5(I_{LC} - I_S)
\end{aligned} \tag{10}$$

The expressions for the invariants in [9] and [10] define the algebraic equivalence class of the nonlinear system that describe the S.B.S. process. Thus, by using the algebraic equivalence of the nonlinear autonomous differential systems, we can answer whether, the stochastic moment equations of the optical field propagating through random media may be (or not), algebraic equivalent to the stochastic moment equations of the intensities of the optical field in the S.B.S. process³.

For algebraic classification of the S.B.S. system we calculate the following expressions:

$$\begin{aligned}
\alpha_1 &= I_2^2 \cdot I_8 - 28 I_2 I_5^2 + 16 I_5 I_{10} = -16(\alpha \sigma)^4 \\
\beta_1 &= 4 I_4^2 - 3 I_2 I_9 - 4 I_3 I_4 = +24 \alpha^2 \cdot \sigma^4 \\
\gamma_1 &\text{ is not defined}
\end{aligned} \tag{11}$$

$$\begin{aligned}\delta_1 &= I_2^2 I_8 - I_2 I_5^2 - 2 I_5 I_{10} = -16(\alpha\sigma)^4 \\ \mu_1 &= 27 I_8 - I_9 - 18 I_7 = -32\sigma^4\end{aligned}$$

The equivalence class is defined as: $\alpha_1 < 0$; $\beta_1 > 0$; $\delta_1 < 0$, $\mu_1 < 0$; $I_1 < 0$; $I_2 > 0$ (12)

and characterized by the properties of the S.B.S. equations⁴:

$\alpha_1 = \delta_1 < 0$, the system is autonomous with real parameters

$\beta_1 > 0$, the system is dissipative; presents separated critical points.

$\mu_1 < 0$, the system has no singularities in phase space.

$I_1 < 0$, the solutions are continuous and limited functions.

$I_2 > 0$, the system allows bifurcation points as in the parameters space.

$I_1^2 - 4 I_2 > 0$, hyperbolic solution.

$I_1^2 - 4 I_2 < 0$, periodical solution.

3. CONCLUSIONS

In this paper, we constructed a model for solving the differential stochastic equations using the formalism of statistical Liouville and of Fokker-Planck equations. In conclusion, when solving a system of nonlinear autonomous differential equations we can use the equivalence classes that give a complete description of the evolution of the dynamic system described by the nonlinear equations in the phase space. Using the properties of the random process we can give a qualitative analysis of the nonlinearity degree of the equations.

4. REFERENCES

- [1]. A. Monin, A. M. Iaglom, "Statisticheskaya Gidrodinamika", Nauka, Moscow, (1967)
- [2]. K. S. Sibirski, "Vvedenie v algebricheskuu teorii invariantov differentsialnih uravnenii", Editura "Stiinta", Chisinau, (1982)
- [3]. V. I. Arnold, "Ecuatii diferentiale ordinare", Scientific and Enciclopedic, Bucharest, (1978)
- [4]. V. Babin, "Deterministic and Stochastic Models in the Stimulated Brillouin Scattering", (1997).

A STUDY ABOUT THE ACTION LASER RADIATION ON THE EVOLUTION OF "IN VITRO" GRAPEVINE CROP

Dana Giosanu, S. Anghel, I.I. Siman

Faculty of Sciences, University of Pitesti, Târgu din Vale Street, No.1, Pitesti - 0300,
phone/fax 048-216448, e-mail: sanghel@electra.upit.ro

ABSTRACT

"In vitro" crop-technics, associated with the action of some physical mutagenous factors (such as laser radiation), allowed the obtaining of new biologic forms, of high productivity, resistant to many diseases or to environmental unfavorable conditions. The large uses of laser as a physical mutagenous factor, is due especially to the specific qualities of its radiation: coherence and high directionality.

Herein we present the results of our study on the evolution of meristems crop of Merlot variety subject to laser radiation. We used a 6 mW power He-Ne laser, with 632,8 nm wavelength. The exposure time ranged from 30 seconds to 10 minutes; we also used a not-irradiated witness lot. Throughout the research, we had mainly in view caulogenesis, rhizogenesis and heterophyly processes.

1. INTRODUCTION

For the long-term development of agriculture and for agricultural yields above the present limits, genetics and variety improvement must structurally modify the features of the agricultural species. These objectives require deep and highly exigent investigations.

The regeneration and the study of the manifestation degree of some mutation on the level of the entire plant, proceeded from "in vitro" crop, could lead to the detection and selection of some agronomical potentially useful mutants. Induced mutations are important in the obtaining of new varieties, with valuable features, process. The large use of the laser – as a physical mutagenous agent is especially due to the specific qualities of the emitted radiation (coherence and high directivity). Due to its monochromaticity, the laser beam action is specific to certain wavelengths, to certain tissues and cellular organits .

The purpose of this paper is to present the laser radiation action on the evolution of grapevine meristem crop, having in view the caulogenesis, rhizogenesis and heterophyly processes.

2. MATERIALS AND METHODS

The research was performed on the "Merlot" grapevine variety, that is known as a sensitive species to both drought and frost.

Because of its high cell division ability, the meristim crop is preferred for the "in vitro" method. Besides, the use of meristems guarantees the genetic stability of descendants. This is why the use of meristem crop is preferable in the study of experimental mutagenesys [2].

Explants were separated from "in vitro" multiplied offshoots, and 3-4 mm size meristems were inoculated. Crops were incubated in a growing chamber, at $26^{\circ} \pm 2^{\circ}$ C temperature, 16 hours daily lighting. Basic culture medium was Murashige Skooge (M.S 1962), with admixtures of 1,5 mg/l BAP and 0,2 mg/l AIA for the initializing stage, and 1,5 mg/l AIA and 0,22 mg/l kinetine for the rooting stage [1].

Irradiation was made separately from the first day, for each explant. We have used the radiation of a He-We laser, with the parameters summarized in Table I.

Table 1

Irradiation time (seconds)	Power (W)	Irradiated surface (mm ²)	Energy (J)
0	0	1	0
30	6×10^{-3}	1	2×10^{-2}
180	6×10^{-3}	1	$3,3 \times 10^{-2}$
300	6×10^{-3}	1	2×10^{-1}
600	6×10^{-3}	1	1×10^{-1}

The radiation wavelength continuously emitted was of 6328 Å; the spot useful cross - section was of 1 mm², covering the whole meristemic tissue. Given the 10 cm distance from the laser to the explant, the divergence of the spot was negligible.

The subsequent evolution of the irradiated seedings was compared to the evolution of an unirradiated witness lot.

3. RESULTS AND DISCUSSION

Thirty days after inoculation and laser treatment, the witness lot contained 15,3% of seedings without evolution, compared to the irradiated lots. Except the 600 sec exposure time variant, we noticed a stimulation of the seedings growth by the increase of the laser treatment time. Offshoots had heights into the intervals (0,5 - 1 cm), (1 - 1,5 cm) or over 2 cm; they presented basic, axillary and basic + axillary multiplication.

After 24 days, on the rooting substrate, only the witness lot contained seedings without evolution. Offshoots had not basic multiplication, but they were more vigorous; in the case of 300 seconds irradiation time, 13,33% of seedings had over 6 cm, and over 8,5 cm in height (figure 1).

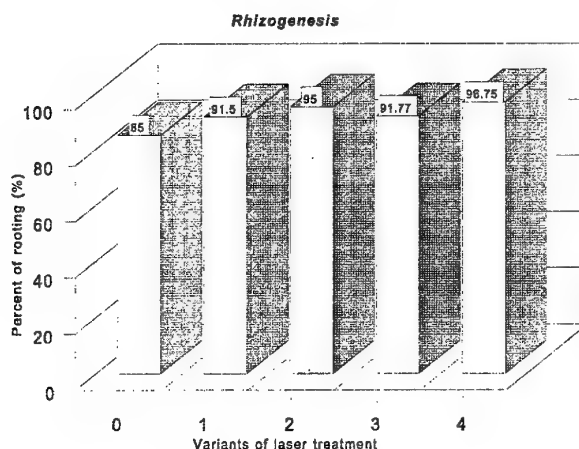


Fig. 1

Rhizogenesis

Under laser treatment, the rhizogenesis process is much more visible; all variats of the treatment yield to more than 90% percent of rooting (the maximum value is 96,75% for 10 minutes irradiation time). The witness lot had 85% percent of rooting (figure 2).

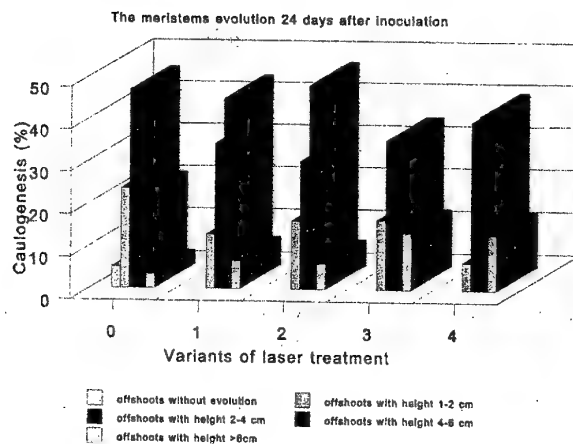


Fig. 2

Heterophyly

Only 5% of the seedlings of the witness lot present the heterophyly phenomenon. The maximum value of the percentage of heterophyly (13.1%) was obtained for 10 minutes of irradiation (Figure 3). We did not notice a proportionality of the number of seedlings which present heterophyly with the irradiation time, as in case of using gamma rays.

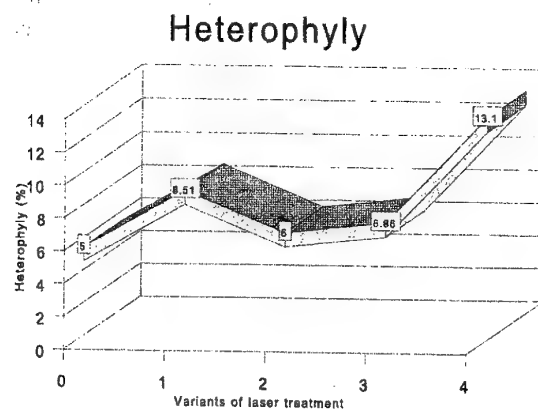


Fig. 3

4. CONCLUSIONS

"In vitro" crop technics, associated with the action of a physical mutagenic agent (laser radiation), allowed us to find new information concerning the role and the importance of physical factors on the evolution of grapevine meristems. Under laser treatment, the rhizogenesis process is much more visible; all variants of the treatment yield to more than 90% percent of rooting. The heterophyly phenomenon occurring in case of using a laser radiation does not present a uniform manifestation. The minimum number of seedlings heterophyly was observed for the witness lot (5%). The above observations point out the stimulating role that laser radiation has on the evolution of meristems of grapevine crop.

5. REFERENCES

- [1]. Baditescu D., Visoiu E., Popescu C., - *Potentialul de regenerare al unor soiuri de vita de vie pe medii aseptice de cultura*, Anale ICVV, p.23-33 (1991).
- [2]. Raicu Petre, Badea Marcela, - *Cultura de celule si biotehnologiile moderne*, Bucuresti, Editura Stiintifica si Enciclopedica, (1986).

HOLOGRAPHIC SOLAR CONCENTRATORS RECORDED ON SPHERICAL SURFACES WITH ACRYLIC PHOTOPOLYMERS

Silvia Nicolau-Rebigan, St. Levai*, B. Nicolae*, Roxana Rebigan*

National Institute of Lasers, Plasma and Radiations Physics,
Magurele-Bucharest, Romania

*University of Bucharest, Faculty of Physics, Magurele-Bucharest, Romania

ABSTRACT

In this paper a method for hologram recording on spherical surfaces is presented. As recording material we used a He-Ne laser obtained acrylic photopolymer. Two holographic photopolymer systems are used in aqueous solutions. The two chemical structures of photopolymer systems are presented and compared. The selected photopolymer is placed between two spherical glass plates that are concentric. The experimental device was used to make holographic lenses by means of interference between a spherical wave and a plane wave. The diameter of the holographic lenses was 5-7 cm and the focal length was 30 cm. The diffraction efficiency achieved with the two chemical systems was measured. The uniformity across the holographic lens was examined. Image quality obtained can be improved by diffraction theory and system tolerances. For applications in science and technology we created solar concentrators with small dimensions and it is possible in future to obtain improved experimental devices.

1. INTRODUCTION

Dye sensitised photopolymerisation of acrylic monomers has been suggested for the hologram recordings [1-5]. This method is important for holography and optical data processing applications because of self-developing, high sensitivity and high resolution [3,5]. Many types of holographic optical elements (HOE's) are being used in different optical systems, and the interest for the design, fabrication and application of these optical systems with HOE's has increased considerably. Even though HOE's offer many advantages, but aberrations are present in HOE's when the geometry and/or the wavelength are changed between recording and reconstruction. Use of spherical instead of planar substrates has been suggested as a method for reduction of both monochromatic [6-9] and chromatic [10] aberrations in HOE's, and the aberrations of holograms recorded on spherical surfaces have been considered in many papers [2,3,7,8]. HOE's recorded on curved surfaces have aberration characteristics different from those recorded on flat surfaces. In the case of HOE's recorded on spherical surfaces, an additional parameter, spherical surface radius, is available and can be used for improvement of imaging quality.

Different materials such as silver halide emulsion, dichromated gelatin or photoresist are used for manufacture of HOE's [3]. However, these materials mentioned above are connected with relatively improved technology, especially in the creation of the photosensitive layer on a monoplane substrate. These materials also require subsequent developing, and dichromated gelatin also requires a cementing procedure. All of these problems make it difficult to experimentally analyze HOE's on spherical substrates. One possibility is to use photopolymers as a recording material for fabrication of HOE's on spherical surfaces. [3,5]. Photopolymers have been shown to have high sensitivity and an excellent signal-to-noise ratio [3,5]. Additionally, they are usually used between two plates of glass, and because they are liquid, they conform to any type of substrate they are deposited upon. This leads us to believe that they can be used to manufacture these holographic systems and that is possible to introduce them between two spherical plates of glass that are concentric so that by use of adequate spacers, we can generate a uniform layer of photopolymer on the spherical substrate. Holographic photopolymer systems

basically consist of a monomer, or a mixture of monomers, and a photoinitiator. We developed holographic recording media by the photopolymerisation of acrylamide and crosslinkable N,N'-methylenebisacrylamide [2-5]. We used a photoredox initiator system composed of a phenothiazine dye, such as methylene blue, as photooxidant, and a photoreductant, such as acetylacetone (ACA) or triethanolamine (TEA). These compositions were selected in connection with solubility to solvent (water), improbability of side reaction, and transparency of produced photopolymer [2-5]. Sample cells were prepared by enclosing the photopolymerizing solution between a pair of 5 cm square glass plates. The thickness of the solution was controlled to be 60-70 μm by polyester film spacing. In order to determine the sensitivity of the photopolymerisation samples, holographic diffraction gratings were formed by the interference coherent beams and the diffraction efficiency for the exposed He-Ne laser was measured [2-5]. The photosensitive system viscosity was tested with an original viscosimeter transducer assisted by a microprocessor [3,4].

We selected chemical systems in order to obtain holographic optical elements recorded on spherical surfaces. The system selected here was formed by mixing of two aqueous solutions [11,12]. The polymerisable system (solution A) was formed with:

- acrylamide 7 M
- zinc acrylate 1 M
- N,N'-methylenebisacrylamide 0.7 M

The photoinitiator system (solution B) was formed with:

- methylene blue $3.6 \times 10^{-2} \text{M}$
- rose Bengal $6.0 \times 10^{-3} \text{M}$
- p-toluensulfuric acid $1.77 \times 10^{-2} \text{M}$

The solution for a laser exposure was formed by mixing of four volumes of solution A with one volume of solution B.

A set of films with the two dyes was submitted to pre-exposure at 546 nm and subsequent irradiation with 633 nm. We changed the intensity and the time of pre-exposure to the beam in order to study the influence both on energetic sensitivity and the layer's rigidity. A previous paper [11] showed that it is possible to increase the energetic sensitivity and at the same time to have a polychromatic system. The solution is placed between two spherical glass plates with a curvature radius of 120 mm. This device was used to make holographic lenses by means of interference of spherical wave with a plane wave.

1. EXPERIMENTAL PROCEDURE AND SET-UP

The polymerisable system (solution A) and the photoinitiator system (solution B) were mixed into a solution in the dark. The to be irradiated solution was formed by mixing of four volumes of solution A with one volume of solution B.

A set of films with the two dyes was submitted to pre-exposure at 546 nm and subsequent irradiation with 633 nm. We changed the intensity and the time of pre-exposure to the beam in order to study the influence both on energetic sensitivity and the layer's rigidity.

The solution is placed between two spherical glass plates with a curvature radius of 120 mm. This device was used to make holographic lenses by means of interference of a spherical wave with a plane wave. The diameter of the usable holographic lenses was 6 cm, and the focal length was 30 cm.

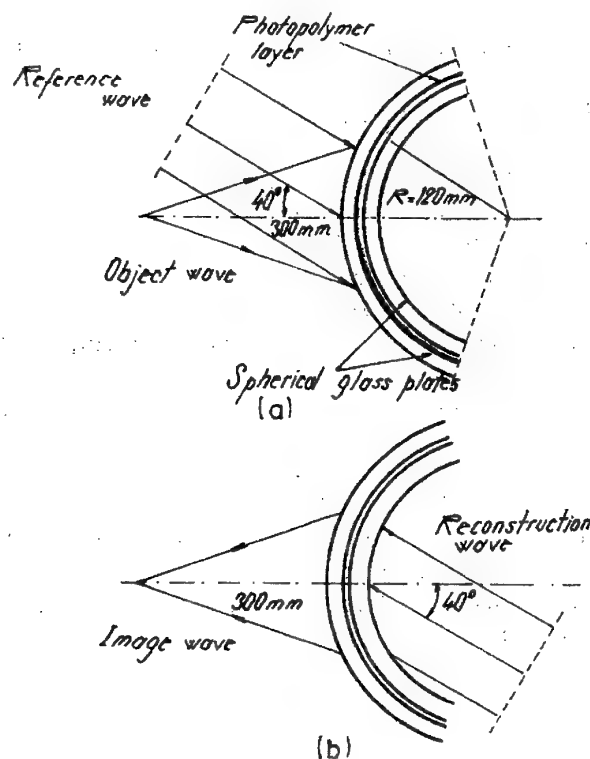


Fig. 1 Geometries of a) recording and b) reconstruction of the holographic optical elements

Figure 1 described the geometries of recording and the reconstruction of the holographic lenses.

The uniformity across the holographic lens was good. In the future, image quality obtained by diffraction theory and system tolerances as well as the angular response of the HOE's will be studied.

HOE's recorded on spherical surfaces might be of great use in the design and the fabrication of solar concentrators. This purpose involved a good testing of holographic lenses obtained by the above mentioned procedure.

2. CONCLUSIONS

Acrylic photopolymers can be used to make holographic lenses by means of interference between a spherical wave and a plane wave. The improved diameter of the holographic lenses was 6 cm and the focal length was 30 cm. The diffraction efficiency was measured and the uniformity across the holographic lens was examined. A rigidity test was applied. Image quality obtained can be improved by diffraction theory calculations and system tolerances accurate determinations. For applications in science and technology we created solar concentrators with small dimensions and it is possible in the near future to obtain improved experimental devices.

4. REFERENCES

- [1]. Nicolau-Rebigan Silvia, St. Cerc. Fiz. 32,1,47 (1980)
- [2]. Nicolau-Rebigan Silvia, Pascu M. L., Fiti M., Pascu Al., Levai S., Alexandrescu R., Morjan I., "Photopolymerisation effects in the uV-IR range at laser interaction with organic monomers",

Com. Second Intern. Conf. "Trend in quantum Electronics", Bucharest 2 -6 September 1985, pub Proc.pp251.

- [3]. Nicolau Silvia, Contributions of Applied Holography, Doctoral Thesis, Central Institute of Physics, Bucharest, Romania, 1987
- [4]. Nicolau Silvia, Sporea D. G., Optoelectronica, 2,1, (1994)
- [5]. Nicolau Silvia, Levai St., Sporea D., Anale. Univ. Buc. 44,1,63-70 (1995)
- [6]. Weldford W. T., Opt. Opt. Commun. 1, 268-269 (1973)
- [7]. Mustafin K. S., Opt. Spectrosc. 37,664-666 (1973)
- [8]. Masajada Y., Novak Y., Appl opt. 30,1791-1795 (1991)
- [9]. Baskars., Sigh K., Y. Mod. Opt.,39,1533-1542 (1992)
- [10]. Weingartner Y., Optik 65,49-61 (1983)
- [11]. Fimia A., Lopez N., Mateos F., Sastre R., Pineda Y., Amat-Inerri F., I. Med. Opt. 40, 699-706 (1993)
- [12]. Fimia A., Lopez N., Mateos F., Sastre R., Pineda Y., Amat-Inerri Appl. Opt. 32,3706-3707 (1993)
- [13]. Yaniv A., Opt. Lett. 18,652-654 (1995)
- [14]. Jost P., Loungnot D. Y., "Modelling of the phenomenon occurring during holographic recording on photopolymers" OPTO 93 Proc.,pp 584-589, ESI Publications (1993)
- [15]. Nicolau-Rebigan Silvia, Levai St.,Rebigan Roxana, Nicolae B., Sporea D., "Acrylic photopolymers for permanent holographic recordings, Anual ses. st., Fac.Physics, Magurele-Bucharest, 28 May 1998.

NEW PHOTOPOLYMERS LASER OBTAINED AND THEIR APPLICATIONS

Silvia Nicolau-Rebigan, M. Ristici, St. Levai*, Roxana Rebigan*, B. Nicolae*, Doina Mitea

National Institute of Lasers, Plasma and Radiations Physics, Magurele-Bucharest, Romania

* University of Bucharest, Faculty of Physics, Magurele-Bucharest, Romania

ABSTRACT

In this paper a study of acrylamide photopolymerization using a He-Se laser radiation is presented, as well as some experimental results. In our experiment aqueous solutions with different concentrations were employed. The X-ray diffraction method was used to study polymer crystallinity that controlled technological parameters of processing. The best polymerisation conditions during laser irradiation were determined. A Sollux lamp of 500 W was used after laser irradiation to determine post-exposure effects. A DRON-2 X ray diffraction goniometer with $\text{CuK}\alpha$ radiation ($\lambda=1.54 \text{ \AA}$) was used.

Optical diffraction method was used and refractive index was measured for standard solutions. Pulfrich refractometer was employed in selected conditions.

Different types of acrylic monomers were employed in laser polymerisation studies for applications in science of materials and to obtain new ranges of utilisation. In this manner we developed a polymer system used as hologram material with improved parameters and useful for Argon ion laser holography and for He-Se laser holography in real procedures.

Different types of acrylic monomers were also used in laser polymerisation studies for applications in dentistry. Our materials obtained by He-Se low power laser procedures present improved technological parameters (mechanical and chemical parameters) providing a good processing and a good stability of colour for a long time.

1. INTRODUCTION

In our papers we presented a study of acrylamide photopolymerization by He-Ne laser irradiation. This study was determined in order to obtain new holographic permanent recording media, that have high diffraction efficiency. The characteristics of the photosensitive system were estimated. The stability of holographic recordings was tested with a BRABENDER REALTEST station and also with different post-laser-exposures in the UV-IR range of the spectrum [1-4].

The photosensitive system viscosity was measured with our original viscosimeter assisted by a Z-80 microprocessor, and obtained results are compared with conventional thermostated Hoppler viscosimeter results [5].

Dye-sensitised photopolymerization of acrylic monomers has been suggested for the hologram recordings. This method is important for holography and optical data processing and applications of holographic interferometry because of self developing, high-sensitivity and high resolution [1,6].

The photopolymerization of acrylamide by laser irradiation can be used in dosimetrical purposes [1].

In this paper, a study of acrylamide photopolimerization using a He-Se laser radiation is presented, as well as some experimental results.

In our experiment aqueous solutions with different acrylamide concentrations were employed. The X-ray diffraction method was used to study polymer crystallinity that controlled technological parameters of processing. The best polymerisation conditions during laser irradiation were determined. A Sollux lamp of 500 W was used after laser irradiation to determine post-exposure effects. In the X-ray diffraction method was used a DRON-2-X ray diffraction goniometer with $\text{CuK}\alpha$ radiation ($\lambda=1.54 \text{ \AA}$).

Optical diffraction method has been used for investigations in real time of dosimetrical parameters evaluated in standard conditions. The refractive index was measured for standard solutions. Pulfrich refractometer was employed in selected conditions.

The acrylamide standard solutions were used for dosimetrical purposes, He-Se laser beam energy estimated.

On the other hand, different types of acrylic monomers were also employed in laser polymerisation studies for applications in Dentistry. Our materials obtained by He-Se low power laser procedures present improved technological parameters (mechanical and chemical parameters) providing a good stability of colour in a long time.

2.EXPERIMENTAL PROCEDURE AND RESULTS

The He-Se laser is a gas laser and the emitted radiations are included to selenium ion spectrum. The active medium consists of helium and selenium vapours, atoms and ions. There are 16 upper levels involved in laser emission on 65 wavelengths, most of them in a visible range of spectrum. The powerful lines are in the green and blue-green region of the spectrum. For 1 meter active length, it is possible to be obtained a total power of 150 mW.

In our experiments, we used a home-made He-Se laser. The laser tube had a 30 cm active length, a total power of 12 mW on 7 beams with the wavelengths in the green range of the spectrum [4].

The technological parameters of the He-Se laser are :

-Gas temperature : $T_{\text{gas}}=500^{\circ}\text{C}$

-Current intensity : $I=130\text{ mA}$

-Power supply : $U=2.5\text{ kV}$

Our photopolymerization results can be obtained also with the Argon laser beam irradiation, but He-Se laser presents many other advantages developed from small dimensions, versatility in different experimental procedures, low versatile power, continuous wave operating mode, negligible thermal effects in some applications, without undesired heat transfer and low price [4,8].

Fig. 1 presents a schematic montage for holographic diffraction grating recording using a He-Se laser. The two lasers have small powers (7-12 mW).

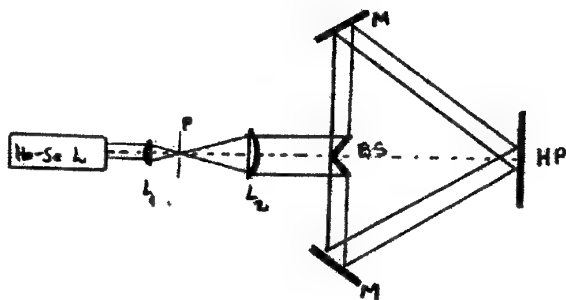


Fig.1

The experimental device and set-up are positioned on a special table with isolated vibrations.

Fig. 2 presents an microscopic image of a holographic diffraction grating obtained by He-Se laser exposure on a special acryle composition. [6]



Fig. 2

Fig. 3 presents an experimental set-up (schematic design) for real time photopolymerization reactions using a He-Ne laser with small power (12 mW).

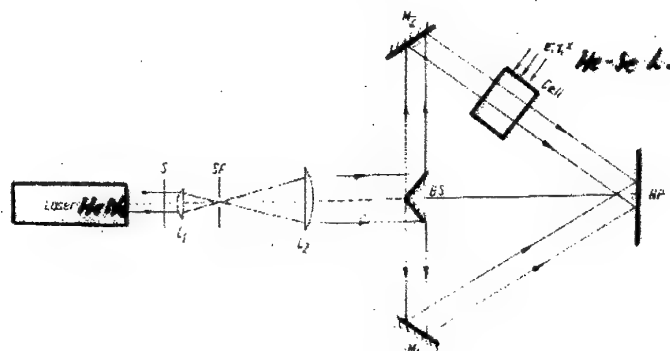


Fig. 3

In our experiment aqueous solutions of acrylamide with different concentrations were employed.

The X-ray diffraction method has been used to study polymer crystallinity that controlled technological parameters of processing. The best polymerisation conditions during laser irradiation were determined. A DRON-2 X-ray diffraction goniometer with $\text{CuK}\alpha$ radiation was used.

Fig. 4 presents a X-ray diffraction diagram for a monomer aqueous solution that shows a crystalline phase.

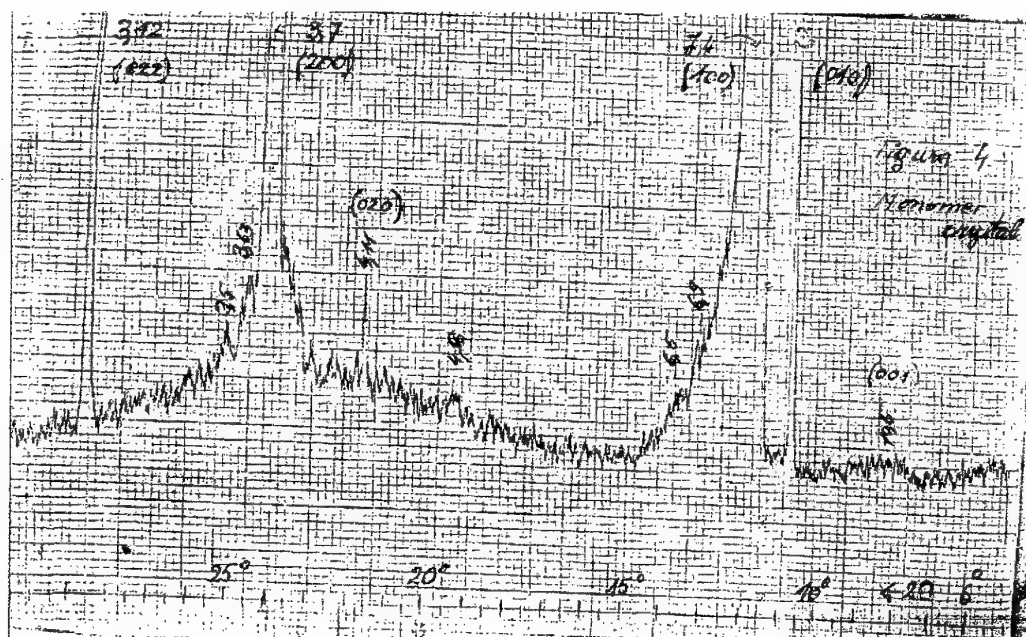


Fig. 4

Fig. 5 presents a X-ray diffraction diagram for a monomer and polymer mixture in an aqueous solution irradiated with a 12 mW He-Se laser operating in a blue-green region of the spectrum.

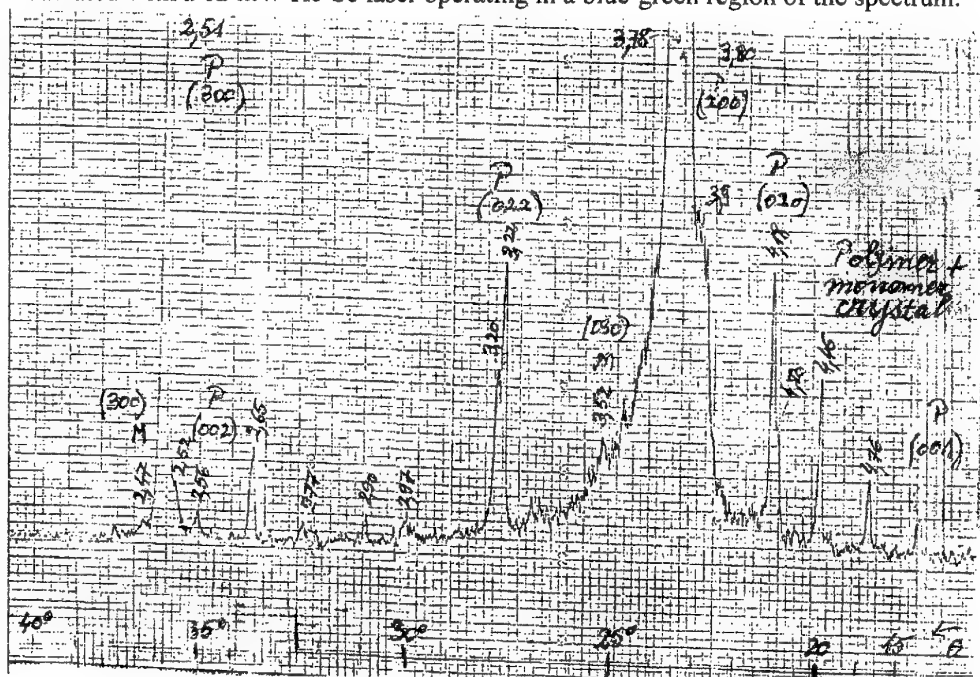


Fig. 5

Different types of acrylic monomers were employed in laser polymerisation studies for applications in science of materials and to obtain new ranges of utilisation. In this manner we developed new polymer systems used as holographic recording media. Different types of acrylic monomers were also employed in laser polymerisation researches for applications in Dentistry. Our materials obtained by He-Se low power laser procedures present improved technological parameters (mechanical and chemical parameters) providing a good processing and a good stability of colour for a long time.

3. POST-EXPOSURE EFFECTS AT HE-SE LASER ON ACRYLIC PHOTOPOLYMERS

A Sollux lamp of 500 mW was used after laser irradiation to determine the post-exposure effects.

We obtained a general study of post-exposure effects at He-Se laser irradiation of acrylic photopolymers. To obtain a good reproductibility of technological parameters of polymers needed in clinical stomatological applications and orthodontic appliances is used an accurate dose of He-Se laser radiation.

Polymeric materials obtained and illuminated with the same He-Se low power laser beam present an undesirable effect that consists in a degradation of colour and mass density with a refractive and reflection index variation, when the additional dose of laser radiation increased with first technological dose of interest. In a monomer solution accidental impurities determined a post-exposure polymerisation effect that consists in a modification of polymer characteristics and material homogeneity. Colour stability was examined by reflection measurements and colorimetric procedures to obtain a 3% dose accidental error. A Sollux lamp of 500 W was used after laser irradiation to determine post-exposure effects of incoherent light in comparison with coherent laser beam. Our materials treated by He-Se laser beam present improved technological parameters (mechanical and chemical) providing a good processing and a good stability of colour in a long time.

4. CONCLUSIONS

In this paper a study of acrylamide photopolymerization using a He-Se laser radiation is presented, as well as some experimental results. The X-ray diffraction method was used to study polymer crystallinity that controlled technological parameters of processing. The best polymerisation conditions during laser irradiation were determined. Different types of acrylic monomers were employed in laser polymerisation studies for applications in science of materials and to obtain new ranges of utilisation. In this manner we developed a polymer system used as hologram recording material with improved parameters. Different types of acrylic monomers were also employed in laser polymerisation researches for applications in Dentistry. Our materials obtained by He-Se low power laser procedures present improved technological parameters (mechanical and chemical parameters) providing a good processing and a good stability of colour in a long time. [2,3,7,9,10]

5. REFERENCES

- [1]. Nicolau Silvia, Contributions of applied holography, Doctoral thesis, Central Institute of Physics, Bucharest, Romania, 1987
- [2]. Nicolau Silvia, Sporea D., Scarlat F., "Testing of the holograms recorded on photopolymer films by means of an interferometric method with an original optoelectronic scheme", Optoelectronica vol.2, No.3, pp.43-46 (1994)
- [3]. Levai S., Nicolau Silvia, Sporea D., Mitea Doina, "Automatic industrial nondestructive testing used computer generated holograms and a holographic method with an optoelectronic device", Optoelectronica, vol.2, No.3, pp. 53-58 (1994)
- [4]. Ristici M., Udrea M.V., Medianu R., Ristici I., Ciura A.I., "A small current He-Se laser", General Conference of the Balkan Physical Union BPU-2, Izmir, Turkey, September 12-14 (1994)
- [5]. Nicolau Silvia, Sporea D., Scarlat F., "Study of viscosimetric flow of polymers with an optoelectronic instrument controlled by computer", Anale. Univ. Buc. vol.44, No.2, pp 77-80 (1995)
- [6]. Nicolau Silvia, Levai S., "Sensitised photopolymerisation of acrylamide for holographic recordings" Anale. Univ. Buc. vol.44, No.1, pp. 63-70 (1995)
- [7]. Mitea Doina, Nicolau Silvia, Vasiliu V., Sporea D., Scarlat F., "Hologram recording media testing by X ray diffraction method with optoelectronic interface" Optoelectronica vol.3, No.4, pp. 37-40 (1995)
- [8]. I. Ristici, M. Ristici, Nicolau Silvia, "Low divergence convex-concave laser resonator", Optoelectronica vol.4, No.1, pp. 136-138 (1996)
- [9]. Nicolau Silvia, Scarlat F., Oproiu C., "Nondestructive testing of photopolymerisation effects with linear accelerator" Turkish Physical Society General Conference, Kas-Antalya, Turkey, September 25-29 (1995)
- [10]. Nicolau Silvia, Scarlat F., Ristici M., Oproiu C., Mitea Doina, "He-Se and accelerator applications to obtain solid polymers with improved properties", Particle Accelerator Conference and International Conference in High-Energy Accelerators, Dallas, USA, May 1-5, (1995)

Session A3

**OPTOELECTRONIC COMPONENTS.
ANALYSIS AND CONTROL METHODS**

INFLUENCE OF STRUCTURAL DEFECTS UPON THE PARAMETERS OF III-V p-i-n PHOTODIODES

V. Dorogan, V. Coseac, T. Vieru

Technical University of Moldova, Laboratory of Microelectronics,
bd. Stefan cel Mare 168, Chisinau MD2004, Moldova.
Phone 247143, Fax 237509.

ABSTRACT

An analysis of technological factors, determining the crystallographic perfection and electrophysical parameters of III-V semiconductor structures (GaAs, InP) and their solid solutions (AlGaAs, InGaAsP) formed by liquid phase epitaxy (LPE) is undertaken in the present paper. It is demonstrated that characteristic for LPE thermodynamic equilibrium between phases is the decisive factor in achieving high-quality structures. The influence of the substrate structural defects upon the epitaxy process was also studied. To accentuate their influence and to exclude other technological factors, the use of a superthin liquid phase with two-dimensional activity respecting substrate was proposed. A new visualize method of substrate's structural defects, which makes contact with heterostructure and determines the devices' dark currents, was proposed. Optimum technological conditions to achieve the InP-InGaAsP structures for p-i-n photodiodes are given.

1. INTRODUCTION

Photoreceivers covering a large spectral range, from ultraviolet to near infrared ($0.2 \leq \lambda \leq 3 \mu\text{m}$), are fabricated on the basis of III-V semiconductor compounds, especially on GaAs, InP, GaP and InAs. Heterostructures for the reception of optic radiation are formed based on the solid solutions of the above compounds. They possess performance parameters, characteristics optimized for different receiving conditions and novel functional possibilities. Of extreme interest are InP-InGaAs, InP-InGaAsP, GaAs-AlGaAs heterostructures which ensure an effective reception of radiation with wavelengths $\lambda = 0.86, 1.06, 1.3$ and $1.55 \mu\text{m}$ utilized for information transmission through atmosphere and optic fibers. Due to low difference between lattice constants, GaAs- $\text{Al}_x\text{Ga}_{1-x}\text{As}$ epitaxial structures with high crystallographic perfection in interval $0 \leq x \leq 0.9$ can be formed on GaAs substrate. Epitaxial layers on the basis of $\text{Ga}_{0.47}\text{In}_{0.53}\text{As}$ ternary compounds or $\text{Ga}_x\text{In}_{1-x}\text{As}_y\text{P}_{1-y}$ quaternary ones can be deposited on InP substrate. Lattice constants of InP and $\text{Ga}_x\text{In}_{1-x}\text{As}_y\text{P}_{1-y}$ are accorded at $y/x \approx 2.2$ [1]. Semiconductor heterostructures are prepared by different technological methods, the most important being: molecular-beam epitaxy, vapour phase epitaxy and liquid phase epitaxy. Due to thermodynamic equilibrium between solid and liquid phases, occurring automatically at their contact, LPE is the most preferable. This method is well-studied and is widely used for semiconductor devices manufacturing, particularly on the basis of III-V compounds and their solid solutions. Investigations in this field tend to determine the most important technological factors, which can improve crystallographic perfection of epitaxial structures and quality of devices made on these structures.

2. PHASES INTERACTION AND INFLUENCE OF LATTICE DEFECTS UPON THE EPITAXIAL GROWTH

One of the most important factors, allows the formation of epitaxial structures with high crystallographic perfection is the presence of thermodynamic equilibrium between phases. From this point of view, LPE is characterized by ideal conditions in case of non-doped layers autoepitaxy. But in this case equilibrium has to be disarranged for epitaxial growing. Programmed changing of thermodynamic equilibrium is as necessary for qualitative epitaxial layers deposition, as the existence of

this equilibrium at initial stage of epitaxial process.

In fact, it is difficult to talk about ideal equilibrium. Several causes to consider are:

- a) the presence of the third phase (vapor phase). Its influence is considerable when the liquid phase has a volatile component;
- b) the diffusion processes in liquid phase;
- c) the presence of uncontrollable (background) impurities in both phases;
- d) temperature gradients in liquid phase;
- e) lattice structural defects going out to the contact surface with the liquid phase.

All these factors, disarranging equilibrium between phases, generate a change of particles between solid and liquid phases to install the same thermodynamic equilibrium. As a result, solid substrate is non-uniformly dissolved, a variable composition layer appears at its surface and the liquid phase changes its composition. In our opinion, the solid phase structure, especially crystallographic structure of the growing surface, is of a primordial importance in the epitaxial growth process and in the creation of perfect structures forming.

Distribution of substrate's superficial energy (type and density of structural defects which go out to contact surface of liquid phase) can be the decisive factor in thin and superthin homo- and heterostructures forming. Crystal's superficial energy has also a great influence upon the selective local etching of crystal by liquid phase. This proceeding is widely used in laser diode technology [2].

Therefore, one of paper's purposes is to determine the factors, tied with substrate condition, influencing the epitaxial structures quality. To accentuate the superficial energy influence and to exclude the other factors, such as convection and diffusion in liquid phase bulk, we had used a liquid phase, with thickness equal to the diffusion length of components dissolved in it. Such a plane liquid phase with two-dimensional activity respecting substrate can ensure a pure kinetic regime which supposes the existence of thermodynamic equilibrium. GaAs(100) and InP(100) were used as crystals and the liquid phase (Ga or In) with thickness 1-10 μm was deposited onto substrates by vacuum thermal deposition. The sandwich, consisting of two substrates (GaAs or InP) and liquid phase between them, was thermal treated. At heating, the liquid phase was saturated dissolving substrate material, and at cooling, the dissolved material was deposited. Investigations showed that the plane liquid phase needs a small amount of material to be saturated, even at high temperatures $T \sim 900^\circ\text{C}$. In such conditions it becomes sensible to the non-homogeneous of the crystalline substrate's superficial energy distribution, i.e. to point defects, dislocations, microcracks etc. At heating, superficial defects become centers of crystal dissolution, and at cooling - domains of dissolved material deposition.

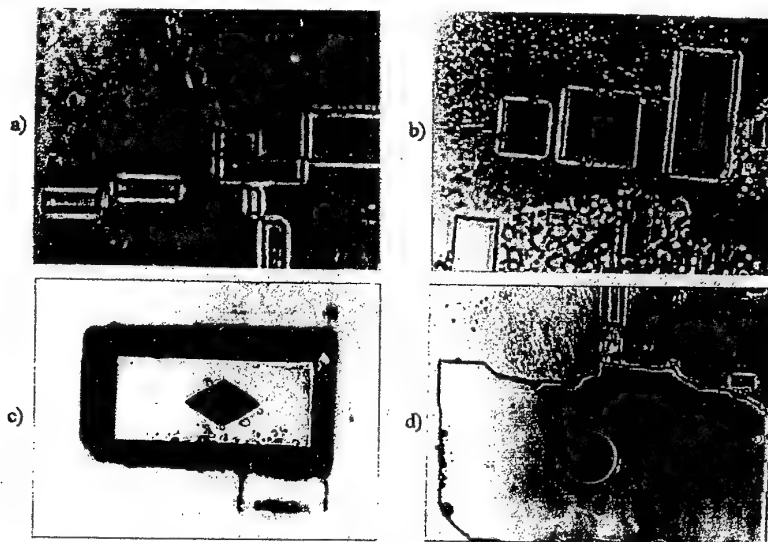


Fig.1 Superficial (a,b) and deep (c,d) structural defects emphasized by liquid phase with two-dimensional activity in etching-deposition process

In such conditions, when diffusion of liquid phase components in perpendicular to crystal surface direction is practically excluded, the etching and epitaxial deposition processes get distinctive aspects. The presence of structural defect (domain with major superficial energy) leads to substrate local etching. Dissolving substrate material in defect place, the liquid phase emphasizes crystallographic plans with minimal superficial energy and annihilates superficial defects [3].

When defects are two-dimensional and are localized at surface (point defects, microcracks, crystallographic steps), substrate etching is not deep. At cooling, the dissolved material is deposited in formed pits, and fills with keeping the substrate crystallographic direction. Fig.1a,b present the figures formed on superficial defects as a result of etching - epitaxial deposition process.

In the deep structural defects case, such as spiral dislocations, the etching process occurs at big depth. Crystallographic directions, emphasized after etching, with superficial energies less than the defect one, do not allow the full filling of the formed pit (Fig.1c,d). Investigations showed that the plane liquid phase remains selective respecting crystal for heating-cooling velocities of 20-30 °C/min. Thus, etching-deposition process occurs at the contact of the saturated liquid phase with the solid one. As a result, the distribution of substrate superficial energy becomes more uniform, but the substrate planarity disappears [4].

The selective etching of superficial defects can be suppressed by strong supersaturation of the liquid phase. In such conditions the lattice atoms become centres of epitaxial deposition and the principles of thermodynamics lose their influence. But this does not remove the influence of superficial structural defects. As a rule, they pass into epitaxial structure. It is reasonable to annihilate them by an etching-growth process, by forming an intermediate layer with uniform superficial energy. Investigations have permitted us to affirm that the presence of a non-uniform energetic field on the substrate surface has the following consequences for the epitaxial growth of crystalline layers:

- a) in near thermodynamic equilibrium conditions, i.e. at thin and superthin films forming, the lattice superficial defects brake the forming of a homogeneous and continuous epitaxial layer;
- b) to remove the defect influence, it is necessary to incline the thermodynamic equilibrium to epitaxial deposition, i.e. to supersaturate the liquid phase. It becomes extremely important in the growing of layers with different chemical composition, i.e. at heterostructures forming;
- c) to exclude the structural defects transfer from substrate to epitaxial structure, an intermediate-buffer layer is necessary. The superficial structural defects are etched and filled during the buffer layer forming.

3. TECHNOLOGICAL FACTORS DETERMINING THE QUALITY OF INP-INGAASP EPITAXIAL STRUCTURES

The manufacturing technology of p-i-n structures on the basis of InP - $\text{In}_{x1}\text{Ga}_{1-x1}\text{As}_{y1}\text{P}_{1-y1}$ and InP - $\text{In}_{x1}\text{Ga}_{1-x1}\text{As}_{y1}\text{P}_{1-y1}$ - $\text{In}_{x2}\text{Ga}_{1-x2}\text{As}_{y2}\text{P}_{1-y2}$ heterostructures, which can be optimized for radiation receiving in the spectral range $1 \leq \lambda \leq 1.65 \mu\text{m}$ has a particularity. The main criterion is the presence of 5-10 °C supersaturation to suppress the solid phase etching, caused by difference between phases' chemical potentials.

It was established that one of the most important factors, considerably decreasing the LPE efficiency, is the presence on InP substrate surface of own oxides and organic compounds, which do not permit the contact between the liquid and the solid phases. As a result, in the epitaxial layer there are discontinuities (Fig.2a & 2c), non-plane domains (Fig.2a & 2d), capture of liquid phase in epitaxial structure (Fig.2c) or shunting of p-n junction by substrate (Fig.2d & 2e).

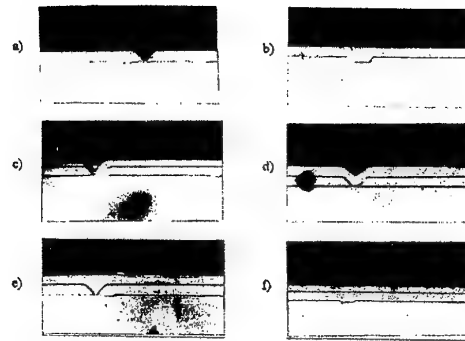


Fig.2 InP-InGaAsP structures with one (a,b) and two (c,d,e,f) epitaxial layers

The second important factor is the degradation of InP substrate surface at epitaxial process's temperature ($T = 650^{\circ}\text{C}$) caused by phosphorus volatilization. The splinter of i-InP - n-InGaAsP structure, oxidized by electrochemical method, is presented in Fig.3a. The semiconductor i-InP substrate does not conduct the current and, therefore, it is not oxidized. A blue own oxide film was formed on n-InGaAsP epitaxial layer. A non-uniform layer, which had lost its insulating properties, was created between the epitaxial layer and the i-InP substrate. The oxide formed on this layer was deep blue. It was established that the substrate's degradation degree is higher in emergence places of structural defects to substrate surface, because they are characterized by major superficial energy (Fig.3b).

The electrochemical oxidation method had permitted us to visualize for the first time the bulk structural defects, which make contact with epitaxial structure, continue in it and, therefore, are responsible for current and for conversion efficiency of optic radiation in photodiodes.

Some tracing methods of superficial structural defects are available. They consist in studying the substrate surface's photoluminescence process [5,6]. Photoluminescence is missing in the place where defect emerges to surface. Methods priority consists in their express and indistructive character. But these methods do not provide any information about the defect form, placing depth, their nature.

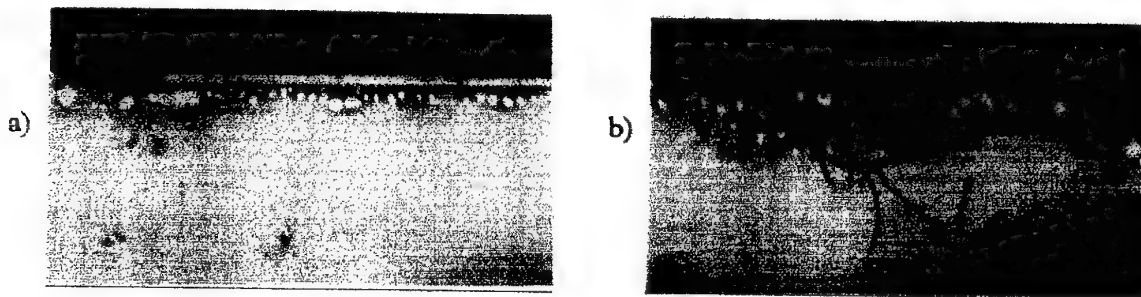


Fig.3 Splinters of electrochemically oxidized i-InP - n-InGaAsP structures

We propose a method which consists in growing a n- or p-type layer on semiinsulating substrate by epitaxial method. Structure is splintered and the splinter is anodic oxidized at voltage $U > 100 \text{ V}$. The epitaxial layer is oxidized forming an oxide film with different thickness and colour in dependence on the applied voltage. The i-type substrate does not conduct electrical current and, therefore, it is not oxidized. Deep structural defects, which make contact with splinter's surface and with epitaxial layer, are oxidized in splinter's plan. Having a low electrical resistance in comparison to the i-substrate, they create channels of current leaking. The splinter of electrochemically oxidized i-InP - n-InGaAsP structure and its schematic view are presented in Fig.4.

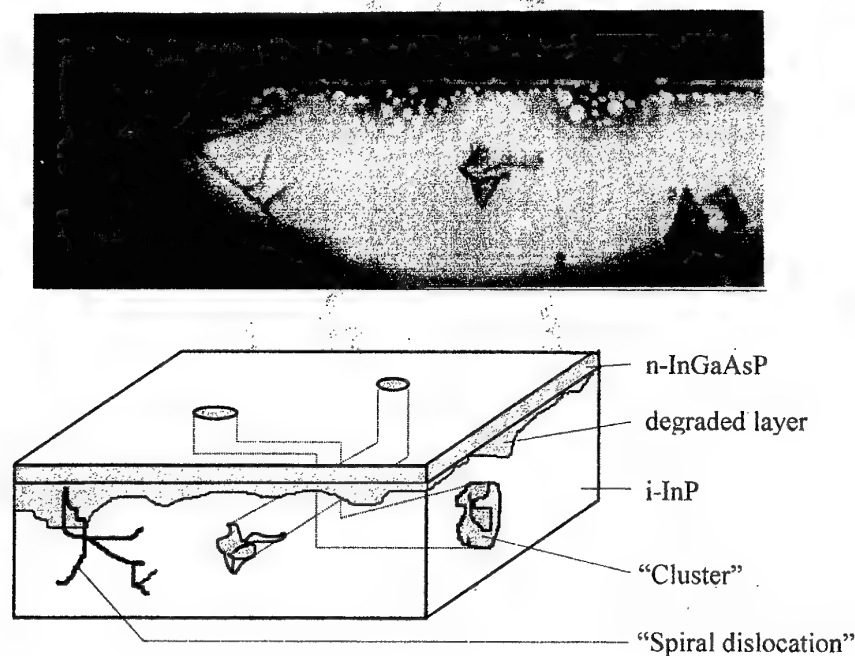


Fig.4 Photograph and scheme of i-InP - n-InGaAsP structure with structural defects visualized by electrochemical method

The defects can be divided in some categories:

- ramified defects of "spiral dislocations" type;
- bulk defects of "cluster" type with size $\sim 30 \mu\text{m}$;
- defects of "Schottky" and "Frenkel" type formed due to phosphorus volatilization.

Investigations had permitted us to conclude that the perfection of InP-InGaAsP epitaxial structures greatly depends on presence of structural defects, coming into contact with growing surface of InP substrate. This influence is manifested in the following:

a) thermodynamic equilibrium between liquid and solid phases, which must be respected in isothermic conditions, is not maintained in the place where structural defects emerge to substrate surface. This causes the substrate local dissolving by liquid phase and a non-plane epitaxial layer forming;

b) deep structural defects can continue also in epitaxial structure, forming channels with low resistivity. Therefore, dark currents in epitaxial structures increase suddenly and even p-n junction is shunted;

c) during p-n junction forming by diffusion method, the diffusant has a much higher diffusion velocity in structural defects region. This does not permit p-n junction exactly placing, destroys junction planarity and creates domains with low break voltage;

d) intensive volatilization of phosphorus from substrate defective surface generates the forming of indium microdrops, which, coming into contact with liquid phase, changes its composition. As a result, the epitaxial layer changes its stoichiometry and crystallographic perfection. This causes the layer's bad morphology (Fig.5) and quick degradation of epitaxial layers electrophysical properties.

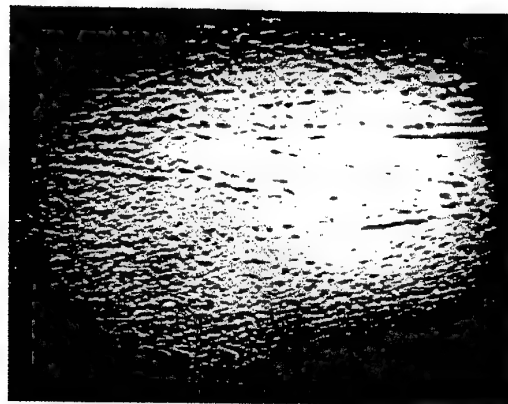


Fig.5 Morphology of InGaAsP layer with disarranged stoichiometry

4. OPTIMIZATION OF INP-INGAASP HETEROSTRUCTURES GROWING TECHNOLOGY

We have established that factors determining the epitaxial structure quality are: substrate disorientation, absence of contact between phases, substrate degradation under temperature influence and existence of structural defects in substrate.

Besides classical methods of organic compounds and oxides removing from substrate surface, such as degreasing in organic dissolvents and oxides dissolution in chemical compounds, we have utilized the semiconductor substrate etching by a non-saturated liquid phase. The liquid phase non-saturation degree must ensure the non-selective etching of solid phase. The substrate etching process was carried out in graphite crucibles, in liquid phase on the basis of In and directly before the start of the epitaxial deposition process. This permitted us not only to dissolve the oxides from substrate growing surface, but also to remove the degraded by phosphorus volatilization layer. To reduce the substrate erosion, homogenization and thermic treatment of liquid phases and substrates were made separately. Moreover, before structure forming a buffer-layer was grown on substrate in conditions ensuring the prevalence of deposition's velocity tangential component upon the normal one. Thus, the growing epitaxial layer gets possibility to fill surface defects etched by liquid phase (Fig.2b). To ensure a tangential growing velocity higher than the normal one, we have observed the following conditions:

a) use of InP substrates with crystallographic orientation (100), since, as a rule, crystallographic directions with higher indexes have a higher growing velocity (Fig.2b);

b) use of minimal velocities of liquid phase cooling ($V_{cool} \sim 0.1$ °C/min). Fig.2e shows that for the first epitaxial layer, grown in liquid phase supercooling conditions, the growing velocity normal component is higher than the tangential one. For the second layer, grown with $V_{cool} = 0.1$ °C/min, the tangential component prevails. This permits to ensure the structure's planarity. Fig.2d shows the epitaxial structure grown with $V_{cool} > 1.5$ °C/min. One can see that tangential growing velocity is much lower;

c) before the start of the epitaxial process, etching the substrate in a non-saturated liquid phase is required. Besides removing the degraded superficial layer, this allows the formation of some steps serving as crystallization centres [7].

Besides crystallographic perfection the efficiency of semiconductor photoreceivers is determined also by layers' doping level, i.e. by concentration and mobility of free charge carriers. In order to obtain photodiodes with low dark currents, high break voltages, minimal capacity and maximal thickness of space charge region, the concentration of free charge carriers must not exceed $10^{14} - 5 \cdot 10^{15} \text{ cm}^{-3}$ [8]. As a rule, the impurities background concentration in InGaAsP epitaxial layers is $(5-8) \cdot 10^{17} \text{ cm}^{-3}$. The influence of hydrogen and materials purity, of thermal treatment temperature and time upon the uncontrollable impurities concentration was studied in order to optimize the manufacturing technology of p-i-n photodiodes. Investigations showed that to reduce impurities background concentration below 10^{17}

cm^{-3} , requires a thermal treatment of In metal-dissolvent ($t = 20$ h, $T = 1000^\circ\text{C}$) and of liquid phases ($t = 1-2$ h, $T = 700^\circ\text{C}$). This permits to decrease impurities concentration up to $2 \cdot 10^{15} \text{ cm}^{-3}$, but increases the compensation level and, therefore, increases the mobility of free charge carriers.

The use of rare elements, such as Gd, Yb, Tb, Dy, Y, for doping the liquid phase proved to be more effective. The best results were achieved using yttrium (Y). Mechanism of liquid phase purification by Y doping is summarized below. Being a chemical active element, yttrium gathers uncontrollable impurities from liquid phase and fastens them in to inert conglomerates. Thus, the segregation coefficient of background impurities greatly decreases. We have to mention that yttrium utilization for liquid phases purification is efficacious only in complex with preliminary thermal treatment of metal-dissolvent and saturated liquid phases. Parameters of InGaAsP layers with $E_{g1} = 1.12$ eV and $E_{g2} = 1.18$ eV are presented in the table [9].

No. of series	E_g of InGaAsP layer, eV	Mass of Y in liquid phase, mg/g	Multiplicity of thermal treatment cycles	Concentration of free charge carriers, cm^{-3}	Mobility of electrons (holes), $\text{cm}^2 \cdot \text{V}^{-1} \cdot \text{s}^{-1}$
1	1.12	0	1	(n) $8 \cdot 10^{17}$	1500
2	1.12	0	2	(n) $3.5 \cdot 10^{17}$	2000
3	1.12	0	3	(n) $5 \cdot 10^{17}$	1400
1	1.18	0	1	(n) $6 \cdot 10^{17}$	1600
2	1.18	0	2	(n) $5 \cdot 10^{17}$	1700
3	1.18	0	3	(n) $6.5 \cdot 10^{17}$	1200
10	1.12	0.12	1	(n) $3 \cdot 10^{17}$	3700
11	1.12	0.12	2	(n) $2 \cdot 10^{17}$	2100
12	1.12	0.12	3	(n) $5 \cdot 10^{16}$	1900
10	1.18	0.096	1	(n) $5 \cdot 10^{16}$	1500
11	1.18	0.096	2	(n) $1 \cdot 10^{16}$	1300
12	1.18	0.096	3	(n) $8 \cdot 10^{14}$	900
14	1.12	0.35	2	(n) $1 \cdot 10^{17}$	1500
15	1.12	0.35	3	(n) $1 \cdot 10^{16}$	1300
14	1.18	0.28	2	(n) $4 \cdot 10^{15}$	1300
15	1.18	0.28	3	(p) $5 \cdot 10^{14}$	30
22	1.12	0.19	4	(n) $4 \cdot 10^{16}$	1800
27	1.12	0.19	5	(p) $1 \cdot 10^{15}$	50

Analyzing the results of doping the liquid phase by Y, we can conclude that:

- a) the background concentration of electric active impurities decreases up to $n_i = 10^{15} \text{ cm}^{-3}$ when Y mass increases in liquid phase (in certain limits);
- b) multiple thermal treatment of Y-doped liquid phase reduces the uncontrollable impurities concentration and can invert the conductivity type in epitaxial layers;
- c) the mobility of charge carriers in epitaxial layers decreases with increasing Y concentration in liquid phase;
- d) the lower the initial concentration of background impurities (without Y) is, the lower the probability of conductivity inversion from "n" to "p" in epitaxial layers.

5. CONCLUSIONS

Our investigations showed that liquid phase epitaxy permits the formation of III-V semiconductor structures with high crystallographic perfection. The technological factor determining this perfection is the presence of thermodynamic equilibrium between solid and liquid phases. The new

proposed method of visualizing structural defects allows to trace the most important defects determining the epitaxial structure quality. They are: oxides on substrate surface, deep structural defects going out to contact surface with liquid phase, the layer degraded by V-component volatilization, the presence of uncontrollable impurities with high segregation coefficient. It was established that the influence of lattice structural defects can be minimized by forming a buffer-layer, which heals the deep structural defects responsible for currents in semiconductor structures. The use in liquid phase of added rare elements (Y) permits to reduce background concentration, to form non-doped layers and to manufacture p-i-n structures for photodiodes.

6. REFERENCES

- [1]. Tsang U. Tehnika opticheskoy svyazi. Fotopriyomniki. / M. Mir (1988).
- [2]. Buda M., Cotirlan C., Girtu M., Petrescu-Prahova I. Corodarea GaAs in solutie de Al in Ga. / 14th Annual Semiconductor Conf. (CAS'91). - Sinaia, Romania, P.339-342 (1991).
- [3]. Radautsan S., Dorogan V., Charyev Ya. Vlianie defektov podlojki na formirovanie tonkih plynok fotopreobrazovatelnyh struktur. / IV Int. Conf. "Fizika i tehnologia tonkih plynok". - Ivano-Frankovsk, Ukraina, P.370 (1993).
- [4]. Dorogan V., Kosyak V. Study of crystal surface energy influence on the kinetics of epitaxial layers growth. / 17th Ed. of Annual Semiconductor Conf. (CAS'94). - Sinaia, Romania, Oct. 11-16, V.2, P.577-580 (1994).
- [5]. Colbourne P.D., Cassidy D.T. Dislocation detection using polarization-resolved photoluminescence. / Can. J. Phys. - V.70, No.10-11, P.803-812 (1992).
- [6]. Carver G.E., Moore R.D., Trapp K.D., Kahora P.M., Stevie F.A. Detection of compositional non-uniformities in InP:Fe via spatially resolved photoluminescence and secondary ion mass spectrometry. / 2nd Int. Conf. Indium Phosphide and Related Materials. - Denver, Colo, Apr.23-25, P.428-434 (1990).
- [7]. Kanaya H., Usuda K., Yamada K. Examination of Si(100) surfaces treated by ultrapure water with 5ppb dissolved oxygen concentration. / Appl. Phys. Lett. - V.67, No.5, P.682-684 (1995).
- [8]. Sloan S.R. Processing and passivation techniques for fabrication on high-speed InP/InGaAs/InP mesa photodetectors. / Hewlett-Pack J. - V.40, No.5, P.69-75 (1989).
- [9]. Samusi I., Dorogan V. et all. Factors determining the quality and reliability of InP-InGaAsP epitaxial structures. / Int. Conf. on Microelectronics and Computer Science (ICMCS'97). - Chisinau, Moldova, P.25-28 (1997).

MODELING THE OPTICAL AMPLIFICATION OF $\text{Er}^{3+}:\text{Ti:LiNbO}_3$ CURVED WAVEGUIDE AMPLIFIERS

N. N. Puscas, B. Wacogne*, A. Ducariu, B. Grappe*, I. M. Popescu

Physics Department, University "Politehnica" Bucharest, Splaiul Independentei 313, 77206, Bucharest, Romania, phone: 004014104542, fax: 004013125365, e-mail: pnt@physics2.physics.pub.ro

* Laboratoire d'Optique P. M. Duffieux, URA CNRS 214, UFR Sciences et Techniques Université de Franche-Comté, 25030 Besançon Cedex, France, phone: 33(0)381666563, fax: 33(0)381666423, e-mail: bruno.wacogne@univ-fcomte.fr

ABSTRACT

In this paper, we present the derivation and the evaluation of the spectral optical dependence of the gain and quality factors which characterize the behaviour of a curved Er^{3+} doped LiNbO_3 curved amplifier. Simulations are performed under the small gain approximation, for a pumping wavelength of 1484 nm, various pumping regimes, and Er^{3+} concentration profiles.

1. INTRODUCTION

Over the last years, various theoretical and experimental studies concerning the reduction of the propagation losses in Ti:LiNbO_3 waveguides have been reported [1, 2]. Nowadays, a commonly used technique to obtain lossless components is to perform optical amplification in an Er^{3+} -doped LiNbO_3 crystal. The study of the spectral distribution of the gain and the quality factor defined as the ratio between the gain and noise figure plays an important role in obtaining amplifiers having low noise and high optical gain. In this paper, we present the derivation and the evaluation (in the small gain approximation) of the spectral optical dependence of the gain and quality factor which characterize an Er^{3+} -doped LiNbO_3 curved waveguide amplifier pumped near 1484 nm in the unsaturated regime, and also their evolution under various pumping regimes, waveguide lengths, for both TE and TM polarizations, and several Er^{3+} concentration profiles.

In Sec. 2 we present the basic equations which describe the optical amplification in straight waveguides, and a theoretical study of the spectral distribution of the above mentioned parameters. Sect. 3 is devoted to the optical profiles in the curved waveguide, and Sect. 4 to the discussion of the simulation results.

2. SPECTRAL NOISE ANALYSIS IN STRAIGHT WAVEGUIDE AMPLIFIERS

In order to evaluate the noise characteristics of "z" propagating Er^{3+} -doped LiNbO_3 waveguide amplifiers, we consider a quasi two level system model, and we neglect excited state absorption due to the considered pumping wavelength. Based on the model presented in papers [3, 4], we calculate the net gain, $G(L, \nu)$, and the noise figure $F(L, \nu)$ at the output of the amplifier in the form:

$$G(L, \nu) = \exp \left\{ \int_0^L [\gamma_e(z', \nu) - \gamma_a(z', \nu) - \alpha(\nu)] dz' \right\} \quad (1)$$

$$F(L, \nu) = \frac{1 + 2G(L, \nu) \int_0^L \frac{\gamma_e(z', \nu)}{G(z', \nu)} dz'}{G(L, \nu)} \quad (2)$$

where:

$$\gamma_e = \gamma_e(z, \nu) = \sigma_e(\nu) \int_A N_2(x, y, z) i_m(x, y) dx dy, \quad \gamma_a = \gamma_a(z, \nu) = \sigma_a(\nu) \int_A N_1(x, y, z) i_m(x, y) dx dy \quad (3)$$

" m " corresponds to different polarisation states: TM and TE for waves polarised along the " x " and " y " axis respectively, σ_a and σ_e stand for the absorption (a) and the emission (e) cross sections, respectively, $i_m(x, y)$ is the normalized optical mode profile, A is the waveguide cross section, α_{km} represents the optical losses, $N_{1,2}(x, y, z)$ are the populations of the ground and excited state, respectively. The Er-dopant concentration is $N_T(x, y) = N_1(x, y, z) + N_2(x, y, z)$, and can be written in terms of surface concentration N_{T_0} and normalised dopant distribution $d(x, y)$. Therefore: $N_T(x, y) = N_{T_0}d(x, y)$ with $N_{T_0} = N_T(0, 0)$ and $d(0, 0) = 1$.

As a measure of the gain and the noise characteristics at the output of the waveguide amplifiers, we adopt a quality factor, $Q(L, \nu)$, defined as the ratio between the gain and the noise figure:

$$Q(L, \nu) = \frac{G(L, \nu)}{F(L, \nu)} = \frac{G^2(L, \nu)}{1 + 2G(L, \nu) \int_0^L \frac{\gamma_e(z', \nu)}{G(z', \nu)} dz'} \quad (4)$$

3. OPTICAL PROFILES IN THE CURVED WAVEGUIDE

In order to evaluate the refractive index profile and the optical mode profile in the curved waveguide, we slice the amplifier in elementary portions, each of them being considered straight, and tilted at an angle θ with respect to the " z " axis (see Fig. 1 (a)). At each propagation step (corresponding to a particular angle θ), and for both TM and TE polarisations, we calculate the refractive index profiles using the Fick's diffusion law. For TM polarised waves (oriented along the " x " axis), only the ordinary refractive index is concerned. Therefore, the refractive index profile does not depend on the angle θ and it is given by:

$$n(x, y') = n_0 + \Delta n_0 \exp\left(-\frac{x^2}{a^2}\right) \left\{ \operatorname{erf}\left(\frac{w + 2y'}{a}\right) + \operatorname{erf}\left(\frac{w - 2y'}{a}\right) \right\} \quad (5)$$

where n_0 is the ordinary refractive index, Δn_0 is the surface refractive index variation due to the Ti diffusion, w is the waveguide width, a is a parameter which depends on the diffusion conditions, and y' is the transverse coordinate of the tilted waveguide as seen from Fig. 1 (a).

On the contrary, for TE polarised waves (oriented along the " y' " axis), the refractive index profile involves both the ordinary and the extraordinary indices, and it does depend on the angle θ . It is given by:

$$n(x, y', \theta) = n_s(\theta) + \Delta n(\theta) \exp\left(-\frac{x^2}{a^2}\right) \left\{ \operatorname{erf}\left(\frac{w + 2y'}{a}\right) + \operatorname{erf}\left(\frac{w - 2y'}{a}\right) \right\} \quad (6)$$

where

$$\Delta n(\theta) = \frac{n_0^3 \Delta n_e \sin^2 \theta + n_e^3 \Delta n_0 \cos^2 \theta}{(n_e^2 \cos^2 \theta + n_0^2 \sin^2 \theta)^{3/2}}, \quad n_s(\theta) = \frac{n_0 n_e}{(n_e^2 \cos^2 \theta + n_0^2 \sin^2 \theta)^{1/2}} \quad (7)$$

In order to account for the waveguide curvature, we refer to Fig. 1 (b). In a curved waveguide, the inner part of the wavefront propagates over a shorter distance than its outer part. For the light, it looks as if the refractive index was lower in the inner part than in the outer part of the waveguide. This can be accounted for in the expression of the refractive index profile by using the following conform transformation:

$$n_e(x, y') = n(x, y') \left(1 + \frac{y' - R}{R} \right) \quad (8)$$

where R is the radius of curvature of the waveguide. Once the refractive index profile is calculated, the effective index method is used to compute the profile of the optical modes [5].

4. DISCUSSION OF THE SIMULATION RESULTS

The simulation of the optical amplification in Er^{3+} -doped LiNbO_3 waveguide has been performed using parameters obtained from literature [3, 4]. We numerically calculated the spectral dependence of the gain (Eq. 1), and quality factor (Eq. 4) for the optical amplifier with signal and pump wavelengths at 1531 nm and 1484 nm, respectively.

The Er-profile has been considered erfc, Gaussian or constant in depth and Gaussian in width. These profiles correspond to different diffusion conditions or crystal fabrications. An erfc profile is obtained when the diffusion of the Er ions is not completed, while a Gaussian profile corresponds to case where all the Er ions have diffused into the crystal. The last case (constant in depth) corresponds to the case where the crystal is doped with Er during the growth process. An Er surface concentration of about $1 \times 10^{26} \text{ m}^{-3}$, and a diffusion depth of $20 \mu\text{m}$ have been considered. The radius of curvature of the waveguide is $R = 5 \text{ cm}$, and its length is 2.5 cm .

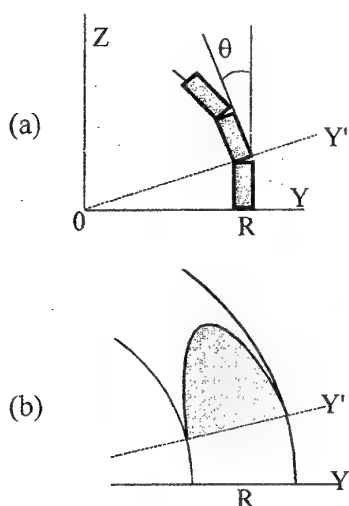


Fig. 1

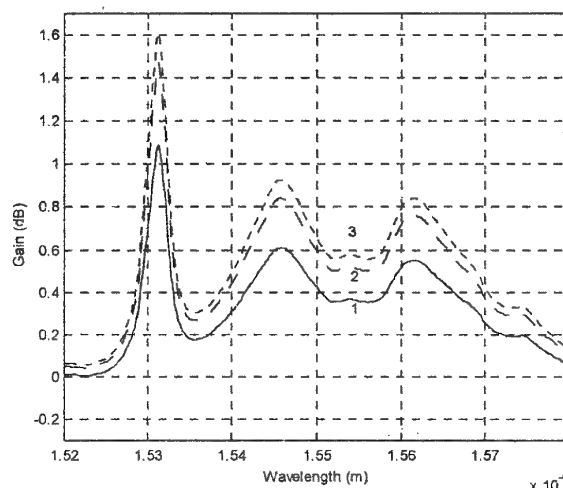


Fig.2

Fig.2 presents the evolution of the gain spectra, for input pump powers of 150 mW (high pump regime) and $1 \mu\text{W}$ for signal in TE polarization. We obtained the following values for the gain at $\lambda = 1.5312 \mu\text{m}$: 1.08 dB for erfc, 1.45 dB for Gaussian and 1.6 dB for constant depth profile of Er, respectively (curves 1, 2, 3). The highest values of the quality factor were obtained for an erfc profile at $\lambda = 1.5312 \mu\text{m}$. However, the noise figure at this wavelength is large ($F=2.31$ for $P=25 \text{ mW}$ and $F=2.49$ for $P=150 \text{ mW}$), which implies quite low values for the quality factor (Fig. 3) ($Q=-1.21$ for $P=25 \text{ mW}$ (curve a) and $Q=-1.21$ for $P=150 \text{ mW}$ (curve b)). In the case of an erfc profile, the variations of the quality factor with the waveguide length and the pump power are presented in Figs 4 (curves a, b for $P=25 \text{ mW}$, 150 mW) and 5 (curve a, b for TE, TM polarization), respectively. One of the conclusions to be drawn from these figures concerns the possibility of obtaining high quality factors. Indeed, for similar amplification performances, it is preferable to increase the pump power that the waveguide length.

5. CONCLUSIONS

In this theoretical analysis we demonstrated that for an Er^{3+} -doped LiNbO_3 curved waveguide amplifier pumped at 1484 nm, high gains, low noise figures and high quality factors can be achieved in high pump regimes and for erfc dopant profile.

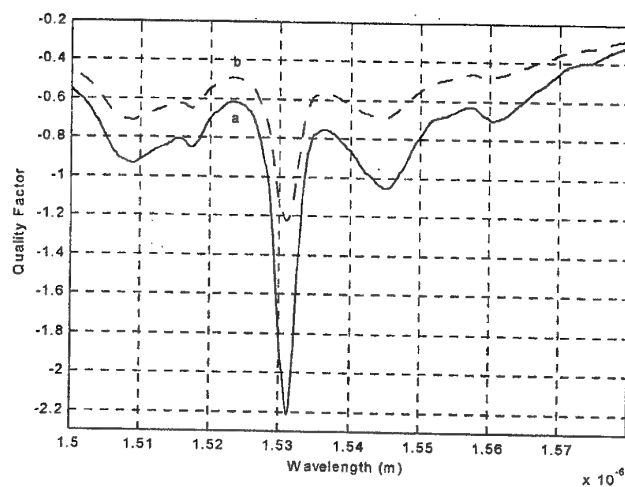


Fig. 3

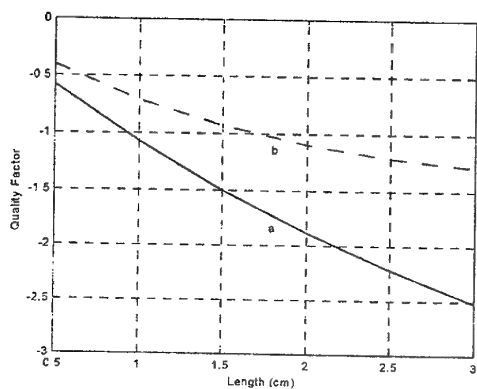


Fig. 4

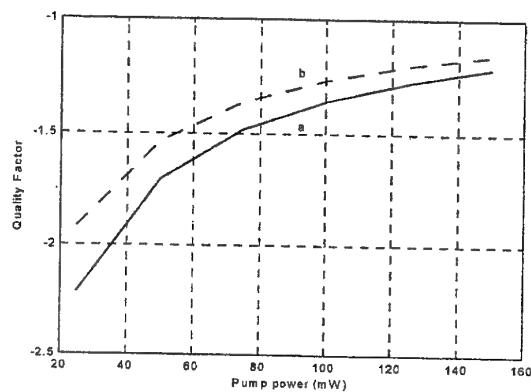


Fig. 5

ACKNOWLEDGEMENTS

This research was partially performed under contract ERBIC 15 CT 960820 of the European Commission.

6. REFERENCES

- [1]. Mansour I. and Caccavale F., *Applied Optics*, Vol. 35, 1492-1498 (1996).
- [2]. Majd M., Schüppert B. and Petermann K., *IEEE Photon. Technol. Lett.*, Vol. 5, 806-808 (1993).
- [3]. Desurvire E., *Erbium-Doped Fiber Amplifiers*, J. Wiley & Sons, Inc. New York (1994).
- [4]. Puscas N. N., Girardi R., Scarano D. and Montrosset I., *J. Mod. Optics*, Vol. 45, 847-859 (1998).
- [5]. Hocker G. B. and Burns W. K., *Applied Optics*, 16 113-120 (1977).

HIGH FREQUENCY TRANSMISSION IN A DISPERSIVE FIBER USING A MULTI LONGITUDINAL MODE LASER DIODE

P. Mollier, C. Gutierrez-Martinez*, H. Porte,
Barbara Sanchez-Rinza*, J.P. Goedgebuer

GTL-CNRS TELECOM, UMR CNRS 6603, 2-3, rue Marconi, 57070 Metz Cedex
Permanent address : Laboratoire d'Optique P.M. Duffieux - 25 030 Besançon cedex- FRANCE
Tel : 33 3 8166 6424 Fax : 33 3 8166 6423. email : pascal.mollier@univ-fcomte.fr
* INAOE - Coordination de Optica - 72 000 PUEBLA. PUE. MEXICO

1. INTRODUCTION

The chromatic dispersion in optical fiber is a physical phenomenon which limits the bandwidth of the fiber optic communication system. Thus, the spectral properties of the optical source are important restrictive parameters. It is generally admitted that the bandwidth of a communication system is inversely proportional to the spectral width of the used optical source. For few years, the use of optical source with a narrow spectral linewidth, DBR laser for example, have been allowing an important increase of the transmission bandwidth. In this paper, we show that the use of a multimode laser diode associated with a dispersive optical fiber allows an optical transmission at a sub-carrier frequency higher than the frequency cut-off generally admitted in the case of a broadband source.

2. MODEL AND PRINCIPLE OF OPERATION

The optical fiber communication system model is represented on figure 1. We consider an Optical Source (OS), a laser diode for example, which amplitude spectral density is $E(\omega - \omega_0)$, ω_0 is the central angular frequency of the diode spectrum. The optical beam is intensity modulated via an external Optical Modulator (OM) to avoid a chirp effect. $S(\Omega)$ is the modulating signal (Ω is the angular frequency of the electrical signal applied to the modulator). The modulated optical signal is launched into a dispersive monomode optical fiber which length is L . The fiber is also characterized by the propagation constant β of the propagated mode. At the output of the fiber, the transmitted optical power, $P(\Omega)$, is detected.

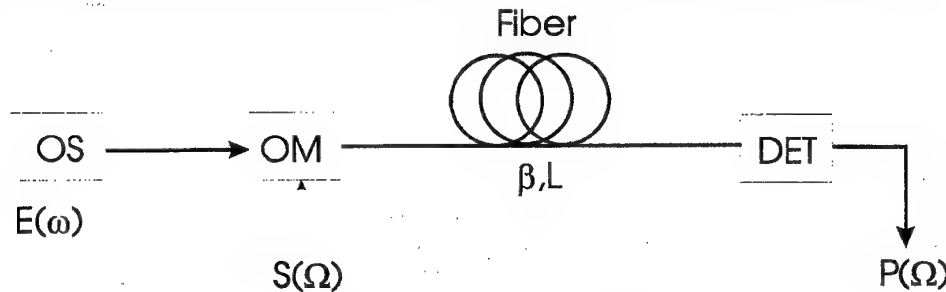


Fig. 1 Communication system model

The amplitude spectrum of the transmitted optical signal is :

$$E_T(\omega) = E(\omega - \omega_0) * S(\Omega).H(L, \beta, \omega) \quad (1)$$

$H(L, \beta, \omega)$ is the transfer function of the optical fiber and $*$ denotes convolution. The transmitted optical power, $P(\Omega)$, is proportional to the integral of the square of the transmitted amplitude spectral density and can be expressed as :

$$P(L, \Omega) \propto \int [E(\omega - \omega_0) * S(\Omega).H(L, \beta, \omega)]^2 d\omega \quad (2)$$

To introduce the chromatic dispersion effect, β can be expand as a second order Taylor series

around ω_0 . From equation (2), we can demonstrate that the transmitted optical power, $P(\Omega)$, is proportional to the Fourier Transform of the power spectral density of the optical source. The reciprocal variable of $(\omega - \omega_0)$ is $\beta''L$. β'' is the second order term of the Taylor series and represents the chromatic dispersion : $\beta'' = \left[\frac{d\beta}{d\omega} \right]_{\omega=\omega_0} = -\frac{\lambda^2}{2\pi c} M$, M is the chromatic dispersion factor (ps/nm.km). From the function $P(\Omega)$ representing the optical power at the output of the optical fiber versus the angular frequency modulation, we can deduce the frequency cut-off. Its expression is $f_c = \frac{1}{\Delta\lambda LM}$, $\Delta\lambda$ is the width of the power spectral density of the source [2]. In this paper we show that the periodic spectrum of the multimode laser diode allows a transmission at a frequency which is $f = \frac{1}{\delta\lambda LM}$, $\delta\lambda$ is the free spectral range between two longitudinal adjacent modes. This frequency is higher than the frequency cut-off generally admitted with a broadband source. The dispersive medium can be considered as a Fourier transformer. An appropriate filtering allows an optical transmission on any sub-carrier.

3. EXPERIMENTAL RESULTS

The experimental set-up is represented on figure 2.

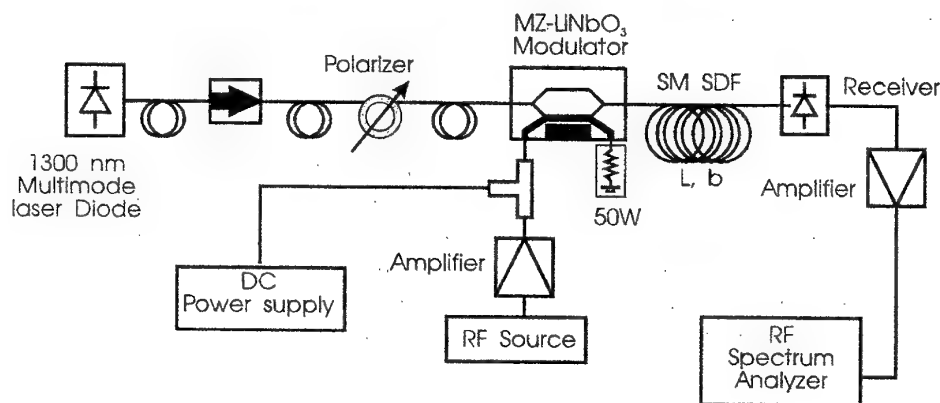


Fig. 2 Experimental set-up

The optical source is a 40 mW Fabry-Perot (FP) laser diode which central wavelength $\lambda_0 = 1300$ nm and which spectral width of $\Delta\lambda = 6.7$ nm. The free spectral range between two adjacent longitudinal mode is $\delta\lambda = 0.33$ nm. An optical isolator and a fiber polarizer are connected in tandem behind the FP laser diode. The fiber polarizer is used to excite the TM mode of an Intensity Modulator integrated in Z-cut lithium niobate substrate. The component is a symmetrical Mach-Zehnder Interferometer (MZI), each straight arms of the MZI have a length of 10 mm, and is designed with travelling-wave electrodes on only one arm. The modulator is driven by a sinusoidal voltage with a frequency ranging between 10 MHz and 10 GHz. A DC voltage is also applied to the modulator for adjusting the operating point. The modulated optical signal is transmitted through a Dispersion Shifted optical Fiber (DSF). The chromatic dispersion of the fiber is given by the factor dispersion: $M = -20$ ps/nm/km, at $\lambda_0 = 1300$ nm. The length of the fiber is $L = 20$ km. At the end of the fiber, a direct detection is used. The detected signal is amplified before to be analyzed with an electrical spectrum analyzer.

The electro-optic response of the optical transmission system is represented on figure 3.

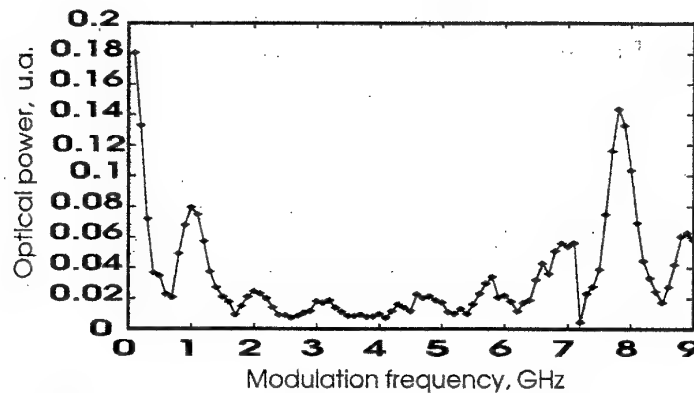


Fig. 3 Electro-optique response of the transmission system

From the width of the central peak at -3dB , we can deduce the bandwidth of a communication system, which is generally admitted in the case of a broadband source which spectral width is $\Delta\lambda$. This bandwidth is $f_c = 350\text{ MHz}$. At higher frequency, a satellite peak, occurs at a frequency $f = 7.9\text{GHz}$ with an attenuation of -1 dB compared with the maximum of transmission at low frequency. The Full Width at Half Maximum (FWHM) of this peak is 700 MHz . This peak is centered at a frequency corresponding to $f = 1/LM\delta\lambda$ which is related to the distance between adjacent longitudinal modes of the FP laser diode. Thus, the use of a multimode laser diode allows an optical transmission at a frequency higher than in the case of broadband source.

According the theoretical model the frequency response of the communication system corresponds to the Fourier transform of power spectral density of the optical. This response can be compared with the autocorrelation function of the laser diode beam. Experimentally, the autocorrelation function is implemented using a scanning Michelson interferometer. The laser diode beam is collimated and launched in a Michelson interferometer. An optical power detector set at the output of the Michelson interferometer is connected to a plotter. The autocorrelation function thus obtained is represented on figure 4.

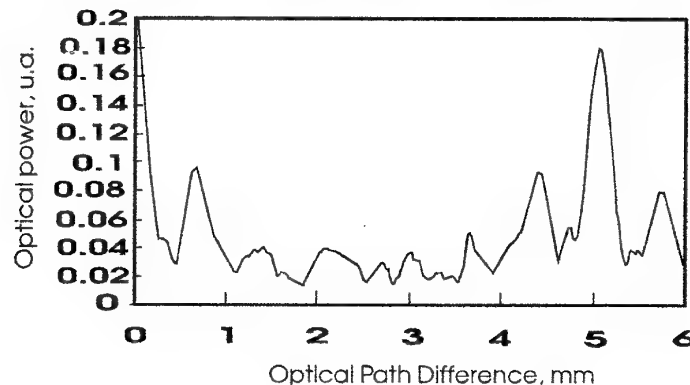


Fig. 4 Shape of the experimental autocorrelation function of the laser diode beam

The optical path difference corresponding to the half width at middle high of the central fringes is $\delta = 250\mu\text{m}$, which corresponds to a spectral width of $\Delta\lambda = 6.7\text{ nm}$ in the density spectral power of the optical source. The presence of an important satellite fringes located at $\delta = 5\text{ mm}$ corresponds to a free spectral range of $\delta\lambda = 0.33\text{ nm}$ which is the distance between two adjacent modes. These results are in good agreement with the spectrum measured by the use of an optical spectrum analyzer. The autocorrelation function which is given by the Fourier transform of the power spectrum of the source has a shape identical to the electro-optic response of the transmission system (compare figure 3 and figure 4). The experimental results are in good concordance with the theoritical model. The periodic spectrum of

the multimode laser diode allows a transmission at a higher than the frequency cut-off generally admitted with a broadband source. The dispersive medium can be considered as a Fourier transformer.

4. CONCLUSION

In this paper we reported a long distance transmission at high frequency in a dispersive optical fiber using a broadband source. The multi-longitudinal mode structure of the laser diode spectrums allows us to overcome the classical bandwidth cut-off generally admitted with such a broadband source. We conclude that a band pass transmission at any frequency carriers is possible in a long distance fiber. A broadband source coupled with a specially designed filters or a multimode laser diode can be used.

ACKNOWLEDGMENT

This work was supported by the Centre national de la Recherche Scientifique (CNRS), an ECOS program (collaboration between France and Mexico n° M97E01) and the CONACYT.

5. REFERENCES

- [1]. G.H. Smith, D. Novak, Z. Ahmed, *IEEE Transactions on Microwave Theory and techniques*, Vol. 45. N° 8, pp.1410-1415, (1997).
- [2]. Y.C. Tong, L.Y. Chang, H.K. Tsang, *Electronics Letters*, Vol. 33., N° 11, pp. 983-985, (1997).

LIQUID CRYSTALS REFRACTIVE INDEX MEASUREMENTS BY INTERFEROMETRIC METHOD

Cristina Sarpe-Tudoran, Marcela Ursache, Liana Socaciu, Violeta Calian, C. Sarpe-Tudoran

University of Craiova, Department of Physics,
13, A.I. Cuza, Craiova

ABSTRACT

A Talbot-Rayleigh type refractometer based on the analysis of the channelled diffraction spectrum observed in the focal plane of a spectroscope illuminated with a white light source where the sample under study is properly inserted is presented. The dispersion curve of both ordinary and extraordinary indices for a liquid crystal material is determined. Using a new configuration for the sample cell, better accuracy results were obtained with a fast data acquisition response time.

1. INTRODUCTION

The refractive index measurements methods for liquid crystals make the object of numerous papers [2-5]. They present both new methods and the auxiliary information resulted as a consequence.

Plotting a dispersion curve is possible if one acquires a large number of experimental data for a set of wavelength values and extrapolate them to the unavailable domains. The refractometry method presented in our paper is a better experimental version of the one derived from the phenomenon first observed years ago by Talbot[7]. It allows the determination of the dispersion curve of a transparent liquid or solid substance which is optically isotropic or anisotropic, for a large number of very closed wavelengths values.

By using this method for liquid crystals, we were able to derive the ordinary and extraordinary refractive index dependence on the wavelength and therefore the substance birefringence. Moreover, the speed of data acquisition leads to an other advantage of the method: the determination of the refractive index dependence on one or more external parameters, i.e. temperature, electric field, etc. In addition, if the measurement domain is well refined in terms of wavelength refractive index values, the anomalous dispersion of a liquid crystal is identified.

2. THE PRINCIPLE OF THE METHOD

In order to record the dispersion curves, a modified experimental set-up of a Talbot-Rayleigh interferometer was used (Figure 1).

We use a white light source (1) from which a parallel light beam is obtained with the L_1 -lens. Afterwards this beam splits in two components: one passes through air, the transparency coefficient of the free space being equal to unity, while the second passes through the liquid crystal sample (4) which may be treated as a transparent plane-parallel plate, normal to the light propagation direction. Its transparency coefficient is taken to be T_l ($T_l < 1$ due to the light absorption in liquid crystal).

Both beams are incident on a diffraction grating (8) having N as total number of traces and p as the grating constant.

The diffracted beam is focalized on the image plane by the L_2 - lens with -focal distance.

Let the Oy - axis be the vertical axis in the grating plane, having the origin on the symmetry axis of the experimental set-up.

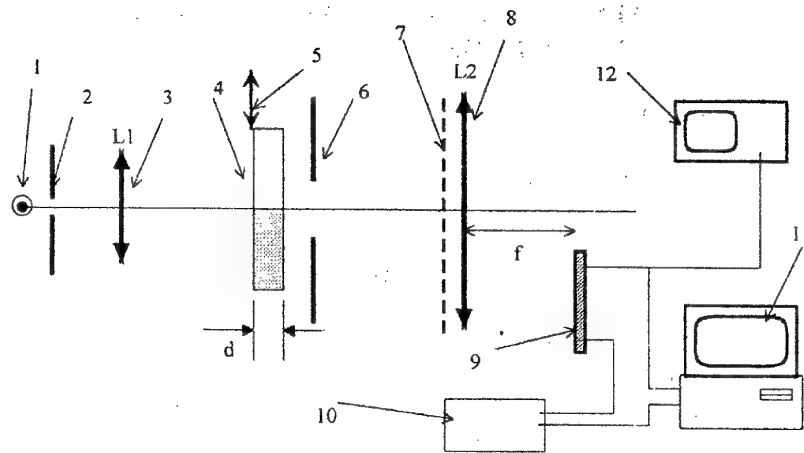


Fig. 1 Experimental set-up of the modified Talbot interferometer.

1; White light source. 2; Rectangular slit. 3; Lens. 4; Sample. 5; x-y displacement mechanism. 6; Rectangular aperture. 7. Holographic grating. 8. Lens. 9. CCD linear array. 10. Function generator for exposure time modification. 11. Computer with data acquisition board in direct memory access mode. 12. Scope

The amplitude of an arbitrary wave emerging from a point with x-coordinate, under the diffraction angle θ is:

$$da = T(x)e^{i\varphi(x)} dx \quad (1)$$

where:

$$T(x) = \begin{cases} T_1 & \text{if } x \in (-\infty, 0) \\ 1 & \text{if } x \in (0, +\infty) \end{cases} \quad (2)$$

is the transparency coefficient of the "object":

$$\varphi(x) = \begin{cases} \frac{2\pi}{\lambda}(x\theta + (n-1)d) & x \in (-\infty, 0) \\ \frac{2\pi}{\lambda}x\theta & x \in (0, +\infty) \end{cases} \quad (3)$$

is the phase after the wave passes through the "object" and the grate.

The amplitude of the resulted wave in an arbitrary point of the image-plane is:

$$a = \int_{-\infty}^{+\infty} da = a_1 + a_2 \quad (4)$$

a_1, a_2 being the contributions of the sample zone and of the free space, respectively.

Calculating the light intensity in an arbitrary point of the image-plane we obtained:

$$I = \frac{N^2 p^2}{4} \left(\frac{\sin \beta/2}{\beta/2} \right)^2 [A + \cos(\alpha + \beta)] \quad (5)$$

where:
$$A = \frac{1 + T_1^2}{2T_1}, \quad \alpha = \frac{2\pi(n-1)d}{\lambda}, \quad \beta = \frac{\pi\theta p}{\lambda} \text{ and } \sin \theta \approx \theta = \frac{x}{f} \quad (6)$$

The zero-value minima of the intensity occurs at:

$$p \sin \theta = 2k\lambda \quad \text{with } k \in \mathbb{Z}^* \quad (7)$$

The central maximum for any wavelength value is obtained at $x = x_0$, for $k = 0$, and has the intensity:

$$I_{M_0} = \frac{N^2 p^2}{4} (A + \cos \alpha) \quad (8)$$

The "channels" have, by contrast, the intensity:

$$I_m = \frac{N^2 p^2}{4} \left(\frac{\sin \beta/2}{\beta/2} \right)^2 [A - 1] \quad (9)$$

with $\beta = (2k + 1)\pi - \alpha$ and $\alpha = (2l + 1)\frac{\pi}{2}$ (10)

i.e. $(n(\lambda) - 1)d = m\lambda$ (11)

where $m = 1 + \frac{1}{2}$ for integer "l". (12)

3. EXPERIMENTAL SET-UP

The interference spectrum obtained in the first order diffraction maximum is recorded with the help of a CCD linear array (1024 points) connected to a computer via a DAS 1601 interface operating in direct memory access mode for a fast acquisition process. In order to calibrate the sensor in terms of wavelength values, a set of interference filters was used. The exposure time is modified with the help of a function generator which gives simultaneously the triggering signal for data acquisition. A monitoring scope is used for a direct investigation of the interference spectra shape.

For the determination of the liquid crystal birefringence, the sample must be a monocrystal with a well known optical axis direction. In case of liquid crystals the easiest way to obtain the ordinary and extraordinary indices is to have a planar texture between parallel polarizers (Fig. 2). The extraordinary index is obtained for polarizers parallel to the optical axis and after a quarter turn of both polarizers, the ordinary index is measured. The liquid crystal must be placed in a sandwich type cell, with the glass plates strongly rubbed to ensure that the liquid crystal is a monocrystal. In order to have a uniform thickness of the sample, we have modified the original Talbot Rayleigh method [1] and a 180 μm thickness glass plate was used as separator in the cell and also as reference material. In order to eliminate the optical path modification induced by this plate, a compensator made of the same glass plate was interposed (Fig. 2.) with the help of an x-y displacement mechanism.

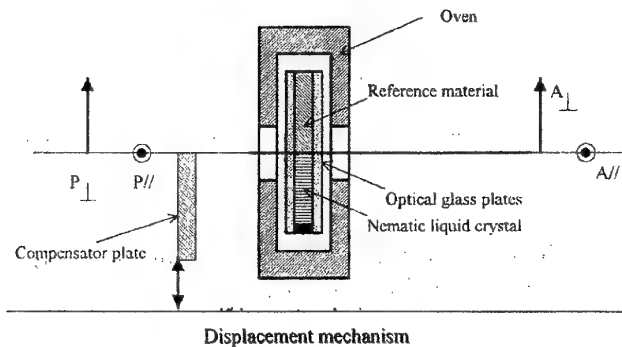


Fig. 2 Sample geometry to study both temperature and wavelength dependence of liquid crystals indices

4. RESULTS AND DISCUSSIONS

The reference point for the investigated liquid crystal has been measured in our lab using an Abbe refractometer with a Na lamp and a set of polarizers to determinate the ordinary and extraordinary indices at a fixed wavelength as function of the sample temperature. This dependence is plotted in Fig. 3.

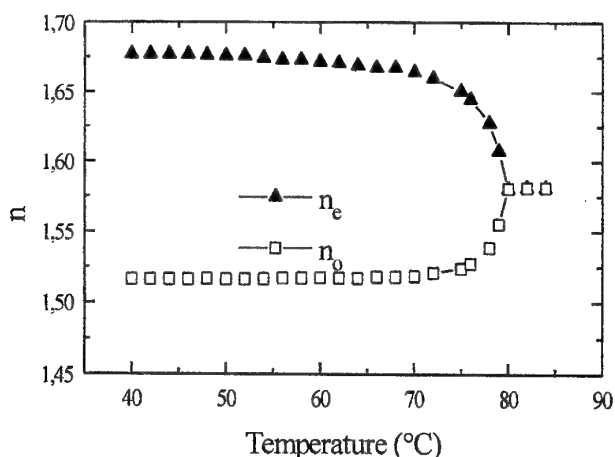


Fig. 3 Ordinary and extraordinary indices versus temperature ($\lambda=589.3\text{nm}$) for EBBA liquid crystal

Using the experimental set-up described in the previous section, Talbot spectra can be recorded at different temperatures, their shapes being as in figure 4. From these plots we can determinate the wavelength values where the interference minima occur. By using relation (11) the refractive index value can be also calculated. In figure 5 there are given the dispersion curves for the extraordinary and ordinary indices, at 65°C calculated for this type of spectra in the 500-750 nm range.

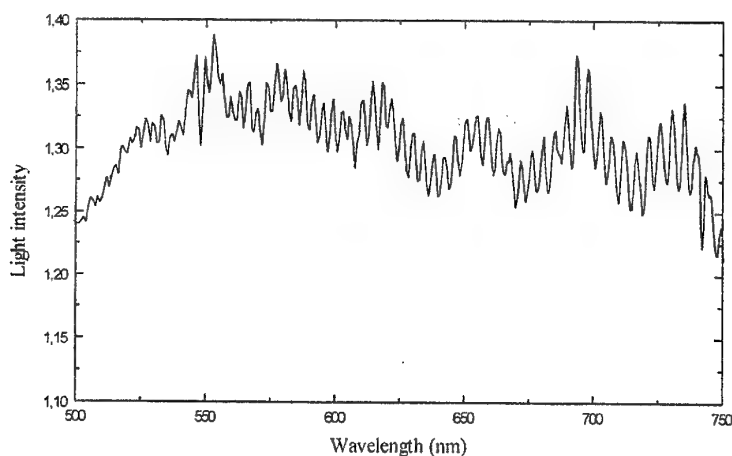


Fig. 4 Talbot bands observed in the first order of diffraction for EBBA, for the ordinary refraction index at 65°C

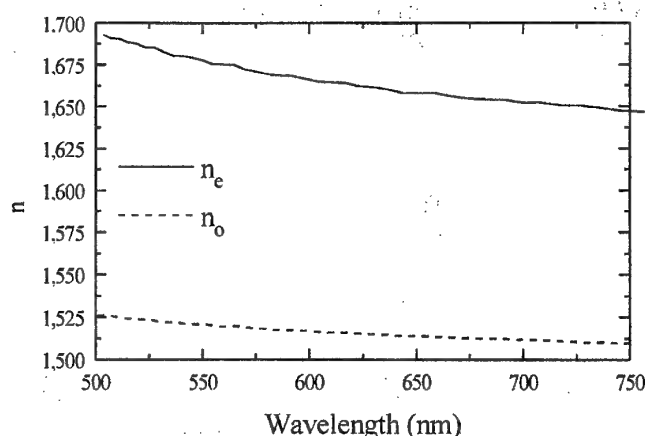


Fig. 5 Wavelength dependence of the extraordinary and ordinary indices on the wavelength, EBBA, 65°C

5. CONCLUSIONS

Once the dispersion curve is recorded, the explicit form of the function can be found:

$$n^2(\lambda) = \sum_i A_i \lambda^i \quad \text{with } i = 0, \pm 1, \pm 2, \dots \quad (13)$$

Therefore we can derive the complete expression of the $n^2(\lambda)$ function by computing the full set of coefficients $\{A_i\}$ for each liquid crystal.

Moreover, the dependence $n=n(\lambda, T, E)$ and the functions $A_i=A_i(T, E)$ may be obtained. Further, the absorption bands can be compared.

The described method offers an accurate tool for the investigation of phase transition regimes and absorption domains of a liquid crystal and high precision measurements of the refractive index dependence on temperature.

6. REFERENCES

- [1]. M. Warenghem, G. Joly, Mol. Cryst. Liq. Cryst., 271, 205-218, (1991).
- [2]. Ivan Haller, H.A. Huggins and M. Y. Freiser, Mol. Cryst. Liq. Cryst., 16, 53-59, (1972).
- [3]. E. G. Hanson and V. R. Shen, Mol. Cryst. Liq. Cryst., 36, 193-207, (1976).
- [4]. W. H. de Jeu and P. Bordewijk, J. Chem. Phys., 68, 109, (1978).
- [5]. R. G. Horn, J. de Phys., 39, 105, (1978).
- [6]. M. Warenghem, C. P. Graser, Rev. Phys. Appl. 23, 116, (1988).
- [7]. H. F. Talbot, Philos. Mag., 1, 364, (1837).
- [8]. M. F. Vuks, Opt. Spektrosk, 20, 644, (1966).
- [9]. S. T. Wu, Phys. Rev., 33, 1270, (1986).

THE DETERMINATION OF THE REFRACTIVE-INDEX PROFILE FROM NEAR FIELD AND EFFECTIVE REFRACTIVE-INDEX MEASUREMENTS

D. Pîrcalaboiu, G. Perrone*, N. N. Puscas**

Optoel. Dept., Univ. "Politehnica" Bucharest, Spl. Independentei 313, 77206, Bucharest, Romania

* Dipartimento Elettronica, Politecnico Torino, Corso Duca degli Abruzzi 24, 10129, Torino, Italia

** Phys. Dept., Univ. "Politehnica" Bucharest, Spl. Independentei 313, 77206, Bucharest, Romania.

ABSTRACT

We report a method based on near field and effective refractive index measurements for the determination of the refractive index profile of optical waveguides. The derivation of the refractive-index profile was performed in the scalar approximation from Helmholtz equation and the evaluation of the effective refractive-index using "m-lines" method. The proposed method has been applied to reconstruct the index profile of a planar optical waveguide obtained by K^+ ion exchange in glass.

1. INTRODUCTION

Many theoretical and experimental papers using several methods dealt in the last years with the determination of the refractive index profile because its knowledge plays an important role in the characterization of optical waveguides (i.e. bandwidth, spot size, single-mode propagation conditions, etc.) [1-3]. In this paper we present the determination of the refractive index profile of a planar optical waveguide obtained by ion exchange (K^+) in a soda-lime glass from near field and effective refractive index measurements. The near field data acquisition was performed using a CCD camera while the effective refractive index was measured by prism coupling method also known as "m-lines" spectroscopy [4].

In Sect. 2 the derivation of the refractive index profile from Helmholtz equation and the evaluation of the effective refractive index using "m-lines" method are presented. The experimental setup used for the near field and effective refractive index measurements are described in Sect. 3 while Sect. 4 and 5 are dedicated to the discussions of the obtained results and conclusions.

2. THEORETICAL CONSIDERATIONS

Based on the model presented in [3] the refractive index profile can be formally determined from the bidimensional (x -width, y -depth) Helmholtz equation as:

$$n^2(x, y) = \left(\frac{\beta}{k_0} \right)^2 - \frac{1}{k_0^2} \frac{\Delta_T \psi(x, y)}{\psi(x, y)} \quad (1)$$

where Δ_T represents the transversal Laplace operator, $\psi(x, y)$ is the transversal electric or magnetic field, $n(x, y)$ is the refractive index profile, β the propagation constant and k_0 the free space wave vector. Considering that the transversal electric field can be written as a product $\psi(x, y) = \psi(x)\psi(y)$ and knowing the local field intensity $I(y) = \psi^2(x_0, y)$ in a fixed point $x = x_0$, the equation for the refractive index becomes:

$$n(x_0, y) = \left[\left(\frac{\beta}{k_0} \right)^2 - \frac{1}{k_0^2} \frac{1}{\sqrt{I(y)}} \frac{d^2 \sqrt{I(y)}}{dy^2} \right]^{\frac{1}{2}} \quad (2)$$

The determination of the refractive index profile from Eq. (2) implies the knowledge of the effective refractive index in order to evaluate the propagation constant $\beta = k_0 n_{eff}$ and the numerical

derivation of the field intensity profile. The local field intensity can be determined from near field measurements using for example CCD camera for the visible wavelengths range while the effective refractive index values can be evaluated by the "m-lines" method. Before the numerical derivation of the field intensity profile the experimental curve must be smoothed because the field derivative is sensible influenced by the noise. The refractive index profile $n(y)$ in the waveguide depth direction can be written in the form:

$$n(y) = n_s + \Delta n f(y) \quad (3)$$

where n_s is the refractive index of the substrate. In our simulations the best fit of the processed data is given by a combination of two Gaussian functions

$$f(y) = \exp \left[- \frac{(y - y_0)^2}{\left(\frac{\sigma_{y, \text{left}} + \sigma_{y, \text{right}}}{2} + \frac{\sigma_{y, \text{left}} - \sigma_{y, \text{right}}}{2} \tanh(y - y_0) \right)^2} \right] \quad (4)$$

In the Eqs. (3)-(4) Δn_{max} represents the maximum value of the refractive index difference, y_0 and $\sigma_{y, \text{left}}$, $\sigma_{y, \text{right}}$ define the center of the Gaussian function and the corresponding variances. Based on the "m-lines" method [4] we measured the effective refractive index values.

3. EXPERIMENTAL SETUP

The experimental set up used to determine the near field intensity profile at the He-Ne laser wavelength $\lambda = 632.8$ nm in the depth direction of a planar optical waveguide is presented in Fig. 1. The effective refractive index for the waveguide mentioned above was measured using "m-lines" method. We used a CCD camera and a computer for of the data field intensity profile acquisition.

4. DISCUSSION OF THE RESULTS

Using the experimental arrangement presented in Fig. 1a we measured the near field intensity in depth of a planar optical waveguide obtained by K^+ ion exchange in a soda-lime glass. Before using the field intensity in the wave equation to determinate the refractive index profile, the measured data were smoothed in order to remove high frequency noise. The measured depth field intensity (TE polarization) and the processed smoothing curve profiles (cubic spline) are presented in Fig. 2 a). and the corresponding measured value of the effective refractive index is $n_{\text{eff}} = 1.5131$.

Using Eqs. (2)-(4) we obtained the refractive index profile shown in Fig. 2b. We find the maximum index changes: $\Delta n = 1.382 \times 10^{-3}$ for the TE polarizations.

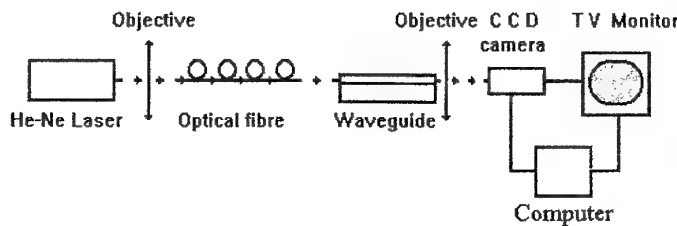


Fig. 1 The experimental set up for the near field measurement

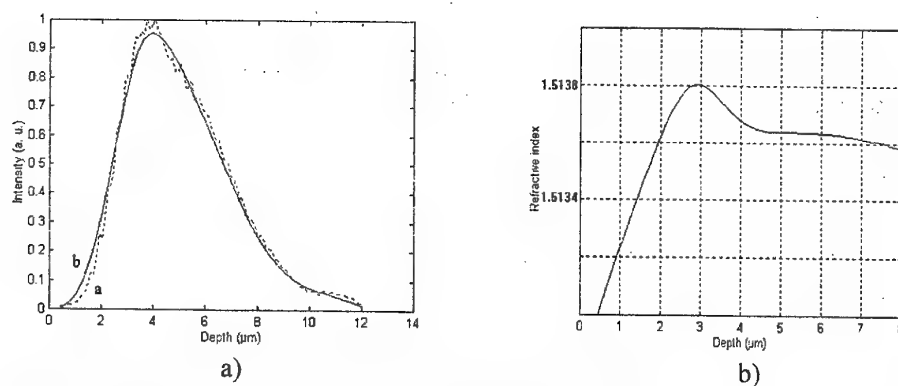


Fig. 2 a), b) The measured depth field intensity (curve a) and the processed smoothing (curve b) profiles (a) and the refractive index profiles for TE polarization

5. CONCLUSIONS

In this paper we presented a method for the determination of the refractive index profile of a planar optical waveguide from near field and effective refractive index measurements. The obtained values of the maximum index change in the case of a planar optical waveguide obtained by K^+ ion exchange in soda-lime glass can be used in the design of several photonic circuits.

6. REFERENCES

- [1]. Nikopoulos J. and Yip G. L., *J. Lightwave Technol.* LT 8, no. 7, 864-869 (1991).
- [2]. Mansour I. and Caccavale F., *J. Lightwave Technol.* LT 14, no. 3, 423-428 (1996).
- [3]. Montrosset I., Guidi M., Puscas N., Popescu I. M., Grobnc D. M., *SPIE* 2461, p. 452-456 (1994).
- [4]. Tien P. K., *Rev. Mod. Phys.* 49, 361-420 (1977).

ON THE IR REFLECTIVITY OF $\text{Bi}_{12}\text{SiO}_{20}$ CRYSTAL IN THE IONIC PLASMA FREQUENCY RANGE

Ana Ioanid

Department of Solid State Physics, Faculty of Physics, University of Bucharest,
National Center of Physics, Bucharest-Magurele, P O B MG-6, R 76900

1. INTRODUCTION

Both bismuth silicon oxide, $\text{Bi}_{12}\text{SiO}_{20}$ and bismuth germanium oxide, $\text{Bi}_{12}\text{GeO}_{20}$ crystals, are of considerable interest in the view of their unusual optical and electro-optical properties. These crystals are isomorphous, possess the $T(23)$ point-group symmetry and belong to the space group $T^3(I23)$. As expected for crystals of this symmetry, both exhibit isotropic optical activity. Herein, we present the reflectance spectra $R(\tilde{\nu})$ evaluated by the spectral analyse of the dielectric optical permittivity, $\epsilon(\nu)$. In the IR spectral range, the zone-center optical modes associated to the lattice vibrations give the main contribution to $\epsilon(\nu)$, so that the complex dielectric permittivity can be expressed in a form of a set of n damped harmonic oscillators as

$$\epsilon^*(\nu) = \epsilon(\infty) + \sum_{\alpha=1}^n \frac{f_{\alpha}}{\nu_{\alpha}^2 - \nu^2 - i\gamma_{\alpha}\nu} \quad (1)$$

where $\epsilon(\infty)$ is the electronic high frequency limit of $\epsilon^*(\nu)$ and $f_{\alpha}, \gamma_{\alpha}, \nu_{\alpha}$ are the strength, the damping frequency and the center frequency of the α -th oscillator, respectively. The reflectivity at normal incidence for a semi-infinite medium, following Cardona [1] is given by

$$R(\nu) = \left| \frac{\sqrt{\epsilon^*(\nu)} - 1}{\sqrt{\epsilon^*(\nu)} + 1} \right|^2 \quad (2)$$

Taking into account the real and imaginary parts of the $\epsilon^*(\nu)$, then

$$R(\nu) = \frac{|\epsilon^*(\nu)| - \sqrt{2(\text{Re}\epsilon^*(\nu) + |\epsilon^*(\nu)|)}}{|\epsilon^*(\nu)| + \sqrt{2(\text{Re}\epsilon^*(\nu) + |\epsilon^*(\nu)|)}} + 1 \quad (3)$$

where

$$\begin{aligned} \text{Re}\epsilon^*(\nu) &= \epsilon(\infty) + \sum_{\alpha=1}^n \frac{f_{\alpha}(\nu_{\alpha}^2 - \nu^2)}{(\nu_{\alpha}^2 - \nu^2)^2 + \gamma_{\alpha}^2 \nu^2} \\ \text{Im}\epsilon^*(\nu) &= \sum_{\alpha=1}^n \frac{f_{\alpha}\gamma_{\alpha}\nu}{(\nu_{\alpha}^2 - \nu^2)^2 + \gamma_{\alpha}^2 \nu^2} \\ |\epsilon^*(\nu)| &= \left[(\text{Re}\epsilon^*(\nu))^2 + (\text{Im}\epsilon^*(\nu))^2 \right]^{\frac{1}{2}} \end{aligned} \quad (4)$$

2. EVALUATION OF THE $\text{Re}\epsilon^*(\nu)$ AND $\text{Im}\epsilon^*(\nu)$

The number of zone-center optical phonons and their symmetry classification according to the irreducible representations of the crystal symmetry can be deduced by a group-theoretical analysis. The crystal structure of $\text{Bi}_{12}\text{SiO}_{20}$ shows that the primitive unit cell contains one formula unit. It can be shown that for this structural unit there are 40 zone-center optical phonons: 8 A (totally symmetric), 8 E (doubly degenerate) and 24 F (triply degenerate). Phonons of all the three symmetries are Raman active in the first order, and only those belonging to F symmetry are infrared active in the first order. The Raman spectrum of $\text{Bi}_{12}\text{SiO}_{20}$ at 15K consists of a total 43 lines in the region $(40 \div 850)\text{cm}^{-1}$ [2]. We consider in (1), $n = 43$ harmonic oscillators taking into account the LO-TO splitting of the polar F modes. For the evaluation of the dielectric permittivity, the knowledge of the each oscillator parameters is needful. The strength f_α of the α -th oscillator has been appreciated by the bond force constant k_r . The value of the bond force constants depends on the distance between the ions of the diatomic oscillators and on the difference between the ions electronegativities. Taking into account the arrangement and the electronegativity of ions in $\text{Bi}_{12}\text{SiO}_{20}$, we consider in the first approximation, $f_\alpha = f \cong f_r \cong 3 \times 10^5 \text{cm}^{-2}$ [3] for all harmonic oscillators. In an ideal harmonic approximation, the damping frequency γ_α would be determined entirely by radiation damping that for the ionic oscillators would have

$$\gamma_\alpha = \frac{(v_{\max}^2)_\alpha}{3\epsilon_0} \frac{e_\alpha^2}{c^3 \mu_\alpha} \quad (5)$$

where v_{\max_α} is the maximum vibrational frequency, e_α and μ_α are the main charge and the reduced mass of the ions of the α -th oscillator. We consider $v_{\max_\alpha} = v_{\max} = \frac{k_B \Theta_E}{h}$ for all harmonic oscillators. Here Θ_E is the Einstein temperature, $\Theta_E = 774\text{K}$ [4]. Considering a main reduced mass $\mu_\alpha = \mu$ the all diatomic oscillators in the SiO_4 , OBi_3 , $\text{Si}(\text{OBi}_3)_4$ groups, we obtain $\gamma_\alpha = \gamma \approx 10^{-11} \text{cm}^{-1}$. The observed widths actually are far greater than this, being of the order $(10 \div 100)\text{cm}^{-1}$. In Fig.1 the values $R(\tilde{\nu})$ are plotted calculated with (1) ($\nu = c\tilde{\nu}$, $\epsilon(\infty) = 40$) for

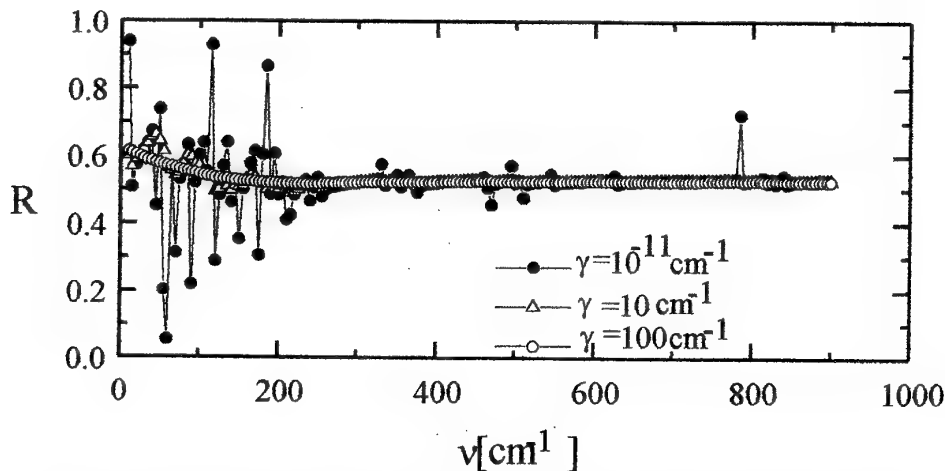


Fig.1 The dependence of reflectivity on frequency for various damping frequencies

$\gamma = 10^{-11} \text{ cm}^{-1}$, $\gamma = 10 \text{ cm}^{-1}$ and for $\gamma = 100 \text{ cm}^{-1}$. The last dependence is typical for the reflectivity in the ion plasma frequency range [5]. Since for $\nu \rightarrow \nu_{\text{plasma}}$ and $\nu < \nu_{\text{plasma}}$, $R \rightarrow 1$ because in the same conditions, $\epsilon(\nu) \rightarrow 0$ and $R(\nu_{\text{plasma}}) = 1$, due to the fact that $\epsilon(\nu_{\text{plasma}}) = 0$. The ion plasma frequency may be evaluated with the expression

$$\nu_{\text{plasma}} = \frac{1}{2\pi} \left[\frac{Nq^2}{\epsilon_0 \epsilon(\infty) M} \right]^{\frac{1}{2}} \quad (6)$$

where N, q, M are the means values of the concentration, of the charge, of the ions mass. Using the known values for the structural and ionic parameters of $\text{Bi}_{12}\text{SiO}_{20}$ [6], we obtain $\nu_{\text{plasma}} \cong 7 \times 10^{12} \text{ s}^{-1}$. In Fig.2 there is plotted the dependence $R(\lambda)$ for $\gamma = 100 \text{ cm}^{-1}$ that has the minimum at $\lambda = 44 \mu\text{m}$.

This value is in good agreement with the evaluated value $\lambda_{\text{plasma}} = \frac{c}{\nu_{\text{plasma}}} \cong 42 \mu\text{m}$.

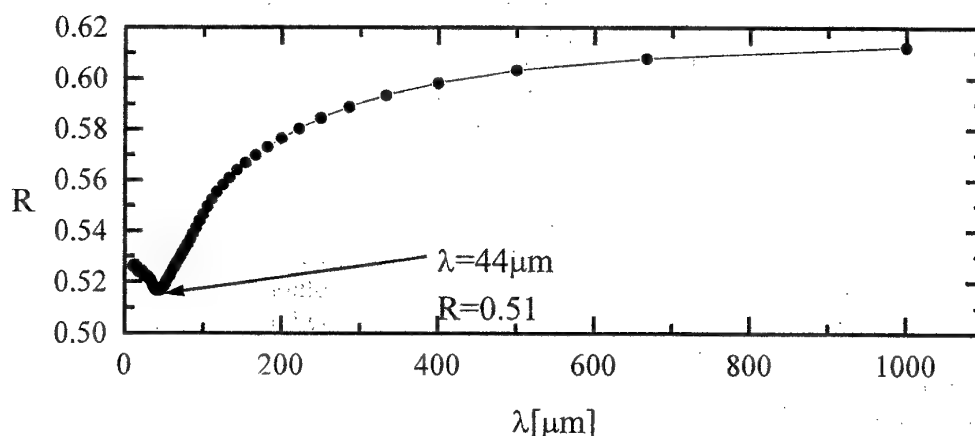


Fig.2 The dependence of reflectivity on wavelength in the ionic plasma frequency range

3. REFERENCES

- [1] M.Cardona, "Modulation Spectroscopy, Solid State Physics, Suppl. 11, Academic Press, 58 (1969)
- [2] S.Venugopalan and A.K.Ramdas, *Phys.Rev.*, **5** (10), 4065 (1972)
- [3] G.A.Babonas, *et al.*, *Sov.Phys.Solid State*, **24** (6), 921 (1982)
- [4] I.Licea and A.Ioanid, *in press*
- [5] J.Pancove, "Optical processes in semiconductors", Prentice-Hall, Inc., New Jersey, 92 (1971)
- [6] R.Oberschmid, *phys.stat.sol. (a)*, **89**, 263 (1985)

NEW TYPE OF SOLITON QUANTIZATION

V. Calian, M. Ursache

University of Craiova, Dept. of Physics, 13 A.I. Cuza, Craiova
email: violetaxx@hotmail.com

ABSTRACT

The problem of soliton quantization is treated in a new framework based on the identification of the Lagrangian density which leads to the soliton propagation equation in optical fibers or to the set of coupled generalised nonlinear Schroedinger equations for optical couplers. The analysis of its nontrivial symmetry properties allow us to use the BRST quantization of the theory.

1. INTRODUCTION

Nonlinear Schroedinger equations and soliton propagation is a frequently encountered problem in many areas of physics, including electromagnetic field propagation in optical fibers with or without birefringence and/or dispersion effects, nonlinear evolution of femtosecond pulses in optical fibers, soliton switching and propagation in nonlinear couplers.

A large number of methods is involved in solving this family of problems [1-7] and only a few methods were identified for defining a quantum theory of soliton propagation, even if the experimental evidences are well known, but confronted with various difficulties or limiting conditions of validity.

2. CLASSICAL THEORY

Our approach starts with the construction of the Lagrangean density associated to the given realistic model, so that the field equation coincides with the differential solitonic equation.

Generality is the main advantage of the method. We will illustrate it by studying the simple case of soliton in optical fibers without dispersion and birefringence effects, although these may be easily included if necessary.

The classical equation is thus:

$$iu_{\xi} + \frac{1}{2}u_{\tau\tau} + |u|^2u = 0 \quad (1)$$

where "u" - is the normalized complex field amplitude, $u_{\xi} = \frac{\partial u}{\partial \xi}$, $u_{\tau\tau} = \frac{\partial^2 u}{\partial \tau^2}$ and ξ, τ - the normalized length and time.

In order to give the standard appearance of the classical field theory to our treatment, we first introduce the following denotings:

$$\varphi_1 = u; \varphi_2 = u^*; t = \xi; x = \tau$$

and keep in mind for a later stage that space and time variables have been "reversed". The interpretation of the quantum theory will then bring us back to an other version of such a theory [1] where equal-space commutation rules were imposed.

The equation (1) is written as:

$$i\varphi_1 + (\varphi_1\varphi_2)\varphi_1 + \frac{1}{2}\partial_{xx}\varphi_1 = 0 \quad (2)$$

while the complex conjugate is obviously:

$$-i\varphi_2 + (\varphi_1\varphi_2)\varphi_2 + \frac{1}{2}\partial_{xx}\varphi_2 = 0 \quad (3)$$

The corresponding Lagrangean density was consequently found to be:

$$L = -i\varphi_2\varphi_1 - \frac{1}{2}(\partial_x\varphi_1)(\partial_x\varphi_2) - \frac{1}{2}(\varphi_1\varphi_2)^2 \quad (4)$$

and is straightforwardly to verify that the equations (2), (3) are the field equations for the given Lagrangean (4).

The next step of the algorithm consists in writing the constraints:

$$\begin{aligned} \phi_1 &= \pi_1 + i\varphi_2 \\ \phi_2 &= 0 \end{aligned} \quad (5)$$

obtained by calculating the canonical variables conjugated to φ_1, φ_2 :

$$\begin{aligned} \pi_1 &= -i\varphi_2 \\ \pi_2 &= 0 \end{aligned} \quad (6)$$

The canonical Hamiltonian is then:

$$H_c = \frac{1}{2}(\partial_x\varphi_1)(\partial_x\varphi_2) + \frac{1}{2}(\varphi_1\varphi_2)^2 \quad (7)$$

which gives, by using the constraints (5), the so-called primary Hamiltonian:

$$H_p = H_c + \lambda_1\phi_1 + \lambda_2\phi_2 \quad (8)$$

used in constraints class analysis.

3. QUANTIZATION PROCEDURE

The classical field Poisson bracket is defined in the usual manner:

$$\{A, B\}_{t_0=t} = \int dx \left(\frac{\delta A}{\delta Q_a(x)} \frac{\delta B}{\delta P^a(x)} - \frac{\delta A}{\delta P^a(x)} \frac{\delta B}{\delta Q_a(x)} \right) \quad (9)$$

and the following set of Poisson bracket has then to be computed:

$$\{\phi_a, H_p\}, (\phi_a, \phi_b)$$

in order to check the first class character of the constraints and to define the Dirac brackets.

The operational realization of the constraints is not a direct result, so the BRST quantization stage uses the Batalin-Vilkoviski functional integration procedure, once the "phase-space" is enlarged by introducing the auxiliary canonical variables (P^a, Q_a) associated to the constraints (5):

$$Z_\psi = \int D\mu \exp \left[\frac{i}{\hbar} \int dt (\pi_a \dot{\varphi}^a + P_a \dot{Q}^a - H_\psi) \right] \quad (10)$$

does not depend on the choice of ψ . We used the following denotings:

$$H_\psi = H_c + P_a V_b^a Q^b - \{\psi, \Omega\}_{\pi, \varphi, P, Q} \quad (11)$$

with:

$$\Omega = \phi_a Q^a + \frac{1}{2}(-1)^{n_a} P_c U_{ab}^c Q^a Q^b \quad (12)$$

and

$$\{\phi_a, \phi_b\} = \phi_c U_{ab}^c; \{H_c, \phi_a\} = \phi_b V_a^b \quad (13)$$

It is also remarkable that the two additional symmetries:

$$\delta_{\varepsilon_a} A = \varepsilon_{a,b} \{A, \phi^b\} \quad (14)$$

of the theory are now manifest: they are introduced by the existence of the two constraints. The number of constraints and symmetries is actually $2 \times \infty^2$ due to the continuum character of the space-time variables.

4. CONCLUSIONS

This paper shows how the classical and quantum theory of soliton propagation in optical fibers is completed in the BRST approach, once one finds the correct form of a Lagrangean density of the field theory that contains equation (1) as field equation. Various difficulties of previous treatments are thus avoided and a rigorous covariant quantization is performed, while the degree of generality is highly recognisable.

5. REFERENCES

- [1] L.G.Joneckis, J.H.Shapiro, J.Opt.Soc.Am.B, vol.10, no.6, (1993), 1102.
- [2] Y.Lai, J.Opt.Soc.Am.B, vol.10, no.3, (1993), 475
- [3] C.R.Menyuk, J.Opt.Soc.Am.B, vol.10, no.9, (1993), 1585
- [4] P.L.Chu, B.A.Malomed, G.D.Peng, J.Opt.Soc.Am.B, vol.10, no.8, (1993), 1379.
- [5] L.Torner, D.Mihalache, D.Mazilu, N.Akhmediev, Opt.Comm.138 (1997), 105
- [6] G.Vilasi, quant-ph/9710022
- [7] R.Jackiw, hep-th/9611185
- [8] G.Vilasi, Phys.LettB174, (1986), 203.

SPECTRAL RESPONSE SIMULATION FOR SOLAR CELLS

G. Stoenescu, N. Baltateanu*, V. Calian

University of Craiova, Dept. of Physics, 13 A.I. Cuza, Craiova 1100,
email: gstoen@hotmail.com

*Institute of Atomic Physics, Bucharest

ABSTRACT

Our experimental and theoretical studies of homojunction solar cells were performed with the purpose of analysing their spectral response variation after irradiation and the specific involved mechanisms. The theoretical approach is based on a rigorous computation of the microscopic parameters contained by the theoretical form of the spectral response, which is made possible if the absorption spectra of the given cells are also measured. Moreover, the structural and conduction mechanisms after irradiation may be theoretically controlled in terms of the whole set of parameters.

1. INTRODUCTION

One of the main criteria in the selection of semiconductor materials for preparing solar cells is the stability of their performances under variations in medium conditions and especially under the action of high energy particle flows (electrons, protons, neutrons, X-quanta).

These types of radiation may strongly change the energy spectrum corresponding to the crystalline defects. Two sets of effects were identified for polycrystalline layers.

The former is due to the recrystallization and reorientation of the interstitial vacancies and atoms, during the energy minimization under high energy particle beams. It leads to an improvement in the parameters which characterise the crystalline structure.

The latter consists in the producing of crystalline defects corresponding to acceptor states.

Two main groups of irradiation induced defects are present:

- a) those which imply an increase in the electron-lattice interaction for the electrons laying in the higher valence states. The electron localisation is thus strengthened.
- b) those which lead to a decrease in the interaction energy and thus of the localisation degree.

One may describe these effects in terms of energy gap and its variation as a function of the electronic valence states. The acceptor and respectively donor character emerges as a consequence.

The measured spectral response V_{oc} (at $J = 0$) showed a sensible displacement of the peak values towards shorter wavelengths after irradiation, and it is usually modelled by a double gaussian.

However, in previous studies, the parameters obtained by fitting from the experimental curve had no physical significance. This deficiency is corrected by our theoretical approach described in section 3 below.

The numerical simulation based on the absorption spectra, on the spectral response data and on the explicit theoretical model allowed us to compute the values of the defects concentration, energy gap, carriers diffusion length, both before and after the irradiation processes, and to establish the specific phenomena which modify the cell response type.

2. EXPERIMENTAL AND THEORETICAL RESULTS

The CdSe thin films obtained by thermal evaporation and vacuum condensation were produced in various experimental conditions. The influence of the technological parameters on their characteristics was also investigated. CdS-CdSe solar cells were obtained by using these thin films.

Subsequently, we analysed the fast electron irradiation on the properties of the produced thin films and on the performance of solar cells.

The crystalline structure, electric conductivity, optical absorption spectra and photoconduction of these polycrystalline layers were finally investigated both before and after the irradiation processes.

The theoretical treatment starts with the expression:

$$V_{oc} = kT \ln \left(\frac{\phi a_1}{a_2 + a_3 + J_{R,B}} \right) \quad (1)$$

where:

$$a_i = f_i(d, \alpha, L_p, L_n, S_p, S_n, D_p, D_n, W)$$

with $i = 1 \div 3$ and the absorption spectra $\alpha(\lambda)$ are known, while the rest of denoting are referring to the diffusion lengths of negative and positive charge carries L_p, L_n , the widths of the spatial charge domains D_n, D_p , recombination rates S_n, S_p , base and top layer width L, d , photon flux ϕ .

The explicit expressions of the "parameters" a_i are the following:

$$a_1/e = \left\{ \left[\frac{\beta_2^2}{\beta_2^2 - \beta_1^2} \right] \left[\frac{\beta_3 \beta_1 / \beta_2 + 1}{\beta_3 \sinh \beta_1 + \cosh \beta_1} \right] \left[\frac{\beta_2^2 \exp(-\beta_2)}{\beta_2^2 - \beta_1^2} \right] \left[1 + \frac{\beta_3 \cosh \beta_1 + \sinh \beta_1}{\beta_3 \sinh \beta_1 + \cosh \beta_1} \right] \right\}_{top} + \quad (2)$$

$$\left\{ [1 - \exp(-\beta_4)] \exp(-\beta_2) \right\}_{barrier} +$$

$$\left\{ \frac{\beta_6^2 \exp(-\beta_2) \exp(-\beta_1)}{\beta_6^2 - \beta_5^2} \left[\frac{\exp(-\beta_6)(\beta_7 \beta_5 / \beta_6 - 1)}{\beta_7 \sinh \beta_5 + \cosh \beta_5} + 1 - \frac{\beta_5}{\beta_6} \frac{\beta_7 \cosh \beta_5 + \sinh \beta_5}{\beta_6 \beta_7 \sinh \beta_5 + \cosh \beta_5} \right] \right\}_{base}$$

$$a_2 = \frac{e D_p n_{p0}}{L_p} \left\{ \frac{\beta_3 \cosh \beta_1 + \sinh \beta_1}{\beta_3 \sinh \beta_1 + \cosh \beta_1} \right\}_{top} \quad (3)$$

$$a_3 = \frac{e D_n n_{p0}}{L_n} \left\{ \frac{\beta_7 \cosh \beta_5 + \sinh \beta_5}{\beta_7 \sinh \beta_5 + \cosh \beta_5} \right\}_{base} \quad (4)$$

while the dimensionless $\beta_i, i = 1, 7$ are given by:

$$\beta_1 = dL_p; \beta_2 = d\alpha; \beta_3 = L_p S_p D_p; \beta_4 = W\alpha; \beta_5 = L L_n; \beta_6 = L\alpha; \beta_7 = L_n S_n D_n \quad (5)$$

and show the interplay of specific combination of cell characteristic lengths and material properties.

The results of the theoretical simulations and of the experimental measurements are in good agreement as illustrated by Fig.1.

3. RESULTS AND CONCLUSIONS

The energy gap changing is recognisable in the spectral response of the photocurrent and of the photovoltage. It is obviously displaced towards smaller wavelengths (larger energy values) in some cases, while in other cases we measured an opposite sense displacement.

The experimental and theoretical results are given in Fig.1.

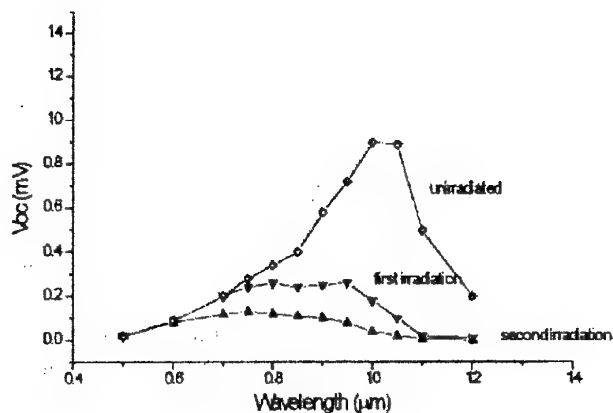


Fig.1 Spectral response of a solar cell before and after irradiation

They show a clear dependence of the spectral shift (and of the energy gap value as a consequence) on the irradiation doses. The fitting of the experimental curve is easily obtained by using double gaussian-like curves, but a more rigorous and meaningful form of V_{oc} is given by our simulation.

4. REFERENCES

- [1] Spanulescu I., "Fizica tranzistorilor si principiile microminiaturizarii", Ed. didactica si pedagogica, Bucuresti, (1973).
- [2] Korsunov F.P., Bogatirev V., Vavilov V.A., "Actiunea radiatiilor asupra circuitelor integrate", Minsk, (1986).
- [3] Electron Devices. March, vol.35, no.3., (1988).
- [4] Rusu A., "Modelarea componentelor microelectronice active", Ed.Academiei, Bucuresti, (1990).
- [5] Dozier C.M., Brown D.B., "Photon energy dependence of radiation effects in MOS structures", IEEE Trans.Nucl.Sci., vol.NS-27, M6, 1694-1699, (1980).

VARIABLE $\lambda/2$ RETARDATION PLATE

Anca Maria Beldiceanu

S.C. PRO OPTICA S.A., Aleea Bucovina, 4
phone 3214985; Fax 3.21.63.17; e-mail: proptic@fx.ro

ABSTRACT

A system of two birefringent plates equivalent with a variable $\lambda/2$ retardation plate effective in a range of wavelengths (480nm÷515nm) is presented. For particular values of the retardation of the two plates and for an azimuth of $\pm 45^\circ$ at the second plate, a resultant phase of 180° and an intensity of the interference unity are easily obtained for different λ , by simple rotation of the first plate of the system.

1. INTRODUCTION

Commercial retardation plates [1], usually operate with a single value of the wavelength λ ; the achromatic and superachromatic ones [2], are designed for two, respectively for four discrete values of λ and are realised as combinations of several cristalline materials.

The combination of two quartz retardation plates with variable azimuths offers the possibility to realize a continuously adjustable retardation, in a desired range of wavelengths.

An adjustable $\lambda/4$ retardation plate resulting from the combination of two rotary mica plates is reported by [3].

A $\lambda/2$ retardation plate that rotates with 90° the polarisation plane of an Ar Ion Laser beam in the 458nm ÷ 514 nm range of wavelengths was required and a particular solution (two zero order quartz plates with appropriate values for retardations and azimuths) is reported here.

2. THEORY

The system of two cristalline plates between crossed polariser and analyser.

The resultant phase δ_r and the intensity of interference I for two birefringent plates are given generally by [4]; in the case of an angle between the polariser and the analyser of 90° , they become :

$$\delta_r = \delta_2 \pm a \tan \frac{\sin 2\nu_1 * \sin \delta_1}{\sin 2(\nu_2 - \nu_1) * \cos 2\nu_1 + \sin 2\nu_1 * \cos 2(\nu_2 - \nu_1) * \cos \delta_1} \quad (1)$$

$$I = \sin^2 2\nu_1 * \sin^2 \frac{\delta_1}{2} + \sin^2 2\nu_2 * \sin^2 \frac{\delta_2}{2} + 2 \sin 2\nu_1 * \sin 2\nu_2 * \sin \frac{\nu_1}{2} * \sin \frac{\delta_2}{2} * \left[\cos \frac{\delta_1}{2} * \cos \frac{\delta_2}{2} - \cos 2(\nu_2 - \nu_1) * \sin \frac{\delta_1}{2} * \sin \frac{\delta_2}{2} \right] \quad (2)$$

ν_1, ν_2 are the azimuths and δ_1, δ_2 are the retardations for the two plates; the subscripts 1 and 2 correspond to the positions of the plates in the light path.

The second term of the equation (1) suggests the possibility of an ajustement of the phase retardation δ_r , while the first plate is rotated (variable ν_1).

In order to make the system of two birefringent plates between crossed polarisers equivalent to a

$\lambda/2$ retardation plate which maintains the linear polarisation state of light and rotates it with 90° , the following conditions have to be fulfilled simultaneously:

$$\delta r = 180^\circ \quad \text{and} \quad I = 1 \quad (3)$$

3. NUMERICAL RESULTS

The problem to be numerically solved is to find the retardations and azimuths of the two plates which allow that the conditions (3) are satisfied at the same time for five different values of the wavelength.

The following values, suggested by the formula (1), were chosen: $\delta_1 \approx 50^\circ$ and $\delta_2 = 180^\circ$ at $\lambda = 550$ nm. From the resultant phase considerations the second azimuth has to be fixed at the particular value $v_2 = \pm 45^\circ$.

At each value of interesting λ the corresponding retardations were calculated with the program for "one plate" parameters. Both retardations were tested then with the program for two crystalline plates for $v_2 = 45^\circ$ and for different possible values of v_1 until the condition of $\delta r = 180^\circ$ was attained. In the meantime the selected values for δ_1 and δ_2 show an important property: the intensity of light is 1 (actually the unity).

To illustrate the numerical results we provide below four values of interest in this case for the wavelength and the corresponding data obtained for the adjustable azimuth :

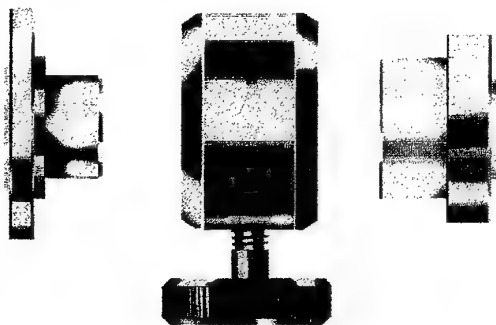
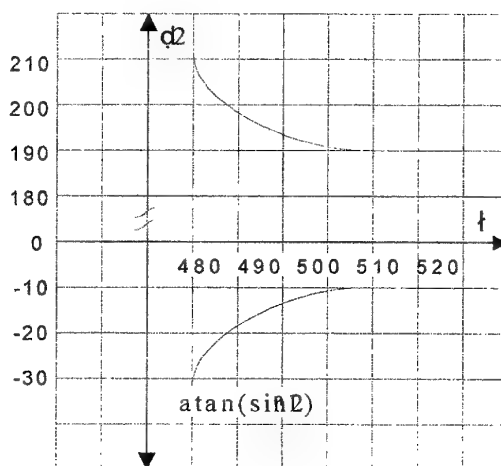
λ	480(Cd)	488(Ar)	509(Cd)	514.4	(nm)
v_1	-30	-26	-16	-14	(°)

The partial numerical results allow the following approximation: in the retardation formula the second term is replaced with $\text{atan}(\sin 2v_1)$ and a suggestive graphical representation for the way in which the retardation of 180° is attained (at every λ in the required range) becomes possible.

The intensity in every case verifies the condition $999 < I < 1.000$.

The data found for parameter v_1 are values easily to fixed on the experimental device.

Better numerical results are obtained if v_2 is also slightly adjusted within $\pm 0.5^\circ$.

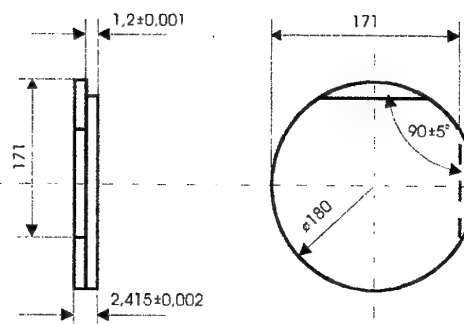


4. THE OPTO-MECHANICAL DEVICE

A simple mechanical device was realized in order to assure the possibility of relative azimuths adjustment of the two plates.

The optical components are two zero order quartz retardation plates for the most usual wavelength, $\lambda = 550$ nm.

These retardation plates are assemblies of two thin plates parallelly cut to the optical axis of the crystal and oriented at 90° to each other by means of the optical contact operation. In the figure are presented the crystalline axis and the corresponding beveled edges. The retardation plates are produced according to the special design and technology for crystalline optical materials and components, including ray tracing for crystals and optical methods for controlling the orientation of the axis during the manufacturing process.

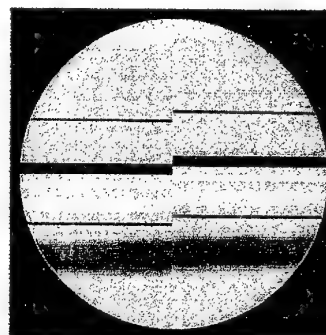


5. EXPERIMENT

Qualitative evaluation in white light

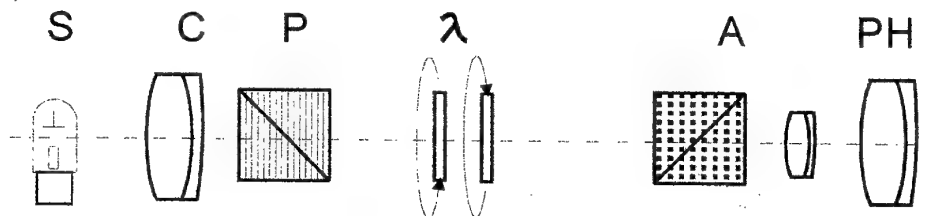
In order to verify the operating principle of the assembly of the two rotary plates, an experiment with white intense light on a polarising microscope was readily performed; a quartz compensating wedge in combination with a $\lambda/2$ and an approximate $\lambda/10$ mica plates were used.

In the microscope field of view, there is a central black fringe corresponding to the $\lambda/2$ retardation at $\lambda=550\text{nm}$; when the $\lambda/10$ plate is rotated from 0° toward -45° , while the $\lambda/2$ is maintained in $+45^\circ$ azimuth, the central black fringe is displaced continuously towards smaller values of the wedge thickness (corresponding to smaller values of λ for which the polarisation is linear).



6. EXPERIMENTAL RESULTS

The opto-mechanical device was tested on a polarimetric bench equipped with a Hg-Cd spectral lamp with spectral lines close enough to those of the Ar Ion Laser (at 480 and 509 nm, instead of 488 nm and 514.4nm).



Optical scheme for EF measurement of a two-plate system

The quality parameter for a polarisation device is the extinction factor (EF) defined as the ratio of the minimum to the maximum intensity polarised transmitted light.

For a crossed position of the polariser (P) and the analyser (A) and for the second plate in 45° azimuth, the first plate was rotated until the minimum value of the intensity was reached. Then the

maximum value of intensity was measured (with P parallel to A). The corresponding EF was better than 10^{-4} for every one of the selected wavelengths. The measurements were made with the precision Spectra Pritchard Photometer (PH) in a dark room (the residual luminance smaller than 10^{-3} cd/m²). The extinction positions were finally fixed by simultaneous fine adjustments of the azimuths of the two plates (announced by the numerical calculations).

The experimental values of v_1 were appreciated to be only in the neighbourhood of the numerical results.

7. CONCLUSIONS

A simple adjustable $\lambda/2$ retardation plate made of two birefringent plates with appropriate parameters was realized. The system is effective in a limited range of wavelengths (the Ar Ion Laser one) and for the 90° rotation of the polarisation plane only.

The design parameters (retardations and azimuths) were established by numerical calculations repeated until conditions (3) were fulfilled. The device was made of two quartz retardation plates manufactured for the common value of the wavelength, $\lambda=550$ nm. The assemble was tested with laboratory methods including classical sources of light in the absence of an adequate Laser.

The numerical results represent values easily attainable in practice for the individual retardations and azimuths. The calculus and experimental results are in good agreement with each other at this stage of the work.

The advantages of the solution are its simplicity in operation and its stability at temperature variations and optical misalignments. The experimentation of the device by means of an Ar Ion Laser and a general mathematical treatment are to be further realised.

ACKNOWLEDGEMENTS

The author wishes to thank to Mihai Miclaus and Sorin Turculeț for preparing the illustrations by computer means and for the English checking up to Matilda Dimer.

8. REFERENCES

- [1]. Melies Griot Catalog 1997-1998
- [2]. Handbook of Optics, vol.2, OSA, edition 1995
- [3]. Goltzer i.v., Kundikova N.D., Darsht M.Ya, Opt.Comm., vol. 97, pp291, (1993)
- [4]. Jerrard H.G., J.O.S.A., vol38, pp35, (1948)

ASTIGMATIC OUTPUT BEAM OF DOUBLE-HETEROSTRUCTURE LASERS

Florina Jitescu, O. Novac, M. Serghie

Military Equipment and Technologies Research Agency
P.O. Box 51-16, Bucharest, Code 76550, Fax : (401)7804863 Romania

ABSTRACT

Astigmatism is an inherent property of the output beam of a diode laser. The aim of this paper is to present the propagation characteristics of the diode laser beam taking into account the astigmatic distance. Moreover, this work presents the relation between the diode laser wavefront aberration and the astigmatic distance, relation available for determining whether a given diode laser is suitable for a precise optical system and for developing a measuring method for the astigmatic distance by using an interferometer and observing the interference pattern.

1. INTRODUCTION

With higher output powers, improved efficiency and better reliability, the diode laser plays an important role in fiber communications, audio-visual devices, optical sensors and optical measuring instruments as an irreplaceable component of modern optoelectronic and photonic systems.

2. ASTIGMATIC DISTANCE OF A DIODE LASER

Astigmatism is an inherent property of the output beam of a diode laser and a potential disadvantage in many applications. The laser beam appears to have different source points for directions normal and parallel to the junction plane. The longitudinal distance ΔA_s between these two emission points parallel and perpendicular to the junction is referred to as the astigmatism of the diode laser beam (Fig. 1).

If the confinement of the laser action to the junction region is ensured by the natural properties of the junction, the confinement of lasing action within a localised strip of the junction (in the plane of the junction) can be obtained by using two basic mechanism: gain guiding (GG) and index guiding (IG).

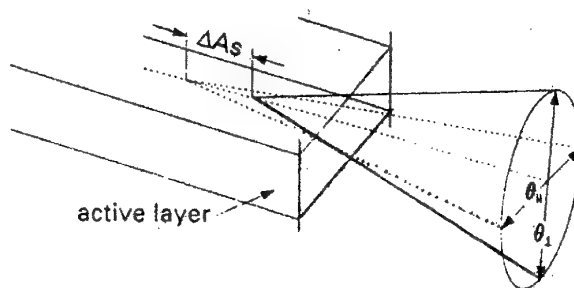


Fig. 1 Astigmatic distance of a diode laser

The guiding mechanism determines how much astigmatism will be present in the wavefront. GG diode lasers usually have between 20 and 50 μm of astigmatism. IG diode lasers typically exhibit an amount of astigmatism between 2 and 10 μm .

3. FAR-FIELD ANALYTICAL APPROXIMATIONS OF DIODE LASERS

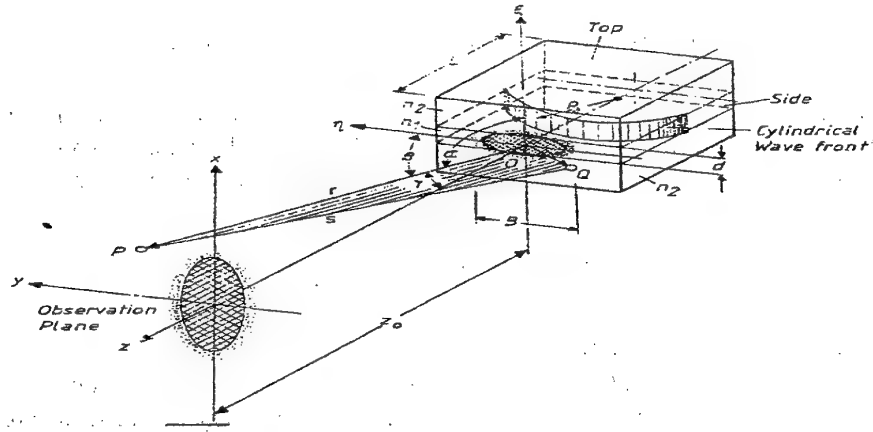


Fig. 2 Schematic diagram showing a diode laser, the far-field emission pattern, and the cylindrical wave front propagating in the active layer

Fig. 2 is an illustration of the notation used in deriving the far-field analytical approximations of double-heterostructure lasers, regardless of their GG or IG structures. The determining of the far-field patterns of double heterostructure lasers through Huygens-Fresnel calculation leads to:

$$U(P) = A \left(\frac{z_0}{r} \right) \frac{\exp(ikr - i\Phi)}{r} \left[k_T \left(1 + \frac{x^2}{h_1^2} \right)^{-1} \right] \exp \left(-\frac{y^2}{W_y^2} \right) \quad (1)$$

where: A is a constant amplitude factor;

$$\Phi = \frac{k \cdot \Delta A s}{2r} y^2 \text{ is the wavefront aberration} \quad (2)$$

$$h_1 = (p/k)r;$$

W_y is the beam width parameter; k is the wavenumber; p is an attenuation coefficient; k_T is a thickness function.

The impact of astigmatism $\Delta A s$ is mainly on the wavefront aberration as shown by Eq. (2).

When the diode-laser beams are severely truncated by the aperture stop of the beam shaping systems, only the central portion of the beam passes through the system. The paraxial portion of the far-field can be expressed in the form:

$$U(P) = A \left(1 + \frac{x^2}{h_1^2} \right)^{-1} \exp \left(ik \frac{x^2}{2R_x} \right) \exp \left(-\frac{y^2}{W_y^2} + ik \frac{y^2}{2R_y} \right) \quad (3)$$

Where: A is an amplitude constant; $R_x = z_0$, $R_y = z_0 + \Delta A s$ are the radius of curvature of the wavefront in the planes normal and parallel to the junction, respectively.

Eq. (3) is known as the Lorentzian-Gaussian model of diode-laser beams and is used in diffraction analysis of truncated diode-laser beams. In other words, the Lorentzian-Gaussian model is valid in the paraxial regime, in which the conventional Gaussian formulation also provides good approximations. This is the basic consideration for the use of the anisotropic Gaussian model far-field of diode-laser beams.

In general, the far-field distribution of double heterostructure lasers is neither Lorentzian-Gaussian nor anisotropic Gaussian if the beam is not severely truncated by the aperture.

4. MEASUREMENT OF DIODE LASER ASTIGMATISM

Because of the astigmatic distance ΔA_s , the beam emitted by the diode-laser and propagating to the pupil of an optical system has a distorted wavefront in the pupil plane that involves a wavefront aberration; for an aberration free optical system, the wavefront aberration is described as:

$$\Phi \leq -\frac{1}{4} \Delta A_s \cdot NA^2 \quad (4)$$

where NA is the numerical aperture of the entrance pupil.

If an optical system is given and a wavefront aberration tolerance of $\lambda/10$ is required for obtaining a precise optical system, the astigmatic distance of the diode-laser necessary to realise the precise, highly efficient system can be determined by using Eq. (4). Consequently, the astigmatic distance of a given diode-laser must be measured before using it, in order to determine if it is suitable for the considered, precise optical system.

The measurement of the astigmatic distance ΔA_s can be made by using a Mach-Zehnder interferometer (MZi) and observing the interference pattern. Fig. 3 shows the MZi setup to measure the astigmatism of a diode-laser wavefront.

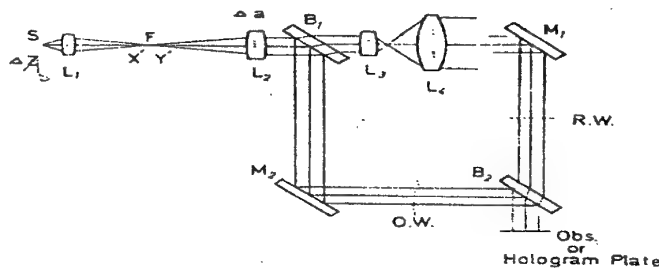


Fig. 3 Mach-Zehnder interferometer arranged for measurement of astigmatism of diode laser

As lens L_2 moves along the axis, the interference pattern changes from elliptical groups of lines to straight, to hyperbolic, to straight and back to elliptical groups of lines. When the focal point F of lens L_2 coincides with X' or Y' (the images of the sagittal and meridional focal points of the diode laser) the interference pattern becomes straight. The distance of this transfer $X'Y'$ of lens L_2 gives $M^2 \Delta A_s$, where M indicates the magnification of the objective lens L_1 .

5. CONCLUSIONS

It can be considered that diode-laser beams emitted from all actual devices are astigmatic and the astigmatic aberration present in the wavefront is a nonnegligible factor in the design of optical systems which use diode-laser beams.

6. REFERENCES

- [1]. Li, Y., Katz, J., Nonparaxial analysis of the far-field radiation patterns of double-heterostructure lasers, Appl. Opt., Vol.35, No.9, p.1442-1451, (1996).
- [2]. Tatsuno, K., Arimoto, A., Measurement and analysis of diode laser wavefronts, Appl. Opt., Vol.20, No.20, p.3520-3525, (1981).

SILICON INTEGRATED ELECTRO-OPTICAL MODULATORS FOR 1.3 μm FIBER-OPTICS

Gabriela Paunescu, Valerica Cimpoca, D. Cengher, Rodica Ghita
N. Olariu*, C. Oros*, Maria Cimpoca**

National Institute for Materials Physics, 76900 Bucharest, Romania, Fax.423.17.00

* Valahia University, Targoviste, Romania, Tel/Fax. (045) 217 683

** National Institute for Microtechnologies, Bucharest, Romania, Fax. 312.77.31

E-mail: gabip@alpha2.infim.ro

ABSTRACT

An all silicon electro-optical modulator for $\lambda = 1.3\mu\text{m}$ is analysed. The device, based on free carrier plasma dispersion effect in silicon and multi-pass Fabry-Perot interferometry, can be built by standard microelectronics techniques. The transmitted light intensity is studied as a function of injection current density, for different lengths of the central Fabry-Perot cavity. The shapes of the transmittivity curves are different for different lengths of FP cavity.

1. INTRODUCTION

It is of great technological importance the ability of making active optoelectronic devices in silicon which can be used as interface between electronic circuitry and fiber optics. Electro-optics and all optical silicon modulators have been proposed and realised. The devices are based on the free-carrier plasma dispersion effect [1].

In this paper we develop a simple silicon electro-optical modulator based on the multiple Fabry-Perot interferometric configuration. The device utilises the free carrier plasma dispersion effect in silicon to achieve phase modulation and three Fabry-Perot cavities to convert the phase modulation into intensity modulation.

2. OPERATION AND DESIGN

The scheme of a Si Fabry-Perot Modulators (FPM) with two lateral trenches and connected to a SiO_2 -on-Si planar waveguide is shown in Figure 1.

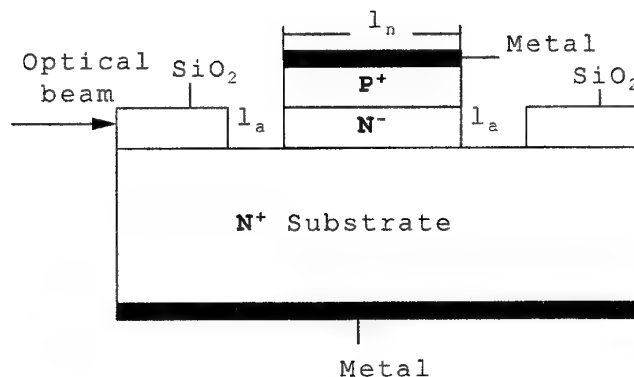


Fig. 1

The device consists essentially of a PIN diode structure ensuring the optical guiding in its intrinsic region. The device operation is based on the fact that the refractive index and the absorption

coefficient of the intrinsic-Si active region are modified by free carrier injection obtained by direct biasing of the diode.

At $\lambda = 1.3\mu\text{m}$, the refractive index and absorption coefficient perturbations produced by injected carriers are expressed, according to [2], by the relations:

$$\Delta n = \Delta n_e + \Delta n_h = -6.2 \cdot 10^{-22} \Delta N - 6 \cdot 10^{-18} (\Delta P)^{0.8}$$

$$\Delta \alpha = \Delta \alpha_e + \Delta \alpha_h = 5.9 \cdot 10^{-18} \Delta N + 2.8 \cdot 10^{-20} (\Delta P)^{1.13} [\text{cm}^{-1}]$$

where ΔN and ΔP are respectively the free electron and the hole concentrations.

The one-dimension model for the direct biased PIN diode shows that the concentration of the injected holes and electrons are equal and are given by:

$$\Delta P \cong \Delta N = N_{D,A} \cdot v,$$

$$\text{with: } v = -\frac{L_i}{2L_c} \cdot \frac{\tau_c}{\tau_i} \cdot \tanh\left(\frac{w}{2L_i}\right) + \sqrt{\left(\frac{L_i}{2L_c} \cdot \frac{\tau_c}{\tau_i} \cdot \tanh\left(\frac{w}{2L_i}\right)\right)^2 + \frac{\tau_c \cdot J}{2L_c \cdot q \cdot N_{D,A}}}$$

To convert the phase modulation into intensity modulation, the device utilises a structure obtained by a cascade coupling of three Fabry-Perot (FP) cavities. The advantages of this configuration has been demonstrated theoretically [3]. This type of device is realised starting from a simple FP modulator where two lateral trenches are engraved by RIE. Each trench works as a FP cavity.

The transmittivity of this multilayer structure was calculated by using the "characteristic matrix" formalism [3]:

$$T = \frac{n_i}{n_f} \left| \frac{2n_i}{b} \right|^2$$

where n_i and n_f are respectively the refractive index of the semi-infinite external media that are at the output and at the input of the multilayer (for example SiO_2 , Si_3N_4 or Si); b is given by

$$\begin{pmatrix} a \\ b \end{pmatrix} = \begin{pmatrix} n_i & -1 \\ n_f & 1 \end{pmatrix} M_1 M_2 M_3 \begin{pmatrix} 1 \\ n_f \end{pmatrix}$$

M_j , $j = 1, 3$, is the characteristic matrix of the j th slab and, if a normal incidence is assumed, they have the form:

$$M_j = \begin{pmatrix} \cos \delta_j & \frac{i \sin \delta_j}{\tilde{n}_j} \\ i \tilde{n}_j \sin \delta_j & \cos \delta_j \end{pmatrix}$$

δ_j is a phase coefficient defined by $\delta_j = 2\pi \tilde{n}_j l_j / \lambda$, where \tilde{n}_j and l_j are respectively the complex refractive index and the length of j th layer.

For the central cavity, we have taken into account the guiding of the radiation, so that the matrix M_j contains the effective complex refractive index \tilde{n}_{eff} . Figure 2 shows the waveguide structure and the index profile in x - direction.

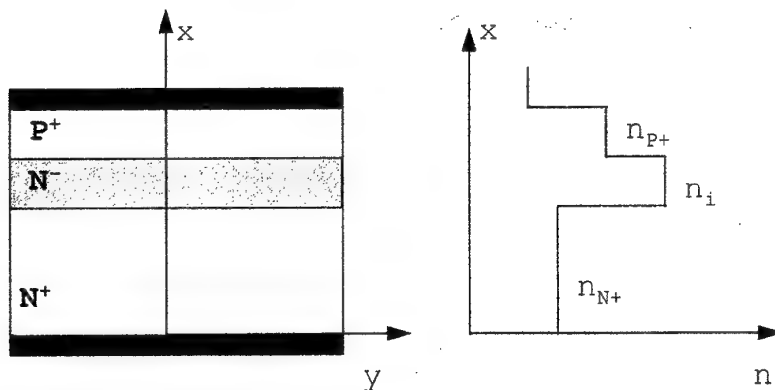


Fig. 2

For the computing of \tilde{n}_{eff} , we have used an efficient numerical method proposed by Anemogiannis and Glytsis [4]. The method is based on the argument principle theorem. It is applied to solving the multilayer waveguide dispersion equation derived from the thin-film transfer matrix theory.

3. NUMERICAL RESULTS AND CONCLUSIONS

The calculus was made using a C++ programme.

Our FPM device has the length l_a of both trenches of $1\text{ }\mu\text{m}$ and different lengths l_n of the silicon active cavity.

Figures 3 and 4 show the transmittivities computed as a function of the injected current density for different l_n . The shapes of the transmittivity curves are different for different lengths of FP cavity. The useful region of the curve is between the first maxim and the first minim.

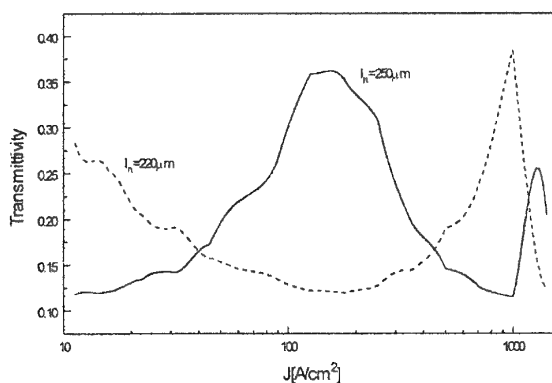


Fig. 3

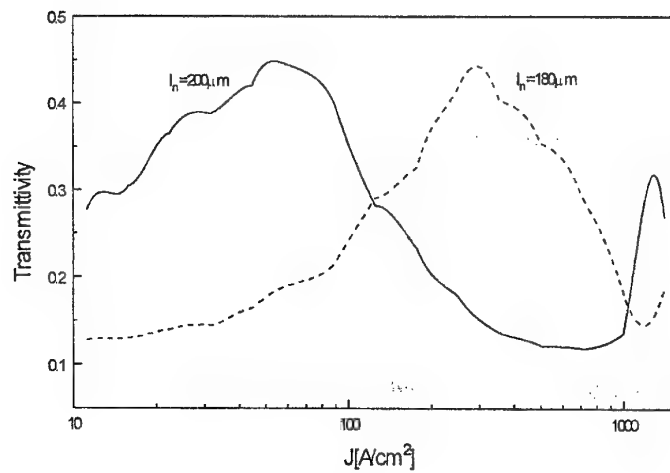


Fig. 4

4. REFERENCES

- [1]. Soref, R. A., Proceeding of the IEEE, vol. 81, no. 12, p. 1687 (1993)
- [2]. Soref, R. A., Bennett, B. R., IEEE Journal of Quantum Electronics, vol. QE-23, no. 1, p. 123 (1987)
- [3]. Cocorullo, G. et al., Optics Communications, vol. 86, no. 2, p. 228 (1991)
- [4]. Anemogiannis, E., Glytsis, E. N., IEEE Journal of Lightwave Technology, vol.10, no. 10, p. 1344 (1992)

APPLICATION OF FINITE ELEMENTS METHOD TO AVALANCHE PHOTODIODE

P. Schiopu, E. Lakatos, V. Degeratu, Stefania Ivan

"Politehnica" University Bucharest, Romania, S.C.Baneasa S.A., 016331464
Bucharest, Romania, University of Bucharest, Faculty of Physics, Romania

ABSTRACT

The finite elements method is an efficient research and development tool, with various utilizations and different applications. This paper shows the application of such a method to the avalanche photodiode design.

1. INTRODUCTION

The purpose of our study was to design an avalanche photodiode with guard ring by means of planar technology.

As shown in fig.1, two impurity diffusions are necessary, one for the photodiode "base", and another one for the guard ring.

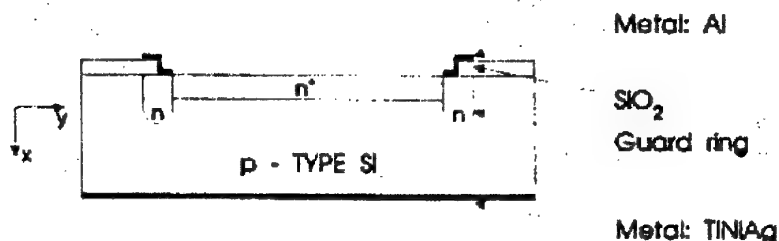


Fig.1 Cross-section view of the planar avalanche photodiode with diffused guard ring

The technological parameters, e.g., temperature and diffusion time, are the only things which make the two diffusions differ. Therefore, we will use a mere theoretical model for the two processes.

2. IMPURITY DIFFUSION IN Si

The phenomenological approach to the diffusion phenomenon is based on the Fick's law. This law was initially applied only to diffusion studied in gaseous and liquid medium; its extension to the solid structure was developed at the end of the XIXth century.

The net flux density J_c of the atoms from one species in the solid (the average number of atoms passing through a unit of area in a unit of time) is determined by the concentration gradient $C(r)$ of the species by a phenomenological relation known as the first Fick's law [1]:

$$J_c(\vec{r}) = -D\nabla C(\vec{r}) \quad (1)$$

where D is the diffusion coefficient [$\mu\text{m}^2/\text{h}$].

From the first equation the diffusion equation can be easily deduced, for the unidimensional case, [2]:

$$\frac{\partial C}{\partial t} = D \frac{\partial^2 C}{\partial x^2} \quad (2)$$

where t = time [h], x = spatial coordinate [μm].

In the unidimensional case, for a homogenous medium which does not contain internal heat sources, we have the following thermal conduction equation [3, 4]:

$$\frac{\partial T}{\partial t} = a^2 \frac{\partial^2 T}{\partial x^2} \quad (3)$$

where $a^2 = \lambda/(c\rho)$ and λ = thermal conduction coefficient, c = specific heat capacity, ρ = mass density, T = temperature.

Because of the similarity between the (2)nd and the (3)rd equation we can approach diffusion problems in solids in the same manner as problems of the conduction heat in solids.

The finite elements method is successfully used for solving the heat conduction problems [5, 6, 7, 8], and therefore we can use this method in the case of diffusion in solids.

2.1 The basic analytical model

We consider a homogenous semiconductor at a specified temperature where impurities of a specified type are injected.

Even if the impurities distribution in the semiconductor in three dimensional, it can be analysed by using a unidimensional model due to the fact that the concentration variation is dominantly unidirectional.

The basic analytical model is expressed by the diffusion equation (2) and the initial conditions, at limit respectively. In the 2nd equation C is the concentration of impurity atoms which is dependent on time (t) and position (x).

2.2 The numerical model

Finite unidimensional elements of linear type are used to discrete the analysed domain V (figure 2).

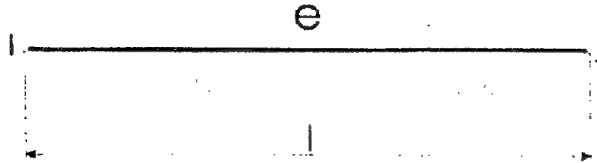


Fig. 2 The finite unidimensional elements of linear type

For a random element e with nodes i and j , the form functions are [5]:

$$\begin{aligned} N_i(x) &= \frac{x_j - x}{1} \\ N_j(x) &= \frac{x - x_i}{1} \end{aligned} \quad (4)$$

where x_i and x_j are the nodes coordinates of i , respectively j , and $1 = x_j - x_i$ is the finite element length.

The approximate concentration function on a finite element domain is:

$$\hat{C}(x) = N_i(x)C_i + N_j(x)C_j \quad (5)$$

where C_i and C_j are the concentration values in the nodes i and j of the considered finite element.

The transform of the basic analytical model in an integral form can be done by either varying the path or using the ponderate residual method. In our case we used Galerkin's method [7]. By introducing the approximate concentration function (5) in the (2)nd equation, applied to the elemental level, this is not anymore satisfied so that a residuum R^e is obtained as follows:

$$D^e \frac{\partial^2 \hat{C}}{\partial x^2} - \frac{\partial \hat{C}}{\partial t} = R^e \quad (6)$$

This residuum is equal to zero only for the limit case where $C(x) = C(x)$. Integrating the residuum on the V^e subdomains of the analysed domain V , we find the weight functions H_i , so that:

$$\sum_{e=1}^n \int_{V^e} H_i R^e dV = 0 \quad (7)$$

In Galerkin's variante, these weight functions are considered to be form functions. The elemental system is further obtained:

$$\begin{aligned} \int N_i (D^e \frac{\partial^2 \hat{C}}{\partial x^2} - \frac{\partial \hat{C}}{\partial t}) dx &= 0 \\ \int N_j (D^e \frac{\partial^2 \hat{C}}{\partial x^2} - \frac{\partial \hat{C}}{\partial t}) dx &= 0 \end{aligned} \quad (8)$$

where the transversal section through a finite element is constant ($A = \text{constant}$).

We see that:

$$\begin{aligned} \frac{\partial}{\partial x} (N_i D^e \frac{\partial \hat{C}}{\partial x}) &= N_i D^e \frac{\partial^2 \hat{C}}{\partial x^2} + D^e \frac{\partial N_i}{\partial x} \frac{\partial \hat{C}}{\partial x} \\ \frac{\partial}{\partial x} (N_j D^e \frac{\partial \hat{C}}{\partial x}) &= N_j D^e \frac{\partial^2 \hat{C}}{\partial x^2} + D^e \frac{\partial N_j}{\partial x} \frac{\partial \hat{C}}{\partial x} \end{aligned} \quad (9)$$

where the (8)th equations can be written as follows:

$$\begin{aligned} \int \frac{\partial}{\partial x} (N_i D^e \frac{\partial \hat{C}}{\partial x}) dx - \int D^e \frac{\partial N_i}{\partial x} x \frac{\partial \hat{C}}{\partial x} dx - \int N_i \frac{\partial \hat{C}}{\partial t} dx &= 0 \\ \int \frac{\partial}{\partial x} (N_j D^e \frac{\partial \hat{C}}{\partial x}) dx - \int D^e \frac{\partial N_j}{\partial x} x \frac{\partial \hat{C}}{\partial x} dx - \int N_j \frac{\partial \hat{C}}{\partial t} dx &= 0 \end{aligned} \quad (10)$$

By integration of the first terms of the upper equations, and by applying the first Fick's law (1) through nodes i and j of the finite considered element and by using mathematical processing we obtain the following matrix system:

$$\begin{bmatrix} \frac{1}{3} & \frac{1}{6} \\ \frac{1}{6} & \frac{1}{3} \end{bmatrix} x \begin{bmatrix} \dot{C}_i \\ \dot{C}_j \end{bmatrix} + \begin{bmatrix} D^e & -D^e \\ -D^e & D^e \end{bmatrix} x \begin{bmatrix} C_i \\ C_j \end{bmatrix} = \begin{bmatrix} j_i \\ j_j \end{bmatrix} \quad (11)$$

where i and j are the net nodal fluxes of the impurity atoms.

The matrix system (11) can be synthetically represented by the elemental numerical model:

$$K_e \dot{C}_e + A_e C_e = B_e \quad (12)$$

By assembling all finite elements of the analysed domain, the final system of working equations is obtained.

$$K\dot{C} + AC = B \quad (13)$$

In the case of the transient regime, the (13)th equation becomes [7]:

$$\left(\frac{2}{\Delta t} K + A\right) C_{n+1} = \left(\frac{2}{\Delta t} K - A\right) C_n + (B_{n+1} + B_n) \quad (14)$$

where (n + 1) and (n) are two consecutive time steps (t and t+Δt).

2.3 Initial conditions. Limit condition

Solid diffusion is most used in the semiconductor technology for obtaining diffused impurities layers. Typically the forms of the diffused layers are realised in a two stage process.

2.3.1 First stage (Pre diffusion)

In this stage the impurities are introduced in the semiconductor and the limit conditions are [9]:

$$C(0, t) = C_s \quad (15)$$

$$C(\infty, t) = 0 \quad (16)$$

respectively the initial condition:

$$C(x, 0) = 0 \quad (17)$$

where C_s is the impurities concentration at surface.

2.3.2 Second stage (Diffusion)

In this stage impurities already introduced in semiconductor are deeper diffused, without adding more impurities in the semiconductor. In this case the limit conditions are:

$$\frac{\partial C}{\partial x} \Big|_{(0,t)} = 0 \quad (18)$$

$$C(\infty, t) = 0 \quad (19)$$

respectively the initial condition:

$$C(x, 0) = \text{distribution of impurities after prediffusion stage} \quad (20)$$

3. THE 2D MODEL

Within one-dimensional description (on the Ox axis) of the two types diffusions, we provide a two-dimensional (2D) map (on the Oxy plan), for the impurity concentrations. In this respect we have used the results obtained in section two and discrete the analysis domain (see fig.1) in finite two-dimensional (2D) elements of triangular type, as shown in fig.3.

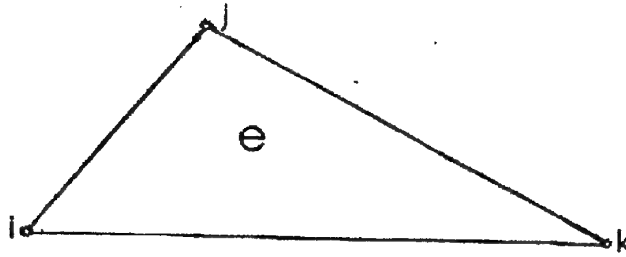


Fig.3 Element of triangular type

For a random element e with the nodes i and j and k the form functions are [5, 7]:

$$\begin{aligned} N_i &= \frac{1}{2A_e} (a_i + b_i x + c_i y) \\ N_j &= \frac{1}{2A_e} (a_j + b_j x + c_j y) \\ N_k &= \frac{1}{2A_e} (a_k + b_k x + c_k y) \end{aligned} \quad (21)$$

where A_e is the finite element area:

$$A_e = \frac{1}{2} \begin{vmatrix} 1 & x_i & y_i \\ 1 & x_j & y_j \\ 1 & x_k & y_k \end{vmatrix} \quad (22)$$

and the coefficient a , b and c are given by

$$\begin{aligned} a_i &= x_j y_k - x_k y_j & b_k &= y_i - y_j \\ a_j &= x_k y_i - x_i y_k & c_i &= x_k - x_j \\ a_k &= x_i y_j - x_j y_i & c_j &= x_i - x_k \\ b_i &= y_j - y_k & c_k &= x_j - x_i \\ b_j &= y_k - y_i \end{aligned} \quad (23)$$

The approximation function of the profile's concentration for each element is given by

$$\hat{C}(x, y, t) = N_i(x, y) C_i(t) + N_j(x, y) C_j(t) + N_k(x, y) C_k(t)$$

Once the 2D map obtained for the profile of the impurity concentrations, one may calculate [9, 10] the internal voltage of pn junction, the intensity of maximum electric field, the concentration gradient for the impurities in junction, and the break down voltage.

4. CONCLUSIONS

Although widely used in different fields, the finite element method is seldom used in the semiconductor case. This is the reason for which the authors considered necessary to theoretically describe the design problem for active electronical components and to provide solutions.

In section two, the starting point was the similar form for both the heat conduction equation and the diffusion equation. The solving principles of using the finite element method for the heat conduction in solids were applied in the case of impurities diffusion. The transformation of the differential basic

analytical model in an integral form was done using Galerkin's method, reaching to a matrix system good for computer processing.

The results concerning the diffusion process have been used in order to provide the two-dimensional (2D) map for the concentration of impurities. By using this profile one can obtain the main characteristics of the avalanche photodiode.

5. REFERENCES

- [1]. C.Kittel, Introducere in fizica corpului solid, Ed.Tehnica, Bucuresti, (1972).
- [2]. F.Reif, Fizica statistica, cursul de fizica Berkeley, vol.5, Ed.Didactica si Pedagogica, Bucuresti, (1983).
- [3]. V.S.Vladimirov, Ecuatiile fizicii matematice, Ed.Stiintifica si Enciclopedica, Bucuresti, (1980).
- [4]. V.S.Vladimirov s.a., Culegere de probleme ale ecuatiei fizicii matematice, Ed.Stiintifica si Enciclopedica, Bucuresti, (1981).
- [5]. D.Garbea, Analiza cu elemente finite, Ed.Tehnica, Bucuresti, (1990).
- [6]. M.Blumenfeld, Introducere in metoda elementelor finite, Ed.Tehnica, Bucuresti, (1995).
- [7]. V.Olariu, C.Bratianu, Modelare numerica cu elemente finite, Ed.Tehnica, Bucuresti, (1986).
- [8]. Proceedings of the 3-rd International Conference on Boundary and Finite Element-Section 3, Constantza, Romania, (1995).
- [9]. A.S. Grove, Fizica si tehnologia dispozitivelor semiconductoare, Ed.Tehnica, Bucuresti, (1973).
- [10]. A.Rusu, Modelarea componentelor microelectronice active, Ed.Academiei Romane, Bucuresti, (1990).

INFLUENCE OF ELECTRON-BEAM RECORDING CONDITIONS ON PROPERTIES OF DIFFRACTION GRATINGS OF SUBMICRON PERIOD

S.A. Sergeev, S.D. Shutov

Center of Optoelectronics, Institute of Applied Physics of the Academy of Sciences of Moldova,
5 Academiei Str., MD-2028 Kishinev, Moldova
Phone: (422) 73.98.05; e-mail: shutov@optoel.moldova.su

ABSTRACT

Phase diffraction gratings of periods from 0.4 to 1.2 μm have been formed in amorphous $\text{As}_{50}\text{S}_{50}$ films by electron-beam recording. The influence of the beam current and energy on the modulation depth of the refraction index Δn_1 was studied. The experimental results are described with the aim of a model accounting for the dose-induced broadening of the recorded lines. The limitation of the Δn_1 value in the gratings of submicron periods is associated with overlapping of successively recorded lines.

1. INTRODUCTION

Diffraction properties of gratings of submicron period formed by electron-beam recording in chalcogenide films [1] are determined to a large extent by the degree of mutual overlapping of neighboring lines (the so called proximity effect) [2]. In the present work, the experimental study of the effect of the recording conditions (current and energy of the beam, grating period) on the refractive index modulation in the films is analyzed with the aid of a model accounting for the dose widening of lines.

2. EXPERIMENTAL RESULTS

The diffraction gratings were recorded line by line a scanning electron microscope BS 300 in $\text{As}_{50}\text{S}_{50}$ chalcogenide-glass films of thickness $d=1.2 \mu\text{m}$ thermally deposited onto glassy substrates. The diffraction efficiency (η_1) of the gratings was measured in the first diffraction order of the transmitted laser beam ($\lambda=0.633 \mu\text{m}$). Based on the measured η_1 values the refraction-index modulation depth (Δn_1) was calculated ($\Delta n_1=(2\lambda/\pi d)\eta_1^{1/2}$). A set of diffraction gratings with period $\Lambda=0.4$ to $1.2 \mu\text{m}$ was recorded with the beam energy $E=15$ to 29 keV and the beam current $I=0.6$ to 8.0 nA .

In Fig.1 there are illustrated the experimental dependences $\Delta n_1(I)$, which represent the dose dependence of the modulation depth for a constant line scanning speed. Lines in Fig.1 are calculated according to the model discussed below. The dependences show a broad maximum, which is observed at greater currents for the higher energies and larger period. The increasing portion of the $\Delta n_1(I)$ curve, which is longer for $\Lambda=0.8 \mu\text{m}$ (Fig.1a), was approximated by almost linear dependence $\Delta n_1(I) \propto I^p$, where $p=1.0$ to 1.1 . The behaviour of the $\Delta n_1(E)$ dependence was determined by the beam current. The greatest change of Δn_1 with increase of E was observed over the decay portion of the $\Delta n_1(I)$ dependence in the range of high currents (Fig.1). In this case the increase of Δn_1 with E (curves 1 and 2 in Fig.2) followed the power law $\Delta n_1 \propto E^q$, and q increased with the beam current from 0.8 and 1.4 to 2.1 and 3.6 for the periods 0.8 and $0.4 \mu\text{m}$, respectively. The maximal value of Δn_1 (curves 3 and 4 in Fig.2) increased with E much weaker.

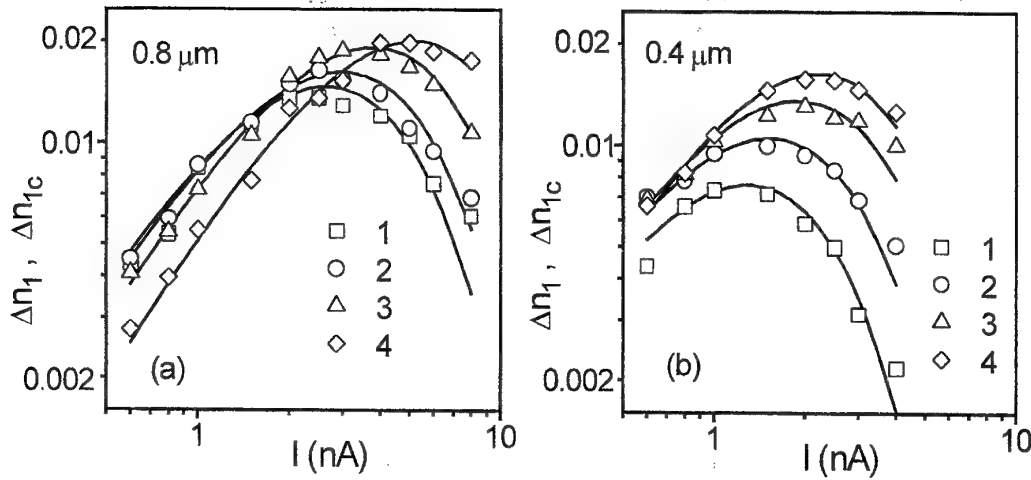


Fig.1 Experimental (symbols) and calculated (lines) dependences of the refractive index modulation depth on the beam current for gratings of periods 0.8 μm (a) and 0.4 μm (b)
The beam energy, keV: (a) - 15 (1), 17 (2), 21 (3), 25 (4); (b) - 15 (1), 19 (2), 23 (3), 25 (4)

3. MODELLING OF GRATING PROFILE

For the record line a Gaussian distribution of refractive-index increment across the line was assumed [3], with the halfwidth of line w_0 and maximal increment Δn_0 in the middle of line. It is known that the cross-section of interaction of the electron beam with a resist increases with the beam current due to scattering, and decreases with the beam energy increase [4,5]. The obtained experimental data indicate that dose increment Δn_0 and record line widening may be described by power law dependencies

$$\Delta n_0 = A \cdot I^\alpha \text{ and } w_0 = B \cdot I^\beta, \quad (1)$$

where A and B are constants for a given value of the beam energy. The distribution of the refractive index increment $\Delta n(x)$ along the grating was expressed as a sum of m equidistant record lines of Gaussian profile

$$\Delta n(x) = \sum_m \Delta n_0 \exp[4 \ln 2 (x - m\Lambda)^2 / w_0^2] \quad (2)$$

The summation of profiles accounted for the repeat irradiation in the overlapping areas of neighbouring lines. Under above assumptions computer calculations of the $\Delta n(x)$ profile have been performed for periods 0.4 and 0.8 μm with I as variable and E as parameter. Then, for the calculated $\Delta n(x)$ profiles, the modulation amplitudes of the first harmonics and calculated $\Delta n_{1c}(I)$ dependence were determined through the Fourier expansion. The coefficients A , B and powers α and β were varied up to the best fit of the calculated $\Delta n_{1c}(I)$ curve and experimental points. Shown in Fig.1 the $\Delta n_{1c}(I)$ curves adequately describe the experimental data thus supporting the suggestions of the model.

The fitting parameters A , B , α and β offer information about the shape of the record line and its variation with both the beam energy and current. The parameters were determined with the accuracy of 2 to 5 %. The powers α and β were almost independent on E , its values were approximately the same for both grating periods and have the mean value 1.1 and 0.5, respectively. Contrary, the coefficients A and B markedly depended on E . The B coefficient decreased monotonously with increasing of E as $B = C/E + B_0$ (line in Fig.3); the difference in B for the two periods vanished at high energies.

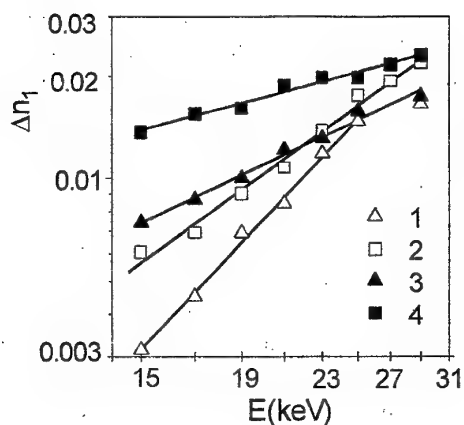


Fig. 2 The dependences of Δn_1 (1,2) and its maximal value (3,4) on the beam energy for grating periods $0.4 \mu\text{m}$ (1,3) and $0.8 \mu\text{m}$ (2,4). Curves 1 and 2 are given for fixed beam currents 3 nA (1) and 8 nA (2).

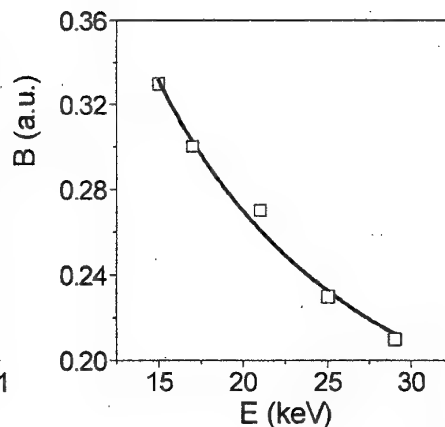


Fig. 3 The dependence of the parameter B on the beam energy.

4. DISCUSSION

Modelling of the grating profile reveals the interrelation between the record line parameters and the system of lines (grating). For a single record line the refractive index increment is described by the Gaussian distribution, the height of which is increased with the irradiation dose up to the value achievable for the given resist, while the halfwidth expands monotonously. As the powers α and β in (1) are weak functions of energy, the dependences of both w_0 and Δn_0 on the current and the energy of electron beam may be separated. The former is determined by the current powers α and β , while the latter is governed by the proportionality coefficients A and B . With increasing the irradiation dose, the height of the line grows faster ($\Delta n_0 \propto I^{1.1}$) than its halfwidth ($w_0 \propto I^{0.5}$). This means that along with the line widening due to the increase in the beam current, the dispersion of the record line decreases.

The dependence of the linewidth on the beam energy is determined by the B coefficient, which is numerically equal to the halfwidth of the line (in micrometers) at a fixed beam current (1 nA). Decreasing B with the beam energy increase, indicates the narrowing of the record line. According to above mentioned empirical relation, the value of B decreases reversely proportional to E approaching to a limit B_0 , which is most likely determined by the diameter of incident electron beam. The calculated halfwidth of the record line for $A=0.8 \mu\text{m}$ varied from $0.16 \mu\text{m}$ (29 keV, 0.6 nA) to $0.93 \mu\text{m}$ (15 keV, 8.0 nA).

Unlike the powers α and β controlling the dose dependence of the single line parameters, the coefficients A and B , which describe the energy dependence of them, were different for the two grating periods. This difference is in the limits of 2 and is caused by submicron period dimensions, when the halfwidth of the record line is close to period ($B/A = 0.27$ to 0.60) and the contribution of the first harmonics of Δn_1 is significantly dependent on the grating period and the beam energy. The A coefficient falls down due to decrease of the resist sensibility to higher beam energies [5].

The regular system of record lines forms the grating of a non-sinusoidal profile. Unlike the record line the grating lines are limited by period and for large periods ($w_0 \ll A$) consist of both irradiated and non-irradiated regions. At low beam currents ($w_0 < A/2$) the record lines are separated and the modulation depth of the refractive index increases in proportion with Δn_0 , i.e. $\Delta n_1 \propto I^{1.1}$. At high beam currents ($w_0 > A/2$) the irradiated areas overlap, i.e. the resist is partly doubly irradiated. The minimal

value of the refractive index in the system of lines is increased and the modulation depth first stops to grow and then becomes decreased. The region of the Δn_1 peak corresponds to the grating profile which is closest to sinusoidal one. Narrowing the record lines at high beam energies weakens overlapping leading to both the strong Δn_1 increase (Fig.2) and shift of the $\Delta n_1(I)$ maximum position to higher doses.

5. CONCLUSIONS

The diffraction gratings may be divided into two groups by the degree of proximity of the record lines: with isolated and with overlapping lines. For the first group of gratings the phase modulation depth increases with dose. The profile of the second group is governed by the proximity factor, in consequence of which the phase modulation depth both decreases with increasing of the dose and increases with the beam energy. Experimental dependences of the diffraction efficiency on the beam current and energy are well described with a model, which considers the grating as a system of single lines of Gaussian profile with parameters depending of both the irradiation dose and energy.

6. REFERENCES

- [1]. Suhara T. and Nishihara H. IEEE J. Quantum Electronics, QE-22, 845 (1986)
- [2]. Deshmukh P.R. and Khokle W.S. IEEE Trans. Electron Devices, 36, 2011 (1989)
- [3]. Nishihara H., Handa Y., Suhara T. and Koyama J. J. Appl. Optics, 17, 2342 (1978)
- [4]. Phang J.C.H. and Ahmed H. Proc. IEE, 128, 1 (1981)
- [5]. McInerney J., Fice M.J. and Ahmed H. J. of Lightwave Technology, LT-4, 1494 (1986)

ACOUSTIC WAVES DETECTION SYSTEM FOR CLOSED AREAS WITH THE HELP OF ACOUSTO-OPTICAL SENSORS

V.Bivol, A.Prisacari, *Gh. Paun

Center of Optoelectronics of Academy of Sciences of Moldova Republic
1 Academiei Str., MD-2028, Kishinev, Moldova Republic.

Tel/Fax: (3732) 739805. E-mail: bivol@as.md

* Institute of Optoelectronics S.A.

P.O.BOX MG-22, 76900 Bucharest-Magurele, Romania. Tel.(401)7806640, Fax: (401) 4232532

ABSTRACT

The object of this paper is the way and system of revealing the presence of acoustic waves in closed areas with the help of acoustic-optical sensors and the method of analysis of these acoustic signals. As a result of additional amplification of acoustic fluctuations by optical interferometer and laser, the system's sensitivity grows. The use of optical interference and laser radiation allows the registration of small fluctuations of reception membranes and provides a high system sensitivity.

1. EXPERIMENTAL RESULTS AND DISCUSSION

The modern security signal systems consist of two groups of means: systems of remote observation and various sensors working in an automatic mode. The video cameras work in wide range of illuminations as well as in darkness by using of Infra- Red illumination. The mesh sizes of video cameras make them little noticeable, but it is not always important: proper equipment allow from several hundreds meters distance to observe the image originating on the monitor screen and thus to estimate the review of video cameras, as well as their layout.

The sensors can be divided into two groups: active and passive. The active sensors fill protected volume by various signals and observe their returning. In case of a change in the parameters of the coming back signals, the sensors give alarm. Such active sensors are the Dopplier sensor of driving, capacity and systems with a security ray. Passive sensors are the magneto controlled contacts (herkones), used on windows and doors as sensors of discovery - closing, inertial contacts (sensors of driving) - for example, on glasses, sensors of deformation, vibration, infra-red radiation, sensors of the fire signal system and destruction (stretched wire).

The use of any type of security device does not ensure 100 % safety of the protected object: it is possible to lull by gas, the layout of herkones can be found out with the help of compass and to neutralize by rather powerful external directed magnetic effect. Desired safety can be ensured only by combination of various types of systems.

Offered acoustic-optical sensors can be used as passive sensors, in structures of active systems (for example, ultrasonic sensor of driving). The high sensitivity of gauges is ensured with the interference circuit of conversion of acoustic oscillations in electrical.

The acoustic-optical system consists of the laser (1), beam splitter (2), mirror (3), membrane (4) and photo diode (5). The laser radiation is divided on beam splitter in two rays. The first ray is reflected from a mirror, the second from a membrane. The reflected rays converge in beam splitter, develop and form an interference picture. Light diode is located between a minimum and maximum of interference lines. With arrival of a signal the membrane is bent, the arms relation of an interferometer varies, the interference picture is floating and the light exposure of the photo diode varies. The material, width and tension of a membrane are selected and calculated so that the membrane changed in a wide range of frequencies - from infra sound up to ultrasonic oscillations. With offset of a membrane on $\lambda/4$ light exposure of the photo diode varies from minimum before maximum value, that ensures registration of very weak acoustic oscillations.

Sensor systems can be applied to listening protected locations in pair with a video camera and work as passive sensors (any sound in closed area is an occasion to check). So, sound of a cutted glass or

opened lock can be registered by the offered system. In Infra-Sound range, steps, the closing of windows and doors can be registered.

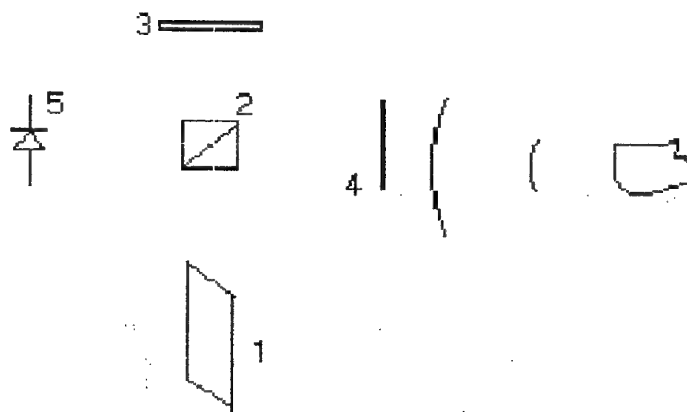


Fig.1 Acoustic-optical detection system

2. CONCLUSIONS

The acoustic-optical sensors take part from the active sensors category, which have, as operating principle, the filling of the protected volume by various signals and the following of their returning. In case of a change in the parameters of the coming back signals, the sensors give alarm.

The system is destined to make evident the acoustic wave presence in a closed circular area, by means of acoustic-optical sensors and analyze methods of acoustic signals.

As a result of acoustics fluctuation magnification by optical interferometry and laser, the system sensitivity grows.

The use of optical interference and laser radiation allows the registration of small fluctuations of reception membranes and provides high system sensitivity.

3. REFERENCES

- [1]. R.A. Marsland, "Balanced Photoreceivers Reject Intensity Noise and Reach the Shot-Noise Limit", Laser Focus World, March 1994, pp. S41-S43.
- [2]. R.A. Marsland, "Selection and Applications of High-Speed Photodetectors", The Photonics Designs and Applications Handbook (1993).
- [3]. William S. Gornall, "Interferometry determines wavelengths precisely" Laser Focus World November (1997).

Session A4 & B6

**TECHNOLOGIES IN OPTOELECTRONICS
AND ENVIRONMENT**

INTERFEROMETRIC DEVICES FOR INTEGRATED OPTICS REMOTE SENSOR SYSTEMS

H. Porte*, W. Elflein, J.P. Goedgebuer

Laboratoire d'Optique P.M.Duffieux, UMR CNRS 6603
Université de Franche-Comté, Institut des Microtechniques
F-25030 Besançon Cedex France

ABSTRACT

This paper reports some recent results obtained in the field of integrated optics technology applied to coherence modulation sensor systems and proposes several examples of integrated Mach-Zehnder interferometers featuring optical delays of some tens to some hundred of micrometers, each of them being specifically designed for one sensing application. The first device is based on the use of lithium niobate technology. This electrooptic device can be used in the demodulation process of the sensor system which uses an electronic feedback to produce a linear phase tracking of the signal supplied by the sensor and yields to a remote sensor system, able to read the phase variations produced by any interferometric sensor. This system is applied to a gas sensing operation involving a second device integrated in glass by using an ion exchange process (K^+ - Na^+). The phase variations are produced here by the interaction of the evanescent wave of the guided light with a thin polymeric layer. The refractive index variation of the latter is proportional to the concentration of absorbed gas, resulting in a chemical sensor, able to detect and measure the concentration in air of organic gases. The last example of integrated optical device uses the silicon technology. The aim is to realize a micromachined pressure optical sensor. Under one waveguide arm, a set of membranes is etched by anisotropic etching using KOH. The variations of optical path delays are obtained here by deformation of the membranes submitted to pressure variations.

1. INTRODUCTION

The application of optical fibers in sensor systems has been investigated for many years, using them as a transmission support, but also for their capability to sense various physical parameters intrinsically [1]. Singlemode fibers become highly sensitive phase transducers for these parameters when used in an interferometric configuration. Several problems need careful attention in such sensor systems in order to achieve good performance. First of all, although all-fiber interferometers feature a high sensitivity, their output is a non-linear cosine function of the phase which can therefore not be read directly and a demodulation process is required to retrieve the original signal. An other drawback of all-fiber interferometers is the difficulty to separate different parameters (e.g. pressure and temperature) at the output.

Coherence Modulation is based on the use of a CW broadband source (BBS) with a low-coherence radiation, and interferometers whose optical path-difference (OPD) is larger than the coherence length. Coherence modulation [2-4], when coupled to integrated optics technology is an attractive way to solve a part of the problems mentioned previously. One advantage of coherence modulation is the possibility to determine the amplitude and the sign of the fringe displacement which is proportional to the signal applied to the sensor. Therefore, the demodulation can be unambiguous, even if the phase variation of the signal is larger than π . The solution consists to detect directly the output power with a receiving interferometer tracking the OPD to be measured. However, as most of the demodulation interferometers previously reported up to the present are all-fiber devices [5], they can suffer from temperature and mechanical instabilities. The development of superluminescent diodes (SLD) whose coherence length does not exceed some tens of microns makes the use of electrically driven integrated

optics transducers possible. These compact devices are inherently more stable and reliable than the large path-imbalanced ($>1\text{m}$) all-fiber interferometers required for laser sources with long coherence length. A system based on the use of integrated optics modulators is quasi temperature independent.

We describe first in this paper a sensor system dedicated to the measurement of concentration of organic gases. This system is based on the use of coherence modulation and allows a remote interferometric measurement. Two different integrated optics technologies are required in a complementary way. Integrated optics in glass is used to realize the sensor itself, whereas lithium niobate technology is used for the demodulation process which performs an active phase read-out [6,7]. The sensor uses a polymer material whose refractive index varies with the gas concentration, and thus modifies the characteristics of the evanescent part of the wave propagating in the glass waveguide.

Then, we investigate theoretically and experimentally the principle of a micromachined pressure sensor integrated in silicon [8-10]. The optical part of the sensor consists of an imbalanced Mach-Zehnder waveguide interferometer. The sensing part of the device consists in a set of membranes obtained by anisotropic etching of the back face of the substrate under the reference arm. The pressure variations applied to the membrane induce a geometrical deformation of the waveguide arm and modify the optical path-difference between the arms. The non linear variation of the phase versus the applied pressure is obtained from the spectral analysis of the channeled spectrum transmitted by the interferometer. The static optical path-delay introduced between the arms allows the sensor to be introduced in a coherence modulation scheme, which can results in a remote sensor system, involving an active demodulation.

2. GAS SENSOR SYSTEM

Description of the system and principle of operation

Integrated optics technology allows solid-state interferometric structures to be realized that are more robust and reliable and whose response is more selective than fiber sensors. Another advantage is that the interaction of evanescent waves with a material deposited directly onto the waveguide is easily realized since the optical waveguides are generally located at the substrate surface [11,12].

Figure 1 shows the setup of the gas sensor system which is based on the former principle. This system includes an optoelectronic central processing unit (OECPU) and an in-line gas sensor connected to the former by optical fiber. The OECPU contains a short coherence length optical source. The latter is a superluminescent diode of optical power $P_o=0.5\text{mW}$ emitting at $\lambda_o=1280\text{nm}$, and of the spectral width $\Delta\lambda=50\text{nm}$. Thus, the coherence length is $\ell_c=\lambda_o^2/\Delta\lambda=32\mu\text{m}$. At the measurement site, a Mach-Zehnder interferometer integrated in a glass substrate is used as a sensor. The two arms of the interferometer are of different length L_1 and L_2 . Here, any wave packet of coherence length ℓ_c , emitted by the continuous wave broadband source (BBS) is divided in two wave packets. At the output of the interferometer, these packets are separated by a fixed optical delay $\delta_o=n_{\text{eff}}(L_2-L_1)$, δ_o being larger than the coherence length ℓ_c . Here, n_{eff} is the effective index of the guided mode.

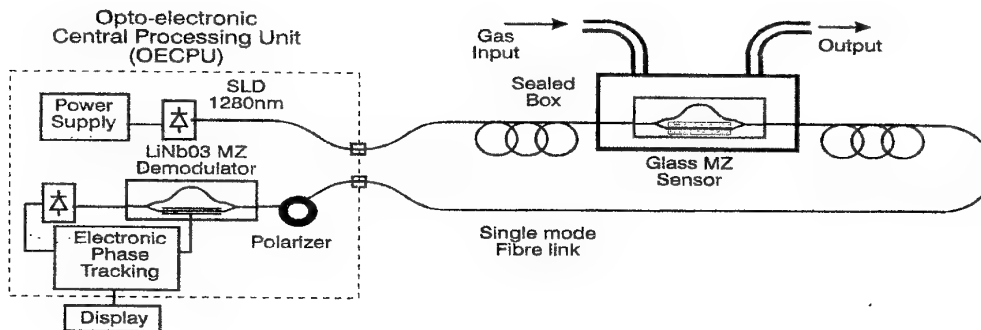


Fig. 1 Experimental setup of the remote gas sensor

The system is based on coherence modulation of light. It includes two integrated Mach-Zehnder devices. One is used as a sensor; the other one is used as an active demodulator. The measurement site is linked to the optoelectronic central processing unit by a single-mode optical fiber.

Under these conditions, no intensity modulation occurs at the output of the Mach-Zehnder and the transmitted optical power remains constant. The sensing process is the following. A thin layer of silicon dioxide is deposited at the surface of the waveguide interferometer. In this isolation layer, a window of length ℓ_s is opened over the sensing arm. The latter is then coated with an organic material. The polymer used is the Dimethyl-phenyl-methyl-siloxane (DPMS), and behaves as a porous material able to absorb organic molecules, proportionally to their concentration in air. It results in a variation of the refractive index of the polymer superstrate proportionally to the concentration, the process being reversible. The mechanism linking the variation of the phase of the guided mode in the sensing arm to the refractive index variation is based on the interaction of the evanescent wave with the polymer.

The total optical path difference (OPD) of the interferometer, including the static path delay and the one depending on the concentration C of gas is thus given by:

$$\delta(C) = n_{\text{eff}}(L_2 - L_1) + \ell_s \frac{dn_{\text{eff}}}{dn_1} \frac{dn_1}{dC} C \quad (1)$$

Here, dn_1/dC is the coefficient of proportionality between the refractive index variation of the polymer and the concentration of gas. For DPMS, dn_1/dC is $4.1 \cdot 10^{-2}$ for the vapor of ethanol and $1.3 \cdot 10^{-2}$ for the butane gas. For our waveguide dn_{eff}/dn_1 was calculated to be $9 \cdot 10^{-3}$. The phase variation obtained with butane per millimeter of interaction length is expected to be $5.8 \text{ mrad/Vol\%/mm}$. The order of magnitude of δ_0 is of some tens to some hundred of microns. The variation of OPD under the influence of the gas concentration C is typically limited to some microns.

After transmission through the sensor, the optical signal propagates in the fiber and is demodulated in the OECPU where a second Mach-Zehnder interferometer featuring the same static OPD converts the variations of OPD in intensity variations. The static OPD of the demodulator introduced between the arms of length ℓ_1 and ℓ_2 of the Mach-Zehnder is given by $\delta_0 = N_{\text{eff}}(\ell_2 - \ell_1)$, where N_{eff} is the effective index of the guided mode in the waveguide. If the OPD of the decoding interferometer remains constant, the signal detected by the photodetector is a cosine function of the variation of phase produced by the sensor.

In order to get a linear phase tracking, the decoding interferometer is realized in a lithium niobate crystal featuring an electrooptic effect. Thus, it becomes possible to control the OPD of the demodulator with an electrical voltage V applied to the electrodes deposited on the Mach-Zehnder arms. The orientation of the crystal, of the applied electric field and of the polarization of the light are chosen in order to get the highest electrooptic sensitivity. With a Z-cut crystal, the applied electric field and the polarization of the light (TM) being parallel to the Z-axis, the total OPD due to the decoding modulator and including the electrooptic effect is given by:

$$\delta(V) = n_e(\ell_2 - \ell_1) + \alpha V \quad (2)$$

with $\alpha = \frac{1}{2} n_e^3 r_{33} (\ell_2 + \ell_1) \frac{\eta}{d}$. Here $n_e = N_{\text{eff}}$ stands for the extraordinary refractive index of LiNbO_3 ($n_e \approx 2.14$), r_{33} is the highest electrooptic coefficient of the crystal ($r_{33} = 30.8 \text{ pm/V}$), η is the coefficient related to the overlap between the electrical and the optical fields ($\eta \approx 0.45$), d is the gap between the electrodes, and $(\ell_2 + \ell_1)$ is the total length of interaction for the electrodes considered here in a push-pull configuration. For instance, with a total length of electrodes of 30 mm, with a gap $d = 10 \mu\text{m}$, and with a voltage ranging between -15 V and $+15 \text{ V}$, the total accessible variation of OPD is about $6 \mu\text{m}$. Thus, this value is comparable to the possible OPD variations of the sensing interferometer due to variations of gas concentration.

The optical signal transmitted by the demodulator and detected by the photodetector is proportional to:

$$I(C, V) = \frac{P_0}{4} \left[1 + \frac{1}{2} \cos \frac{2\pi}{\lambda_0} (\delta_g(C) - \delta_g(V)) \right] \quad (3)$$

The system behaves as if there was only one interferometer in the system, with one sensing arm on the measurement site and the other one in the OECPU. This is the key point of the system, since it is possible to keep the phase constant with the help of the voltage V , and to control and measure the phase variations of a sensor which can be distant of some hundred of meters up to some kilometers. The former aspect is of particular interest since this system does not require any electrical wires between the measurement site and the processing site. Hence, the phase remains constant and equal to 0, as long as the feedback voltage V verifies:

$$V = \frac{\ell_s}{\alpha} \frac{dn_{eff}}{dn_1} \frac{dn_1}{dC} C \quad (4)$$

This equation shows that it is possible to convert the concentration of gas into an electrical signal with an optical sensor system. Since the phase is measured directly, the system is insensitive to spurious intensity fluctuations, that may be caused on the transmission line.

Description of the integrated optics devices

Glass waveguide device:

The Mach-Zehnder interferometric sensor integrated in glass is represented in figure 2. The device was realized using standards techniques : first a thin layer of aluminum was evaporated onto the glass sample. Using photolithography and chemical etching, the masking metal layer was opened to form stripes of $4\mu\text{m}$ wide. One arm of the Mach-Zehnder follows a straight line, while the other one is composed of four circle arcs with a bend radius $R=50\text{ mm}$. The geometrical difference of length between the arm is $58\mu\text{m}$.

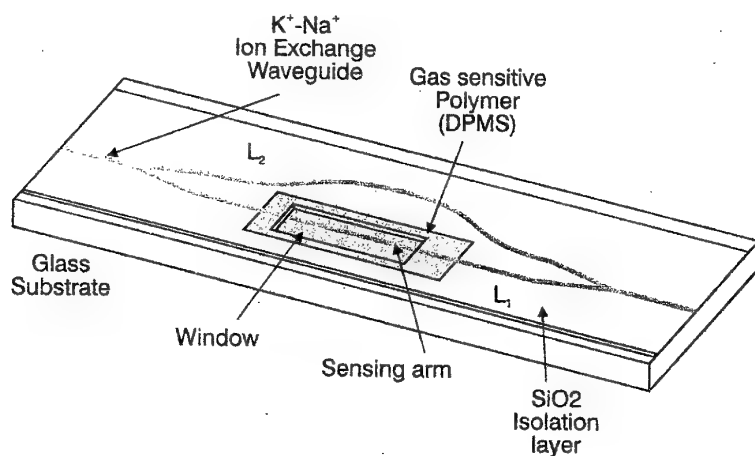


Fig. 2 Interferometric Mach-Zehnder sensor integrated in glass by $\text{K}^+\text{-Na}^+$ ion exchange process

The waveguide is obtained by standard $\text{K}^+\text{-Na}^+$ ion exchange process in pure molten KNO_3 during 2-3 hours at 380°C , resulting in a single mode waveguide at 1300nm -wavelength. The time of exchange was chosen in order to optimize the size of the optical field for an efficient coupling with a single mode fiber. The end faces were optically polished and a SiO_2 protecting layer was evaporated at the surface of the sample. A lift-off process was used to remove this protecting layer in order to open a window over the sensing arm. The length of the window corresponds to the length of the straight arm, i.e.

$\ell_s=24\text{mm}$. The polymer DPMS was diluted in dichloromethane (9%) and then coated onto the sensing arm. The device was then pigtailed with single-mode fibers, resulting in -5dB total insertion losses. The OPD was measured to be $91\mu\text{m}$.

Lithium niobate waveguide device :

The lithium niobate demodulator depicted in figure 3 was realized using a conventional diffusion process. A 50 nm thick titanium layer is evaporated using an electron beam at the surface of a Z-cut crystal. The waveguide pattern is then reproduced by a photolithographic process and the layer is etched by $\text{SiCl}_4/\text{Cl}_2$ reactive ion etching. The width of the titanium stripes is $6\mu\text{m}$. The geometrical difference of length between the arms is $38\mu\text{m}$.

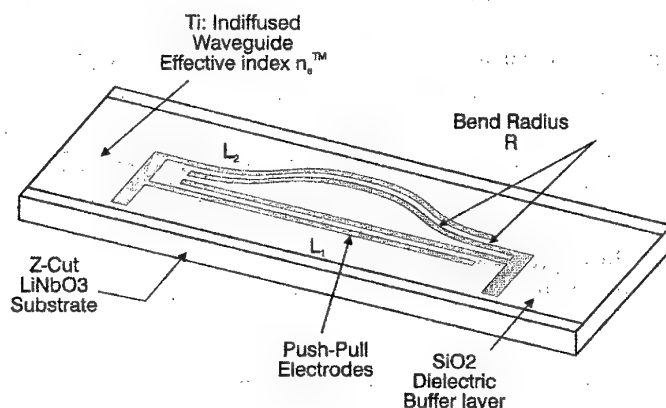


Fig. 3 Lithium niobate integrated optics Mach-Zehnder interferometer

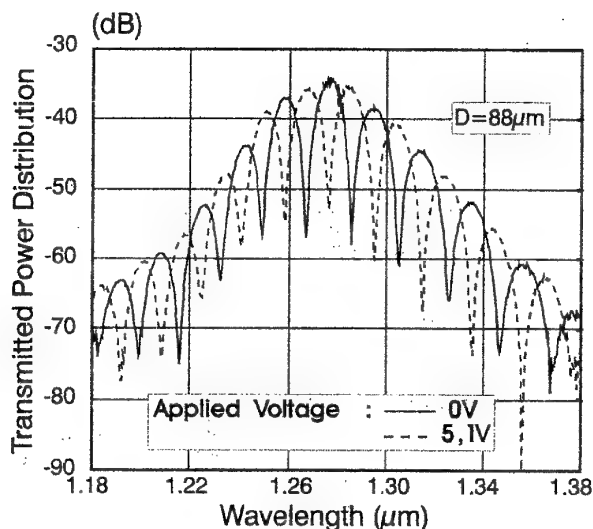


Fig. 4 Channeled spectrum transmitted by the lithium niobate Mach-Zehnder interferometer. The fringe spacing is 18.3nm . The curve in dotted line is obtained for an applied voltage of 5.1V corresponding to the half-wave voltage V_π .

The waveguides are then formed by high temperature diffusion (1050°C) of the titanium layer during 8 hours in a wet oxygen atmosphere. After diffusion, the end faces are polished and the sample is coated with a silica dielectric buffer layer of thickness 180 nm , and with an aluminum layer. The electrodes are patterned in the aluminum layer by chemical etching. The waveguide pattern represented

in figure 3 is designed in order to optimize the efficiency of the electrooptic interaction. The total insertion loss of the singlemode pigtailed device is better than -6dB.

The characteristics of the device were measured by spectral analysis. The transmission spectrum is represented in figure 4. The distance between adjacent peaks is here of $\Delta\lambda=18.3nm$ yielding a group static OPD introduced by the Mach-Zehnder of $89.5\mu m$. The sensor and the demodulator have their OPDs matched with an accuracy better than 2%. The curve in dotted line is in phase opposition with the one in solid line, corresponding to the application of the half-wave voltage V_π , which was measured here to be 5.1V, in good agreement with the predicted value that can be calculated from the parameters given in section 2.

3. EXPERIMENTAL RESULTS

Testing and calibration were carried out by setting the sensor waveguide coated with the DPMS polymer into a hermetic package. Input and output pipes were used to inject a flow of air into the box with a known and previously calibrated gas concentration. The DPMS polymer has a good sensitivity to hexane methane and other gases. The results reported here are obtained with butane and vapor of ethanol.

The demodulation process and the optoelectronic feedback circuit which performs the linear tracking of the interferometric sensor signal were described in ref.7. The performances of the latter are the following : the output voltage range is -13V to +13V. This is equivalent to a total phase range of $\Delta\phi_{max}=5\pi rad$. Due to noise, the smallest detectable phase shift (SDPS) is found to be $\Delta\phi_{min}=2mrad$. The dynamic range is thus $DR = 10\log(\Delta\phi_{max} / \Delta\phi_{min}) = 39dB$.

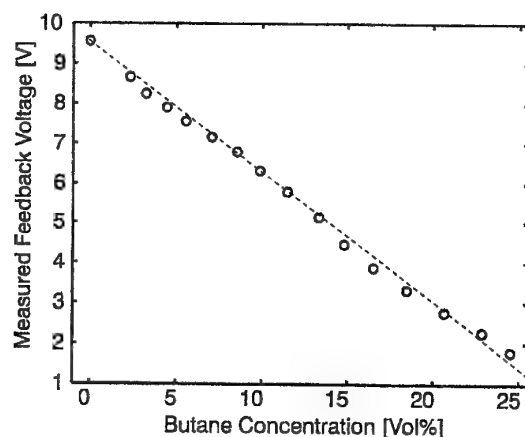


Fig. 5 Measured feedback bias voltage versus the concentration in air of the butane gas

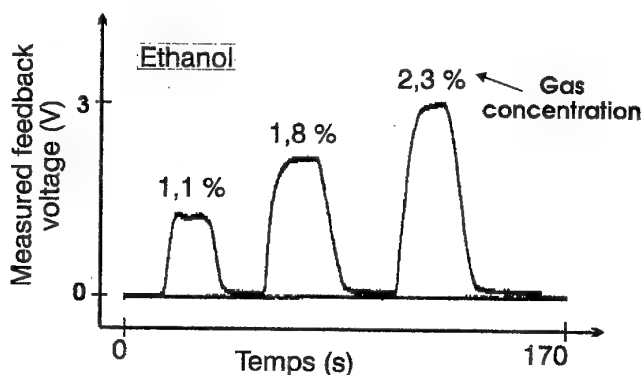


Fig. 6 Temporal response of the sensor system. Three pulses of vapor of ethanol are applied. The measured feedback voltage is plotted versus time in seconds

Figure 5 shows the results obtained with the measurement of concentration of butane gas in air. The gas concentration varies between 0 and 25% in volume. The feedback bias voltage variation is 8.1V and the resulting sensitivity can be assessed to be 8.3mrad/%Vol/mm. This value can be merely compared with the theoretical value of 5.8mrad /Vol/% /mm. The absolute sensitivity for a 24 mm-long interaction is thus 0.2 rad/Vol %. Since the SDPS is 2mrad, the sensor has a resolution of gas concentration of 0.01% in volume. Figure 6 shows the response obtained when applying to the sensor three pulses of vapor of ethanol of calibrated concentrations equal to 1.1%, 1.8% and 2.3% respectively. Here, the sensitivity is of 0.8rad/Vol% and the response time of the sensor was measured to be 6 seconds.

4. SILICON PRESSURE SENSOR

Description

The pressure sensor described here can be introduced in the processing system represented in figure 1. The device is depicted in fig. 7, and consists of a (100) silicon substrate. An imbalanced Mach-Zehnder interferometer is integrated on the top face of the substrate. One interferometer arm is bent in order to introduce an optical path-delay. This bent arm is the reference arm. The straight arm is the sensing arm. Under the latter, three membranes of thickness e are micromachined from the back face of the substrate.

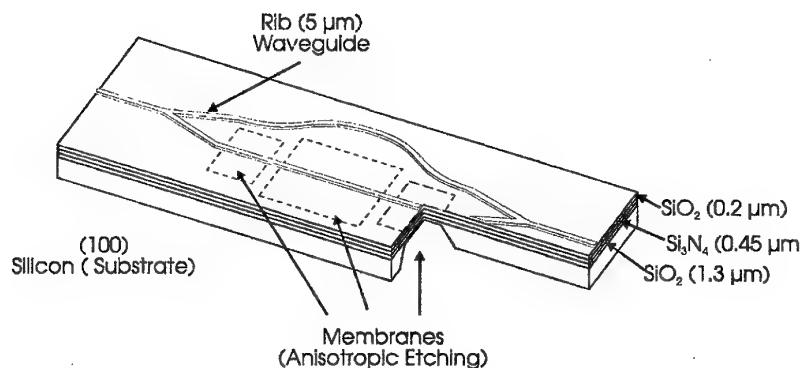


Fig. 7 Mach-Zehnder pressure sensor integrated in silicon. The waveguide is obtained with a silicon nitride layer set between two layers of silicon dioxide. Three membranes are etched under the sensing straight arm

The fabrication of the device is carried out with the following steps: the substrate is first oxidized on both faces at high temperature. The resulting thickness of silica (SiO_2) is of $1.3 \mu\text{m}$. A second layer of silicon nitride is deposited by PECVD on the top face of the substrate. The thickness of Si_3N_4 is of $0.45 \mu\text{m}$. A third layer of silica of thickness $1.4 \mu\text{m}$ is deposited by PECVD. The silicon nitride layer of refractive index $n_{\text{Si}_3\text{N}_4}=1.9$ is the guiding layer, and the two layers of silica of refractive index $n_{\text{SiO}_2}=1.45$ form the upper and lower cladding of the planar waveguide. The lateral confinement of the light is obtained by etching of a rib waveguide of width $5 \mu\text{m}$ in the upper silica layer, by using reactive ion etching (RIE). The thickness of etching is chosen in order to create a difference of effective index of 0.004 between the rib waveguide and the planar waveguide. The influence of the etching process becomes significant when the thickness of oxide is smaller than $0.5 \mu\text{m}$. For larger values, the evanescent part of the guided wave does not propagate in air. The value of 0.004 for the effective index difference is obtained for a thickness of oxide of $0.2 \mu\text{m}$. The thickness etched in the silica layer is thus $1.2 \mu\text{m}$. The resulting effective index of the TE_{00} guided mode considered here is $n_{\text{eff}} \approx 1.725$.

The length of the straight Mach-Zehnder arm is $L=20 \text{ mm}$. The deflection of the S-shape bent arm is $630 \mu\text{m}$ and the bent radius is 40 mm . The resulting length of the bent arm is thus 20.049 mm . The

optical path-difference (OPD) introduced between the arms of the Mach-Zehnder interferometer is $\delta_{MZ}=n_{eff}(L_2-L_1)=84.5 \mu m$. As a broadband source will be used in this work, it is interesting to express the group optical path-delay which takes into account the chromatic dispersion of the waveguide. The group effective index of the guided wave propagating in a highly confined ($0.45 \mu m$) waveguide is approximated by $n_g \approx 2$ at $1300 nm$ wavelength. This corresponds to a group optical path difference of $\delta_g=98 \mu m$. After the waveguide fabrication, the membranes are realized by anisotropic etching in KOH from the back face of the crystal through the three windows opened in the oxide protecting layer chemically etched in buffered HF. The final thickness of the membranes is $21 \mu m$. The membranes are of rectangular shape with a ratio $b/a=2$ between the length and the width. The sizes are $b_1=2.61 mm$ and $a_1=1.32 mm$ for the center membrane and $b_2=1.93 mm$ and $a_2=0.96 mm$ for the two side ones.

Principle of operation

The application of a pressure P under the membrane induces a deformation of the latter. The mechanical deformation of an elastic membrane can be described analytically. More particularly, the value of the deflection at the center of the membrane can be easily expressed and linked versus the pressure variation to the value of the variation of optical path difference by lengthening of the sensing arm. References 13 and 14 give the analytical expressions required to solve the problem.

We use the hypothesis, experimentally verified when using anisotropic etching, that the membranes are of rectangular shape of length b and width a . The thickness e is considered to be small compared to the sizes a and b . The thickness is assumed to be uniform and the four edges are assumed to be rigidly clamped to the substrate. The deformation is assumed to be perfectly elastic, which is the case with silicon membranes. We will neglect here for simplification the permanent stress produced by the first SiO_2 layer obtained by oxidation of the silicon substrate whose coefficient of dilatation is different from the one of the oxide layer. With these conditions, the pressure P can be expressed versus the deflection h_o at the center of the membrane by :

$$P = \frac{E}{1-\nu} \frac{e^3 h_o}{a^4} \left[\frac{1}{12\alpha(1+\nu)} + C \frac{h_o^2}{e^2} \right] \quad (5)$$

with: $E=168200 \text{ Mpa}$: silicon Young's modulus and $\nu=0.279$: Poisson's ratio

α is a coefficient given by Timoshenko, depending on the ratio b/a . In our case $b/a=2$ and $\alpha=2.54 \cdot 10^{-3}$. Tabata gives in ref. 14 an analytical expression of the coefficient C : the Tabata coefficient calculated with $m=a/b=0.5$ is equal to $C=10.94$. We can now assess the phase shift produced by a pressure P . Here we will only consider the phase variation produced by the lengthening of the sensing arm submitted to the deformation. As the waveguide is centered on the membrane, the elasto optical effects are negligible as demonstrated by other authors. The deflection is assumed to be small compared to the sizes of the membrane, and as the edges are rigidly clamped to the substrate, the slope of the deformation close to the edges is considered to be zero. One can deduce the excess length ΔL and thus the total optical phase variation. The latter is given for the three cascaded membranes by :

$$\Delta\phi(P) = \frac{2\pi}{\lambda} n_{eff} \Delta L(P) = \frac{\pi^3 n_{eff}}{2\lambda} \left[\frac{h_{o1}^2}{b_1} + 2 \frac{h_{o2}^2}{b_2} \right] \quad (6)$$

The subscripts 1 and 2 stand for the large and the small membranes respectively. The non linear relationship of P with $\Delta\phi(P)$ is obtained by combining Eq.(5) and Eq.(6).

Experimental results

The device was designed as previously discussed to work in a coherence modulation scheme requiring a static optical path-difference to encode the information. In a first step, the main characterization was carried out by a spectral analysis of the light transmitted by the interferometer. Figure 8 represents the results of the spectral analysis obtained as a pressure $P=0 \text{ Bar}$ then $P=2.25 \text{ Bar}$ is

applied to the membranes. This figure shows periodical transmission peaks in the spectrum of the source. This transmission peaks result from interferences at the output of the interferometer. The distance between adjacent peaks can be considered as the Free Spectral Range (FSR) of the filter : $FSR = \Delta\lambda = \lambda_o^2 / \delta_g$. Measuring the FSR yields the value of the group OPD δ_g . Here $\Delta\lambda$ is measured to be 16.8 nm , corresponding to a static OPD $\delta_g = 97.5 \mu\text{m}$ in good agreement with what was expected from the waveguide design ($98 \mu\text{m}$). The contrast of the fringes is 17 dB , yielding bend propagation losses in the bent arm of -2.2 dB .

In figure 8, one can measure the wavelength shift produced by the pressure variation. This wavelength shift can be linked to the variation of length of the waveguide arm.

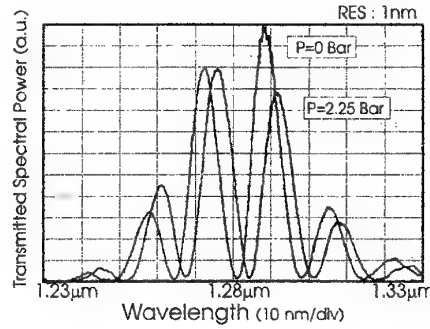


Fig. 8 Channeled spectrum transmitted by the imbalanced interferometer for an applied pressure of 0 and 2.25 Bar. The Free Spectral Range is 16.8 nm

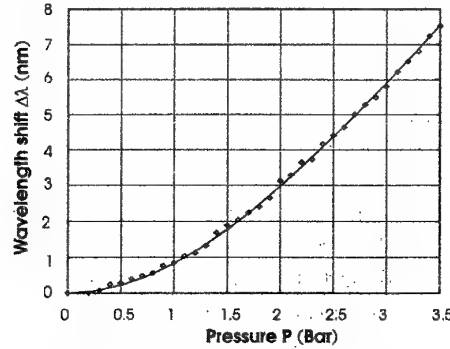


Fig. 9 Variation of the wavelength shift of the channeled spectrum versus the pressure variation. The solid line represents the curve obtained from the analytical model.

The wavelength shift of the channeled spectrum was measured between 0 and 3.5 Bar. Fig.9 shows the variation of $d\lambda(P)$ against the pressure variation P . The curve in solid line is the analytical curve calculated from Eq.(5) and Eq.(6). It shows a good agreement with the experiments. The experimental curve of Fig.4 confirms that in the center of the membrane, the influence of the elasto-optic effects is much weaker than in the edges. The main contribution to the optical path variation comes mostly from the geometrical extension of the membrane. The accuracy of the measurement of the wavelength shift obtained in the experiment is about 0.1 nm yielding a relative accuracy in the determination of P of about $\Delta P/P = 1.4\%$ around 3 Bar. This can be obviously improved by using of specially designed detection schemes [6,7].

5. CONCLUSIONS

We have discussed in a first time the feasibility of a gas sensor system based on coherence modulation of light for the remote interferometric measurement of gas concentration. The sensor uses an imbalanced interferometer integrated in glass and a demodulating interferometer integrated in lithium niobate. Sensitivity to the concentration of organic gas is achieved by the use of a layer of a specific polymer (DPMS) coated onto the sensor interferometer. The sensitivity thus obtained is 0.2 rad/Vol% for butane, and 0.8 rad/Vol% for ethanol vapor. The smallest detectable concentration of butane is 0.01% (0.0025% for ethanol) and the response time is 6 seconds. The observed resolution can certainly be increased by using an improved demodulation process. In the second part, we demonstrated the feasibility of an optical pressure sensor based on the use of an imbalanced Mach-Zehnder interferometer integrated on silicon and associated with micro-machined membranes. Such an imbalanced interferometer compared to previous symmetrical interferometers allows simultaneously remote sensing and linear-phase read-out process at the output of the system, by coherence modulation scheme for instance or by spectral analysis. The latter system was used to measure the fringe displacement in a channeled spectrum produced by pressure variation ranging between 0 and 3.5 Bar, of the channeled spectrum transmitted by the device. The pressure required to produce a phase variation of π -rad is equal to 3.75 Bar. The description used introduces a non-linear deflection of the membrane versus the pressure applied. The experiments are in good agreement with the numerical and analytical models proposed here.

ACKNOWLEDGEMENTS

This work was supported by the "GDR Microsystèmes" programme of the CNRS and by the INCO/COPERNICUS programme of the European Community.

6. REFERENCES

- [1]. D.A. Jackson, and J.D.C. Jones "Fiber Optics Sensors", *Opt. Acta*, **33**, 12, pp. 1469-1503, (1986).
- [2]. J.L. Brooks, R.H. Wentworth, R.C. Youngquist, M.Tur, B.Y.Kim, H.J. Shaw "Coherence multiplexing for fiber-optic interferometric sensor", *J.Lightwave Technol.*, **3**, pp.1062-1072, (1985).
- [3]. R.H. Wentworth "Theoretical noise performances of coherence multiplexed interferometric sensors" *J. Lightwave Technol.*, **7**, pp. 941-956, (1989).
- [4]. K. Bløtekjaer, R.H. Wentworth and H.J. Shaw "Choosing relative optical path-delays in series-topology interferometric sensor arrays" *J.Lightwave Technol.*, **5**, pp. 229-235, (1987).
- [5]. M.Farhadiroushan and R.C.Youngquist, "Polarimetric Coherence Multiplexing using High-birefringence Optical-Fiber sensors and Short Coherence sources", *Opt. Lett.*, vol. 15, no. 15, pp. 786-788, (1990).
- [6]. H. Singh, J.S. Sirkis, J. Andrews, and R. Pulfrey "Evaluation of integrated optic modulator based detection scheme for in-line fiber etalon sensor" *J. Lightwave Technol.*, **13**, pp. 1772-1779, (1995).
- [7]. H. Porte, J.-P. Goedgebuer, W.Elfllein, A.Terras, F.Ledeventec, and N.Butterlin "Linear phase tracking in a coherence modulation electrical sensor system using integrated LiNbO₃ modulator/demodulator" *IEEE J. Selected Topics in Quantum Electron.*, **2**, 2, pp. 319-325, (1996).
- [8]. M.Ohkawa, M.Izutsu, T.Sueta "Integrated optic pressure sensor on silicon substrate" *Applied Optics*, Vol.28, No.23, pp.5153-5157, (1989).
- [9]. G.N. De Brabander, J.T.Boyd, G.Beheim "Integrated optical ring resonator with micromechanical membrane for pressure sensor" *IEEE Photonics Technology Letters*, Vol.6, No.5, pp.671-673, (1994).

- [10]. G.N. De Brabander, G.Beheim, J.T.Boyd "Integrated optical micromachined pressure sensor with spectrally encoded output and temperature compensation" *Appl.Opt.*, **37**,15, pp.3264-3267, (1998).
- [11]. F. Rehouma, W. Elflein, D. Persegol, A. Kevorkian, G. Clauss, P. Benech, R. Rimet "Improved structures for evanescent waves sensors", *Appl.Phys.Lett.*, **66**,12, pp.1461-1462, (1995).
- [12]. B.J. Luff, J.S. Wilkinson, J.Piebler, U. Hollenbach, J.Ingenhoff, N. Fabricius "Integrated Optical Mach-Zehnder biosensor", *J. Lightwave Technol.*, **16**, 4, pp. 583-593, (1998).
- [13]. S.Timoshenko, S.Woinowsky-Krieger "Theory of plates and shells" Ch. XIII, McGraw-Hill, Book Company, Inc., (1959).
- [14]. O.Tabata, K.Kawahata, S.Sugiyama, I.Igarashi "Mechanical property measurements of thin films using load-deflection of composite rectangular membranes" *Sensors and Actuators*, **20**, pp.135-141, (1989).

PARTICLE REFLECTION FROM ROUGH SURFACE IN BINARY COLLISION MODEL

V.I.R.Niculescu, A.O.R. Cavaleru*, Rodica Candea**

National Institute for Laser, Plasma and Radiation Physics, Electron Accelerators
Laboratory, P.O. Box MG-36, R-76900, Romania, e-mail : nicval@roifa.ifa.ro

*National Institute of Research and Development for Optoelectronics- INOE 2000, 1 Atomistilor St.,
P.O. Box MG-5, Bucharest-Magurele, Romania

** Semanatoarea S.A.

ABSTRACT

Based on the binary collision model, the angular distribution of reflected ions has been investigated under various surface conditions. The unidimensional surface depends on the fractal dimension D . Computer simulations were performed for Ti target. We have found that the particle reflection depends on surface topological characteristics.

1. INTRODUCTION

The modern electronics industry needs new materials and technologies. The surface structures are changed by ion bombardment resulting in surface roughening [1,2,3]. By ion irradiation topographical changes such as cones, pyramids, steps, ripples etc. are developed [4].

The majority of studies relate to ion bombardment of crystalline and amorphous flat-surfaces [5,6 and references therein]. The surface roughness was rarely considered in classical literature on ion sputtering by Monte-Carlo codes [7,8,9].

2. THE BINARY COLLISION MODEL

Many computer simulation programs [10] use the binary collision approximation which was borrowed from the field of atomic collisions in the gas phase.

In the laboratory system, θ_1 (the angle of the scattered projectile) and θ_2 (the angle of the recoiling target atom in respect to the initial direction of the projectile) are functions of $M_1, M_2, E_0, E_1, E_2, Q$ (where M_1 -projectile mass, M_2 -target mass, E_0 -initial energy, E_1 - energy of the scattered projectile, E_2 - energy of the scattered target, Q -inelastic energy loss). In the center of the mass system the relative energy is given by:

$$E_r = \frac{A}{1+A} E_0, A = \frac{M_2}{M_1} \quad (1)$$

Taking into account the relations between laboratory and center of mass systems for scattering angles, the relations expressed by $\bar{\theta}$ the scattering angle in the center of mass system were obtained:

$$\cos(\theta_1) = \frac{1 + Af \cos(\bar{\theta})}{(1 + 2Af \cos(\bar{\theta}) + A^2 f^2)^{1/2}}, f^2 = 1 - Q/E_r \quad (2a)$$

$$\cos(\theta_2) = \frac{1 - f \cos(\bar{\theta})}{[2 - 2f \cos(\bar{\theta}) - (1 - f^2) \cos^2(\bar{\theta})]^{1/2}} \quad (2b)$$

Similarly, for the energies of projectile and recoil particle in the laboratory system, the following expressions were obtained:

$$\frac{E_1}{E_0} = \frac{1}{(1+A)^2} \left((1+Af)^2 - 4Af \sin^2 \frac{\bar{\theta}}{2} \right) \quad (3a)$$

$$\frac{E_2}{E_0} = \frac{1}{(1+A)^2} \left((1-f)^2 + 4f \sin^2 \frac{\bar{\theta}}{2} \right) \quad (3b)$$

The angle $\bar{\theta}$ is given by the relation:

$$\bar{\theta} = \pi - 2p \int_R^{\infty} [r^2 g(r)]^{-1} dr \quad (4)$$

where

$$g(r) = \sqrt{1 - \frac{V(r)}{E_r} - \frac{p^2}{r^2}} \quad (5)$$

and p - is the impact parameter

The apsis of the collision R is obtained from the equation: $g(R) = 0$ (6)

For some particular potentials such as hard-sphere, Coulomb, inverse-square, the scattering angle $\bar{\theta}$ was given by analytical expressions. For others we must integrate eq.(4).

From the screened Coulomb potentials, one often used is the Nakagawa-Yamamura [11] potential:

$$V(r) = \frac{Z_1 Z_2 e^2}{r} \Phi\left(\frac{r}{a}\right) \quad (7)$$

The screening length a is given by:

$$a = \left(\frac{9\pi^2}{128} \right)^{1/3} a_B Z_{12}^{-1/3}, Z_{12} = (Z_1^x + Z_2^x)^y \quad a_B - \text{the Bohr radius} \quad (8)$$

The parameters x, y can have different values: $(x = 1/2, y = 2)$ [12], $(x = 2/3, y = 3/2)$ [13]

For heteronuclear pairs the screening function $\Phi(r)$ is:

$$\Phi(r) = \exp(-A_{12}r + B_{12}r^{3/2} - C_{12}r^2) \quad (9)$$

where the constants are:

$$A_{12} = \left[\frac{1}{2} (A_{11}^{3/2} + A_{22}^{3/2}) \right]^{2/3}, B_{12} = \frac{1}{2} (B_{11} + B_{22}), C_{12} = \left[\frac{1}{2} (C_{11}^{3/2} + C_{22}^{3/2}) \right]^{2/3} \quad (10)$$

The constants for homonuclear potentials are given in tabel 4.2 from [10].

3. RESULTS AND DISCUSSIONS

The fractal surface used for ion-surface interaction is represented by the following model [14]. We used a fractal function $f_r(x)$ band limited and zero mean. The unidimensional surface depends on the fractal dimension D . The fractal dimension D varies between $D = 1$ (line curve) and $D = 2$ (a curve which cover the whole surface). The following expression was used:

$$f_r(x) = \sigma C \sum_{n=0}^{N-1} (D-1)^n \sin(K_0 b^n x + \phi_n), C = \left\{ \frac{2D(2-D)}{1-(D-1)^{2N}} \right\}^{1/2} \quad (11)$$

where $D(1 < D < 2)$ is the fractal dimension, K_0 is the fundamental spatial wave number, $b(b > 1)$ is the scaling spatial frequency, ϕ_n arbitrary phases, N tones number. In figure 1 expression (11) is represented for parameters: $b = e \approx 2.78128$ and $D = 1.20$ ($N = 5, \phi_n = 0.2, K_0, \sigma = 0.5$)

Fig.1 functia fractala fr(x)

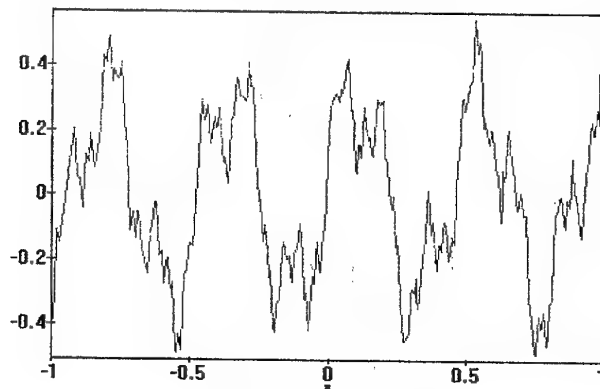


Fig. 1 Fractal function fr(x)

The preliminary Monte-Carlo simulation was realized for the fractal dimension $D = 1.08$ and energy $E_0 = 12$ eV, and for $D = 1.5$ and $E_0 = 12$ eV. We observed a decrease of the reflected ions with the increase of the fractal dimension. Given the reduced statistics, the conclusion can be only of nature qualitative.

4. REFERENCES

- [1]. Kanapickas A., Pranevičius L., Lith. J. of Physics **37**, no. 2, 136 (1997)
- [2]. Lapujoulade J., Surf. Sci. Rep. **20**, 191 (1994)
- [3]. Ed. Berish R., "Sputtering by Particle Bombardment" **2**, Berlin, Springer-Verlag (1983)
- [4]. Carter G., Nobes M., Nucl. Instr. Methods **B90**, 456 (1994)
- [5]. Pranevičius L., Durand N., Delafond J., Templer C., Vacuum **46**, 77 (1995)
- [6]. Andersen H.H., Nucl. Instr. Methods **B33**, 466 (1988)
- [7]. Yamamura Y., Mossner C., Oechsner H., Radiat. Eff. **103**, 25 (1987)
- [8]. Hautala M., Liknen J., Nucl. Instr. Methods **B33**, 526 (1988)
- [9]. Makeev M.A., Barabasi A.L., Phys. Lett. **73**(10), 1445 (1998)
- [10]. Eckstein W., "Computer Simulation of Ion-Solid Interactions", Berlin, Springer-Verlag (1991)
- [11]. Nakagawa S.T., Yamamura Y., Radiat. Eff. **105**, 239 (1988)
- [12]. Firsov O.B., Zh. Eksp. Teor. Fiz. **33**, 696 (1957)
- [13]. Lindhard J., Nielsen V., Scharff M., Mat-Phys., Med. K. Dan. Vidensk. Selsk **36**, no. 10 (1968)
- [14]. Jaggard D.L., Sun X., J. Opt. Soc. Am. A **7**, no. 6, 1131 (1990).

PLASMA PARAMETERS DETERMINATION IN A PULSED DUOPIGATRON ION SOURCE

V. Braic, C.N. Zoita, A. Kiss, Mariana Braic

National Institute for Optoelectronics, POBox MG05, 76900 Bucharest, Romania
Tel/fax: 4201001, email: vbraic@alpha2.infim.ro

ABSTRACT

Some aspects of the low-pressure regime ($9 \cdot 10^{-5}$ - $6 \cdot 10^{-3}$ mbar) of plasma generation in a pulsed duopigatron ion source are presented below. Two working regimes of the ion source were identified. In the normal one the discharge current displays the same pattern as the applied pulsed negative potential. In addition, the plasma parameters such as: carrier concentration, electron temperature and plasma potential were analyzed. In the other regime self-oscillations of the discharge current during the applied pulsed voltage are exhibited.

1. INTRODUCTION

Pulsed operation of ion sources is nowadays issues of particular interest due to the enhanced performance of power sources available which permit the investigation of special short time/high frequency physical process developing within these systems [1-3]. Even in normal pulsed operated systems, (e.g. a duopigatron ion source [3]), different patterns of the current discharge signal may be detected for particular operating conditions.

The aim of this paper is to investigate the working regime of the pulsed duopigatron ion source and to characterize the plasma parameters in a regime without self-oscillating behavior, using the information provided by a Langmuir probe.

2. EXPERIMENTAL SETUP

The duopigatron ion source is presented schematically in Fig.1. The cathode of the duopigatron ion source is supplied continuously and a negative electrical pulse is applied to the cathode-anode gap [4]. The intermediate and the reflex electrodes are biased automatically via serial resistors.

The pulsed plasma freely expands into the working chamber where it is analyzed. The ion source operated in to a 99.99% hydrogen atmosphere. The working regime pressure ranged between $5 \cdot 10^{-5}$ - $6 \cdot 10^{-3}$ mbar. The investigations were carried out for two discharge currents (24 A and, respectively 30 A) at a frequency of 10 Hz and a pulse duration of 250 μ s.

Plasma characteristics (i.e. carrier concentration, electron temperature and plasma potential) in a cylindrical volume around the axis of the working chamber were determined using a Langmuir probe [2]. The probe characteristics measurements were performed using a 100 MHz digitizing oscilloscope and a data acquisition system which allow the investigation of time evolution of the expanding plasma. Probe characteristics were carried out for different time delays after plasma ignition in the working chamber at about 10 cm distance from the extraction electrode. The value of the magnetic field was kept constant for all the presented measurements ($B = 600$ G).

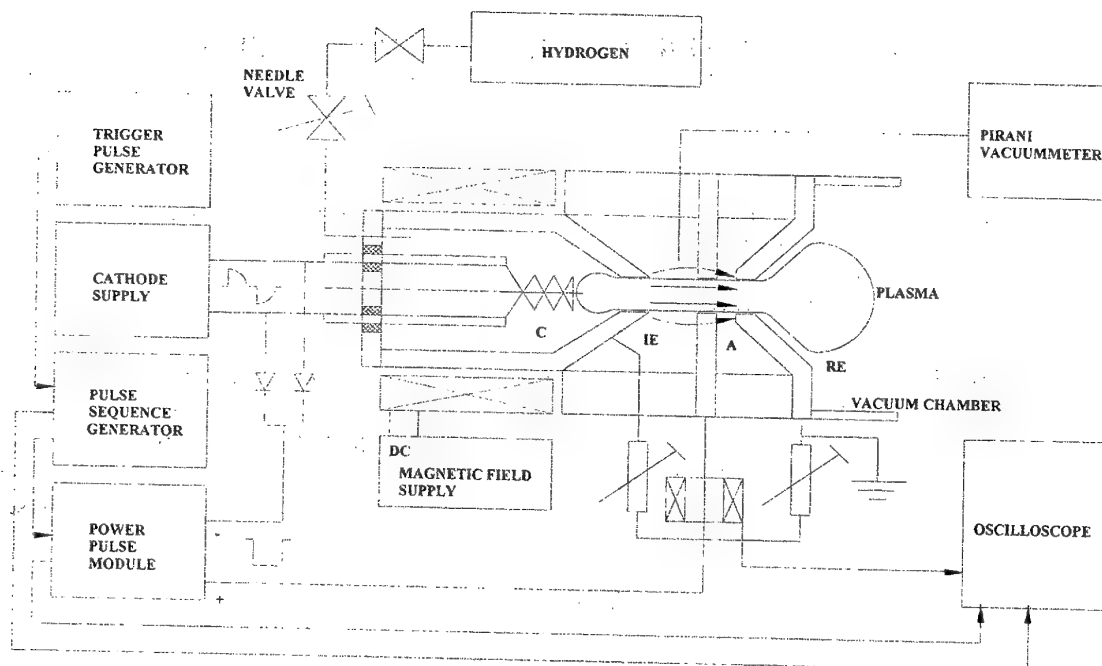


Fig.1 Schematic view of the duopigatron plasma source

3. RESULTS AND DISCUSSIONS

Independently of the pulse frequency and pulse duration there were evidenced two working regimes of the ion source were revealed (Figs.2 and 3). For pressures lower than 10^{-4} mbar, self-oscillations of the discharge current superimposed on the external driven pulse appear. Fig.2 illustrates the shape of the discharge current as obtained on the oscilloscope display for a pressure of 9.10^{-5} mbar. The amplitude of the discharge current oscillations is limited by the filament temperature and is slightly dependent on the discharge voltage. As elsewhere reported [1,5] plasma produced in devices by thermoemission with applied external magnetic field for ionization enhancement may present in certain conditions an oscillating behaviour, mainly due to a lack of carriers in front of the electrodes, where a double layer is formed.

For higher pressures (e.g. $p > 10^{-4}$ mbar) the discharge current pulse displayed a normal rectangular shape, following the applied pulse voltage, as illustrated in Fig.3.

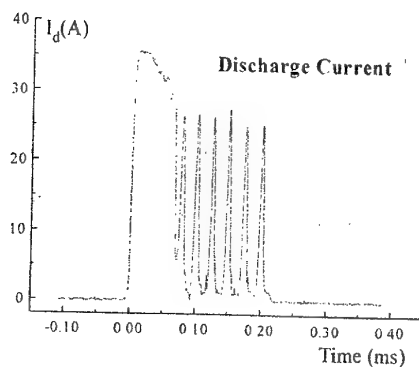


Fig. 2 The shape of the discharge current pulse for a pressure lower than 10^{-4} mbar

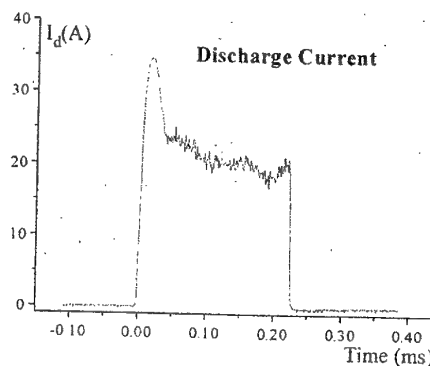


Fig. 3 The shape of the discharge current pulse for a pressure of $1.5 \cdot 10^{-4}$ mbar

A better understanding of the processes developing in such devices with external magnetic field may be achieved by plasma parameters investigation using an electrical probe. Carrier concentration $N(\text{cm}^{-3})$, electron temperature (eV) and plasma potential (V) exhibit, as expected, different values for different working pressures.

At relatively high pressures ($p > 10^{-3}$ mbar), when no oscillating feature is present, plasma characteristics show a continuous variation during the discharge pulse. These variations are presented for electron temperature (Fig. 4), for plasma potential (Fig. 5) and for carrier concentration (Fig. 6.).

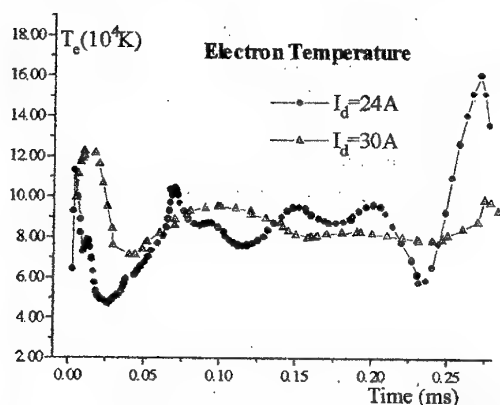


Fig. 4 Electron temperature variation during the discharge pulse

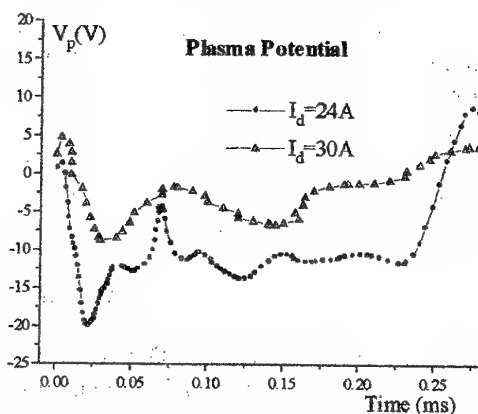


Fig. 5 Plasma potential variation during the discharge pulse

The analysis reveals that after plasma ignition these parameters reach a maximum with a delay of about 1-2 μs from the applied discharge pulse. Carrier concentration shows a real maximum at the beginning of the impulse and presents a steady decrease during the pulse evolution. On the contrary, plasma potential and the electron temperature show a saddle pattern in between the beginning and the end of the impulse, and a sharp increase at the pulse end.

The increase of electron temperature and plasma potential after the driving pulse cut-off may be ascribed to the destruction of the double layer structure located nearly the anode which suddenly transfers its energy to the plasma. The carrier density increase in the first part of the pulse evolution is determined by the sharp increase of the discharge current amplitude. On the other hand, the continuous decrease of the carrier density during pulse evolution could be determined by the enhanced loss of the carriers to the walls in the working chamber due to diffusion. The energy transferred from the double layer to the plasma cannot affect the carrier density.

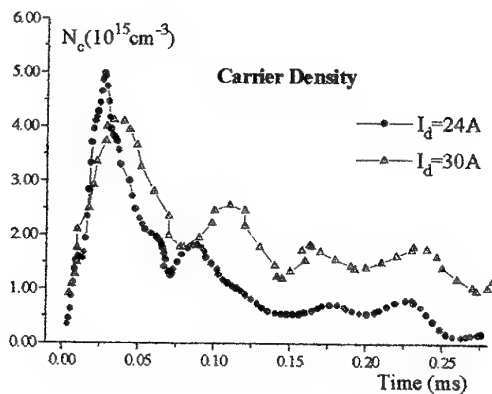


Fig. 6 Carrier density variation during the discharge pulse

When the pressure decreases below 10^{-4} mbar, the oscillatory feature of the discharge current is also reflected in plasma parameters, but it is difficult to be correlated with the oscillations present in every pulse. This subject is still under research. However, despite the oscillatory pattern of the pulse, a pattern similar to that in the normal working regime can be observed for all of all values of plasma parameters.

4. CONCLUSIONS

Two working regimes, depending on the pressure values of the pulsed duopigatron ion source were identified. At low pressure values ($< 10^{-4}$ mbar) self-oscillations of the discharge current during the applied pulsed voltage are exhibited. In the so called normal regime ($> 10^{-4}$ mbar) the discharge current displays the same pattern as the applied pulsed negative potential.

In the normal regime, the rise of electron temperature and plasma potential after the applied pulse voltage can be ascribed to the destruction of the space charge structure of the discharge. The energy accumulated in the double layers accelerates the post discharge electrons and rises their temperature.

5. REFERENCES

- [1]. C.Arnas Capeau, G.Bachet, F.Doveil, Le Vide: Sci.Tech.Appl., 275 (1995) 321
- [2]. A.Brockhaus, C.Borchardt, J.Engemann, Plasma Sources Sci. Technol., 3 (1994) 539
- [3]. L.Valyi, Atom and Ion sources, John Willey&Sons, London (1977)
- [4]. V.Braic, Rev.Optoelectronics, 4/3 (1997) 31
- [5]. D.L.Morse, Phys.Fluids, 8/3 (1965) 516

OPTIMISATION OF WAVELENGTH SELECTIVITY IN RESONANT MICROCAVITIES FOR C³SL, VCSEL AND RCE PHOTODETECTORS

C. Cotîrlan, B. Bălăsoiu

Institute of Optoelectronics S.A., 1 Atomistilor Street, P.O. Box MG-22, 76900, Bucharest
Phone: (401) 7806640, Fax: (401) 4232532

C³SL - Cleaved coupled-cavity semiconductor laser

VCSEL - Vertical cavity surface emitting laser

RCE photodetector - Resonant cavity enhanced photodetector

ABSTRACT

Several optical logic schemes for modern optical communication networks combine the response spectra of RCE detectors with the nearly monochromatic output of VCSELs or C³SLs resulting cascable optical input/output circuits, which are able to incorporate the wavelength as an additional logical variable.

Due to the wavelength selectivity of the Fabry-Perot microcavities, only resonant wavelength are admitted or emitted.

The first section of this paper provides the expressions of the field transmission and reflection coefficients of the gap separating cleaved sections of laser versus gap separation d , the magnitude T and the phase ϕ of the coupling constant between the two cavities versus d/λ .

These data emphasize that mode selectivity depends stronger on the phase ϕ than on the magnitude T and may be used to determine which is the optimum phase for the minimum gap loss.

The second section of this paper shows that superior performance of the RCE photodetection scheme depends critically on the achievement of a low-loss cavity.

1. INTRODUCTION

The aim of experimental and theoretical work on coupled-cavity semiconductor lasers is the achievement of lasers maintaining single frequency operation with the nonlasing modes greatly suppressed during pulsed operation; otherwise excessive errors due to mode partition noise are encountered.

The **Cleaved coupled-cavity semiconductor lasers** have two selection mechanisms to provide narrower lasing modes. The first is based on one section acting as a resonant reflector. The second is diffraction loss in the gap between the cleaved sections.

The **RCE photodetector** structure is capable of operating over a large and continuous wavelength range, either by tuning within a material system or by moving to a complementary material system.

The **VCSELs** are structurally similar to RCE detectors and modulators and can therefore be manufactured alongside one another or a single device can perform both functions.

Such a combination (RCE photodetector and VCSEL or C³SL) provides both wavelength selective photodetection and narrow band emission, ideal for multiple wavelength photonics.

2. MODE SELECTIVITY

There are two selection mechanisms. The former works best when one cavity acts as a resonant reflector which modulates the end losses of the "lasing cavity". The reflection from the resonator is periodic in photon energy and has maxima at energies between the modulator cavity resonances. This is a

relatively weak mode selection mechanism providing gain-loss differences of the order of 1 cm^{-1} in 15 mm long devices.

The second mechanism is related to diffraction losses in the gap between the two cavities.

The modes of highest net gain avoid gap losses by interfering in such a way as to reduce transmission into the lossy gap. This reduction is maximized when the gap width d is an integral number of half wavelengths and when the cavities are both resonant. The condition of simultaneous cavity resonances leads to sharp mode discrimination with gain-loss differences of the order of $5\text{--}10 \text{ cm}^{-1}$ in 15 mm long devices. Both mechanisms derive their mode selectivity from the registration of the two sets of cavity resonances.

2.1 Equations of Steady-State Operation

The fields in the two cavities of a coupled-cavity are indicated in Fig. 1. The magnitudes of the complex transmission and reflection coefficients T_2 and R_2 which completely characterize the gap are plotted in Fig. 1. The field E'_1 at gap results from reflection of E_1 and transmission of E_2 :

$$E'_1 = R_2 E_1 + T_2 E_2 \quad (1)$$

On the other hand from the round trip through cavity 1 a relation between E_1 and E'_1 results:

$$E_1 = R_1 \exp[(g_1 - \alpha)L_1 + 2ik_1 L_1] E'_1 \quad (2)$$

where g_1 is the gain, α the loss, L_1 is the length, and k_1 is the propagation vector given by $k_0 n_1$ where $k_0 = 2\pi/\lambda$ and n is the refractive index of cavity 1.

Eliminating E'_1 from (1) and (2) and dividing the resulting equation by $\exp[(g_1 - \alpha)L_1 + 2ik_1 L_1] R_1 R_2$, we find

$$\{(R_1 R_2)^{-1} \exp[-(g_1 - \alpha)L_1 - 2ik_1 L_1] - 1\} E_1 = (T_2/R_2) E_2 \quad (3)$$

Similar considerations for cavity 2 lead to

$$\{(R_1 R_2)^{-1} \exp[-(g_2 - \alpha)L_2 - 2ik_2 L_2] - 1\} E_2 = (T_2/R_2) E_1 \quad (4)$$

The homogeneous equations (3) and (4) have solutions only if the secular equation is satisfied

$$\{(R_1 R_2)^{-1} \exp[-(g_1 - \alpha)L_1 - 2ik_1 L_1] - 1\} \{(R_1 R_2)^{-1} \exp[-(g_2 - \alpha)L_2 - 2ik_2 L_2] - 1\} = (T_2/R_2)^2 \quad (5)$$

The key parameter describing the coupling between the two cavities is:

$$T_2/R_2 = T \exp(i\Phi). \quad (6)$$

Setting each bracket to zero in (5) determines the lasing condition for each cavity if the cavities were uncoupled.

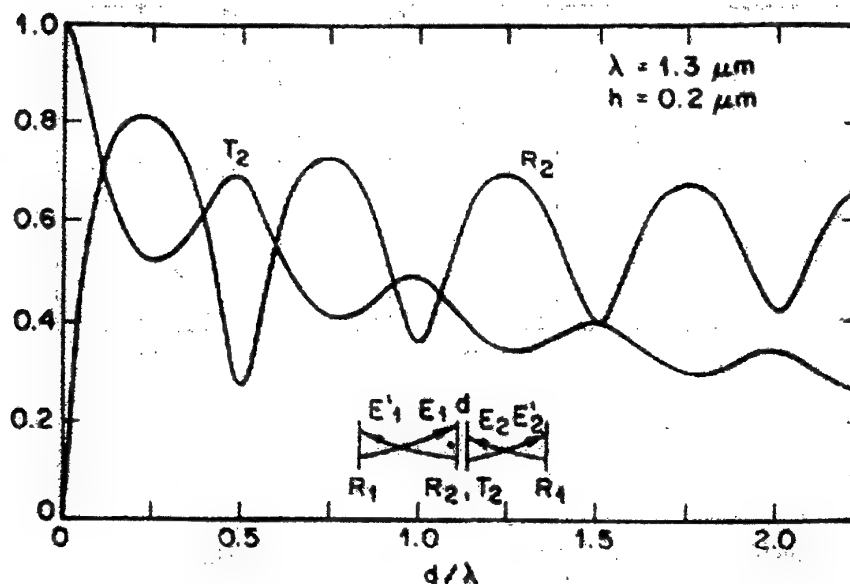


Fig. 1 Field transmission and reflection coefficients of the gap separating cleaved sections versus the separation d .

2.2 Gap Parameters

The values of R_2 and T_2 are readily calculated using the standard treatment of a two-surface Fabry-Perot resonator, once the transmission losses due to diffraction have been estimated. These diffraction losses have been calculated by Charles H. Henry *et al.* [1], who neglected diffraction spreading parallel to the junction plane and used a Gaussian model to estimate diffraction spreading perpendicular to the junction plane. Using the calculations of T_2 and R_2 (their magnitudes are plotted in Fig. 1), we plot the magnitude of the coupling coefficient T in Fig. 2 and its phase Φ in Fig. 3 as a function of d/λ .

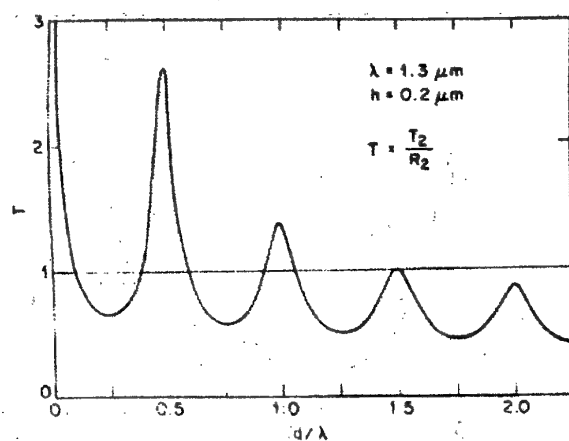


Fig. 2 Magnitude of the coupling constant T on d/λ

We notice that selectivity varies slowly with T and has a maximum near $T \approx 1$. Mode selectivity depends stronger on the phase Φ than on T . The optimum phase for the gap loss mechanism is zero,

which occurs every half integral wavelength as seen in Fig. 3.

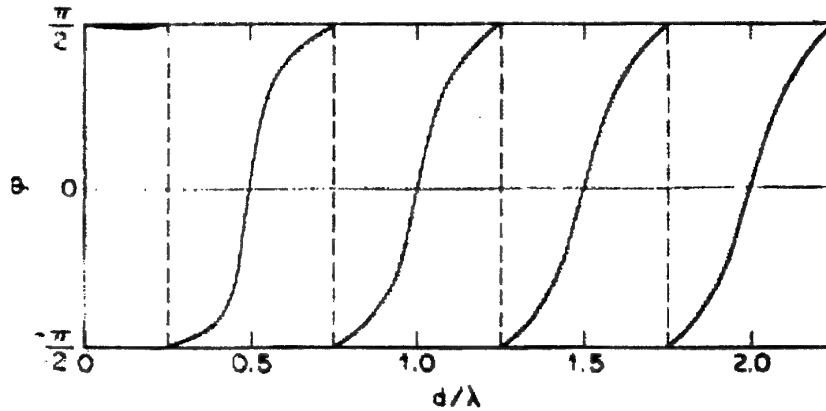


Fig. 3 Phase of the coupling constant Φ versus d/λ

The best conditions for the resonant reflector mechanism occur at very small gaps where T is large and $\Phi = 90^\circ$. Equation (5) is unchanged if Φ is changed by 180° . This allows us to fold the plot of Φ in Fig. 3, keeping Φ within the range of $-90^\circ \dots +90^\circ$.

The conclusion of the first section refers to the best conditions for the resonant reflector mechanism versus gap dimension and width of waveguide issued from the effective mirror concept.

The effective mirror formalism provides an intuitive grasp of the device behavior in various conditions of laser operation, and alone it is sufficient to show the preferred coupling junction phase.

3. THE QUANTUM EFFICIENCY FOR RCE PHOTODETECTORS

The quantum efficiency for RCE photodetectors can be written :

$$\eta = \{ (1 + R_2 e^{-\alpha d}) / [1 - 2(R_1 R_2)^{1/2} e^{-\alpha d} \cos(2\beta L + \psi_1 + \psi_2) + R_1 R_2 e^{-2\alpha d}] \} (1 - R_1)(1 - e^{-\alpha d}) \quad (7)$$

Since the propagation constant β has a wavelength dependence, η is a periodic function of the inverse wavelength. This is easily seen in Fig. 4 which illustrates the calculated wavelength dependency of η .

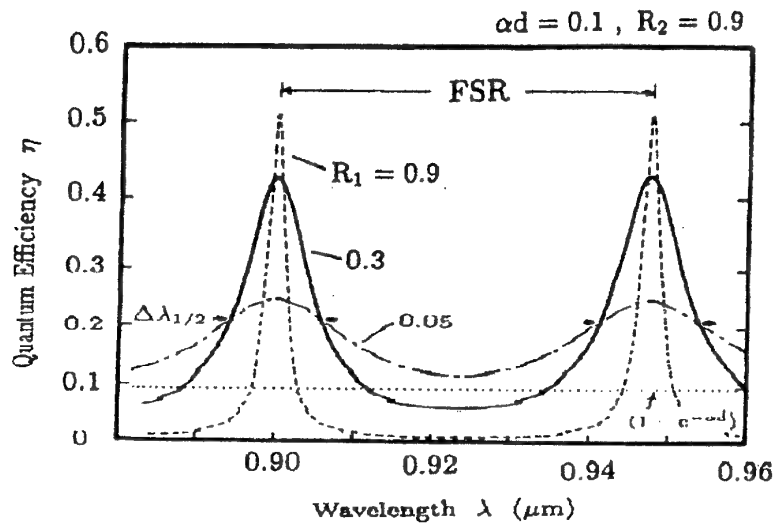


Fig. 4 Wavelength dependence of η for RCE detectors having various top mirror reflectivities for fixed $L = 2 \mu\text{m}$, $R_2 = 0.9$ and $\alpha d = 0.1$

η is enhanced periodically at the resonant wavelengths which occur when $2\beta L + \psi_1 + \psi_2 = 2m\pi$ ($m=1,2,3,\dots$).

On the right hand side of (7), the term inside the braces represents the cavity enhancement effect. This term becomes unity when $R_2=0$ giving η for a conventional detector. The flat dotted line in Fig.4 indicates the maximum η attainable for conventional photodetectors for the same active layer thickness ($\alpha d=0.1$). Conventional photodetectors provide roughly constant η across a broad wavelength range while RCE photodetectors can be designed to have significantly improved η at specific wavelengths.

4. WAVELENGTH SELECTIVITY OF RCE PHOTODETECTION

A spatial distribution of the optical field inside the resonant cavity arises from the standing wave formed by the two counter propagating waves. It follows that η , which was derived from power absorbed in the active region, is a function of the placement of the active region in the optical field.

We refer to this as the standing wave effect (SWE), and Fig.5 shows the wavelength dependent cavity field distribution calculated for a GaAs based RCE photodetector.

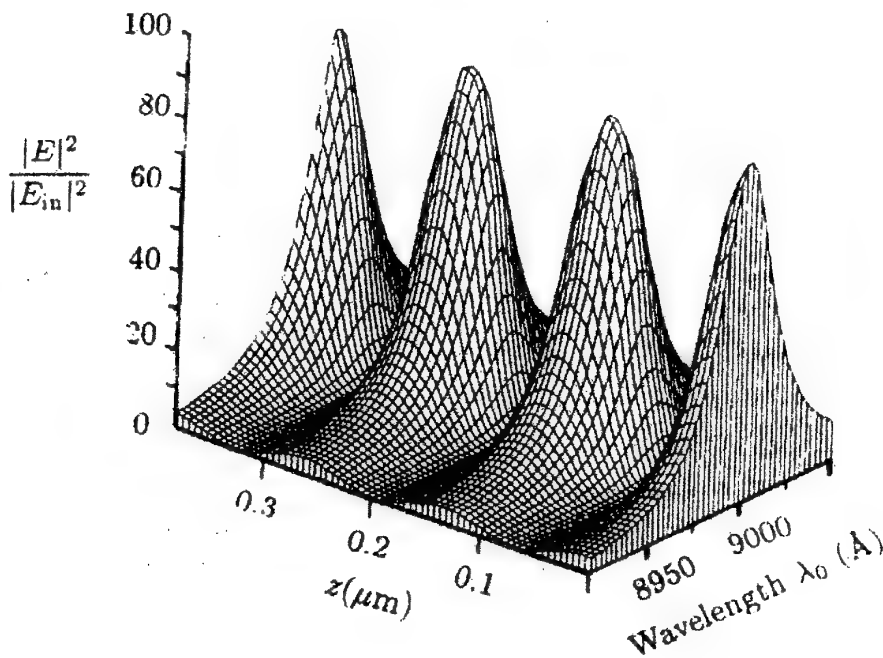


Fig. 5 Optical field distribution in a RCE detector as a function of wavelength and position. Top and bottom mirrors are 5 and 15 periods GaAs / AlAs, respectively, with a center wavelength of $0.9 \mu\text{m}$

Fig.6 shows the wavelength dependence of the SWE for various active layer thicknesses d

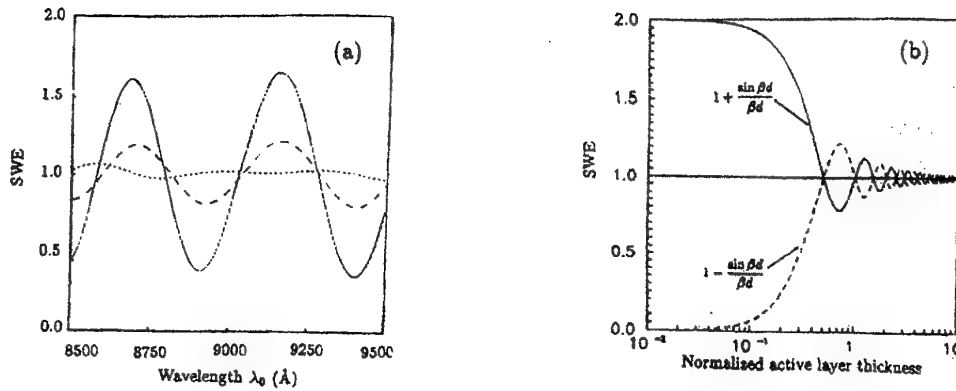


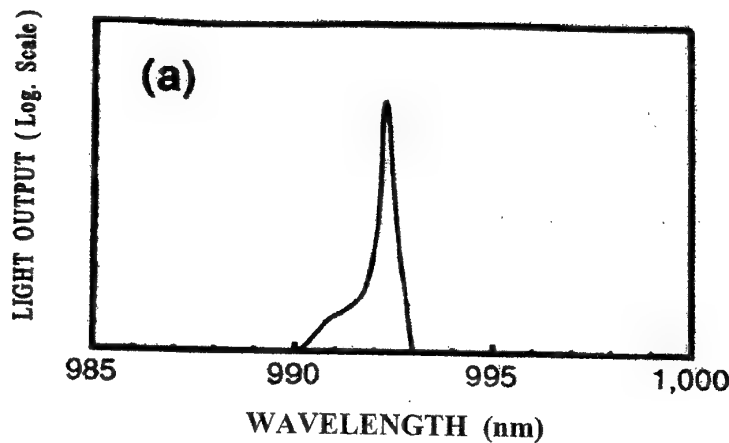
Fig. 6 The SWE as a function of wavelength for three different active layer thicknesses: $d = 650$ Å (solid), $d = 1300$ Å (dotted), and $d = 2000$ Å (dashed) for a cavity with 20 pairs GaAs / AlAs bottom mirror and native GaAs surface as the top mirror ($L_1 = L_2 = 2\mu\text{m}$).
(b) Dependence of the SWE on the active layer thickness. The extremes of the SWE are shown.

At $d \approx \lambda_0/4n$ (solid line) the SWE ranges between 0.35 and 1.7, resulting in drastic variations in the device photosensitivity at different wavelengths.

At the off-resonance wavelengths, when $2\beta L + \psi_1 + \psi_2 = (2m+1)\pi$, $m=1,2,3,\dots$, the cavity field amplitude decreases due to the destructive interference of the forward and backward traveling waves, resulting in suppressed η (Fig.4). The wavelength selectivity of a RCE photodetector is similar to that of Fabry-Perot filter device placed in front of a conventional detector. In this case, the filter and the detector can be designed and optimized separately. Since filters can be fabricated out of transparent materials, a high finesse can be achieved. However, the design of the overall structure will be more complicated and a different filter for each wavelength will be required. Besides, for the filter detector combination, the overall efficiency is the product of the filter transmission coefficient and the quantum efficiency of the conventional detector. The advantages of the RCE approach are simplified design and drastic quantum efficiency enhancement.

5. CONCLUSION

The main conclusion of both sections, the first treating lasers and the second treating RCE photodetectors, is that photodetectors and lasers adopt the highly wavelength selective response of the cavity in which they are situated. Due to the wavelength selectivity of the microcavities, only resonant wavelengths are admitted or emitted.



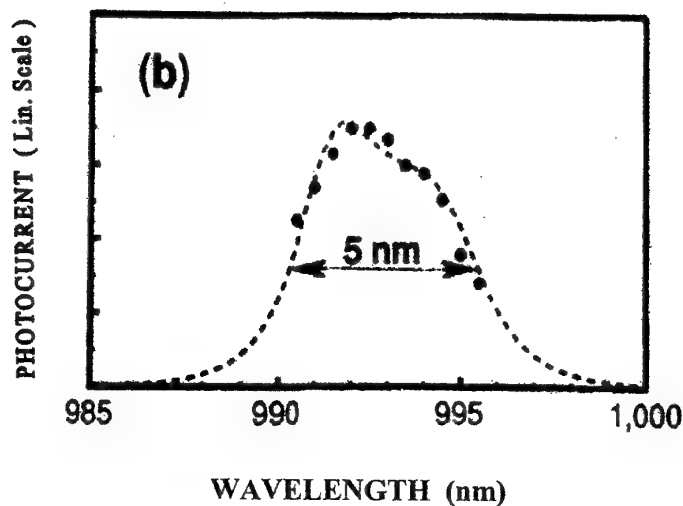


Fig. 7 (a) Emission spectrum of the VCSEL and
(b) photocurrent response of the HPT (Heterojunction phototransistor) together
with the calculated absorption spectrum

They also benefit from increased amplitude of the resonant field, allowing much thinner absorption regions in order to achieve greater quantum efficiency.

Higher bandwidth contributes also to the natural capabilities of RCE devices to greater speed and wavelength demultiplexing.

RCE detectors and phototransistors have vertical structures which are quite similar to VCSELs, simplifying integration.

Several optical logic schemes can be proposed to combine the sharp response spectra of RCE detectors and HPT with the nearly monochromatic output of VCSELs (Fig.7), resulting in cascable optical input/output circuits which are capable of incorporating the wavelength as an additional logical variable. Present day optical logic schemes will increase dramatically in power and flexibility when dynamic tuning of individual elements is fully incorporated.

6. REFERENCES

- [1]. Charles H. Henry, R.F. Kazarinov, IEEE J.Q.E., vol. QE-20, No. 7, 733, July 1984;
- [2]. M. Selim Unlu, S. Strite, J.A.P., vol. 78, No. 2, 607, 15 July 1995.

EXPERIMENTAL TESTS FOR THE CHARACTERIZATION OF ULTRASONIC PROBES UTILIZED FOR NON DESTRUCTIVE EXAMINATIONS IN THE INDUSTRIAL FIELD

C. Cantore, Maria Robu*

Isotest, via Roma, 8, 10090, Reano (Torino), phone: 39 11.93.103.18, fax: 39 11.93.103.52, Italy

* Institute of Optoelectronics, 1 Atomistilor str., Bucharest-Magurele, Romania

1. INTRODUCTION

The continuous needs of industry, concerning the preventive security and quality of products, have required the manufacturers to improve the constructive technology of ultrasonic devices and the quality and inalterability of probes supplying characterization cards and conformity declarations.

Thus all essential parameters, such as resonance frequency and probe width, are known and the operator can work correctly and reproducibility of results is guaranteed. Irrational variation of instrument, or damping value, or adapter, obviously causes significant difference in the results.

In regard to the contact system, the wire length and the use of adapter do not influence the quality control in case of working at low frequency. On the contrary, in the immersion system, when probes at very high frequency (above 5 MHz) are used, the wire length and the adapters cause important variations in the impulse form, with quantifiable consequences by spectral analysis.

For the geometrical characterization of contact probes (form of emission cone, symmetry, distance-amplitude curve, etc.), it is necessary to have special sample-blocks with rounded bottom holes and special adapters in order to block up and move the examined probes.

2. TESTING INSTRUMENTS

Figure 1 illustrates instruments used in the characterization of ultrasonic probes and the spectrum analyzer that allows the evaluation of certain parameters such as: fundamental frequency, bandwidth, damping value and the identification of undesirable harmonics.

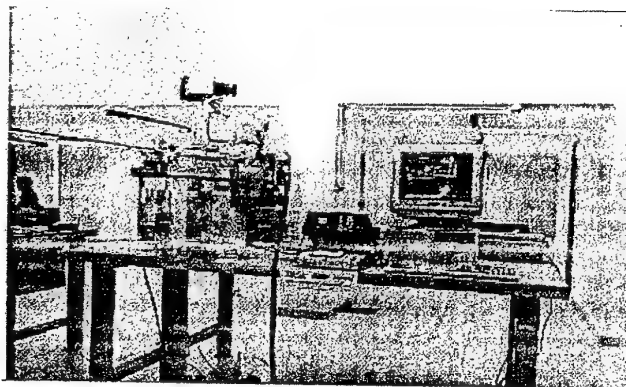


Fig. 1

Figure 2 illustrates the instrument for geometrical characterization of ultrasonic probes. The system consists in a mechanical-hand probes-holder able to shift on the three axes (x,y,z), a computer, a ultrasonic device and a printer for graphics plotting.

The mechanical system is interfaced with a process computer that allows the acquiring in the space of acoustic pressure reflected by a reflector. The ultrasonic signal is generated by the system made up of an ultrasonic instrument, coaxial wire and probe.

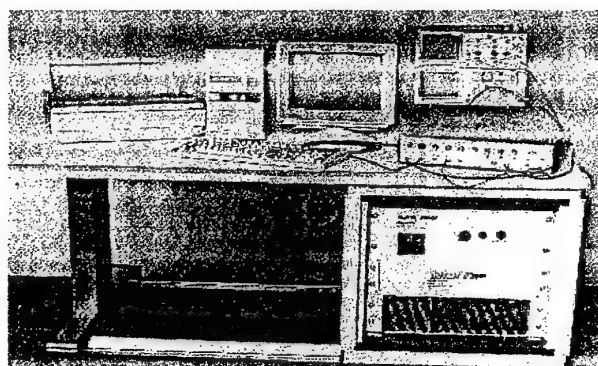


Fig. 2

The mechanical shifting is of high resolution (<0.1 mm) and is computer controlled. It is possible to construct a coloured map of the ultrasonic beam on the perpendicular plane (immersion tests) to the acoustics axis.

3. DYNAMIC CHARACTERISATION OF ULTRASONIC TRANSDUCERS

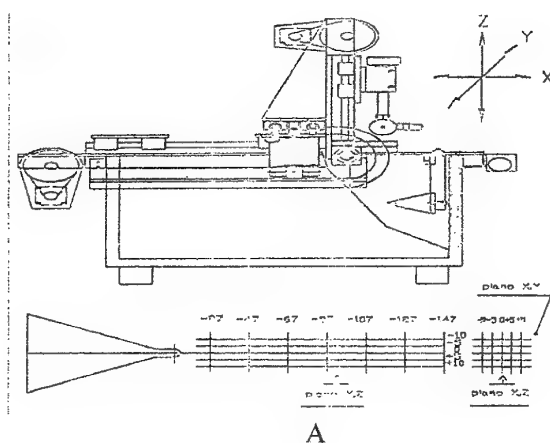
This test has been carried out utilizing the instrumentation shown in figure 1 and a flat commercial probe, that had already been used on field.

These are the characteristics of the probe: flat probe of diameter 25 mm, frequency 2,25 MHz; the probe is coupled with oil film and membrane.

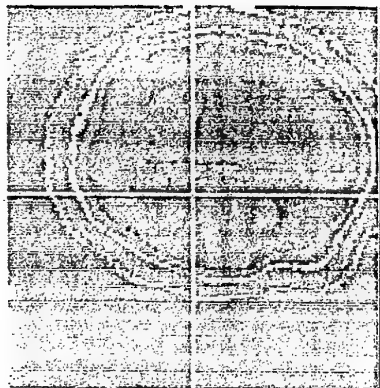
For the purpose of this investigation, a suitable locking was designed in order to utilize the probe beam on a parallel plane, submersed and centred on a truncated cone reflector with a 5 mm diameter. This probe is placed at decreasing distances from 27 to 147 mm from the reflector plane.

Each Y-Z plane is created by performing a scanning with a 0.1 mm resolution. The acoustic pressure values are recorded here in. The resulting maps (B,C,D,E,F,G and H) show the effective value of ultrasonic beam, point by point.

The dimensions of the scanning are of 30x30 mm and the mechanical centring of the probe is marked on the maps by a white cross. This test shows that the beam of the probe is out-of-track by 5+5 mm as compared to the mechanical centre. Hence, by taking down the position of defects, the operator

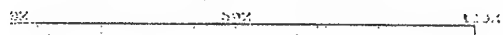


makes an error whose intensity is indicated above.

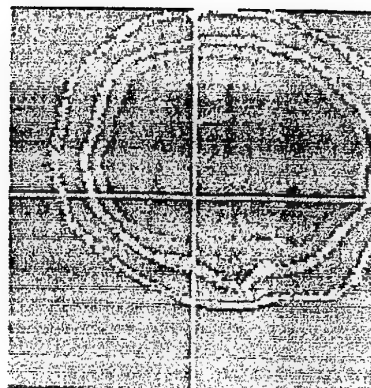


Y=30 Z=30

PIANO Y-Z POSIZIONE #27

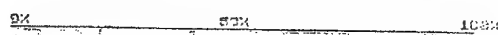


B

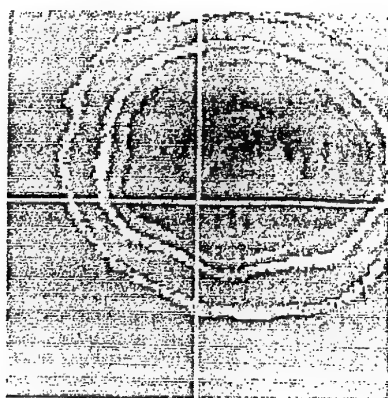


Y=30 Z=30

PIANO Y-Z POSIZIONE #17

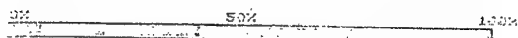


C

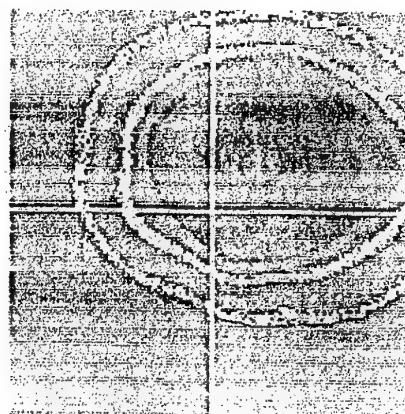


Y=30 Z=30

PIANO Y-Z POSIZIONE #67

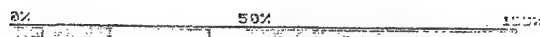


D

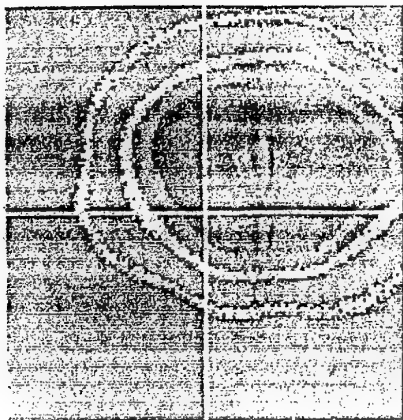


Y=30 Z=30

PIANO Y-Z POSIZIONE #07

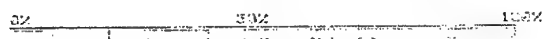


E

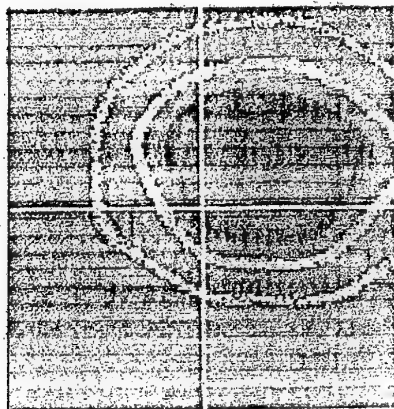


Y=30 Z=30

PIANO Y-Z POSIZIONE +107

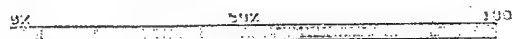


F

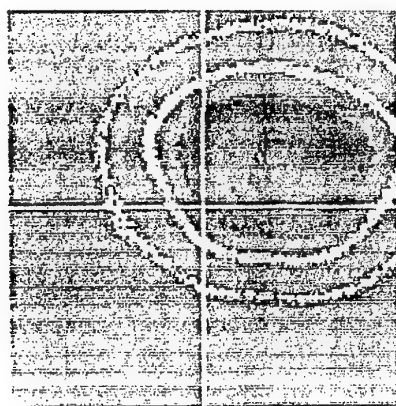


Y=30 Z=30

PIANO Y-Z POSIZIONE +127

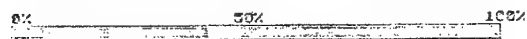


G



Y=30 Z=30

PIANO Y-Z POSIZIONE +147



H

4. ELECTRIC CHARACTERISATION OF ULTRASONIC INSTRUMENTS

The second test is related to the correct adjustment of the damping parameter of the ultrasonic instrument. This is a very subjective parameter and has to be adjusted each time the operator carries out an examination. If this parameter is wrongly adjusted, it is possible to achieve results that are not in conformity with the specifications. Actually, if the transducer does not resound at the right frequency, the system is badly tuned and the examination is unreliable. The length of cables does also cause some incompatibilities between transducer and transmitter, which can be reduced by a correct adjustment of the damping parameter.

Tests have been carried-out utilizing the instrumentation shown in figure 2, where an oscilloscope and a spectrum analyzer are parallel connected to the transducer/transmitter cable. The examination has been executed with the same probe firmly submersed at the optimum focal distance in order to reflect the signal of a specular flat target.

We have obtained significant results i.e., the resonance value change largely without a considerable change of the radio-frequency signal amplitude.

5. CONCLUSIONS

In the light of the results presented so far, we may conclude that the choice of ultrasonic waves and a correct planning of electronic parameters is fundamental to guaranteeing the reliability, the sensibility and the repeatability of control required by the specifications of work. Please, note that in this regard, the technical standard that govern the correct application of ultrasonic testing, do not provide any rigorous, indication on the operative parameters variation.

Our tests suggest that, both qualitatively and quantitatively, the behaviour of conventional ultrasonic probes is function of planned electronical parameters and potential wear of probes. The research results obtained so far, have underlined the importance of preliminary analysis and characterization of probes. In any case, without them the control would become very subjective and linked to the operator's good faith.

Nevertheless, in a Quality Control system the verification of operative parameters and of probes performances is binding.

6. REFERENCES

- [1]. Calgano G., Cantore C., Sandrone C., Marmigi R., Peri F., *"Problems of instrumentation and standardization in the polyethylene pipe joints inspection first results of a computerized ultrasonic system application for flaws detection"*, Second European Conference on Joining Technology, Eurojoin 2, 16/18 May (1994).

RADAR SYSTEMS FOR INTELLIGENT CRUISE CONTROL OF ROAD VEHICLES

A. Stoica, Alexandra Caramizoiu, Denise Jianu

Institute of Optoelectronics, 1 Atomistilor str., Bucharest-Magurele, Romania,
phone: 780.66.40; fax: 423.25.32

ABSTRACT

This paper presents the current status of research in the areas of autonomous intelligent cruise control and collision warning/avoidance for vehicles. The current position in terms of perceived requirements of the automotive industry as well as the suitability of present systems for meeting those requirements are reviewed.

1. INTRODUCTION

Over the past couple of years, the activity in the areas of autonomous intelligent cruise control and collision warning/avoidance for vehicles has significantly increased [1-3]. The first systems are now in the low-level production (e.g., the vehicle collision warning system as installed by Vorad Safety Systems Inc. on the Greyhound Bus business in North America). In Occident the automobile manufacturers have started to define their requirements for volume production units, while several potential suppliers have proposed different system solutions.

2. REQUIREMENTS OF THE AUTOMOTIVE INDUSTRY

Due to the technological advance, the cost and performance of electronic components has changed dramatically. Large-scale integration in silicon chips and the advent of "supercomputers" has opened up new avenues for the automotive industry (e.g., electronic engine management module, Radio Data System - RDS, Car Area Network - CAN).

These advances, together with those in radar and laser technology, meant that potentially, accurate range-finding equipment is now available to the industry. Radar and LIDAR technology both offer the possibility to search ahead several hundred metres and measure accurately the distance to the nearest objects.

Automobile manufacturers have identified several applications for such a device, including:

- Autonomous Intelligent Cruise Control (AICC),
- collision warning/obstacle detection;
- collision avoidance; and
- parking aids.

Generally, vehicle manufacturers carried out extensive market research in order to establish which feature would enhance the sales of their vehicles. A study by Daimler Benz showed that 60% of rear-end collisions could be avoided if drivers had an extra 0.5 seconds to react (and 90% with a full one second!).

From these statistics, it would appear that collision warning would be the first requirement. However, there are several potential problems, namely:

- the legal implications for system malfunction, and
- the very high level of signal processing required to limit the number of false alarms.

In a few applications, collision warning systems found acceptance (especially for long distance driving of large vehicles with professional drivers). However, a more acceptable concept for the introduction of this type of technology is AICC. In AICC, if the system 'malfunctions' then the driver is made aware that the system has lost 'cruise lock' and resumes full control.

Within AICC there are two main categories:

1. urban cruise - where the system controls the speed of the vehicle, down to a standstill and then back up again; and

2. motorway cruise - where the system controls the vehicle from low speed (25 km/h typically) to high speed (160 km/h) only.

The major technical difference between urban and motorway cruise systems is in the area of coverage by the antenna. For stop-start systems, the total area between the vehicle and the 'targeted' object ahead must be surveyed when the vehicles are stationary - or very slow moving. This is primarily to detect pedestrians walking between traffic. Both urban and motorway cruises require very good angular resolution, to establish the position of all vehicles of interest in a forward zone that can be extended for 150 - 200 m.

Vehicle manufacturers have to decide whether AICC will access both the brake and accelerator, or just the accelerator. The legal implications of accessing the brake need special considerations, as does the Man Machine Interface (MMI).

The greater the perceived value to motorists, the more expenses they will accept. However, the first systems may have limited performance (e.g., motor AICC, accessing accelerator only) and consequently will command only a low price.

Therefore, the ultimate system requirement appears to be for collision avoidance. It is generally accepted that 'driver in the loop' systems (for example, AICC) will first emerge, but such systems will need a progressive 'upgrade' to secure full collision avoidance. A potential route for exploitation could be:

- motorway AICC - accessing accelerator only;
- motorway AICC - accessing brake and accelerator;
- urban AICC - accessing brake and accelerator;
- collision warning;
- AICC with collision warning; and collision avoidance.

3. SYSTEM TECHNOLOGY

There are three basic technologies which may be used for the sensors in these applications, each one with its own merits, (see table 1):

- millimetre-wave radar (77 GHz);
- LIDAR; and
- video (pattern-recognition) techniques.

Table 1 Relative Merits of Competing Sensor Technologies.

Method	Advantages	Disadvantages
Radar	• Excellent performance in adverse weather conditions.	• Limited angular resolution
	• Complies with health legislation for radiation levels in non-ionising energy.	
	• The sensor can be mounted in a concealed place.	
LIDAR	• Excellent angular resolution	• Energy levels give potential health worries.
		• It has to be mounted in a visible position.
		• Very limited performance in adverse weather.
Video	• Excellent angular resolution	• It has to be mounted in a visible position.
	• Information available over wide azimuth and elevation	• Very limited performance in adverse weather.
	• Multi-application	• High demands on signal processing

3.1 Radar

The major advantage of a radar-based system operating at 77 GHz is its excellent performance in adverse weather. Radar has the ability to penetrate fog, rain and in recent tests it was shown that the range (150 - 200 m) was not significantly affected by adverse weather conditions. The power transmitted by the millimetre-wave radars to achieve this range is well within the American National Standards Institute (ANSI) recommended safety levels. The radar sensors can be quite small (dependent on the required antenna beamwidth). The radar projected by GEC Plessey Semiconductors (GPS) has a predicted production size of 120 mm x 120 mm x 60 mm and can be mounted behind glass or plastic panel at the front of a vehicle.

The current limitation in radar-based systems is in angular resolution of targets, especially in a multi-target, cluttered environment. Electronic beam steering and beam-sharpening techniques are currently being examined to overcome this problem.

3.2. LIDAR

Most current laser-based LIDAR systems use high power, 850 nm lasers. The beam width is very narrow (0.8°) giving excellent angular resolution. However, the major problem with LIDAR is its inability to penetrate rain and fog. In adverse weather, the system range is limited to the driver's visible range. There is also a potential problem with false returns from spray etc. The safety aspect of high power pulsed lasers is also in question. The eye safe distance is a real consideration especially for urban cruise etc. Mechanically-scanned lasers have the added potential problems of scanning failure, when the beam is in one fixed position transmitting all the energy in one direction.

The current systems proposed use LIDAR and work quite well in AICC applications. However, they may not find acceptance longer term for collision warning/avoidance systems.

3.3. Video

With frame capture and the application of extensive high-speed signal processing techniques, videocameras can play a very important role in the vehicle sensor market. With potential applications (in lane recognition, for example) as well as AICC and collision warning/awareness, this multi-purpose sensor may well find applications in the vehicle market. The main disadvantages of video systems are:

- lack of visibility in poor weather and bad lighting conditions (at night, for example), and
- very high demands in signal processing capacity.

However, video is an excellent candidate for sensor fusion techniques, where the advantages of radar and video are combined in one system.

4. SELECTION OF RADAR SYSTEM

Having established the benefits of a radar-based system, GEC Plessey Semiconductors has developed a technology for AICC/collision avoidance applications. To select which type of radar system is best for the application, the target specification for the sensor need to be derived. This specification is shown in table 2.

Table 2 Outline Specification

Range	0.5 m - 150 m
Range accuracy	± 0.25 m over 0.5 - 50 m ± 0.50 m over 50 - 150 m
Differential speed resolution	< 5 km/h
Beamwidth (switchable over 3 positions to give 10° coverage)	3°
Operating frequency	76 - 77 GHz
Transmit and receive polarisation	Circular
Size	10 cm x 7.5 cm x 6.5 cm
Environment	Harsh/exposed (automobile)
Interface	Car Area Network (CAN)/ Vehicle Area Network (VAN)

There are potentially many different types of radar, but the four considered for this applications are compared in table 3.

Table 3 Relative Merits of Competing Radar Systems

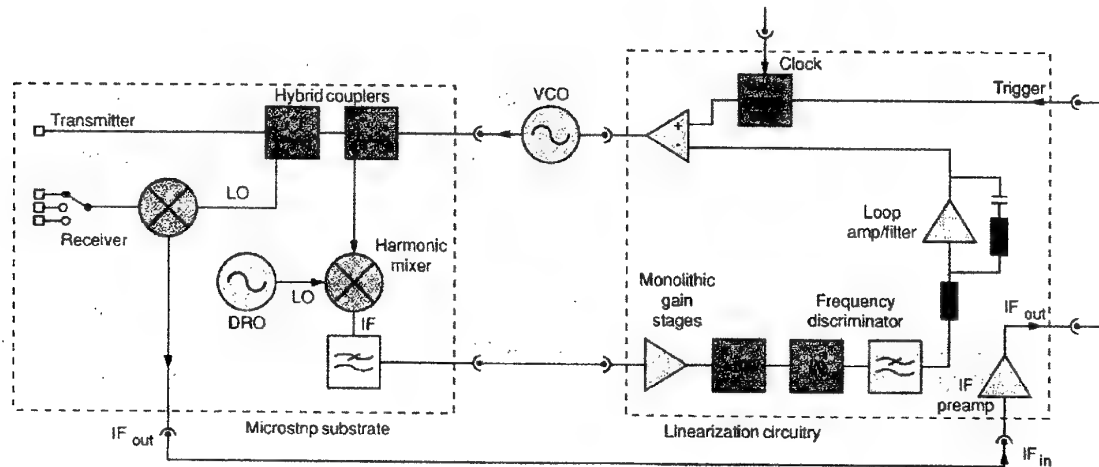
Radar technique	Minimum range (aprox) (m)	Source phase noise requirement	IF bandwidth	RF complexity	Mean power transmitted
FMCW	0.5	High	Low	Lowest	Medium
Pulsed FM	3	Low	High	Medium	Low
Pulsed AM	3	Low	High	Medium	Low
BPSK/QPSK [@]	0.5	High	Low	High	Lowest

[@] BPSK = Bi-Phase Shift Keying; QPSK = Quadrative Phase Shift Keying.

The minimum range for the system needs to be approximately 0.5 m to detect anything very close to the vehicle. With pulsed systems, there is a time lapse between the transmission of the pulse and receiving it back. As the velocity of RF propagation is 3×10^8 m/s, for short distances there are literally just a few nanoseconds between transmitted and received signals. This leads to prohibitively high speed signal process requirements. FMCW (Frequency-Modulated Carrier Wave) is a natural choice for the detection of short range targets.

The FMCW radar requires a phase noise of better than -80 dBc/Hz (that is, -80 dB/Hz relative to the carrier power level) at 100 kHz to enable the system to discern adjacent targets with good resolution.

The IF bandwidth of the system is particularly important in the automotive environment, where EMC and interference levels are high. It is vital to use as limited a bandwidth as possible. With FMCW systems, the IF receiver bandwidth can be limited to a few hundred kHz. Mutual interference problems are also reduced with reduced IF bandwidths.



The front-end schema of a 77 GHz radar sensor.

RF complexity again can be directly measured in terms of unit cost. FMCW is extremely simple, with very few millimetre-wave components as this may be seen also from the above block-schema of a 77 GHz radar sensor.

5. CONCLUSIONS

The 77 GHz sensor realised in prototype form, has now been evaluated extensively and is the basis for AICC and collision avoidance programmes in Europe, North America and the Far East. Further work on the antenna to improve angular resolution is continuing, and alternative methods of quasi-optical

beam steering are being evaluated.

A full programme looking at high volume manufacturability of the sensor has been undertaken at GEC Plessey Semiconductors, with an outcome which has proved that, with current technology, the unit production price for the sensor should be < \$100. As new technology becomes available (for example, GaAs MMICs etc.) it should be possible to reduce prices further after high-volume product introduction.

6. REFERENCES

- [1]. Lowbridge, P.L., "*Low-Cost Millimetre-Wave Radar Systems for Intelligent Cruise Control Applications in Road Vehicles*", GEC Review, vol.10, no.2, (1995).
- [2]. Stove, A.G., "*Automobile radar*", Applied Microwave, vol.5, no.2, (1993).
- [3]. Ulke, et al., "*Radar based automotive obstacle detection system*", Society of Automotive Engineers Conference, Detroit, February (1994).
- [4]. Takimoto et al., "*Automotive anticollision radar*", Applied Microwaves, Fall 1992.
- [5]. Lowbridge, P.L., "*High power, high stability wave Gunn diode oscillators using graded gap transfer electron devices*", MIOP Conference, (1990).

Session B5 & B7

**OPTOELECTRONICS DEVICES AND
COMPUTERS IN OPTOELECTRONIC
RESEARCH**

THE "3EYES" ACTIVE VISION SYSTEM FOR METROLOGICAL APPLICATIONS

D. Cojoc, P. Grattoni*, R. Nerino**, G. Pettiti*

University "Politehnica" of Bucharest, Romania,

* Centro di Studio per la Televisione - CNR ,

** Istituto Elettrotecnico Nazionale Galileo Ferraris Strada delle Cacce, 91 - 10135 Torino - Italy.

E-mail: grattoni@cstv.to.cnr.it

ABSTRACT

3Eyes is an active vision system based on three TV cameras and designed for metrological purposes. In this paper the main features of the system are presented together with some of its applications.

1. INTRODUCTION

3Eyes is an active vision system that has been designed and developed at CSTV laboratory of the Italian National Council of Research (C.N.R.) in the frame of the project "Safeguard of Cultural Heritage". The original goal of the project was the development of a visual system able to acquire dimensional and pictorial information of works of art, with high accuracy, for restoration and conservation purposes. Nevertheless, its features make it useful for a wider range of applications, like performance assessment of robots and low accuracy co-ordinate measuring machines. Transportability, simplicity of use and low cost (compared with the costs of traditional close-range photogrammetric system) were set as constraints. In short, 3Eyes is composed by three B/W TV cameras aligned along a common axis (see Fig. 1).

Two of them (telegoniometers TL_1 and TL_2 in the following) are equipped with long focal-length lenses, so to frame only small portion of a scene at high resolution; they can rotate around the parallel axes α_1 , α_2 and the tilt axis γ , to perform fixation of points in a scene.

The third camera is equipped with a wide-angle lens (WA) which allows to frame the whole region of interest of the scene at lower resolution. In a typical task the WA image is processed to find structures of interest. Once they are found, the system automatically drive the attention of the two TLs to fixate these structures and then performs the measure of their spatial positions and/or acquires their images at higher resolution. If required, one of the TLs is equipped with spectral filters which allow to acquire high accuracy colour images or to measure the spectral reflectance of the examined surface. Aim of this paper is the description of 3Eyes and of some of its applications. In Section 2 the 3Eyes system will be described from the structural point of view.

In Section 3, control aspects and the related image processing techniques needed to supply the system with the required functionalities, are presented. The system applications and their possible extensions are described in Section 4. Concluding remarks are presented in Section 5.

2. THE 3EYES STRUCTURE

Since 3Eyes system has been designed for metrological applications, particular attention has been paid to find out the best technical solutions compatible both with accuracy goals and with cost constraints. From the point of view of three-dimensional measurements, 3Eyes works like a telemeter with a fixed measuring base (see Fig. 1)

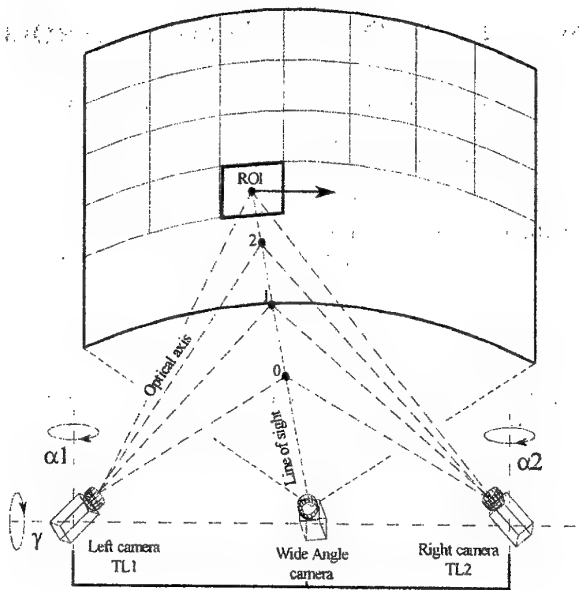


Fig. 1 The 3EYES system

The position of a point in a scene is measured by computing the intersection of the optical axes of the two telegoniometers TL_1 and TL_2 , while fixating at the examined point. Apart from the distance between 3Eyes and the point to be examined, the accuracy of the measure depends on the accuracy by which the values of the measuring base and of the angles of sight of TLs are known and, more in general, on the accuracy of the calibration of the system geometry. For these reasons, great care was devoted to mechanical assembling and registration aspects, leaving the task of compensating small residual errors to a simpler calibration process. All the mechanical structure is made in aluminium in order to guarantee homogeneous dilation with temperature. The base width is 800 mm and the arm temperature is monitored to take into account possible dilations during measures. Micro-Controlled rotating tables are used as angular actuators for the pan and tilt movements respectively. They supply absolute angular positions with resolution and repeatability better than $17 \mu\text{rad}$.

Critical components of the system are the two TV cameras to be used as telegoniometers. Indeed they are used both for dimensional measurements and for color or spectral measurements so they must satisfy many requirements. To guarantee the required resolution and repeatability in color or spectral measurements, the Signal-to-Noise ratio must be greater than 60 dB in any working condition.

To satisfy all the requirements, two digital cameras iCAM 18 produced by the D.T.A. of Pisa, have been used. These cameras are based on a 1024×1024 square-pixel CCD sensor, and are cooled by means of Peltier cells so to guarantee a true 14 bits digital output and an integration time up to hundreds seconds. These cameras can be equipped with filter wheels mounting up to 9 filters.

At present the system is not operative yet, so the software development and tests are carried out on a smaller resolution prototype (Fig. 2).

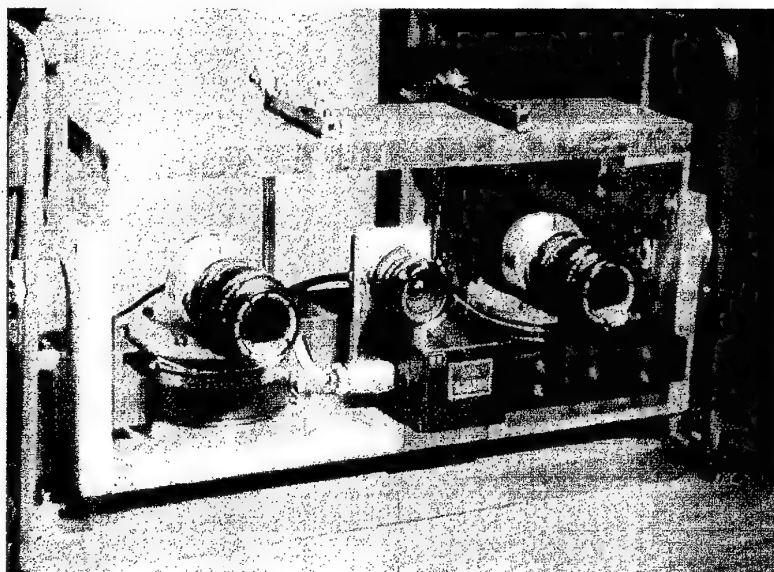


Fig. 2 The low resolution prototype

This last system is based on conventional rotating tables whose accuracy is 10 time worse than the new ones. Its measuring-base-length is 280 mm and only B/W, standard CCIR, TV cameras are used. Performances of this system were tested on a calibration target and a result is shown in Fig.3.

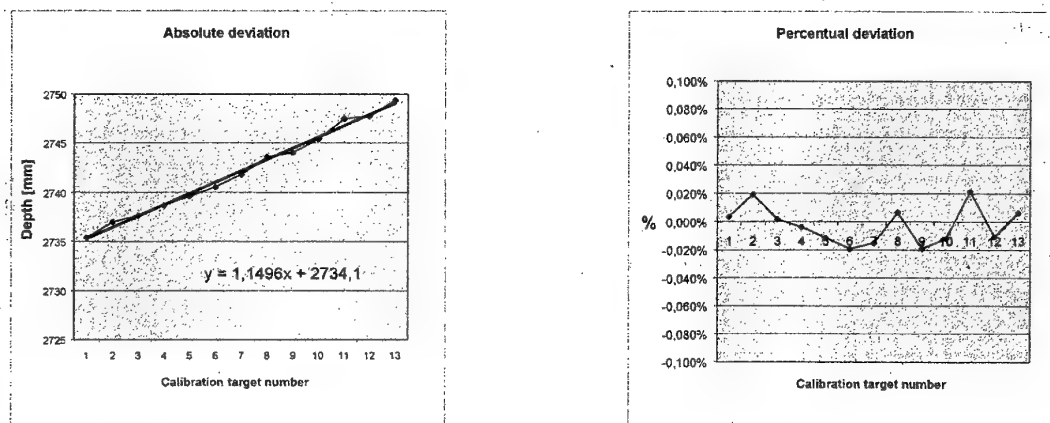


Fig. 3 Depth measurement accuracy. The test measures were carried out on 13 calibration points aligned along the same axis, and evaluated as the deviation from linearity

3. 3EYES CONTROL AND RELATED IMAGE PROCESSING TECHNIQUES

One of the basic functions of 3Eyes consists in performing the fixation task for any physical point whose image has been detected in the WA image.

Fixation is the process that make the optical axes of the two telegoniometers TLs to converge on a desired point in the space.

The accuracy of this process will affect more or less heavily the results of tasks that are carried out, consequently, the fixation task is worthy of the maximum computational effort. A typical fixation procedure is carried out as follows: once a structure of interest is found in the WA image by means of a specific algorithms of image processing or by means of human operator who interactively selects the region of interest while looking at a monitor, the system must drive the telegoniometers to point this structure. But the WA image is a monocular view, so the only information the system can supply to TLs to make them to converge, is the line-of-sight under which the examined structure is seen by the WA camera and some description of the structure to be pointed at. Then, the TLs are driven to scan the line-of-sight at convenient steps, from the point nearest to the cameras to infinity (see Fig.1). At each step, the description of the contents of each TL image is compared with the description of the reference structure until they become similar. At this point, the offset between the description of the examined structure in the WA e TL images is computed and zeroed in by acting on the rotating tables of TLs. Finally, since WA and TL images have different spatial resolution, the last step consists in the direct comparison of the two higher resolution TL images to get the maximum fixation accuracy. From a practical point of view, the implementation of the above procedure requires the solution of a number of problems which are concisely described hereafter.

- a) **Geometric calibration of the system.** Assuming that the geometry of 3Eyes (parallelism, orthogonality, intersection of rotating and optical axes) has been assured by the mechanical working and registration, the aim of the geometric calibration is devoted to the evaluation of the base-line length and to establish a common reference system for the three TV cameras. This common reference system, which is centered in the middle of the base-line, also allows the TLs cameras to share the line-of-sight parameters of the WA camera during the fixation process. The calibration is obtained by solving a system of non-linear equations relating the 3D position of number of calibration points to their images in the WA camera. The 3D positions of the calibration points are computed through fixation processes by the TLs. The pin-hole model has been used to account of the WA camera geometry.
- b) **Image comparisons and disparity computation.** Fixation procedure require both the description and recognition of a structure and the computation of the disparity in its representation in two different images. Two approaches are possible depending on the kind of structure has to be pointed at: structures which are known in advance and structure for which no a priori knowledge is available. In the first case, optimized algorithms can be developed to localize them with accuracy of some 1/100 of pixel. In the second case, the luminance signal itself or some suitable transformation of it is used to describe the unknown structure. The recognition of the presence of the same structure in two images and the computation of the disparity in its representation are obtained by matching the two signals. By this way, an accuracy of the order of one 1/10 of pixel is possible in natural images.
- c) **Management of images at different resolution levels.** The first part of the fixation process is carried out by comparing two images of the same scene taken at different resolution: the WA and TL images. To allow their comparison using the matching techniques described at point b, TL images are scaled down to the WA resolution. In particular, since the WA and TL lenses have a focal length of 12.5 mm and 100 mm respectively, the scale factor is 8.
- d) **Automatic detection and characterization of "pointable" structure in WA image.** Not all the points of an image are useful to get high accuracy in the fixation process. Only those points

(Characteristic Points) carrying the most significant portion of information should be selected, e.g. various types of junction, grey level corners, line termination, spots. In order to detect these points a new method [1], that has been proposed recently, has been implemented. This method localizes characteristic points in correspondence of local maxima of the "Energy Map" of an image. The local energy map is calculated by band-pass filtering an image using pairs of even- and odd-oriented Gabor functions. In addition, a powerful description of each characteristic point is associated to its image co-ordinates to allow the detection of more reliable correspondences between couple of images of the same scene, taken from different point of view, as it happens in stereo and motion problems [2].



Fig. 4a) One of the poster tiles



Fig. 4b) Part of the reconstructed image (4 tiles)

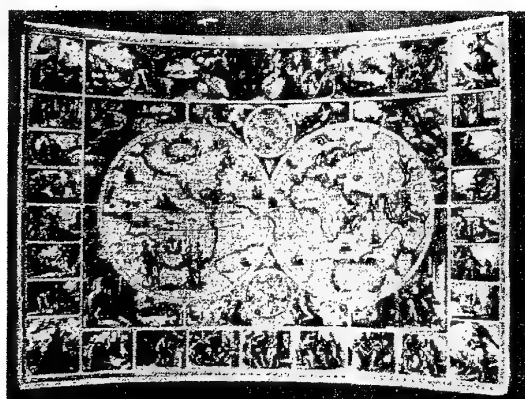


Fig. 4c) Reconstructed image of a curved poster used as test scenery

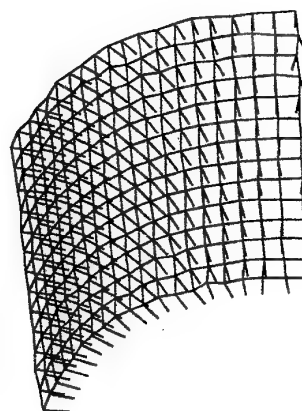


Fig. 4d) The reconstructed surface geometry of the curved poster

4. EXAMPLE OF APPLICATIONS

3Eyes has been designed for the acquisition of pictorial and dimensional information of three-dimensional painted surfaces, but its features make it useful also for other applications. In this Section we will review some of them.

4a) Acquisition of three-dimensional painted surfaces

3Eyes is placed in front of the subject to be acquired (frescoes, mosaics, large paintings) and set to frame the whole region of interest by the WA camera. The WA image is processed to detect its characteristic points (see point d in Section 3). The 3D position of each characteristic point is measured through the fixation process and used to compute the spatial evolution of the painted surface by interpolation with suitable surfaces. The knowledge of the painted surface geometry with respect to 3Eyes position is used to plan the geometry of the illumination sources for the best acquisition. At this point, the system starts the acquisition of the painted surface as a set of partially overlapping tiles (Fig.1) by sequentially scanning it by the TLs. For each tile the C.I.E. chromatic components X , Y , Z are acquired together with its spatial position and orientation. In the end, the whole surface is spatially reconstructed by positioning and sticking together all the image tiles as in a mosaic. By this procedure all the framing geometry (light sources-subject-TV camera) is fully controlled by 3Eyes and can be saved for reliable repetitions of the acquisition at different times. In Figure 4, an example of 3D image acquisition by B/W TV camera, in laboratory environment, is shown.

4b) Monitoring of the visual art degrade

Monitoring of some characteristics (colour, geometry, size of fissures, ...) of work of arts is of utmost importance in the field of the conservation and restoration. This task usually involves the repetition of measures only over small and well defined areas of the subject (e.g. some squared centimeters) and, sometimes, in almost uniform areas. In addition, results can be heavily influenced by the spatial measuring position, so that very different values will be obtained from different measures on slightly shifted areas even if they are performed closed in time. So it is extremely important to be able to restore the reference setting conditions in different measuring campaigns. Using 3Eyes the monitoring process is carried out as follow. In the first measurement campaign, the setting procedure of the system, the detection of characteristic points in the WA image, the measure of their spatial position with respect to 3Eyes and their description are performed as said in the application (4a). These data represent in some way a geometric description of the scene and are stored for future reference. At this point, a human operator interactively drives the system to point at the regions of interest and starts the measuring procedure, e.g. the spectral distribution of the surface reflectance, the width of a fissure, and so on, by looking at the scene through a monitor. For each test point TP the measure results are saved together with the 'address' of the point itself expressed as the sum of the angular co-ordinates of its nearest characteristic point CP_{near} (which acts as a reference) and of the angular deviation (pan and tilt) of TP with respect to CP_{near} . In a successive measuring campaign, the system compute again its position with respect to the subject by repeating exactly the same procedure carried out in the first campaign to detect and describe the characteristic points. Then, the offset of 3Eyes current position with respect to the reference one is computed by finding the correspondences between characteristic points in the two configurations. This is allowed thanks to the comparisons of the associated descriptors and to a global approach describe in [3]. Once the offset has been zeroed, recovering the reference position, the original measures are automatically repeated, first by fixating the nearest reference point CP_{near} and then by moving the TL of the associated angular offset. In Figure 4 the results of this procedure carried out in laboratory environment are shown.

4c) Performance assessment of robots and measuring machines

Theoretical evaluations and the practical experience carried out by means of our prototype (see section 2) allow a realistic estimation of 3Eyes accuracy in 3D measurements: using calibrated targets

(high contrast disk), in a working volume of 1 m³, 0.01 mm is expected. This feature make the system useful for some interesting applications like the performance assessment of robots and low accuracy co-ordinate measuring machines (e.g. horizontal arm structures). In this case the measuring procedure could be as follows. A high-contrast target (possibly accommodating more than one basic 2D feature) is firmly fixed at the end effector of the system under test, which is then moved within the working volume to predefined points. 3Eyes measures the true position of each testing point in its own reference frame and acts as a 3D external measuring system, whose results are to be compared with the information about the end effector position (eventually orientation) delivered by the system under test.

4d) Multiresolution survey of monuments

There is a strong demand in the field of cultural heritage for the acquisition of documentation and for the building of archives of works of art for restoration purposes and conservation. Speaking of monuments, typical documentation consists in dimensional measurements associated to photographic data. The classical technique used to this purpose is the short-range photogrammetry, but both the huge number of subjects and the complexity of the acquisition process prevents from an adequate response to this request. In this case 3Eyes can be the right response. On these working volumes (about 10³ m³), it is less accurate than conventional photogrammetric systems, but it is easily transportable, flexible and easier to use. 3Eyes can acquire and link together in short time: - dimensional data, by fixating either natural structures or fiducial marks; - images at different resolutions (the WA for the whole subject and the TL for details); - colorimetric or spectral information about some test points of the surface. And what is very important, 3Eyes allows the in-field analysis of the acquired data.

5. CONCLUDING REMARKS

The active vision system called 3Eyes and its applications have been presented in this paper. It has been designed for metrological applications and it has been shown that it can be a very powerful tool in this field.

3Eyes can perform both dimensional and photometric measurements and it has been designed to be easily transportable and usable in different environments, so it can find applications in a wide range of field. At present it has been planned for the monitoring and conservation of works of art and for performance qualification of robots and co-ordinates measuring machines.

Its performances in dimensional measurements are both limited by its intrinsic structure, i.e. the fixed base length, and by the accuracy of the components, e.g. the rotating tables, which is mainly limited by cost constraints. At present the cost of the 3Eyes components only is about 60000 \$.

Future developments in this field will be devoted to increase the 3Eyes performances and flexibility mainly by working on the algorithmic aspects.

6. REFERENCES

- [1]. B. Robbins, R. Owens, "2D feature detection via local energy", *Image and Vision Computing* 15, pp. 353 - 368, (1997).
- [2]. D.Cojoc, P.Grattoni, R. Nerino, G. Pettiti, "Image Description using Gabor Wavelets", *OPTIKA'98 - 5th Congress on MODERN OPTICS*, Budapest, Hungary, 14-17 Sept., (1988).
- [3]. D.Cojoc, P.Grattoni, R. Nerino, G. Pettiti, "Pose Estimation of an Active Stereo System by Principal Moments of Point Features", *OPTIKA'98 - 5th Congress on MODERN OPTICS*, Budapest, Hungary, 14-17 Sept., (1988).

OPTICAL FIBER METHANE SENSOR

S. Micloș, T. Zisu, B. Robea, I. Munteanu

National Institute of Research and Development for Optoelectronics,
P.O. Box MG-5, 1 Atomistilor Str., Măgurele - Bucharest, 76900, Romania
E-mail: miclos@mail.infim.ro

ABSTRACT

Optical fiber methane sensors are a good choice in explosive environments due to their electrical isolation and electromagnetic interference immunity. A high-sensitive and compact methane sensor, based on a differential method, is described in this paper.

1. INTRODUCTION

Chemical sensors penetrated markets as medicine, pollution monitoring, industrial hygiene, domestic appliances, burn diagnosis items. A large variety of chemical sensors are now commercially available and many more are under research. One of the most promising sensor type for future development is the optical fiber sensor.

Optical fiber sensors are currently used to measure the temperature, the pressure, the pH, but actually the largest demand of such sensors was for real-time spectroscopic analysis.

Optical fiber sensors offer multiple advantages over usual sensors: high sensitivity, fidelity, electrical passivity, hard environment resistance, compact construction, high response speed, electrical isolation and electromagnetic interference immunity. They also have expandability capabilities and they may be easily connected into networks and remotely controlled.

Optical fiber gas sensors used in explosive environments have an additional important advantage, i.e., they do not need any precaution, since they cannot produce accidents.

2. THE METHANE SENSOR LAYOUT

The block diagram of the optical fiber-based methane sensor is shown in Fig. 1. From the IR light source 1 (about 1300 nm), built around the LED 2, the emitted infrared radiation is injected into the optical cable 3. The cable, FC-PC connectorised, transmits the infrared radiation, focused by the objective 4 (with EFL 40 mm) through the methane atmosphere 5. The infrared radiation, refocused in the optical cable, is switched by the optical switch 6, alternately, in two branches. The "Measurement" branch comprises an interferential filter 7, centered on 1331 nm, while the "Reference" branch comprises an interferential filter 8, centered on 1300 nm. The switch is controlled by the Optical Switch Control and Lock-in Reference Block 13. The two branches are then merged, using the fiber optic coupler 9, on the photodiode 10 of the receiver 11. The signal from the photodiode is applied on the signal input of the lock-in amplifier 12, while the control signal for the optical switch is applied on the reference of the lock-in amplifier. The electronic block consists of the low voltage source, the optoelectronic transmitter, the optical switch control and lock-in reference block, and the optoelectronic receiver.

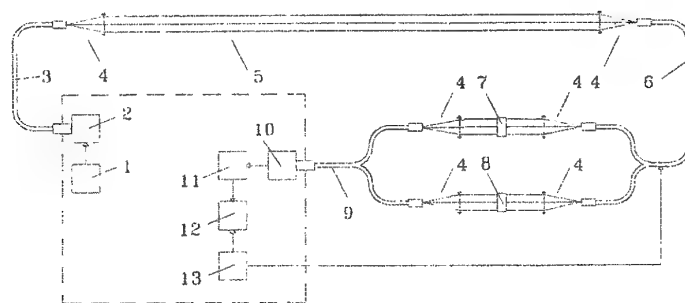


Fig. 1 Block diagram of the methane sensor

3. THE METHANE SENSOR DESIGN

Infrared optical fiber gas sensors have a large specificity among various gases; yet, the choice of a high power light source, compact and cheap for wavelengths greater than $2\ \mu\text{m}$ is frequently a problem. For wavelengths shorter than $2\ \mu\text{m}$, semiconductor laser diodes may be used as light sources. For instance, methane detection motivated the elaboration of a $1,66\ \mu\text{m}$ laser diode sensor system. For wavelengths greater than $2\ \mu\text{m}$, a more expensive laser or a narrow-filtered wideband light source (having low power, and thus low sensitivity) must be used.

The studies of Chan, Ito and Inaba [1], [2] demonstrated the possibility of developing methane sensor using fiber optics and laser diodes in the $1300\ \text{nm}$ and $1660\ \text{nm}$ windows. We chose the $1300\ \text{nm}$ one as its components are cheaper. The methane absorption curve for this window is shown in Fig. 2.

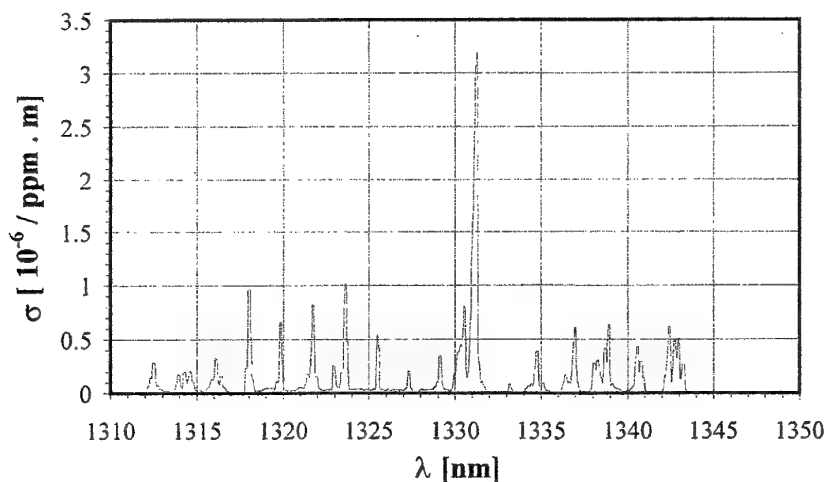


Fig. 2 Methane absorption in the $1331\ \text{nm}$ window

As light source we used a FC-PC connectorized $14\ \mu\text{W}$ LED. The emission spectrum of this LED is shown in Fig. 3.

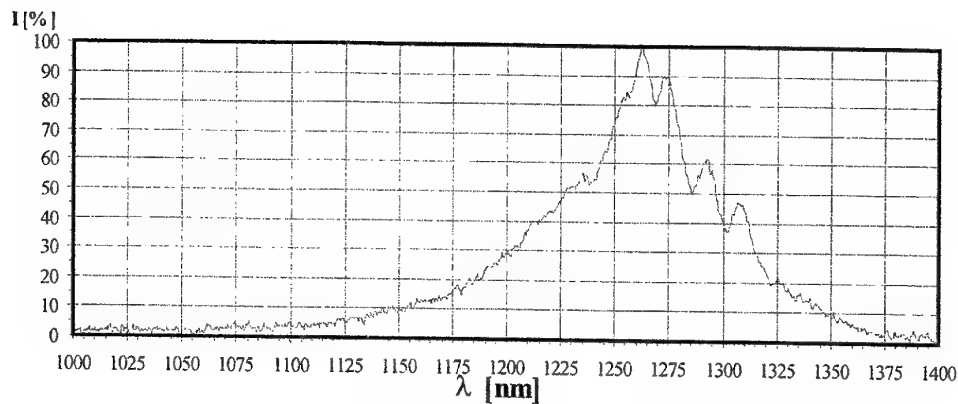


Fig. 3 Emission spectrum of the 14 μ W LED

The power budget of the system calculation is needed to evaluate the sensitivity level which has to be imposed to the photodiode. Table 1 shows the power budget elements.

Table 1 The power budget

BUDGET ITEM	VALUE
Connectors insertion losses: 4 connectors \times 0.4 dB	1.6 dB
Optical fibre attenuation losses: 2 km optical cable \times 1,2 dB/km	2.4 dB
Optical switch insertion losses	0.5 dB
Optical fibre coupler connectors insertion losses	0.5 dB
Optical fibre coupler insertion losses, excluding the connectors	1.0 dB
Interferential filter attenuation	4.0 dB
Objective losses: 4 objectives \times 0.5 dB	2.0 dB
TOTAL LOSSES:	12.0 dB

Taking into account the emission spectrum of the LED and the methane absorption in the 1330nm window, we evaluated the power losses due to the methane absorption (as function of methane concentration) and to the optical filter (as function of the filter bandwidth). The results of this study are summarised in Table 2.

Table 2 Power losses vs. filter bandwidth and concentration

$\Delta\lambda$ [nm]	Ref (0 %) [dB]	Methane 1 % [dB]	Methane 5 % [dB]	Methane 100 % [dB]
2	-24.1051	-24.1190	-24.1760	-25.2395
4	-21.2031	-21.2106	-21.2424	-21.8191
6	-19.0860	-19.4785	-19.5007	-19.9023
8	-18.1543	-18.1590	-18.1774	-18.5184
10	-17.1216	-17.1254	-17.1404	-17.4196
12	-16.2844	-16.2883	-16.3027	-16.5786
14	-15.6286	-15.6325	-15.6454	-15.8953
16	-15.0630	-15.0673	-15.0818	-15.3707
18	-14.5617	-14.5657	-14.5791	-14.8480
20	-14.0973	-14.1013	-14.1153	-14.3999

The minimum reference value (-14.0973 dB) is that of a 0 % methane concentration and a filter bandwidth of 20 nm (at bottom). For concentrations up to 5 % - LEL, the influence of the concentration on power losses modification is insignificant.

The maximum loss, for a 100 % methane concentration and a filter bandwidth of 2nm is -25.2dB.

Using a 14 μW (11,5 dB μ) LED, the photodiode sensitivity is of:

$$\begin{aligned} 11,5 \text{ dB}\mu - 12 \text{ dB} - 24,2 \text{ dB} &= -24,7 \text{ dB}\mu \text{ (methane 5\% and } \Delta\lambda = 2 \text{ nm)} = 3,4 \text{ nW} \\ 11,5 \text{ dB}\mu - 12 \text{ dB} - 14,1 \text{ dB} &= -14,6 \text{ dB}\mu \text{ (methane 5\% and } \Delta\lambda = 20 \text{ nm)} = 34,7 \text{ nW} \end{aligned}$$

Using a 70 μW (18,5 dB μ) LED, the photodiode sensitivity is of:

$$\begin{aligned} 18,5 \text{ dB}\mu - 12 \text{ dB} - 24,2 \text{ dB} &= -17,7 \text{ dB}\mu \text{ (methane 5\% and } \Delta\lambda = 2 \text{ nm)} = 17 \text{ nW} \\ 18,5 \text{ dB}\mu - 12 \text{ dB} - 14,1 \text{ dB} &= -7,6 \text{ dB}\mu \text{ (methane 5\% and } \Delta\lambda = 20 \text{ nm)} = 173,8 \text{ nW} \end{aligned}$$

We chose the solution of a 14 μW LED and a 20 nm interferential filter.

4. REFERENCES

- [1]. K.Chan, H. Ito, H. Inaba, "Absorbion measurement of $\nu_2 + 2\nu_3$ band of CH_4 at 1.33 μm using an InGaAsP light emitting diode", Applied Optics, Vol. 22, No. 23, December 1983
- [2]. K.Chan, H. Ito, H. Inaba, "Remote sensing system for near-infrared differential abssorbion of CH_4 gas using low-loss optical fiber link", Applied Optics, Vol. 23, No. 19, October 1984

ENHANCED OPTICAL FIBER REMOTE EXPLOSION STARTER

I. Munteanu, T. Zisu, S. Miclos, B. Robea

National Institute of R&D for Optoelectronics - INOE 2000,
Bucharest-Magurele, P.O. Box MG 5, Romania

ABSTRACT

This paper presents an enhanced optical fiber remote explosion starter, that can be used in mining of quarries and surface or deep coal pits. The common explosion starters, using electrical cable links between the control center and the explosion place, present the major drawback that they may unexpectedly initiate the explosion, due to the electromagnetic induction generated by the atmospheric electric discharges. The optical fiber remote explosion starter that we propose uses coded ignition command, that both improve the security in use and the system's versatility. The ignition command coding allows a versatile and easy multiple configuration of the system.

1. INTRODUCTION

The common explosion starters used in mining of quarries and surface or deep coal pits utilize electrical cable links between the control center and the explosion place. Their major drawback is that they may unexpectedly initiate the explosion, due to the electromagnetic induction generated by the atmospheric electric discharges.

The optical fiber remote explosion starters [1][2], remove this drawback by transmitting through an optical fiber cable, insensitive to the electromagnetic induction generated by the atmospheric electric discharges, the explosion start signals.

Optical fiber transmission systems offer a large range of advantages in respect to other transmission systems (radio, electric cable) due to features [3] such as:

- low transmission losses for wide bandwidth;
- small size and weight;
- immunity to electromagnetic interference ;
- electrical isolation;
- signal security;
- inexpensive raw material.

Such a transmission medium appears to have ideal qualities and it opens new opportunities for multiple other similar users.

An enhanced variant is proposed for an optical fiber remote explosion starter, that can be also used in mining of quarries and surface or deep coal pits. This enhanced version [4] uses coded ignition command, that both improves the security in use (by eliminating the on/off switches and by dramatically reducing the power consumption of the receiver) and system versatility. The ignition command coding allows a versatile and easy multiple configuration of the system.

2. SYSTEM DESCRIPTION

The schematic layout of the simplest system, is described in fig.1, and it is composed by the following units:

- | | |
|-------------------|---------------------|
| ☞ coder | ☞ optical receiver |
| ☞ optical emitter | ☞ decoder |
| ☞ optical cable | ☞ explosion starter |

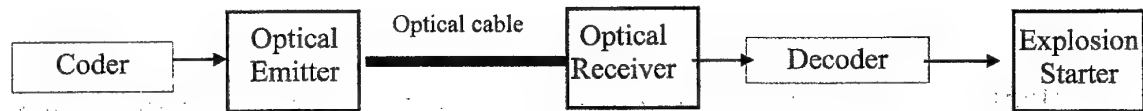


Fig. 1 The block diagram

In designing such systems we should give a special attention to security factors. In order to increase the security, the system uses an enhanced design for both the optoelectronic emitter and the receiving unit. These units do not use mechanical switches for coupling the power supply, but electronic switches. Thus, a toucher for supplying and generating the coded ignition command it is used for the optical emitter (a pulses sequence with pulse recurrence frequency of 1 kHz, duty cycle of 0.5), and a photodiode for supplying, receiving the coded ignition command and initiating the explosion it is used for the optical receiver. Briefly, the system improvements consist in :

- decrease the stand-by supply current;
- work only in the codifying and the transmitting of the ignition signal time for the emitter, and
- work only in the receiving, decoding and initiating explosion time for the receiver.

A maximum length of 1 km of monofilar multimode optical cable is usually sufficient. Because part of the fiber together with the optoelectronic receiver is lost during the explosion, we considered necessary to cut the cable in two segments, the first of 900 m, and the second of 100 m (the lost out segment), linked by optical connectors.

3. THE SYSTEM OPERATING DESCRIPTION

The operating units are supplied from batteries.

The generated code of the optical emitter (any number between 01 and 99 chosen by means of the coincidence of a two outputs, each one belonging to one of the two Johnson 4017 CMOS decade counters) is transmitted through optical cable as the same number of optical pulses. These impulses are generated by a LED with $\lambda = 850$ nm and power $P_0 = 60$ μ W. After generating of the ignition code the emitter returns to stand-by. The command by code avoids hazardous explosion.

The optical receiver recognizes the generated code by means of a coincidence similar to the above mentioned one (having two Johnson 4017 CMOS decade counters with the same used outputs) that is validated by a 4098 CMOS monostable multivibrator. If another sequence is transmitted, the receiver does not recognize the code and returns to stand-by mode. Also if the explosion does not take place, the receiver returns to the initial state.

4. CONCLUSIONS

The device, presented in the simplest layout, may be used either in the present form (Fig. 1) or in a more complex layout with several detonation points and using either a serial configuration or a star one.

5. REFERENCES

- [1]. Optical fiber remote explosion starter, T. Zisu, S. Miclos, B. Robea, C. Beldiman, patent request no. C- 2454 / 20.12.1996, OSIM
- [2]. T. Zisu, S. Miclos, B. Robea, Optical fiber remote explosion starter, ROMOPTO '97, SPIE, 5th Conference on Optics, 9-12 Sept. 1997.s
- [3]. J. Wacker, "A basic fiber optic communication system", *Optical Communication Workshop*, TH Darmstadt, p. 1/1, Bucharest, 17-21 May 1993
- [4]. T. Necsoiu, D. Oancea, T. Zisu, S. Miclos, C. Beldiman, "Dispozitiv cu fibra optica destinat amorsarii detonarilor", patent request no. C 1274 / 21.06.96, OSIM.

IMPACT OF THE NIGHT VISION DEVICES ON THE OCULAR PHYSIOLOGY

Lucia Iorga, Cristina Iliuta*, C. Ispasoiu *, Rodica Copot **

Psychological Examination Army Department,

* Institute of Medicine for Air-Force

** Institute of Optoelectronics, 1 Atomistilor Street, PO Box MG-22, Bucharest, ROMANIA
Phone:(401)7806640, Fax:(401)4232532

ABSTRACT

In the process of operating with night vision devices, the observer's eyes are subdued to simultaneous and/or successive processes of adaptation (at dark) and desadaptation (at light) because of the change of typical scotopic scenes into photopic scenes. This paper describes the theoretical and experimental studies we have performed in order to establish whether observer's eyes are endangered.

1. INTRODUCTION

Our theoretical and experimental studies were intended to emphasize the consequences of the efforts that the operator's eyes are forced to face during the adaptation - desadaptation processes of the operations with night vision devices with image intensifier tube.

We present the absolute spectral reply curve of the phosphor screen of the image intensifier tubes - in Figure 1, and the spectral sensibility of the human eye - in Figure 2. For both curves the wavelength is reflected on the abscissa. In figure 2 curve V_λ represents the relative spectral sensibility of the photopic vision while $V_{\lambda'}$ represents the relative spectral sensibility of the scotopic vision.

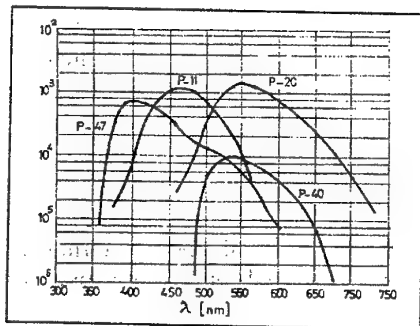


Fig. 1

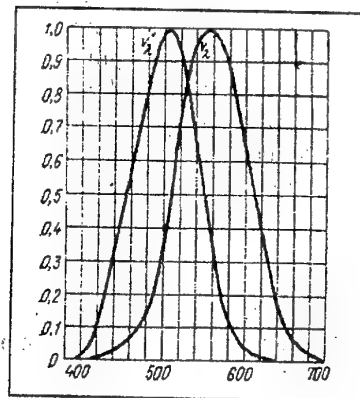


Fig. 2

2. THEORETICAL BACKGROUND AND EXPERIMENTAL PROGRAMME

As the performance of the visual analyser depends on both its integrity and the quality of the specific psychological processes, a complete evaluation of the visual analyser should be performed both by objective means (medical functional exploration) and subjective means (proper psychological tests). Therefore a programme of preliminary psychological and physiological tests was designed in order to select the operators.

Please note that we have carried on the experiments upon lots of operators who had been subjected to three former psychological examinations. These are: recruitment, conscription and before being employed in the army. The tests regard general intelligence and personality characteristics.

The real world impacts on the human receivers and the resulted reflections in the brain are sensations and perception. The threshold of the sensation varies with the following factors: fluctuation of subject's attention, changes in the functional conditions of the analyser, tiredness.

We assume that the visual analyser is the most solicited by concentrated attention.

That is why the subjects who have successfully passed the above tests are required to comply with the concentrated attention test.

In case of voluntary attention, the orientation and the concentration of the activity is realised by verbal means, and this is why the test instruction is important.

Taking into consideration that these studies were directed towards physiological aspects of the visual analyser (acting, accommodation, resistance), it is important to remove those subjects who could falsify experimental results because of reduced capacity of concentrated attention.

In order to test concentrated attention three barrage tests were applied and these are:

- Toulouse-Pierron;
- Concentrated attention - figures;
- Klazov.

From the physiological point of view we intended to select operators without troubled accommodation, visual sensation and visual reflex, in order to examine their visual acuity and adaptation - desadaptation processes, before and after operating with night vision devices.

Visual acuity is the capability to distinguish specific details and it varies indirectly with the size of the projected details on the retina. Visual acuity is expressed by the inverse of the visual angle caused by the distance between the nearest separately perceived points. Clinical assessment of the visual acuity is made using specific test patterns named optotypes, containing signs, letters, drawings.

The human eye has the property of changing the sensitivity of the receivers according to light intensity. The adaptation to low levels of illumination is done by means of three mechanisms: change of pupilar's diameter, increase of retinian's sensitivity, and neuronal adaptation.

If after the complete adaptation at dark, the subject is exposed to light, the adaptation is cancelled by means of desadaptation, which is the opposite phenomenon to adaptation. The control of this process important for many professions which are carried on in an attenuated light and short luminous environment might occur. The desadaptation (or the adaptation at light) is faster than the adaptation at dark and both processes are retinian phenomena without relative influence between the eyes.

For the selection of the operators the following medical examinations were established:

- refraction measurement;
- biomicroscopy and
- ocular back examination.

Refraction measurement emphasizes accommodation disorders and ocular back examination the integrity of retina. By biomicroscopy the anterior pole of the eye is examined (sclera, conjunctiva, cornea, anterior chamber, iris, pupil), as well as the pupilar photomotory reflexes, position and transparency of the crystalline lens, anterior third of the vitreous body transparency.

In addition to these examinations, the preliminary physiological test programme contains examination of the visual acuity and of the desadaptation process. After the preliminary tests, 14 subjects were selected for the first experiment, and 20 subjects for the second.

The proper experiment consisted in operating the night vision devices and subsequently examining the visual acuity and desadaptation process of each subject.

The following programme was established for the first experiment:

- short duration operating with night vision devices (a usual night mission);
- ophthalmological examination;
- long duration operating with night vision devices (a period of two months with usual night missions);

- ophthalmological examination.

For the second experiment the programme was simplified given certain organisational and scientific reasons:

- the impediments in making up and monitoring the experimental sample of subjects;
- long duration operating is not conclusive, because two months of sporadic operating does not induce changes of the ocular physiology;
- duration of the short operating was increased from 15+20 minutes to 100 minutes in order to experiment a longer continuous operating.

The programme of the second experiment was as follows:

- a) monitoring operation with night vision device for about 1.5 hours;
- b) ophthalmological examination of the subjects during operating (nocturnal visual acuity with night vision device) and after operating (desadaptation process by means of the Niktometer).

3 EXPERIMENTAL RESULTS

3.1 Visual Acuity

The values of visual acuity by night when sighting with night vision devices are presented in Table

1.

Table 1

VA values	Frequency		
	Counting	Absolute values	Relative values (%)
1/8	I	1	2,941
1/6	IIIII	5	14,705
5/24	IIIII	5	14,705
5/18	I	1	2,941
1/3	III	3	8,823
5/12	III	3	8,823
1/2	IIIIIIIIII	11	32,352
5/8	IIII	4	11,764
2/3	I	1	2,941

The frequency values corresponding to the nocturnal visual acuity presents normal distribution having a bimodal configuration: the first maximum is 1/5 and the second 1/2. The subjects having these nocturnal visual acuity with night vision device are about 29.41%, and respective 32.35% of the total amount of subjects. The explanation consists in the differences between the characteristics of the "night" in the two experiments: illumination level, reflectivity of the optotype poster, performance of the device (we used different devices and they were equipped with batteries in different stages of life).

3.2 Desadaptation Process

The desadaptation process is a function of the visual acuity depending on time and it was examined and recorded with the aid of the Niktometer. The results are presented in Table 2 and 3.

Table 2

Niktometer's values at preliminary examination	Frequency		
	Counting	Absolute values	Relative values (%)
0,4	II	2	5,882
0,5	IIII	4	11,764
0,6	IIIIII	6	17,647
0,7	IIIIIIIIIIIIIIII	15	44,117
0,8	III	6	17,647
0,9	I	1	2,941

Table 3

Niktometer's values after operating with night vision device	Frequency		
	Counting	Absolute values	Relative values (%)
0,4	II	2	5,882
0,5	IIIIII	6	17,647
0,6	IIIIIIIIIIIIIIII	12	35,294
0,7	IIIIIIIIII	9	26,470
0,8	III	3	8,823
0,9	II	2	5,882

The frequency values corresponding to the Niktometer's values obtained at both examinations present normal distribution. The maximum of the preliminary examination is 0.7 and it was obtained by 44.12% of the subjects. The maximum of the second examination is 0.6 and it was obtained by 35.29% of the subjects

4. CONCLUSIONS

The values of the nocturnal visual acuity emphasise the extension of human eye vision in scotopic circumstances by means of the night vision device.

The curves recorded by Niktometer present not only the values but also the evolution in time of the desadaptation process. If the two recordings of each subject are compared, one can find the same value of the visual acuity (23.53% of subjects), increasing or decreasing with one step of the first value (76.47% of subjects). It is interesting to notice that the trend is the decrease in the desadaptation duration from about 80÷110 seconds to 50÷80 seconds.

Our theoretical and experimental studies did not emphasise noxiousness of the night vision devices during the usual night tactical missions. Furthermore, the collected subjective data lead to the general conclusion that there are advantages of operating with night vision devices following to proper training.

5. REFERENCES

- [1]. ***, Electro-Optics Handbook, RCA Corporation, (1974).
- [2]. P. Cernea, Ocular Physiology, Medical Publishing House, Bucharest, (1986).
- [3]. I. Radu & colab., Introduction in Contemporary Psychology, Sincron Publishing House, Cluj, (1991).

MODULAR MINIATURIZED POWER SUPPLY FOR REPETITIVE MEDIUM POWER SOLID STATE LASERS

S. Sârbu, I. Pricop*, Carmen Radu, Silvia Radu, N. Mincu

National Institute of Research and Development for Optoelectronics-INOE 2000, Bucharest, Romania

*Institute of Optoelectronics, Bucharest, Romania

ABSTRACT

In this paper we propose a new type of modular miniaturized power supply for solid-state lasers, capable to make a dynamic change of its output parameters, in an automatically process of monitorization of the laser head parameters, in order to compensate the output laser parameter due to aging of flash lamp or other changes which would require periodical manual settings.

1. INTRODUCTION

The operating features of a laser head determine that power supplies of solid state lasers to present drawbacks, such as: 1) modification of output laser parameters due to the flash lamp aging, active medium, other mechanic-optical components which require periodical manual settings; 2) large size as a result of low efficiency in the convention of electrical energy to radiation.

In this paper we propose a new type of modular miniaturized power supply, which overtakes these shortcomings and presents better performances. The miniaturization has been achieved by using performant, small size electric and optoelectronic components, as well as a modular architecture of the power supply (the circuits were made on printed cards). The reproducibility of laser parameters is ensured by a control card that continuously displays the laser head and power supply parameters. The optoelectronic components draw the ignition of the flash lamp and the laser emission and then correlate them with the voltage on the charge capacitor.

In addition, the new power supply illustrate other important features: the versatility of the primary supply (mains or battery), optional preset of the working voltage, a continuously and efficient display of the state parameters, autotesting function, optional interface with a computer which is set up for a specific application.

2. THE MAIN BLOCK DIAGRAM OF A SWITCHED-MODE D.C. CONVERTOR

The power supply employed in pumping repetitive medium solid state lasers is a switched-mode d.c. convertor (SMCC) [1]; its block diagram is illustrated in Fig.1. As compared to a common linear power supply, SMCC presents several advantages, such as: enhanced efficiency, higher power/volume rate, low cost, diminished dissipation, and absence of big, expensive and heavy components (power transformers at mains frequency, smooth capacitors with high capacity).

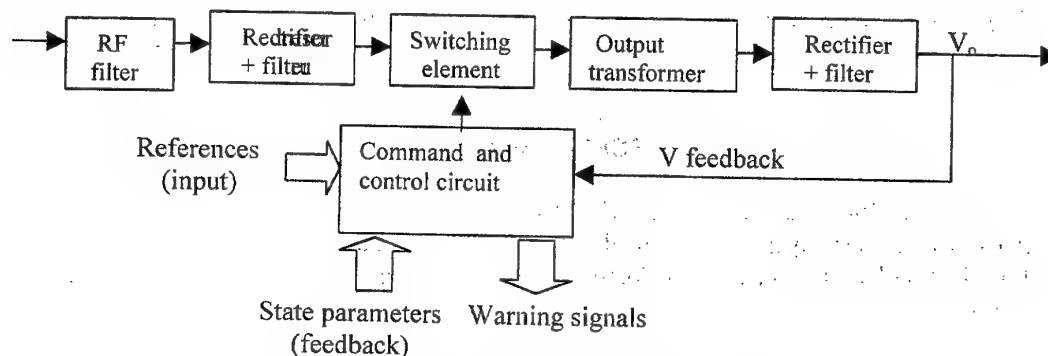


Fig.1 Block diagram of switched-mode d.c. convertor

We used a flyback convertor which had the simplest inductive circuit – its output transformer was a multifunctional device (choke, set-up transformer and mains separator [2]). An advantage of this structure is the possibility to obtain an increase of the output power and thus to have a modular construction of the power supply by connecting more sources in parallel. For instance, if we want to increase twice the power, in addition to the corresponding output stages (containing the switching transistors, the output transformers and the afferent rectifier diodes), only two supplementary cards are necessary: the command card and the power module. A complete power supply should also be equipped with several specific components [3] such as: the charge capacitor, the triggering transformer and the triggering pulse circuit (Fig.2). Due to technological considerations, the charge capacitor and the triggering transformer are located outside the power supply unit close to the laser head. The triggering pulse is an integral part of the power supply, being made on a printed card.

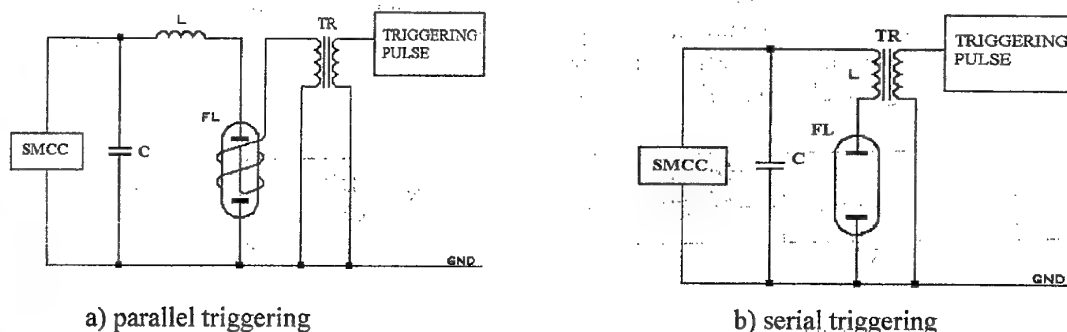


Fig. 2 Flash lamp supply circuit.

If a serial triggering is chosen (more convenient as it avoids the current leakage to the laser head), then the block diagram of power supply will contain the components presented in the Fig.3.

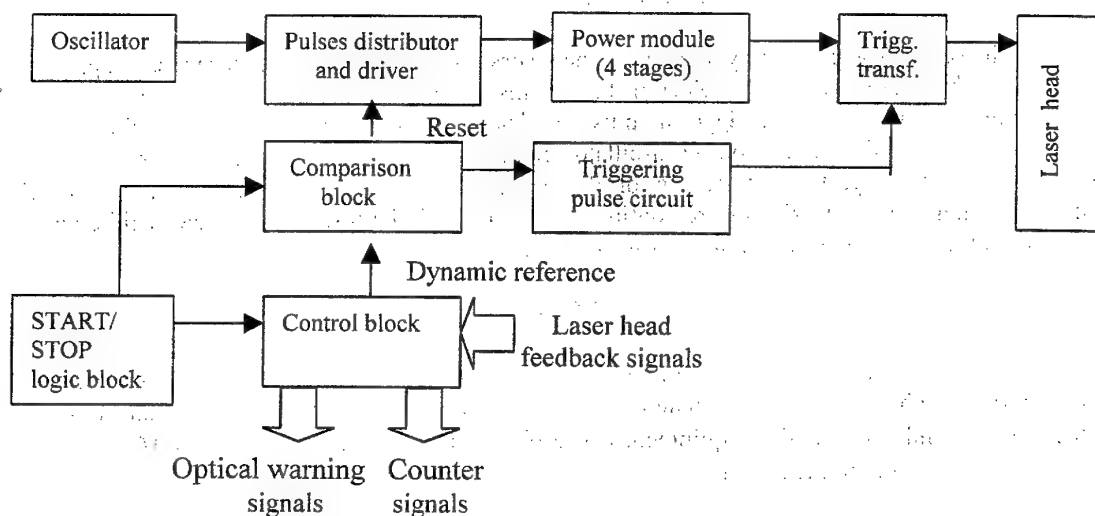


Fig.3 Power supply block diagram

We preferred discrete components (most of them CMOSs), as they can ensure the imposed functions, an enhanced reliability and an easy maintenance of the power supply with low energy consumption. Previous experiments showed that a device with only one specialized integrated circuit diminished control opportunities (no access to internal stages) and provided low system reliability.

The power supply operates by charging the energy storage capacitor to a preset voltage (the system enables the selection of the working voltage) – and then simultaneous commands stop the charging (the pulse distributor device is reset) and release the trigger pulse.

The novelty brought by our power supply consists in the monitorization of operation and modification, as necessary, of the dynamic reference, i.e. the charge voltage level. Thus, when the triggering pulse appears, a train of pulses well localized on the charge-discharge curve of the charge capacitor is released and they are compared to the signals received from the laser head. In this way, the occurrence of the laser emission can be ascertained and the point corresponding to this emission can be localized on the charge-discharge curve. If necessary, the dynamic reference can be varied in order to obtain an optimum working of power supply. All the information that is automatically processed by the system is provided at the output both as optical warning signals (advanced pulse, delayed pulse, missing effect, optimum working) and as command signals for the system's counters (triggering pulses, flash lamp, laser effect). The analysis of such data provides complete information about the system at any moment.

In conclusion, the main element of the power supply is the circuit for setting the dynamic reference. The block diagram of the circuit is presented in Fig. 4.

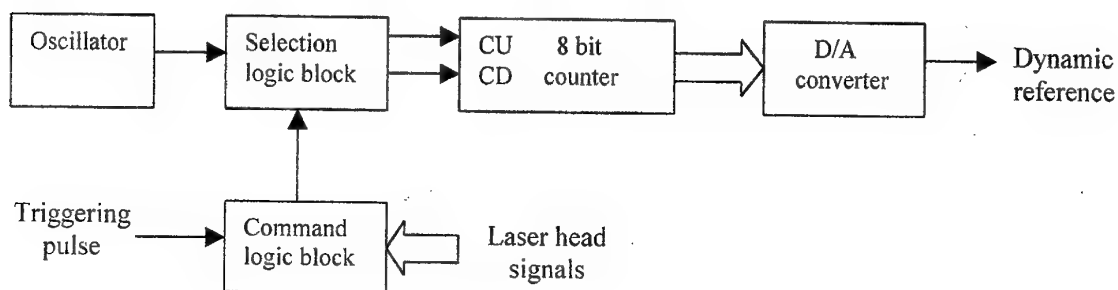


Fig. 4 Dynamic reference settling circuit block diagram

The setting stage of the dynamic reference works as follows: an oscillator pulse is applied to the 8 bits counter by means of a logic selection block; this block is turned on by the logic command block which compares the moment of triggering pulse application to the moment of laser emission appearance.

Following this comparison the oscillator pulse will be applied either to the count up entry or to the count down entry, thus increasing or decreasing the reference voltage level, namely charging capacitor voltage level. As signals are continuously compared, the reference voltage will be permanently fitted providing an optimal functioning of the device.

3. CONCLUSION

The proposed modular miniaturized power supply has a modern design, low electric power consumption, high reliability, easy handling and maintenance. The power supply can be successfully integrated in solid laser medical equipment based on IR pulsed lasers such as Nd:YAG ($\lambda = 1.064\mu\text{m}$), Ho:YAG ($\lambda = 2.1\mu\text{m}$) and Er:YAG ($\lambda = 2.94\mu\text{m}$).

4. REFERENCES

- [1]. Popescu V.,- Switched-mode power supply (in Romanian), ELECTRONICA APLICATA, West Publishing House, Timisoara, 1992.
- [2]. * * * - Switched - mode power supply, Third edition, MBLE, 1982.
- [3]. * * * - High performance flash and arc lamps, Book 3, 2nd edition.

Session B8 & B9

**OPTOELECTRONICS IN ANALYTICAL
INSTRUMENTATION AND MEDICINE**

COMBINED SCANNING OPHTHALMOSCOPE AND OPTICAL COHERENCE TOMOGRAPHIC SYSTEM FOR OCCULAR STUDIES

D. A. Jackson, A. Gh. Podoleanu

School of Physical Sciences, University of Kent, Canterbury, CT2 7NR, UK
Phone: 44 1227 764000/3762; Fax: 441227827558; e-mail: A.G.H.Podoleanu@ukc.ac.uk

ABSTRACT

A new instrument for simultaneous display of an en-face optical coherence tomographic (OCT) image and of a confocal image (similar with that produced by the scanning laser ophthalmoscope (SLO)) for the retina in vivo is demonstrated. The system is based on a fiberised OCT configuration, where a separate bulk optical confocal receiver is introduced between the transversal galvanometer scanner and the OCT fiber arm. The system could produce four different types of transversal OCT images from the retina, each with a different potential for diagnostic.

1. INTRODUCTION

OCT has been applied to ophthalmology in the attempt to obtain better depth resolution than offered by confocal imaging. The depth resolution of confocal imaging, using SLO instruments, is limited to 300 μm , dictated by the restricted entrance aperture of the eye [1]. In the OCT case [2-4], better depth resolution can be achieved, limited by the coherence length of the source and not by the object as in the SLO case. The images offered by the two systems are complementary and admit different interpretations. An SLO system provides an indirect *en-face* image by scanning a laser beam across the eye while the OCTs have evolved mainly as longitudinal imaging systems. The longitudinal images cannot be directly compared with the transversal images provided by the SLO. We have demonstrated that OCT can also be used to deliver transversal images [5,6]. This brings the OCT technique closer to the existing SLO technique in terms of the image aspect. However, we have also shown that simultaneous production of a confocal image as that presented by SLO and an en-face image, obtained by OCT is possible [7]. The set-up was based on a fiberised OCT system to which a bulk confocal receiver was added, to perform the function of an SLO.

In this paper we show that further versatility could be added to the system by software processing and combination of the images. We show that it is possible to produce four types of transversal images: OCT image, SLO image and a software generated intensity transversal image, similar with that offered by the SLO but produced using a large collection of OCT transversal images collected at different depths. We also demonstrate a superposition of the OCT and SLO images. All these four types of transversal images offer complementary information and may present great potential for clinical applications.

2. CONFIGURATION

Fig. 1 shows the basic diagram of the stand alone OCT/SLO system. The apparatus comprises an OCT interferometer excited by a pigtailed superluminescent diode, SLD, central wavelength $\lambda = 0.85 \mu\text{m}$, bandwidth $\Delta\lambda = 20 \text{ nm}$, which sends 100 mW power to the eye. The OCT system used was reported elsewhere [5], using a configuration of two directional single mode couplers and balance detection. In the sensing arm of the OCT, which could be either free space or fiberised, a splitting device is needed to redirect part of the returned light from the object towards the confocal receiver. Placing this device between the galvanometer scanner and the fiber input of the OCT makes possible pixel to pixel correspondence of the two images. Different choices exist for the splitting device and for the confocal receiver. We refer here to a bulk confocal receiver, using a plate beamsplitter and a pinhole.

The signals of the OCT and SLO are applied to a dual input frame grabber, which can display one or both of these signals under the computer control. Alternatively, the signal delivered by the OCT and the signal delivered by the optical confocal receiver, (the SLO channel) are weighted by the potentiometers at the inputs of a summator S, and the summator signal displayed by the frame grabber.

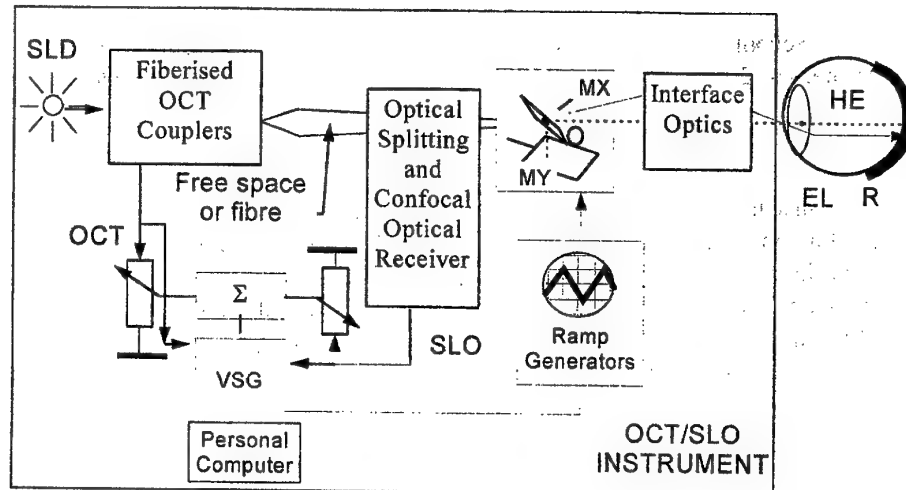


Fig. 1 Basic set up of the stand alone OCT/SLO system where a separate confocal receiver diverts parts of the light returned from the object
SLD: Superluminescent diode; MX, MY: orthogonal galvanometer mirrors; HE: patient's eye; EL: eye lens; R: human retina; VSG: dual input variable scan frame grabber for displaying and manipulating the two images simultaneously.

3. DEPTH PROFILE

Fig. 2 left shows the schematic of a confocal receiver where the object is a mirror. It has been shown that the resulting profile for the intensity returned to the photodetector equipped with an infinitesimal small pinhole, is described by the equation:

$$C(u) = \left(\frac{\sin \frac{u}{2}}{\frac{u}{2}} \right)^2 \quad (1)$$

where

$$u = \frac{8\pi}{\lambda} z \sin^2 \frac{\alpha}{2} \quad (2)$$

and $\sin \alpha$ represents the numerical aperture of the objective lens, in our case the eye lens. The minimum FWHM corresponds to a value $u \approx 5.6$. Using a 2.5 mm pupil opening diameter, an index of refraction $n = 1.336$ and a 1.7 cm focal length, a depth resolution of ≈ 180 mm results [8,9]. However, practically the depth resolution is about 300 mm, which shows that the eye is not a diffracted limited system.

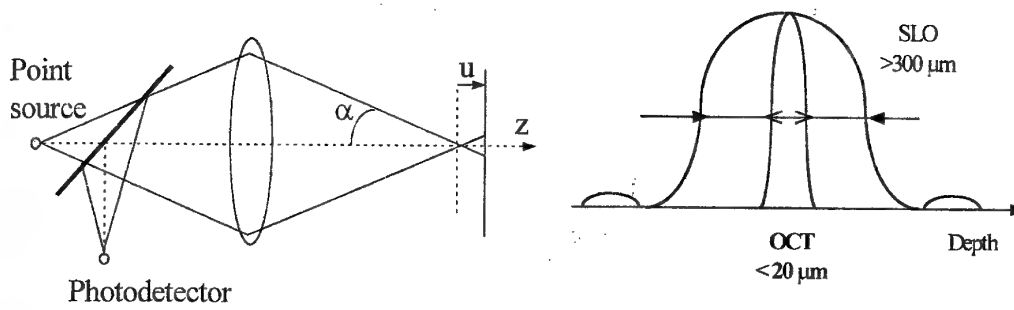


Fig. 2

As opposed to this value, the depth resolution in the OCT channel is much better. The coherence profile for a source with a Gaussian spectrum of DI FWHM is described by :

$$\Gamma(z) = \exp\left[-\ln(2)\left(\frac{2z}{l_c}\right)^2\right] \quad (3)$$

where the coherence length l_c has the expression:

$$l_c = \frac{4 \ln 2}{\pi} \frac{\lambda^2}{\Delta\lambda} \quad (4)$$

With $DI = 20 \text{ nm}$, (4) gives $l_c = 32 \text{ mm}$ and a depth pixel size of 16 mm .

In the OCT channel, the depth profile can be represented as the product of $G(z)$ with the confocal profile due to the fibre aperture, $C_F(z)$. For the fibre used, this profile has a FWHM of $\approx 1 \text{ mm}$, so the final depth profile is dominated by $G(z)$. A qualitative representation of the profiles in (1) and (2) is shown in Fig. 2 right.

The confocal profile due to the fibre aperture can in principle be used to produce a confocal image. However, this is not viable for the simultaneous production of OCT and SLO due to the noise associated with the reference power.

For OCT guiding, it is useful for the SLO to have a much larger depth sectioning interval than the OCT, to accommodate for positions of the eye largely out of focus during initial patient alignment with the system.

We chose a 10X microscope objective and a 30 mm pinhole which give an experimental FWHM confocal profile of the pinhole receiver of $\approx 3.7 \text{ mm}$. As far as a very good depth resolution is delivered by the OCT image, apparently there is no need to improve the SLO depth resolution above this value or to adjust the SLO depth resolution. However, these two issues have to be clarified by imaging patients during further investigations with the system. Anyhow, the SLO depth resolution should be sufficient to reject the light reflected by the eye lens.

4. CHOICE OF THE BEAMSPLITTER RATIO

An important issue is how much from the signal returned from the eye is split between the two systems. An optimum design should address the trade-off between the percentage of the light diverted from the OCT by the beamsplitter, c , and the SLO depth resolution. The larger c , the greater the power collected by the SLO photodetector and smaller size for the pinhole could be achieved before reaching the noise floor. The smaller the pinhole size, the better the SLO depth resolution. However, at the same time with the increase in c , the signal to noise ratio in the OCT image worsens. If larger depth resolutions are acceptable for the SLO channel in our stand alone system than in the commercial SLOs, the beamsplitter ratio can be reduced considerably in order to keep the OCT disturbance at a minimum.

It can be shown that due to the fact that the line scanning rate in our systems is less than in the state of the art SLOs, greater attenuation for the object signal before reaching the confocal receiver pinhole can be accepted. For instance, for $c = 21\%$, it can be shown that the quality of the image should

be the same as in the state of the art SLOs. For our set-up, in order to keep the OCT disturbances at a minimum, we chose a 4% beamsplitter



Fig. 3 Confocal image, two OCT images and the superposition of all OCT images.

3 mm x 3 mm, 2frames/s, 600 Hz line scanning rate.

5. IMAGES FROM

THE RETINA

Initially, the lens and pinhole positions were finely adjusted to insure that the images supplied by the two systems, OCT and SLO coincided pixel by pixel. To this end, the SLO signal and the OCT signal were subtracted on an oscilloscope when imaging an eye model. Then, MX was driven only, while zero dc signal was applied to the Y galvanometer scanner. We repeated this procedure with MY driven and MX at rest. The procedure was repeated until the peaks of the reflected signals in the two channels were perfectly superposed on the oscilloscope. The images produced by the SLO and OCT are in this way in correspondence pixel to pixel and are produced simultaneously at the same rate.

The interface optics is the same for both systems. As the interests lays with the fine details in the OCT, the angular extension of the raster is less than 17° , much less than in the state of the art SLOs, where it could cover about 40° to display both the fovea and the optic nerve.

Four types of transversal images can be generated with the system: OCT images for different depths, a confocal image, a transversal generated compound image by software superposition of a number of the OCT transversal images and also a superposition of OCT and SLO images. Such images of the retina in the right eye of a volunteer, (after full consent was obtained), are shown in Fig. 3 and Fig. 4. The volunteer was asked to orient his eye at about 10° temporal to bring the optic nerve in the centre of the image. The images have been collected at 2 frames/s and running the translation stage at a 60 mm/s speed. In this way, in 22.5 seconds, 45 images for a 1.35 mm depth were collected. The confocal image is in the top left corner and two OCT images in the right column. The TS position is given underneath each OCT image. The initial position was arbitrary, a few tens of micrometers in front of the retinal nerve layer, where no OCT signal could be obtained. Parts of the retinal fibre layer (RNFL), of the photoreceptor layer (PL) and of the retinal pigment epithelium (RPE) can be distinguished.

Superposing all 45 images, an intensity image is obtained as shown in the bottom left of Fig. 3. No processing and no corections have been applied to the images. An animation with such sets of transversal OCT images can be viewed via the OSA link to biomedical images [11], where the effect of eye movement can be noticed. The image in the bottom left in Fig. 3 shows that even if the eye disturbances are not removed, sufficient resolution can be obtained.

We are now developing algorithms and software to process and align the images in order to reduce the disturbances introduced by the eye movements. Once aligned, better resolution for the image resulting by superposing the OCT transversal images should result. Varying the number N of the images superposed, leads to an image with an equivalent depth resolution Nl_c .

The OCT image has a depth resolution of 16 mm, the SLO image of 3.7 mm and the superposed image, adjustable between 16 mm and a maximum given by the range the images cover in depth. Once the set of OCT transversal images is collected, longitudinal images can also be produced by software means.

As the two images are in pixel to pixel correspondence, they admit superposition which leads to a 4th type of transversal image. Fig 4, right presents a 50/50 superposition of the OCT image (left) and SLO image (middle) for the eye of another volunteer.

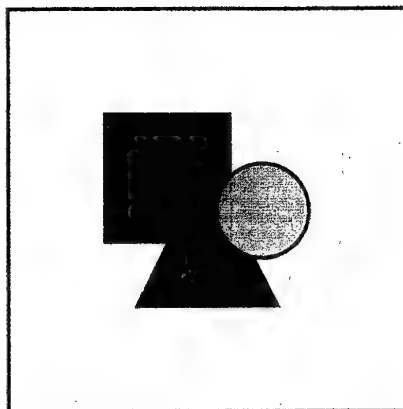


Fig. 4 OCT, SLO and superposition of SLO and OCT images from the optic nerve.
5 mm x 5 mm, 2 frames/s, line rate 700 Hz.
No processing of the images

Two particularities can be noted, the fragmented aspect of the images and their curved characteristic. The fragmentation is the consequence of the much shorter coherence length than the height of the features being imaged. The curved aspect is a consequence of the optics used to image the eye, with the fan of rays brought to a point on the eye lens. For a flat retroreflector behind the eye lens, the higher the angular deviation of the beam entering the eye, the higher the path difference between the extreme rays and the ray in the middle of the fan. This effect should also happen whenever the retina deviates from a spherical surface whose centre is on the eye lens. This has not been an issue for the SLO imaging, as in this case the out of focus of the most deviated ray was still less than the sectioning interval width (i.e. the pixel imaged by the most deviated ray was still in focus). This has been discussed elsewhere [5] where a correction procedure for the longitudinal OCT images has also been demonstrated. This is an issue which has to be properly taken into account when transversally imaging the eye. Different ways to proceed in order to compensate for this distortion are possible, which are subjects of a different study.

6. CONCLUSIONS

Experiments are presented for a combined OCT/SLO system, using a fiberised OCT integrated with a confocal receiver based on a bulk beamsplitter and a pinhole. The system can deliver simultaneously two transversal images with different depth resolutions, a confocal image with a depth resolution which in principle can be adjustable from a few mm to the minimum achievable to date, 300 nm and a second image with OCT depth resolution, fixed and determined by half of the source coherence length, 16 nm in our case.

The lower the coherence length, the more fragmented the OCT image appears. The usefulness of the OCT images for the ophthalmologists is greatly improved as the fragments sampled by OCT of the fundus are uniquely in correspondence with fundus images produced by SLO. In addition, the ophthalmologists have built large data bases of SLO images for diseased eyes. A stand alone system as described here permits the exploitation of this knowledge in the interpretation of the OCT transversal images.

The combined system retains the capability of the OCT system to perform both transversal and longitudinal OCT. When in the longitudinal OCT regime, the SLO channel signal is not displayed, as it refers to a one line in the en-face image raster.

ACKNOWLEDGMENTS

The authors acknowledge the support of the UK Engineering and Physical Sciences Research Council and also acknowledge the support of Superlum Moscow.

8. REFERENCES

- [1]. Webb R. H., "Scanning laser ophthalmoscope", pp. 438-450 in *"Noninvasive diagnostic techniques in ophthalmology"*, ed. Masters, B. R., Springer-Verlag, New York, (1990).
- [2]. Huang D., Swanson E.A., Lin C. P., Schuman J. S., Stinson W. G., Chang W., Hee M. R., Flotte, Gregory K., Puliafito C. A. and Fujimoto J. G., *Science* 254, pp. 1178-1181, (1991).
- [3]. Bouma B., Tearney D. J., Boppart S. A., Hee M. R., Brezinski M. E., Fujimoto J. G., "High-resolution optical coherence tomographic imaging using a mode-locked Ti:Al₂O₃ laser source", *Opt. Lett.*, vol. 20, No.13, pp.1486-1488, (1995).
- [4]. Fercher A. F., "Optical coherence tomography", *J. Biomed. Opt.*, 1(2), pp. 157-173, (1996).
- [5]. Podoleanu A. Gh., Seeger M., Dobre G. M., Webb D. J., Jackson D. A. and Fitzke F., "Transversal and longitudinal images from the retina of the living eye using low coherence reflectometry", *J. Biomed Optics*, 3(1), pp. 12-20, (1998).
- [6]. Podoleanu A. Gh., Dobre G. M. and Jackson D. A., "En-face coherence imaging using galvanometer scanner modulation", *Opt. Lett.*, 23, pp. 147-149, (1998).
- [7]. Podoleanu A. Gh. and Jackson D. A., "Combined optical coherence tomograph and scanning laser ophthalmoscope", *Electron. Lett.*, Vol. 34, No. 11, pp. 1088-1090, (1998).
- [8]. Corle T. R., Kino G. S., *Confocal scanning optical microscopy and related imaging systems*, Academic Press, San Diego, (1996).
- [9]. Wilson T., "The role of the pinhole in confocal imaging systems", Chapter 11, pp. 113-126, in *Handbook of biological confocal microscopy*, J. B. Pawley ed., Plenum Press, New York, (1990).
- [10]. Kimura S. and Wilson T., 'Confocal scanning optical microscope using single-mode fiber for signal detection', *Appl. Opt.*, Vol. 30, No. 16, pp. 2143-2150, (1991).
- [11]. <http://www.osa.org/homes/BIOOPTIC/defaultLinks.htm> and then click on the University of Kent link, or directly: to <http://kiwi.ukc.ac.uk/physical-sciences/> or <http://speke.ukc.ac.uk/physical-sciences/aog/>.

RESULTS OF ON-SITE MONITORING OF PHENOL AND RELATED CHEMICALS, USING AN INTENSITY MODULATED FIBER OPTIC SENSOR

M. Vladescu, M. Guina*

Electromagnetica GoldStar Ltd., Calea Rahovei 266-268, Bucharest, Romania,

Phone/Fax: +40-1-423-2676, e-mail: vladescu@joe.tehfi.pub.ro

* "Politehnica" University of Bucharest, Faculty of Electronics and Telecommunications,
Blvd. Iuliu Maniu 1-3, Bucharest, Romania, e-mail: guina@joe.tehfi.pub.ro

ABSTRACT

Fiber optic techniques based on absorption are used in order to monitor phenol and other related chemicals. The aim of our work is to design a chemical fiber optic sensor capable of performing on-site measurements.

Usually, the presence of chemicals can be determined by analyzing the absorption spectra of a sample with a spectrophotometer. The major disadvantage of this method is the delay between the moment of taking the sample and the moment of measuring.

On-site monitoring techniques have the advantage of instantaneous signaling chemicals presence and allow immediately action avoiding in the way the environment contamination.

An intensity modulated fiber optic sensor has been used in a transmission system in order to evaluate the absorption spectra. A lock in amplifier has been used to recover the signal processed by the sensor, rejecting the large amount of noise that usually accompanies on-site measurements. The results demonstrate a high noise immunity of the presented sensor.

1. INTRODUCTION

A range of optical phenomena, such as absorption, scattering, fluorescence and phosphorescence can be used in chemical sensing. The simplest of these is the absorption of radiation at specific wavelengths. Precise absorption measurements can be performed with a spectrophotometer, in the laboratory, usually with the purpose of classifying chemical species. The concentration of a chemical sample can also be determined by the above device.

Absorption works for chemicals which do not change their properties in time, but it may cause inconveniences when chemicals are not stable and change during transportation to the laboratory. This may affect the accuracy of the measurements. Considering that the spectrophotometer is not a portable equipment, the major requirement is to shorten the period between the selection of the sample and the performance of the analysis.

When this is not practically possible, the alternative solution is to perform on-site measurements with appropriate sensors, in order to ensure a proper monitoring of chemicals.

Our study is focused on phenol and related chemicals.

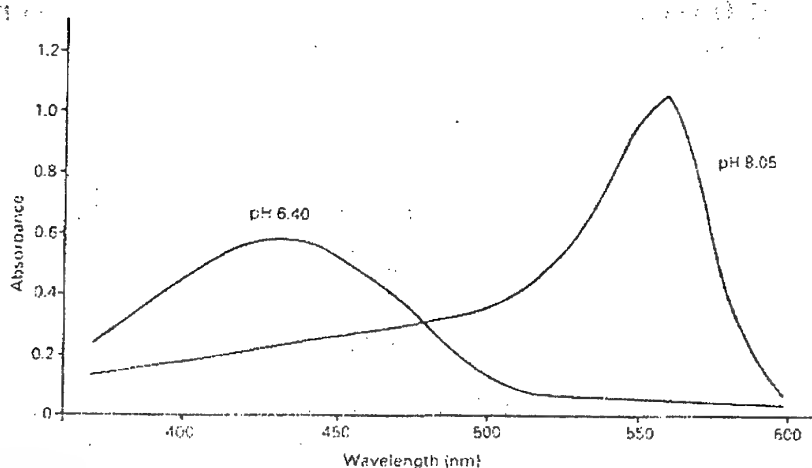


Fig. 1 Absorption spectra of phenol red dye for 10ppm concentrations

2. ABSORPTION SPECTRA OF PHENOL AND RELATED CHEMICALS

The absorption spectra of phenol, as well as the concentration measurements, have already been reported in the literature. The absorption spectra for aqueous phenol red dye at specified pH and given concentration are presented in Fig. 1.

Other two phenol related chemicals, resorcinol (1,3 dihydroxi-benzen) and hydroquinone (1,4 dihydroxi-benzen) have been the target of our investigations. Both of them are photosensitive and change their optical properties in time.

The transmission of the above chemicals at various concentrations has been measured using a spectrophotometer. The results in case of using aqueous resorcinol, 25% concentrated are presented in Fig.2. Measurements of transmission for solutions 5%, 10%, 50% and 75% concentrated have also been made.

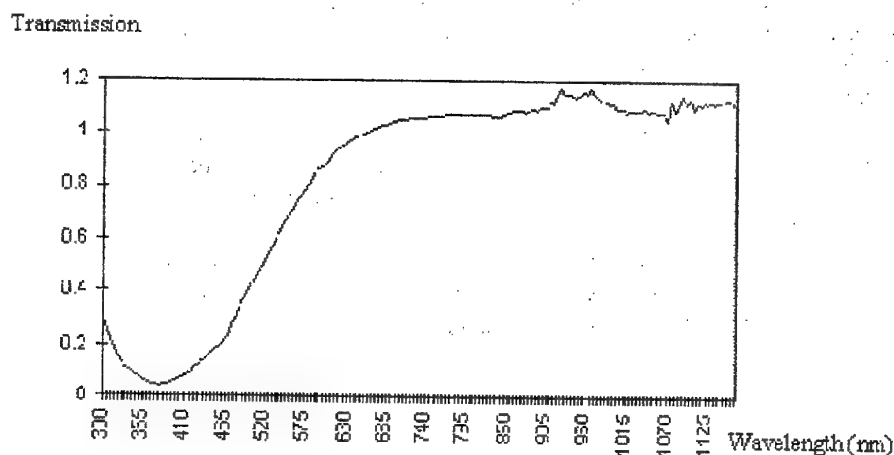


Fig. 2 Transmission of aqueous resorcinol, 25% concentrated

The results in case of an aqueous hydroquinone 5% concentrated are illustrated in Fig.3. Measurements of transmission have also been made for a 10% concentration.

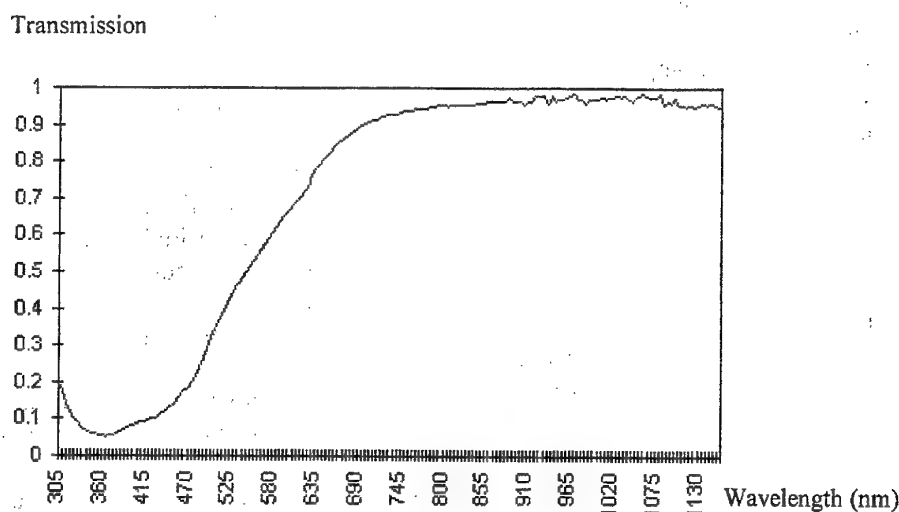


Fig. 3 Transmission of aqueous hydroquinone 5% concentrated

3. OPTICAL FIBER SENSOR IMPLEMENTATION

The optical fiber sensor that we found to be adequate for the concentration measurements is an "extrinsic" one, based on absorption of specific wavelength radiation. Two important criteria must be satisfied:

(1) The difference in transmitted light intensity corresponding to the possible dynamic range of the interest parameter (e.g. minimum and maximum concentrations of a particular chemical that is to be measured) must be high enough to give a good sensitivity.

(2) The optical transmission in the maximum absorption condition must be high enough in order to be an adequate signal given the existent noise sources. This means that the "insertion loss" for the sensing element should not be so high that the transmitted signal to become difficult to be separated from effects, such as the ambient light leakage.

The second requirement does not necessarily mean that the transmitted signal has to be larger than the ambient light signal. If a light-source modulation and a narrow band detection are used, a much smaller signal can be tolerated. In this situation care should be paid that the total light levels not saturate the photodetector or the processing electronics.

Optical domain filtering may be added to improve noise immunity, but this approach proved to have its limitations regarding low signal levels in the presence of electrical and optical noise sources, thus affecting the sensor sensitivity.

The electrical output of optical fiber sensors is influenced by many parameters and it is important to evaluate the contribution of each of them. The detected signal can be represented as follows:

$$\text{Electrical Output} = SP * D * FT * M * Q * FR * S \quad (1)$$

where:

SP represents the operations performed by signal processing within the detection electronics;

D represents the signal generated by the photo-detector in response to the optical input to the detector;

FT represents the transmission function of the fiber that connects the sensor to the detector;

M represents the modulation function applied to the optical signal when it passes through the modulator;

Q represents the quantity to be measured as interpreted through the modulation characteristics of the modulator;

FR represents the transmission function of the fiber that connects the source to the modulator and

S represents the output from the source itself coupled to the fiber.

The signal processing unit in the detection system is intended to correct for any spurious element detracting from **Q** in equation (1).

One of the most common techniques used in optical fiber sensor signal processing is the frequency domain filtering. A narrow band filter is recommended for this kind of applications.

The signal processing system can also be used to enhance sensitivity and selectivity, and the most important technique is the lock-in amplifying that use a source modulation and enables very small alternating signals to be extracted from a very noisy background.

In order to achieve the best results, the signal processing unit we designed for this sensor combines both techniques presented above.

Two 1mm diameter optical fibers of polymer have been used to connect the optical source and the optical detector to a cuvette. The optical path length can be modified from 1 mm up to 10 mm in order to fit various transmissions of the monitored chemical.

For precise absorption measurements at least two wavelengths of light need to be monitored simultaneously in order to compensate common mode effects, changes in light source intensity and the aging of components. The block diagram of the sensor is presented in Fig.4.

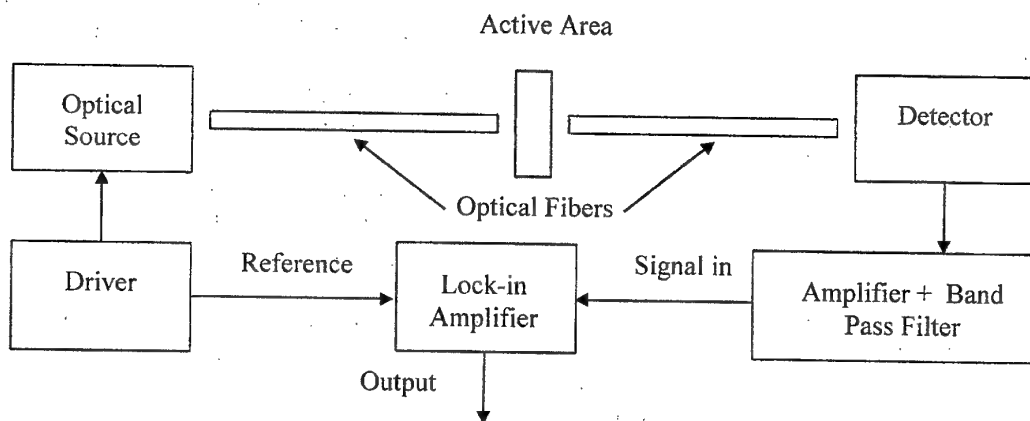


Fig. 4 Optical fiber sensor block diagram

4. RESULTS AND CONCLUSIONS

The experiments have been performed in a cuvette having a 10 mm optical path length. The results for various concentration of aqueous resorcinol are summarized in Fig. 5. The optical path length has been reduced up to 5 mm for low concentration measurements.

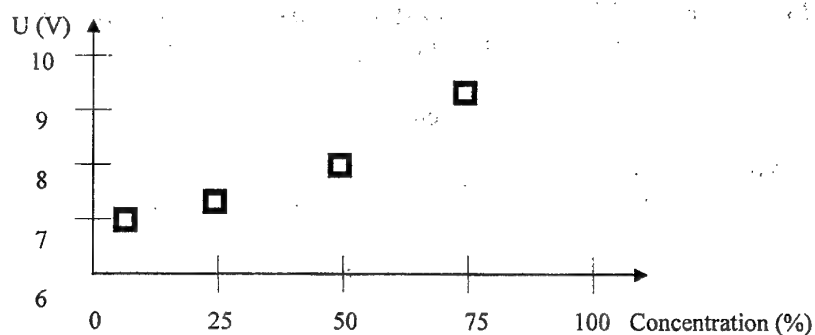


Fig. 5 Output characteristics of the sensor

Measurements performed at several days interval proved that both chemicals changed their optical properties. We have also observed changes in their colour, from light yellow for resorcinol and light pink for hydroquinone to dark brown after prolonged exposure to natural light.

Measurements can be extended to concentrations below 5% and the accuracy can be improved by using a reference optical path. The sensor need to be further characterized in order to be used for continuous changes in concentration.

5. REFERENCES

- [1] Dakin, J., Culshaw, B., Optical Fiber Sensors: Principles and Components Volume 1, 1988
- [2] Dakin, J., Culshaw, B., Optical Fiber Sensors: Systems and Applications Volume 2, 1989
- [3] Krohn D.A., Fiber Optics Sensors – Fundamentals and Applications, 1988

THE STUDY OF THE FRACTAL STRUCTURE OF COLLOIDAL AND SMOKE AGREGATES BY LIGHT SCATTERING

T. Nicula, G. Costache

Military Chemistry Application School, Marasti no. 48, Campulung-Arges,
code 0425, Romania, Tel: 048/812500; Fax: 048/823679

ABSTRACT

In this paper we present the results of our research concerning colloidal and smoke aggregation in the new perspective provided by fractal geometry.

In our measurements, we paid attention to effect of different factors (reagent concentrations, reaction rate, etc.) over fractal dimensions. Furthermore, we explored the dynamics of the growth process by estimating the first moment of the cluster mass distribution. The measurements were performed by light scattering techniques.

In order to reduce noxious emission, we tried to diagnose car engine combustion by using an optoelectronic device based on light scattering.

1. INTRODUCTION

Fractal geometry provides a new perspective of nature and allows us to consider irregularities as intrinsic entities (Mandelbrot, 1982 [1]; Vicsek, 1992 [2]). The subject of our interest is the kinetic aggregation in the new perspective offered by statistical physics of random kinetic growth processes, of which the colloidal aggregation is a prime example. The clusters produced in the aggregation process are scaled invariant structures characterized by noninteger ("fractal") dimensions. The knowledge of the structure allows the determination of the physical properties of the aggregates as they grow, as well as their mutual interactions, which generate the growth process itself.

2. LIGHT SCATTERING AS A TOOL FOR STUDYING THE AGGREGATION PROCESSES

The scattering techniques are based on the fact that, in the limit of weak scattering, the intensity $S(q)$ of the scattered beam is the Fourier transform of spatial autocorrelation function, $c(r)$, where q is the scattered wavevector. This relationship is true for all types of scattering, including for example light, x-rays, and neutrons. The measured intensity $S(q)$ will reflect not only the scale invariant correlation of the fractal regime, but also the cut off effects due to the finite extension of the fractal range.

Sinha et al. [3] has developed an analytic expression for $S(q)$ from fractal aggregates. In the fractal range of scattering, $a \ll q^{-1} \ll R$ (where a is the individual particle radius and R is the size of the whole cluster), the scattering becomes

$$S(q,R) \sim (qR)^{-D_f} \quad (1)$$

where D_f is the fractal dimension of aggregates. Thus, D_f can, in principle, be determined directly from the scattering. Using the scaling of the mass and the cluster size, relation (1) becomes

$$S_M(q) \sim M^{-1} q^{-D_f} \quad (2)$$

There are two potential issues which should be considered in order to properly interpret the scattering data. First, it must be checked that the scattering is weak enough so as not to be distorted by multiple scattering. Second, the effect of polydispersity in the cluster mass distribution must be considered. The effect of the multiple scattering within a cluster has proved to be insignificant. [4] The total intensity from the distribution of clusters is

$$I(q) = \int N(M) M^2 S_M(q) dM \quad (3)$$

where $N(M)$ is the cluster mass distribution. Replacing $S_M(q)$ for fractal range in (3), we obtain

$$I(q) \sim \int N(M) M dM \quad (4)$$

which is the first moment of the distribution function. Thus, we have the possibility to measure mean cluster mass, taking into account that after a long enough time the cluster mass distribution reaches a stationary state. That result is demonstrated by CCA model (cluster-cluster aggregation) [2,5].

3. A SHORT REVIEW OF KINETIC AGGREGATION

Since the aggregation is a kinetic process, the cluster structure is intrinsically related to the dynamics of the aggregation process itself. The dynamics have been studied through computer simulations of time evolution of the cluster mass distribution. The results suggest that the mean-field Smoluchovski equations give a reasonable representation of the cluster mass distribution behaviour. A theoretical model well suited to aggregation processes is the cluster aggregation models (CCA)[6,7]. In the CCA models one starts from a very low concentration of particles diffusing on a lattice. When two particles meet, they form a cluster of two, which can also diffuse. When the cluster meets another particles or another cluster, a larger cluster is formed. In this way larger and larger clusters are formed. The fractal dimension is $D_f \cong 1.4$ in $d=2$ and $D_f \cong 1.8$ in $d=3$ (d is the Euclidean dimension). CCA appears to be a good model for smoke aggregates in air and for gold aggregates. [8]

Another factor involved in kinetic aggregation is the energy barrier between two initial particles. If energy barrier is reduced to much less than $k_B T$, a very rapid aggregation results, that is limited only by the diffusion of the particles leading to their collisions. If, on the other hand, energy barrier remains comparable to or larger than $k_B T$, the aggregation rate is reduced, and slow coagulation results. Thus, from this point of view, there are two extreme regimes: diffusion limited aggregation and reaction limited aggregation.

4. OUR RESULTS CONCERNING COLLOIDAL AND SMOKE AGGREGATION

We used light scattering techniques to test fractal structure of AgI colloids and we observed a remarkable fractal behaviour on the q range probed by light scattering (Fig. 1). Another field of research was the influence of different factors (reagent concentration ratio, temperature, etc) on the fractal dimension D_f .

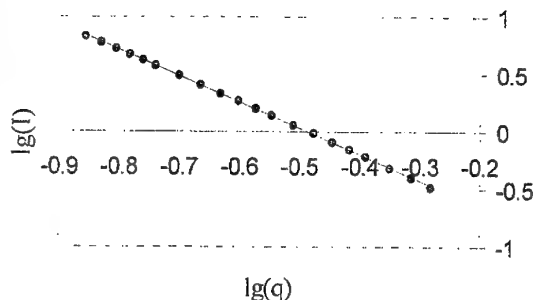


Fig. 1 The logarithmic plot of scattered light by AgI colloids with reagents concentration ratio 1:1 versus q wavevector. The slope leads to $D_f = 1.85 \pm 0.05$

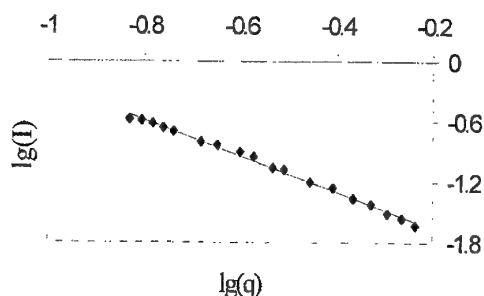


Fig. 2 The logarithmic plot of scattered light by Diesel engine smoke versus q wavevector. The slope leads to $D_f = 1.79 \pm 0.05$

As mentioned above, the kinetic aggregation is involved in a large variety of phenomena. Starting from this assumption we tried to apply aggregation models to smoke clusters produced by engine combustion. The assumption that combustion reaction generates smoke aggregation clusters was confirmed by light scattering experiments (Fig. 2). Furthermore, from equation (4) it can be observed that first moment of cluster mass distribution function is the intercept of the line with $\lg(I)$ axis. Thus, based on a sole data set, we obtained information about the mean cluster mass and the spatial correlation in clusters by means of D_f .

Both phenomena presented here (Fig. 1, Fig. 2) seem to be in a good agreement with CCA model. In addition, our research leads to the conclusion that the aggregation is sensitive to initial conditions of kinetic aggregation (the local concentration fluctuations, energy barrier between particles), but is not to the history of aggregation, thus not requiring a fine tuning of any parameters.

Our present activity consists in developing a procedure to diagnose the engine car combustion using the above described techniques. The starting point in our attempt was the aggregation sensitiveness at initial reaction conditions. The smoke clusters formed under various conditions are quantitatively measured by means of fractal dimension D_f . Furthermore, if the fractal dimension is known, we have information about the reagents state (their spatial distribution, concentration ratio) on the length scale tested by light scattering (500 nm to 10 μ).

5. CONCLUSIONS

The light scattering techniques offer a powerful tool to study aggregates formed under a wide variety of conditions, and to compare the structures of the clusters formed in a quantitative manner.

6. REFERENCES

- [1]. Mandelbrot B. B., The Fractal Geometry of Nature (Freeman, San Francisco, 1982).
- [2]. Vicsek T., Fractal Growth Phenomena (World Scientific, Singapore, 1992).
- [3]. Sinha S. K.; Freltoft T. and Kjems J., Kinetics of Aggregation and Gelation, (ed. By F. Family and D. P. Landau, Elsevier, Amsterdam, 1984).
- [4]. Weitz D. A., Huang J. S., Lin M. Y. and Sung J., Phys. Rev. Lett. 54, 1416 (1985).
- [5]. Jullien R. and Botet R., Aggregation and Fractal Aggregates (World Scientific, Singapore, 1987).
- [6]. Meakin P., Phys. Rev. Lett. 51, 1119 (1983).
- [7]. Kolb M., Botet R. and Jullien R., Phys. Rev. Lett. 51, 1123 (1983).
- [8]. Bunde A. and Havlin S., Fractals and Disordered Systems (Springer Verlag, Heidelberg 1991).

SELF-ORGANIZATION PROCESSES IN LOW-PRESSURE PLASMAS

B. Oprescu, M. Sanduloviciu*

The Faculty of Science, University of Pitesti, Gh. Doja, No. 43, Pitesti, 0300, Romania, fax: 048-216448,
E-mail: chidu2@yahoo.com

*The Department of Plasma Physics, Al. I. Cuza University, Iasi, 6600, Romania, fax: 032-213330, E-mail: msandu@uaic.ro

ABSTRACT

The purpose of this paper is to present the various issues relating to the non-linearity of the volt-ampere characteristics, the self-organization processes occurring within the ionized medium, the properties of the oscillations generated by the transition from the negative charge layer to the double layer, as well as the characteristics corresponding to the emergence of the moving double layer. The phenomenological explanation of the experimental results is presented below.

1. EXPERIMENTAL DEVICE. EXPERIMENTAL RESULTS

In order to obtain a double layer within ionized gas, an area of electron acceleration must exist within the plasma. As shown at length in a previous paper [1], we managed to obtain optimal conditions for the generation and investigation of the double layer by building an experimental device of which design is illustrated in Fig.1.

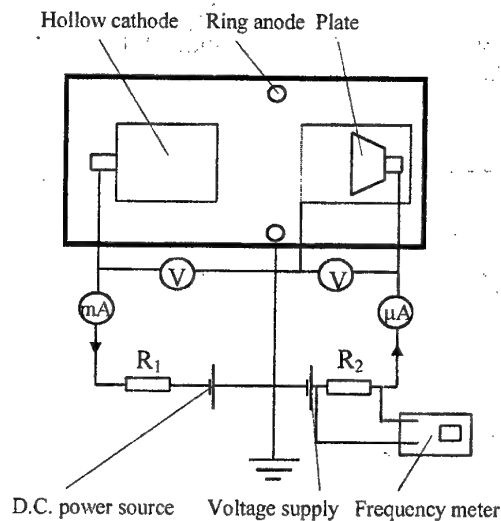


Fig.1 Experimental device

By increasing the volt-ampere characteristic of the electron acceleration area, we obtained the results shown in Fig. 2. For certain experimental situations, as a result of the periodic transitions from the negative charge layer to the double layer oscillations in the shape of current peaks within the electron acceleration electric circuit appear. These transitions correspond to the CD region of the volt-ampere characteristic. Both the frequency and the amplitude of the current peaks corresponding to those transitions depend upon the average intensity of the plate current, as illustrated in Fig. 3 and 4.

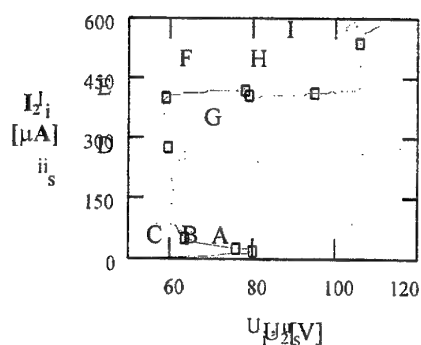


Fig.2 The current-voltage characteristic.

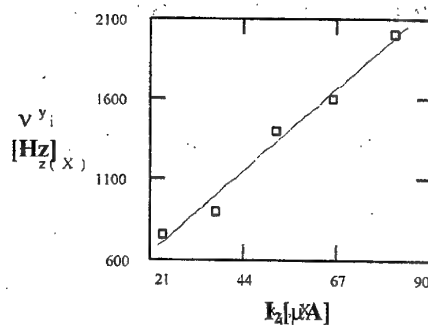


Fig.3 The dependence on current intensity of the appearance frequency of the double-layer

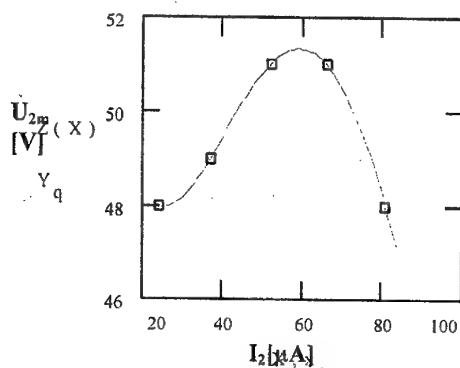


Fig.4 The dependence of the amplitude of the voltage peaks, selected from the R_2 resistor, upon the average value of the plate current

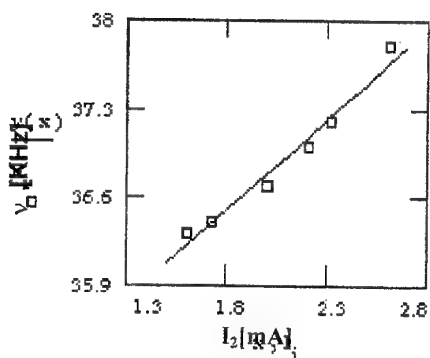


Fig.5 The dependence of the frequency oscillations upon the average intensity of the plate current

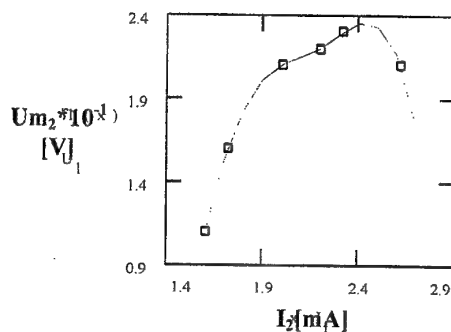


Fig. 6 The dependence of the amplitude of the oscillations upon the intensity of the plate current

If the device works in a regime which corresponds to the FG area of the characteristic, new oscillations within the circuit appear. These oscillations have a higher frequency than those in the CD region, and a much lower amplitude. The characteristic values of these oscillations depend upon the intensity of the plate current, as shown in Fig.5 and 6.

2. PHENOMENOLOGICAL INTERPRETATION OF EXPERIMENTAL DATA

In order to explain the experimental results, one has to proceed from the mechanism of double layer generation within the electric discharge, as discussed in detail in [1].

By following the logic of the phenomenological model presented in [1], while the average intensity of the current increases, the speed of the ionization process near the plate increases, too. This determines the occurrence of a larger number of ions bounded to the grid. The increase in the number of ions near the grid leads to a substantial reduction of the retarding electric field for electrons. As a consequence, the flow of those electrons heading for the plate increases, and the time for the making up the new double layer diminishes. Therefore, in keeping with the theoretical considerations, there must be a relation of proportionality between the frequency of the transitions from the negative charge layer to the double layer and the average intensity of the plate current.

According to the assertions made in [1], when the positive electric charge inside the stationary double layer exceeds the value of the negative electric charge, the double layer becomes mobile. The oscillations of ions concentration around the grid, which are caused by the periodic injection of ions in that region, determine oscillations of the plate current. Since the time for making up a new mobile double layer (measured from the moment the previous double layer is detached) is given by the time passed from the detachment of the first double layer till its breaking up, plus the time which is needed by the electrons in the breaking up zone to go through the layer up to the plate, one can assume that the way the double layer goes up to its breaking up decreases as the continuous component of the plate current increases. Admitting that there is a linear dependence between the distance over which the breaking up of the double layer occurs and the average intensity of the plate current, a linear dependency between the frequency of the plate current oscillations and its average intensity is obtained. This is the situation that can be experimentally proved.

Both groups of oscillations have a dependence of the amplitude upon the average intensity of the plate current which is specific to a resonance phenomenon. Within the region between the grid and the plate there are, for both the CD and the FGH regions of the volt-ampere characteristic, an "excitator" and a "resonator". As discussed, in both cases the electric charge around the grid can oscillate under the influence of a periodic ion injection.

3. REFERENCES

- [1]. B. Oprescu, M. Sanduloviciu, *Rom. Journ. of Optoelectronics*, Vol.6, N^o.1, 27 (1998).
- [2]. B. Oprescu, M. Sanduloviciu, Gh. Dima, IXth Conference on Plasma Physics and Applications (Bucharest, 1996), Abstracts, P2;
- [3]. B. Oprescu, M. Sanduloviciu, Gh. Dima, 3rd General Conference Of The Balkan Physical Union (Cluj-Napoca, 1997), Programme And Abstracts, 323;
- [4]. M. Sanduloviciu, B. Oprescu, Xth Conference on Plasma Physics and Applications (Iasi, 1998), Abstracts, NS 12.

CONSIDERATIONS ABOUT THE VIBRATORY STATES OF PIEZOELECTRIC STRUCTURES BY A FINITE ELEMENT METHOD

Irinela Chilibon

National Institute of Research and Development for Optoelectronics, INOE-2000,
R-76.900, PO Box MG 5, Bucharest, ROMANIA
Fax/tel.: (401) 420.10.01; e-mail: chilib@alpha2.infim.ro; qilib@yahoo.com

ABSTRACT

The purpose of this paper is to present a finite element simulation of resonance phenomena of piezoelectric structures used in echographic ultrasonic probes. The ultrasonic probe is an electro-acoustic transducer whose structure is made of viscoelastic and piezoelectric materials. Because of their piezoelectric properties the piezoceramic materials of PZT type are used for the realization of piezoelectric elements, which achieve the conversion of electrical energy into a mechanical energy and reverse. Depending on their applications, the ultrasonic probes are able to emit or/and receive acoustic signals.

1. INTRODUCTION

The ultrasonic probe generally used in medical imaging is an electro-acoustic transducer whose structure is made of viscoelastic and piezoelectric materials. This is one essential element influencing the quality of the echographic image. For the one-dimensional model the vibratory state of the piezoelectric bars with losses has been taken into consideration. This phenomenologic model is particularly adapted to multielement transducers.

If it is assumed that the vibration of the transducer is piston-like, i. e. the vibratory velocity is uniform over the radiating surface, and that any given echographic chain can be modeled, for a homogeneous and nonattenuating propagation medium.

In the frequency domain, some parameters can be measured: acousto-electric transfer at emission, emission diffraction transfer, reception diffraction transfer and acousto-electric transfer at reception. Like all ultrasonic devices used in medical diagnosis, the piezoelectric transducers must fulfill the following main requirements:

- they must have a fast impulse response in transducing; this is closely connected to the bandwidth of the transducer;
- they must have good sensitivity; this improves the signal-to-noise ratio of the signal to be processed;
- they must have a directivity as sharp as possible.

2. STUDY OF VIBRATORY STATES OF PIEZOELECTRIC STRUCTURES

In the study of vibratory states of piezoelectric structures it was considered that these structures have two dual roles, mechanical and electrical. Thus, the input is mechanical when the structure operates in reception. It becomes electrical when the structure operates in emission. The study concerns conservative piezoelectric resonators and is treated within some boundary conditions (mechanical and electrical conditions) (Figure 1).

The three-dimensional vibratory state of these elements is approximated by a one-dimensional vibratory state called the piston type. This model (the piezoelectric equations, the mechanical and electrical conditions) uses a method of finite elements and permits a rapid, high precision simulation, of the main characteristics (the intrinsic characteristics of the material, the resonance and anti-resonance frequencies, electro-mechanical coupling coefficients, electric impedance, etc.) and, additionally, the

simulation of the deformation of a resonant cavity [1].

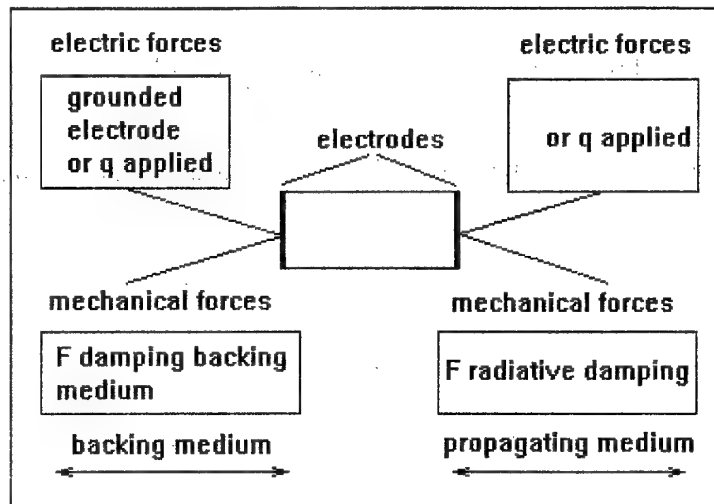


Fig. 1 Boundary conditions, mechanical and electrical

For the one-dimensional model, the vibratory state of the piezoelectric bars with losses has been taken into consideration for simulation we have used a basic element of piezoceramic transducer of a parallelepipedic shape made of piezoelectric ceramic of dimensions W , T , L and placed between two electrodes (Figure 2). The electrodes are equipotential and of a known potential. As reference potential, one can use the potential of one electrode, preferably the lower electrode which is grounded. The finite element matrix formulation of the piezoelectric model without structural damping is presented below:

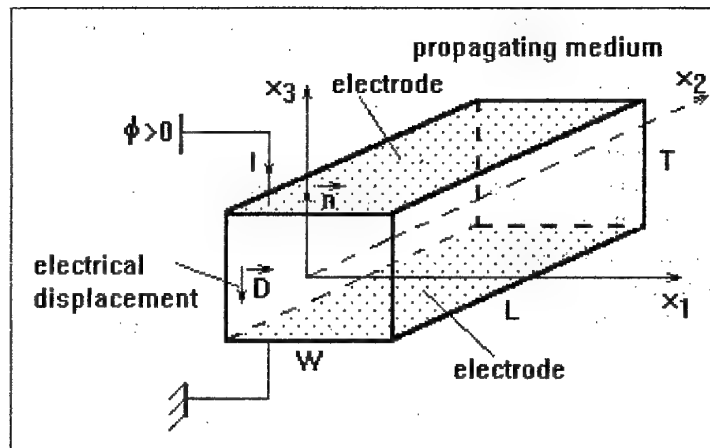


Fig. 2 Basic element of ultrasonic multielement probes

$$\begin{bmatrix} M_{UU} & 0 \\ 0 & 0 \end{bmatrix} * \begin{bmatrix} U \\ \phi \end{bmatrix} + \begin{bmatrix} K_{UU} & K_{U\phi} \\ K_{U\phi} & K_{\phi\phi} \end{bmatrix} * \begin{bmatrix} U \\ \phi \end{bmatrix} = \begin{bmatrix} F \\ Q \end{bmatrix} \quad (1)$$

where: M_{UU} is mass matrix, K_{UU} elastic stiffness matrix, $K_{U\phi}$ piezoelectric stiffness matrix, $K_{\phi\phi}$ dielectric stiffness matrix, U and ϕ are respectively the column vectors for nodal mechanical displacements and for nodal electric potentials, and F is the column vector of the mechanical forces to the surface nodes, Q the column vector of the electric charges in the same nodes.

These vectors are defined by:

$$F = \left(\int_{\delta V} T_{n,h} \cdot b_k dS \right) \quad \text{and} \quad Q = \left(\int_{\delta V} (D_h \cdot n) a_k dS \right) \quad (2)$$

The interior potentials ϕ_p are a function of the displacements U and of the surface potentials ϕ_p . The condensed differential system is:

$$\begin{bmatrix} H_{UU} & H_{U\phi} \\ H_{U\phi}^t & -H_{\phi\phi} \end{bmatrix} \begin{bmatrix} U \\ \phi_p \end{bmatrix} + \begin{bmatrix} M_{UU} & 0 \\ 0 & 0 \end{bmatrix} \begin{bmatrix} U \\ \phi_p \end{bmatrix} = \begin{bmatrix} F \\ Q_p \end{bmatrix} \quad (3)$$

by assuming:

$$\left. \begin{aligned} H_{UU} &= K_{UU} + K_{U\phi} K_{\phi\phi}^{-1} K_{U\phi}^t = K_{UU} + \Delta K, \\ H_{U\phi} &= K_{U\phi} - K_{U\phi} K_{\phi\phi}^{-1} K_{U\phi}, \\ H_{\phi\phi} &= K_{\phi\phi} - K_{\phi\phi}^t K_{\phi\phi}^{-1} K_{\phi\phi}, \end{aligned} \right\} \quad (4)$$

After some approximations and assuming that the H matrix is $4N$ dimensional we obtain the linear system in the formulation of a H type without structural damping:

$$\begin{bmatrix} H_{UU} & H_{U\phi} \\ H_{U\phi}^t & -H_{\phi\phi} \end{bmatrix} \begin{bmatrix} U \\ \phi \end{bmatrix} + \begin{bmatrix} M_{UU} & 0 \\ 0 & 0 \end{bmatrix} \begin{bmatrix} U \\ \phi \end{bmatrix} = \begin{bmatrix} F \\ Q_p \end{bmatrix} \quad (5)$$

The balance of forces $H_{UU}U + H_{U\phi}\phi + M_{UU}\dot{U} = F$ corresponds to the following forces:

- elastic force $H_{UU}U$,
- electromechanical force $H_{U\phi}\phi$,
- inertial force $M_{UU}\dot{U}$,
- surface mechanical force F ;

the balance of electric charges $H_{U\phi}^t U - H_{\phi\phi}\phi = q$ corresponds to the following charges:

- polarization charges due to the piezoelectricity $H_{U\phi}^t U$
- dielectric condensation charges $H_{\phi\phi}\phi$
- resultant free charges q

The scalar $H_{\phi\phi}$ is the capacity of the system equivalent to a condenser, by only tacking into account the dielectric polarization.

3. EXPERIMENTAL RESULTS

The resonance characteristics were obtained experimentally from the measurement of the resonance and antiresonance frequencies and the electric impedance of piezoelectric elements. The study was made on piezoceramic disks 0.3 - 2 mm thick having high resonance frequencies (1-10 MHz). The lower thickness difficult be achieved [2]. The piezoceramic material used for the piezoceramic transducer is of PZT type (lead titanate zirconate) with various additions (Ni, Bi, Mn) and presents piezoelectric and dielectric characteristics as: 7.2 g cm^{-3} density, 1000 permittivity, 70 quality factor, 0.55 coupling factor and $20 \times 10^{-12} \text{ m}^2 \text{ N}^{-1}$ compliance constant.

4. CONCLUSIONS

The quantification of the modal electromechanical coupling allows to evaluate the relative impedance of the resonance states of piezoelectric structures. This method can be easily applied for optimization of more complex multielement piezoelectric structures used for radiated ultrasonic signals. Automatic-scanning ultrasonic imaging systems are tending to supplement the first echographs based on the manual displacement of a single-element transducer. By using a method of finite elements in modeling on the piezoelectric equations and on mechanical and electrical balances allows the rapid simulation of some characteristics with a high precision and the simulation of deformation of the resonant cavity.

5. REFERENCES

- [1]. M. Naillon, Analysis of piezoelectric structures by a finite element method, ACTA ELECTRONICA, 25, 4, (1983).
- [2]. I. Chilibon, Sistem de transmisie ultrasonică în mediu acvatic de mare sensibilitate. Dispozitive hidroacustice piezoceramice, Teză de doctorat, UPB, Bucuresti, (1997).

LASER BIOSTIMULATION USED IN THE TREATMENT OF HAIR LOSS

Costilena Chelarescu MD, D. Chelarescu MD *

Private room, str. 22 Dec. 1989 nr. 53/30 Tg-Mures, Romania phone 065/123765, fax 065/162433,

* UM 0709, Ministerul de Interne Tg-Mures, Romania

ABSTRACT

Total or universal alopecia is a result of the extension or generalization of alopecia from limited areas. The apparently healthy hair falls easily when it is touched. In a few weeks this process may lead to complete baldness. However there remain small tufts of healthy hair here and there. The disease is difficult to deal with and it is generally definitive. We found this disease at a 29- year old woman, an active person, after an emotional stress. Her pathological antecedents mentioned peripheric circulation disorders. She had undergone a treatment with corticoides, vasodilators and vitamins for 8 months without any result. Eventually the patient resorted to laser biostimulation. The laser used for treatment was a diode laser (810 nm, 50 - 400 mW -CW). A dose of 3 - 6 J/cm² was applied 3 times a week for 6 months. As a result, healthy hair started to grow in the areas formerly devoid of hair.

1. INTRODUCTION

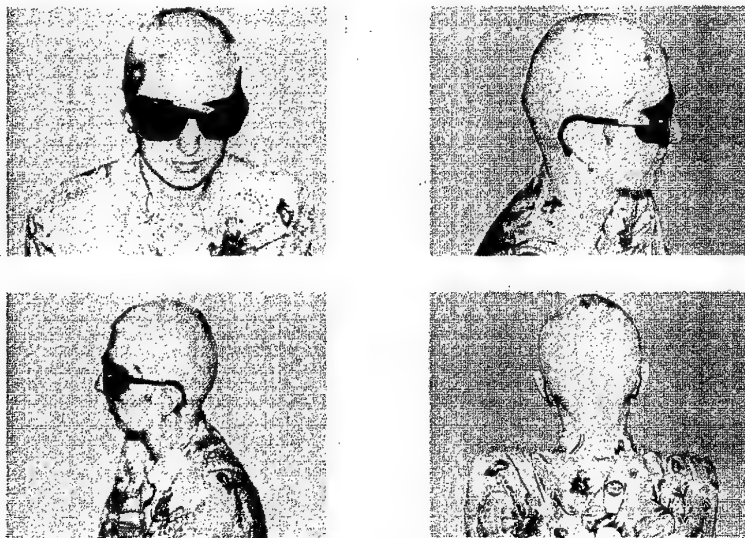
Total alopecia is an extension of alopecia. This change is met in 5% to 10% of cases. It begins as a common alopecia. The apparently healthy hair falls easily when touched and in a few weeks the person may become completely bald. A few tufts of healthy hair can still be found. This is a stubborn type of alopecia, resistant to treatment and it is of definitive nature in most cases. The histopathologic examination reveals an atrophic root. In recently reported cases, a perifollicular lymphocytic infiltrate has been noticed. Tegumentum is sometimes atrophied usually only keratin can be found instead of cells. The main factors which lead to alopecia are: genetic factors, endocrine, immunologic, neuropsychiatric factors, as well as autoimmune disease. Sympathetic disturbances of hypertonia type seem to lead to the appearance of a partial angiospasm followed by the hair loss. The evolution of the disease is constant: although there were cases with a spontaneous healing, a few months later relapses of the diseases were noticed in 20 - 30% of the cases, and in 40 - 80% of the cases after 5 years [1-16].

2. MATERIAL AND METHOD

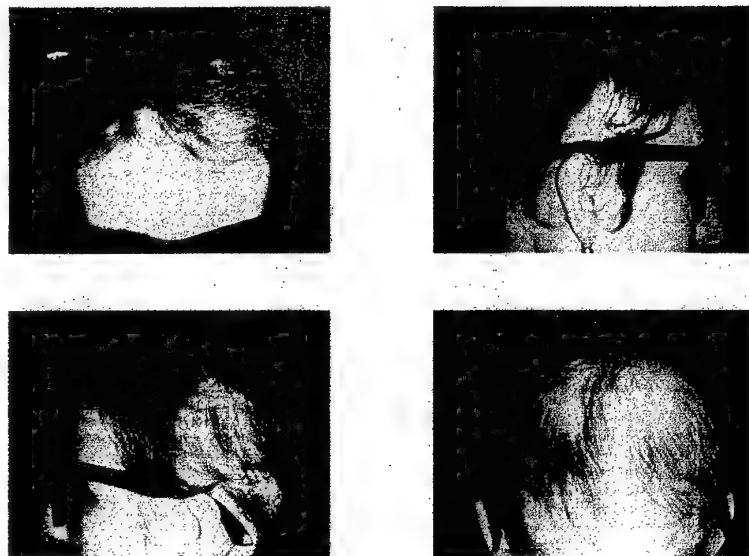
T.A., a patient of 29, an active person of an A type constitution, with heavy responsibilities in her job, has finally resorted to laser biostimulation for treatment. It followed to a previous treatment with locally injected corticosteroids, vasodilators, vitamins, and massage. She had undergone this treatment for 8 months without success. The physiologic and pathologic antecedentes revealed a pregnancy 15 months ago and disorders of Raynaud type. The laser used for treatment was a diode laser with an emitting radiation of a 810 nm wavelenght and a power of 50 - 400 mW. A dose of 3 - 6 J/cm² was applied 3 times a week. The treatment had 2 stages: the first lasted for 3 months, and it was followed by a break of 1.5 months, while the second stage of the treatment lasted for 3 months. At the beginning of the treatment the patient had a feeling of warmth at the level of her scalp. It was noticed immediately at the end of the first treatment session and it lasted about 4 hours. One hour and a half after the treatment the feeling of warmth extended to face and neck. As the patient complained of cold at night, she was recommended to wear a cap while sleeping. The feeling of cold disappeared after 1.5 months. This moment coincided with the appearance of the first hair. It appeared at the level of the frontal area at the border between forehead and head. The first hair lacked the original colour or was mixed with hair of original colour. The aspect was also different: straight or curly rather friable. The initial seborrheic scalp became normal after a 3 - month treatment (10 sessions of laser treatment). In the second stage the hair

became thicker and only healthy hair grew. The hair was straight, normally coloured, and resistant when pulled. Similarly, when washed, it did not fall. The areas devoid of hair were gradually covered with hair and the hair existing before the treatment grew thicker. Degenerated and malformed hair disappeared. The scalp was covered with old and new hair. The old hair had cut ends, while the new hair had different dimensions and pointed ends. During the treatment the hair was cut twice. An improvement in the memorizing ability, as well as a shorter time of response were noticed during the treatment. Towards the end of the treatment the feeling of warmth was much diminished [9, 17].

AT THE BEGINNING OF TREATMENT



AFTER ONE YEAR



3. DISCUSSION

In classic dermatology, total alopecia is treated with sedatives, tranquillizers, neuroleptics in order to correct neuropsychic disturbances. General corticotherapy applied for longer periods gives satisfactory results, but in 60 - 70 % cases patients experience hair loss when the treatment is interrupted.

Vitamins as well as vasodilators can also be useful. Photochemiotherapy or massage with carbonic snow can be used locally. The local use of laser biostimulation leads to a process of neovascularization, rises local temperature with 1 to 7°C. These facts were proved by angiographic methods, transillumination, cutanate thermography. At cellular level, laser biostimulation determines the stimulation of enzymes production of procollagen and metabolism acceleration.

4. CONCLUSION

Alopecia is a disease that gives rise to an aesthetic handicap. It cannot be completely healed with conventional methods of dermatologic treatment. Laser biostimulation is an efficient alternative in treating this disease. The inconvenient factor regarding this treatment is the long but absolutely necessary time the hair needs to grow. The case presented above is the most relevant of the 10 cases treated by using this method, each of them having its own specific and duration.
[12, 13, 14]

5. REFERENCES

- [1]. Bucur G., Mică enciclop. de boli dermatovenerice, Ed. Stiintifică si Enciclop., Buc., p.430, (1987).
- [2]. Conu Aurel, Bucur Nicolescu, Atlas de dermatovenerologie, Ed. Medicală, Buc., pag.102, (1980).
- [3]. P. Vulcan, A. V. Mozaceni, Chirurgie Dermatologica Editura Junimea Iasi, 1998 pag 160-163
- [4]. F.R.C.S. (Ed.) Sarah A., Utilizarea laserului - afectiunilor derm., Update, v. III, nr. 5, Dec.1997
- [5]. C. Popescu, R. Popescu, Laserele in chirurgie, Laserele in derm. Vol I, nr.2 , 03 '98 p. 17 - 22
- [6]. W. Glinkowski, L. Pokora, Lasers in Teraphy, Warsava, 1993
- [7]. Pascal C., L'energie douce face a la douleur, Collection Laser, Techno - Synthese - 1985, Paris
- [8]. B. Achauer, V. V. Kam, M. W. Berns, Lasers in Plastic Surgery and Dermatology, 1992
- [9]. BTL. Laser terapie neinvaziva folosita in dermatologie, 1998
- [10]. J. Kert, L. Rose, Clinical laser therapy, Low level laser therapy, 1989, pag. 9 - 73, 159 - 179
- [11]. T. Ohshiro and R.G. Calderhead, LLLT: A practical introduction, John Wiley & Sons, 1987
- [12]. C Popa: Flashscanner-ul la un laser cu CO2 in transplantul de par, LCM, 03 '97, p. 25 - 26
- [13]. W. P. Unger, M. D., Laser Hair transplantation II, Elsevier Science Inc., pag. 759 - 765
- [14]. G. Goodman, Update on LLT in derma, The M.J. of Australia, v.164, no. 11, 03/06'96, p. 681 - 686
- [15]. A. Conu, F. Nicolescu: Atlas de dermato-venerologie, Ed. Medicala, 1980, pag. 98 - 99
- [16]. G. Baxter, Therapeutic Lasers, Theory and Practice, Churchill Livingstone, 1994
- [17]. Therapy Laser - Model CTL - 1106 MX, Operation Manual, vers. 2.0, nov. 1995

LOW ENERGY LASER TREATMENT IN LICHEN PLANUS AND FINGERS PULPITS

T. Ciuchita, S. Anghel*, C. Stanescu*, C. Antipa**,
A. Nicolescu***, M. Usurelu****

Military Hospital. Pitesti, 0300, <http://www.pcnet.ro> e-mail: yamaha @ mediacom.pcnet.ro;

*Faculty of Sciences, University of Pitesti, Tg. Din Vale, No.1, Pitesti, 0300, phone/fax 048-216448,

** Coltea Clinical Hospital Bucharest; ***"N.G.Lupu" Clinical Hospital Bucharest;

****Military Hospital Cluj-Napoca.

ABSTRACT

The purpose of our research was to verify whether the Low-Energy-Laser (LEL) is a useful therapeutical means against infectious finger pulpits (IFP) and Lichen Ruber Planus (LP). We noticed that the pruritus (and cutaneous lesions) disappeared for both diseases, in the case of 83,3 % of patients. We concluded therefore that LEL is a possible therapy for LP and IFP. Currently, we study the effects of a He-Ne laser on similar skin samples. We have undertook optical determination on the variation of skin samples transmittance, as well as holographic studies on the effects of laser radiation, in order to identify other objective macroscopic methods able to reveal the effects at cellular level.

1. INTRODUCTION

Low-Energy-Laser (LEL) have been used in dermatology for about 20 years [1]. Separately the skin will continue to be an important organ for diagnosis and therapy. The classical therapy used for Lichen Ruber Planus (LP) and infectious finger pulpits (IFP) of the hand is not very efficient [2], and therefore we focused on alternative efficient therapy of these diseases based on LEL.

2. PATIENTS, MATERIAL AND METHOD

The 54 patients (15 men and 39 women; 38 patients were treated for LP, respectively 16 patients for IFP) aged between 21 and 56 years, having similar characteristics, were divided in three groups:

- a) a LEL group: 24 patients (19 LP cases – 2 men, 17 women, and 5 IFP cases - only men) were treated for 4÷5 minutes in the first 5 days for 6 weeks (30 sessions), using a red 8 mm diode laser with continuous emission, $\lambda = 668$ nm, spot size of 4 mm;
- b) a placebo laser group: 11 patients (6 LP cases - only women, and 5 IFP cases – 2 men, 3 women), were treated with placebo red light source;
- c) a control group: 19 patients (13 LP cases – 4 men, 9 women, and 6 IFP cases – 2 men, 4 women) were treated only with classical therapy.

Before and after any kind of treatment, histological samples and cutaneous echographies were made, as objective methods to measure the effects of the treatment.

3. RESULTS

The pruritus and clinical lesions disappearance, confirmed by histopathological examination and cutaneous echography, was obtained as follows:

- LEL group – 20 cases (83,3 %);
- placebo group – 5 cases (45,5 %);
- control group – 12 cases (63,2 %)

The results are represented in figure 1.

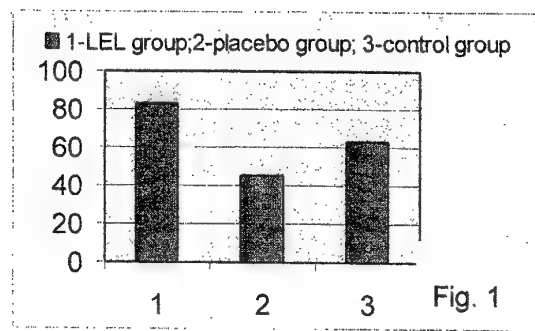


Fig. 1

No side-effects of the LEL therapy was recorded on the laser group patients during the period of treatment (45 days) and monitoring (90 days), but in 3 cases (15,8 %) side-effects (nausea, teleangiectases, cutaneous folliculitis) were observed after the classical treatment.

A post-therapeutic relapse was detected for all three groups: 15 cases treated by LEL therapy (only LP cases) after 63 days (75 % from cases with favourable effects), 12 cases treated by classical therapy after 35 days (LP cases), respectively 27 days (IFP cases) (100 % cases with favourable effects).

4. DISCUSSIONS

By analysing the results synthetically presented above, we can conclude:

- 1) more positive results for the LEL treatment (83,3 %), as compared to the classical treatment (63,2 %) were obtained;
- 2) we observed a significant shortening (50 %) of the time interval required for the appearance of favourable effects on the LEL group (45 days), as compared to the control group (90 days);
- 3) the time interval for the post-therapeutic relapse is shorter for the control group (27-35 days) comparatively to the LEL group (63 days);
- 4) the most rapid favourable effects for the LEL therapy were obtained for the young patients (21-35 years) in comparison to the old patients (40-56 years).

Hence, LEL therapy can be part of a complex clinical therapy for LP and IFP.

5. OPTICAL STUDIES

We have also made some optical studies on the effects of laser irradiation, in order to point out the physical macroscopic effects of laser treatment, using a He-Ne laser, 6328Å wavelength.

We analysed the transparency variations of skin samples under the action of a laser beam, using the exponential law of the attenuation: $I = I_0 \cdot \exp(\kappa d)$, where I_0 is the incident and I the transmitted intensity of the beam, d – thickness and κ - sample attenuation coefficient. The experimental set-up is illustrated in figure 2.

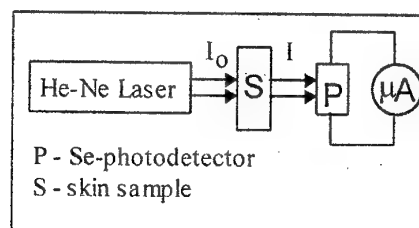


Fig. 2

We measured the extinction $e = \ln(I_0/I)$ as a function of relative exposure (E/E_0); where E_0 is the total exposure used for therapeutic irradiation (about 600 J/cm^2). We studied both sick and normal skin samples. The typical results we have obtained are presented in figure 3.

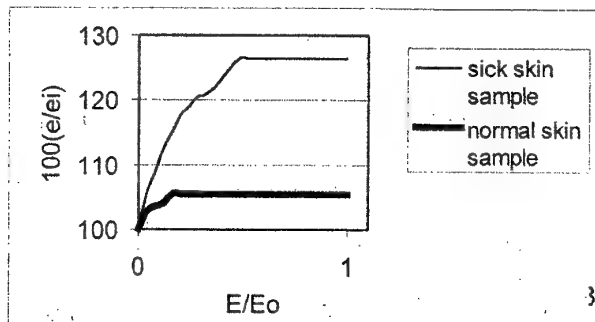


Fig. 3

In both cases, the extinction of the studied pieces increases (non-specific effect) while the sick pieces present a higher and slower increase (specific effect). This different behaviour suggests a specific effect of the irradiation at cellular level. Please note that the observed increase of extinction stops before the whole dose used in therapy is applied.

We have also undertaken a holographic study of the skin samples using the set-up showed in figure 4. The double exposure method is used, in order to reveal the modifications in dimension and refractive index of the samples. We did not notice the supposed modification, probably because of the too large thickness (over $10 \mu\text{m}$) of the studied skin samples.

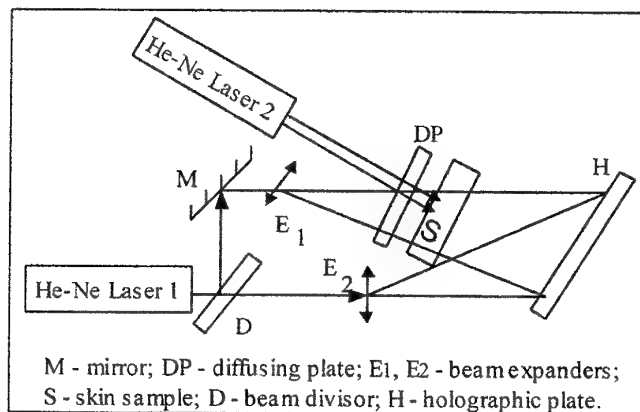


Fig. 4

6. REFERENCES

- [1]. Antipa C., Moldovan C., Podoleanu A. "LEL - a Synthetic View", *Proceedings SPIE ROMOPTO*, 2461, Bucharest, pp. 366-373 (1994)
- [2]. Blanc F., "Photothérapie de la dermatite atopique: quels effets ont les UVA 1 sur les cellules?", *Abs.Derm.*, 313, pp.6-7, (1997).
- [3]. Friedmann H., Lubart R., "Mechanisms of Photobiomodulation by Visible and IR Light", *Laser therapy*, 8, pp. 14-35, (1996)

- [4]. Goldman L., "Future of Laser Dermatology", *Lasers in Surg. And Med.*, 22, pp. 3-8, (1998)
- [5]. Mester A., Nagylucskay S., Mako E., "Radiobiological Effects of Laser Irradiation", *Laser Therapy*, 2, pp. 1-9, (1990)
- [6]. Nagylucskay S., Mester A., Mako E., "Reactions of Lymphocytes to Different Laser Wavelength", *Laser Therapy*, 8, pp. 66, (1996)
- [7]. Sheehan-Dare R.A., Cotteril J.A., "Lasers in Dermatology", *Br.J. Dermatol.*, 129, pp. 1-8, (1993)
- [8]. Vasiliu V. Bruckner I., Brătilă F., Antipa C., Moldovan C. "Multiwave Low Laser (MWL) Therapy in the Pain Treatment ", in *Proceedings SPIE ROMOPTO*, Bucharest 2461 pp. 395-397 (1984).
- [9]. Barabash A.G., Kats A.G., Getling Z.M., "Experience in treating patients with lichen ruber planus by using a helium-neon laser", *Stomatologiia*, 74(1), pp. 20-21 (1995).
- [10]. Walsh L.J. "The current status of low level laser therapy in dentistry. Part 1. Soft tissue applications" *Aust. Dent. J.* 42(4), pp.247-254 (1997)
- [11]. Bélicovsky C., Thil R. "Les lasers à colorant: toute la gamme", *Abs. Derm.*, 247, pp.15-16 (1995)

LOW ACOUSTICAL SENSITIVITY PYROELECTRIC LASER ENERGYMETER

E. Smeu, N. Puscas, I. M. Popescu

"Politehnica" University of Bucharest, Physics Dept., Spl. Independentei 313, Bucharest 77206, Romania, fax: (401)4104488, e-mail: pnt@physics2.physics.pub.ro

ABSTRACT

A pyroelectric digital laser energymeter having a maximum resolution of $0.1 \mu\text{J}$ and a maximum input pulse energy of 1 J is reported herein. Its main features, which distinguish it among the huge variety of similar apparatus, are: the lower acoustical sensitivity and the higher repetition rate of the measured laser pulses. The energymeter is also provided with a reliable AutoRanging (achieved by original circuitry), unlike other similar apparatus (even complex and, consequently, expensive), which have only ManualRanging.

1. BLOCK SCHEMES SHORT DESCRIPTIONS

Figure 1 presents the block scheme of the reported apparatus (where "ARS" means "Automatic Range Selector").

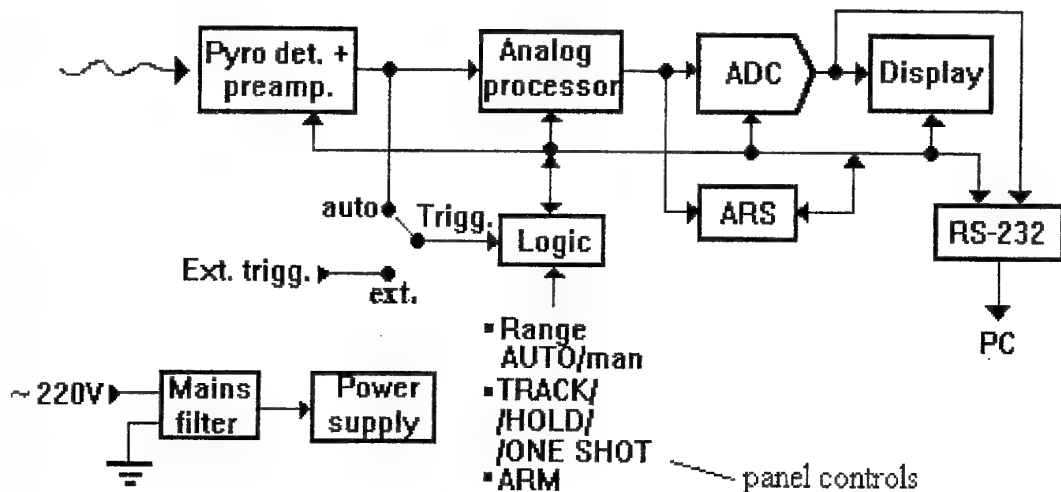


Fig. 1 Block scheme of the energymeter

The "heart" of the apparatus is an analog (digitally-assisted) "Analog processor". Its main functions are:

- to "capture" the peak of the pulse delivered by the pyroelectric detector (through its preamplifier) and to hold it during the analog to digital conversion;
- to restore the base-line of high repetition rate laser pulses, which lead to electrical pulses delivered by the pyroelectric detector having thermal relaxation "tails" un-completely relaxed - in other words, to increase the maximum repetition rate of the measured laser pulses;
- to reduce the acoustical sensitivity (pyroelectric detectors are inherently piezoelectric [1], [2], etc.). The block scheme of the "Analog processor" is shown in Figure 2 (where "T&H" means "Track&Hold").

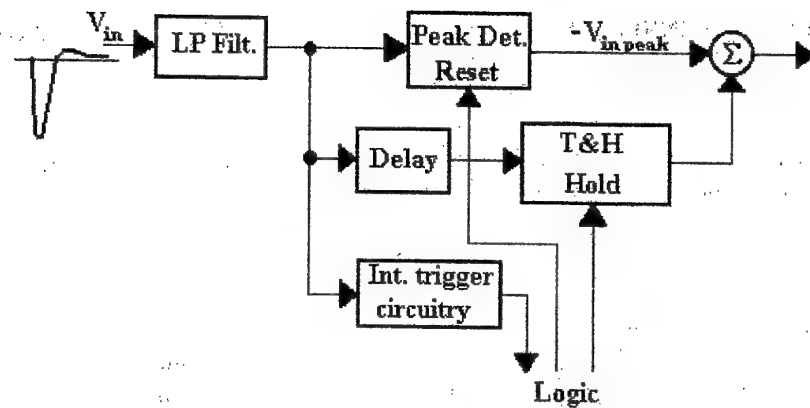


Fig. 2 Block scheme of the "Analog processor"

The low-pass filter at the input of the circuit is used to reduce the amplitude of the acoustical signal (this is possible as its bandwidth is placed much higher in respect to the thermal signal that "represents" the energy of optical pulses). In order to increase the maximum repetition rate of laser pulses, an optimized "artificial" delay line with concentrated constants was used. The signals in the "Analog processor" are shown in Figure 3 (where "EOC" means "End of Conversion"). There are two signals worth to note: the Peak Detector output (light grey, first time axis) and the Σ output (dark grey) ε_1 is the voltage value of the thermal "tail" of the previous pyroelectrically generated pulse when the actual one occurs (ε_1 is held by T&H after proper delaying). The trigger source is considered to be internal, but the figure is essentially the same for external trigger (only the falling edges of the trigger pulses may differ).

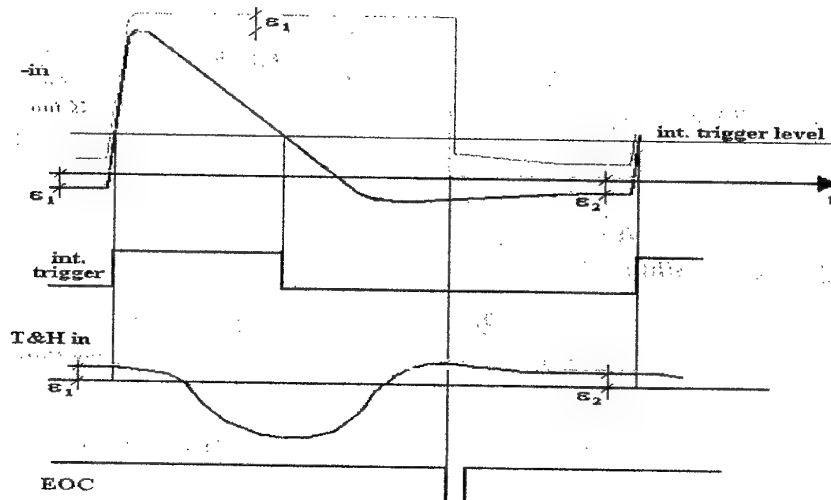


Fig. 3 Signals in the "Analog processor"

2. MAIN EXPERIMENTAL RESULTS

The maximum repetition rate is higher compared to the reference model Rm-3700 (Laser Probe, Inc. - USA) which works only at 40 Hz with the same detector head [3] as the reported energymeter.

The most important improvement in comparison to other similar apparata consists in the considerable decrease in sensitivity to acoustic noise. For generating reproducible, repetitive acoustic

pulses, a common loudspeaker was used. It was "pumped" with 1 ms current pulses (they are quite similar acoustically to real laser-generated pulses, as demonstrated by using a microphone and a memory scope). In Figure 4 the indications of the reported energymeter (noted "UPB") and those of the reference model Rm-3700 (both with the same detector head) are represented against the current amplitudes of the loudspeaker pulses.

3. TECHNICAL DATA OF THE REPORTED ENERGYMETER

The main technical data and facilities of the apparatus are:

- Full scale ranges / resolution (3 digit display): 100 μJ / 0.1 μJ ; 1 mJ / 1 μJ ; 10 mJ / 10 μJ ; 100mJ / 100 μJ ; 1 J / 1 mJ;
- Facilities: AUTO/man. ranging; TRACK / HOLD / SINGLE PULSE; ARM (for SINGLE PULSE); INT/EXT TRIGGER (EXT only on the leading edge of a TTL pulse); with INT TRIGGER sensitivity: 10% of full scale;
- Pyroelectric detector: RjP - 734 (Laser Probe, Inc. - USA);
- Sensing area: 5 cm^2 (circular input);
- Detector configuration: cavity;
- Active area uniformity: $\pm 5\%$ with 5 mm spot size;
- Spectral response: 0.4 to 3 μm : $\pm 0.5\%$; 0.25 to 16 μm : $+0.5\%$ -4%;
- Maximum peak power density: 1 MW / cm^2 ;
- Maximum average power: 10 W;
- Linearity: $\leq 1\%$ up to 20% of max. average power; $\leq 5\%$ at max. average power;
- Input optical pulse width: < 1 ns to 1 ms;
- Maximum repetition rate of optical pulses: 75 Hz;
- Calibration uncertainty: $\pm 5\%$ of reading $\pm 0.1\%$ of full scale.

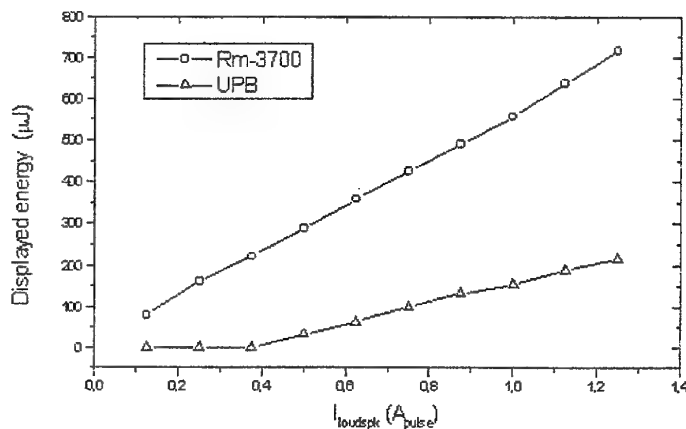


Fig. 4 The response to acoustical pulses

4. CONCLUSIONS

A cheap (no microprocessor-inside), yet good quality digital laser energymeter is reported. It is provided with a reliable AutoRange, unlike other similar apparata which have only Manual Ranging made by well-known companies (for instance, Laser Probe, Inc. - USA). It also has a higher maximum repetition rate limit of the measured laser pulses (75 Hz, versus 40 Hz for Laser Probe Rm-3700). But most important, it is less sensitive to acoustical noise.

ACKNOWLEDGEMENTS

The reported apparatus was partially built and tested under INCO COPERNICUS Contract no. IC15 - CT96 - 0820 (DG12 - MUYS) subsidised by the European Community.

5. REFERENCES

- [1]. *Pyroelectric detectors and detection systems*, Laser Precision prospect PS-30-02, pp. 4-6, (July 1984)
- [2]. Greenfield, E., *Laser Focus*, March 1986, pp. 134-142
- [3]. Laser Probe, Inc., "Rm-3700 UNIVERSAL RADIOMETER Operating Instructions"

ON THE PHOTODYNAMIC THERAPY OF CARCINOMA IN BUCCAL CAVITY

Evantya Ungureanu-Coles, Silvia Nicolau*, M. Ristici*

Faculty of Medicine, Craiova, Romania

* Institute of Atomic Physics, Bucharest, Romania

ABSTRACT

The paper presents some clinical results on the photodynamic therapy with PHOTOFRIN II applied in the buccal cavity, especially for tumors located on the tongue. The first class of patients presented an epidermoid carcinoma, invasive, located on the base of the tongue. The second class of patients had two or four lesions located in the buccal cavity, a micro-invasive carcinoma on the side of the tongue and a displasia of the palate. The light induced fluorescence signal shows a high contrast between the tumor and the surrounding normal tissue at short times after "in vivo" injection. The magnitude of this contrast is correlated with the stage of the cancer. We intend to develop a fluorescence microscopy method for prospecting the dye content of the cancer tissue.

1. INTRODUCTION

Clinical studies of Photofrin II by fluorescence spectroscopy demonstrated new results for a group of patients presented early cancer in the buccal cavity. The light-induced fluorescence signal shows a relatively high contrast between tumor and surrounding normal tissue at short times after "in vivo" injection. The magnitude of this contrast is correlated with the stage of the cancer, the more invasive tumors showing the highest contrast.

An important problem in cancer photodetection [1-4] with Photofrin II is the optimization of the time after "in vivo" injection in a way at which the contrast of the "fluorescing fraction" of Photofrin II between tumor and surrounding normal tissue is high and the absolute concentration of the marker is also optimal for detection without clinical damage. Clinical tests of these porphyrins in early cancers of the oesophagus and buccal cavity [4,5,6,7,8] present a good stability in a long time and a low chemical damage. The phototoxicity of the skin being a non negligible side effect in PDT, we have also determined the effect on the skin.

2. EXPERIMENTAL PROCEDURES

The experimental set-up has been described previously [5,9,10,11,12]. The desired excitation wavelength is selected by passing the light of a Xe lamp through a monochromator. This excitation light is transmitted through a dichroic mirror and projected by a microscope objective into a (0.5-0.7) mm core diameter quartz, optical fiber. The end of the fiber is positioned, for instance, via the biopsy channel of an endoscope on the surface of a superficial cancer or its neighbouring normal tissue. The fluorescence spectrum induced by the excitation wavelength in the sample is collected by the same optical fiber, reflected by the dichroic mirror, filtered to remove the excitation light, and focussed onto the entrance slit of a spectrograph coupled with an intensified diode array. The signal obtained is displayed on the optical multichannel analyzer (OMA) and can be further processed by a personal computer [12,13,14,15].

After recording the autofluorescence spectrum of the tumor and normal surrounding tissue with this apparatus, the Photofrin II is "in vivo" injected and the procedure of measuring the fluorescence spectrum at these two locations is repeated at different time delays. The spectra thus obtained now consist of both the autofluorescence spectrum of the tissue and superposed fluorescence from the injected porphyrins. Knowledge of the autofluorescence spectrum prior to injection allows the subtraction of this component to get the fluorescence spectrum due to the fluorescent fraction of Photofrin II at various delays after injection. In order to compare the Photofrin II fluorescence between different measurements, the power of the excitation light and the intensity of the fluorescence spectrum induced by this light in a

fluorescent reference solution are measured. This allows the correction of the variation of the excitation light intensity and slight changes in the optical alignment [12].

3. CLINICAL RESULTS

The patients are selected in the Polyclinical Center and Hospital "Dr. Cantacuzino" from Bucharest and divided in two groups. The first group of patients has a tumor located on the base of the tongue. This epidermoid carcinoma was invasive. The second group of patients selected in the Stomatological Center No. 4 from Bucharest has two or three lesions located in the buccal cavity. These lesions are:

- a microinvasive carcinoma on the side of the tongue
- a displasia of the palate.

The patients were injected with 0.4 mg of Photofrin II per kg of bodyweight [12,13]. The used excitation and emission wavelengths are respectively 405 and 630 nm. The acquisition time per spectrum is about 1 second. For all patients the Photofrin II fluorescence intensity as a function of time is measured at several locations.

The fluorescence of the carcinoma divided by the fluorescence of the normal surrounding tissue is called the fluorescence ratio or selectivity (noted ratio). The time $t = 0$ corresponds to the end of the injection.

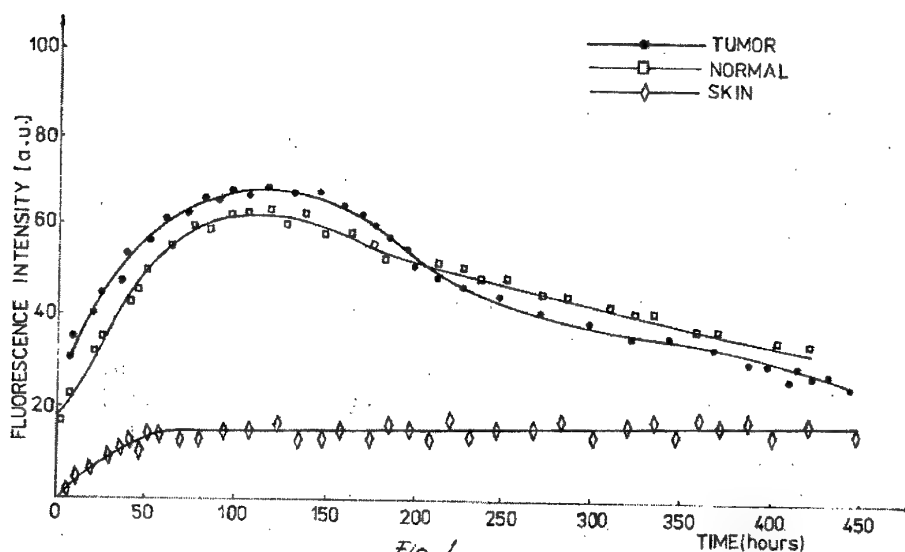


Fig. 1

In fig. 1 the Photofrin II fluorescence signal as a function of time is presented.

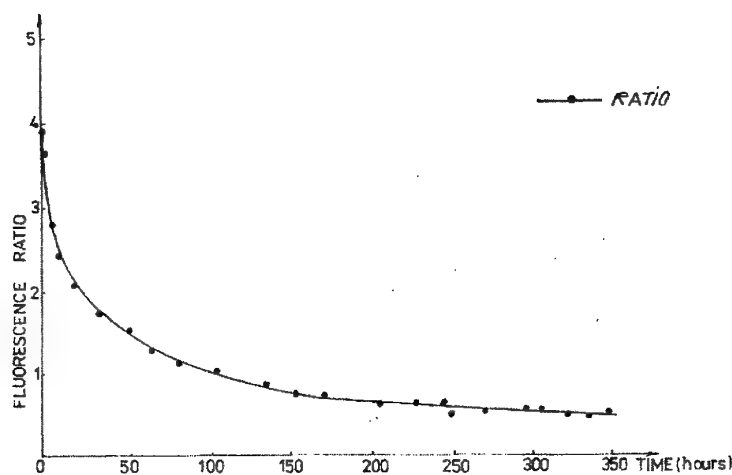


Fig. 2

Fig. 2

In the fig. 2 the resulting fluorescence ratio as a function of the time is presented.

In the design the symbol "tumor" is the signal from the invasive carcinoma on the base of the tongue, "Normal" is the signal from the normal tissue (mucosa) near the tumor, "Skin" is the signal from the skin of the forearm, "Ratio" is the selectivity between the carcinoma and the normal surrounding tissue.

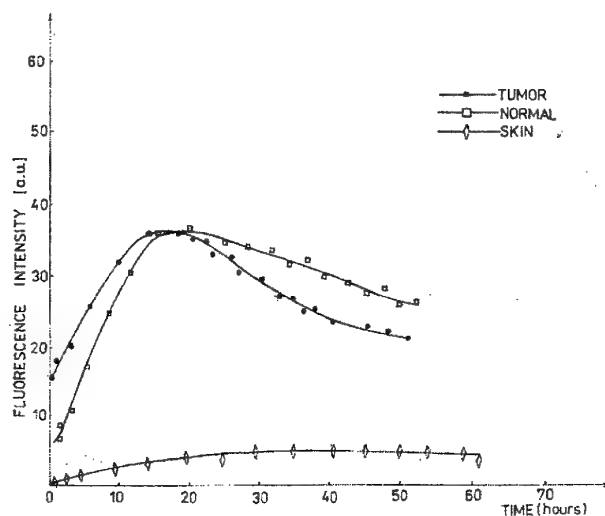


Fig. 3

Fig. 3

In fig. 3 the Photofrin II fluorescence signal as a function of time is presented, where "Tumor" is the signal from the microinvasive carcinoma located on the side of the tongue.

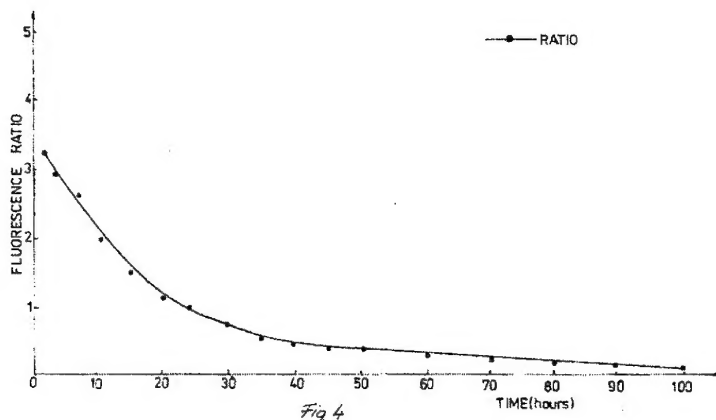


Fig. 4

In fig. 4 the Photofrin II fluorescence signal as a function of time is presented, where "Tumor" is the signal from the displasia located on the palate.

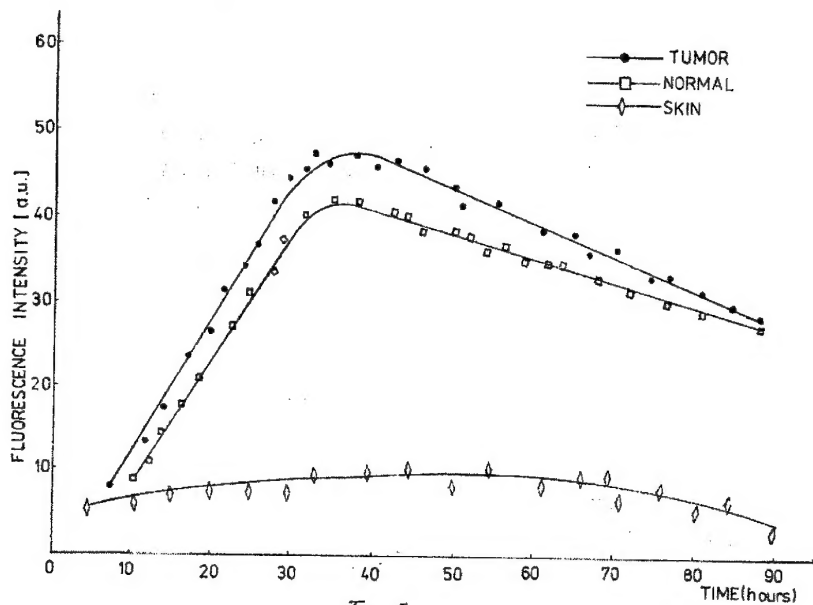


Fig. 5

In fig. 5, the resulting fluorescence ratio as a function of time is presented, where "Tumor" is the displasia located on the palate.

4. CONCLUSIONS

The highest Photofrin II fluorescence ratio between tumor and normal tissue is reached at very short times after the end of the injection. At longer times the apparent selectivity decreases and tends to unity after about 30 hours (fig. 1,2).

The selectivity (fluorescence ratio) is dependent on the photosensitizer uptake in the tumoral tissue. The highest contrast is always reached right after the injection. It is possible that the vascularisation to play a major role in the selectivity obtained.

In conclusion, the best photodetection time for Photofrin II is at a very short delay after injection for these early stage carcinomas of the buccal cavity. Similar observations have been obtained in the oesophagus and the tracheobronchial tree [14]. We intend to develop a fluorescence microscopy method for prospecting the dye content of the tumor and accurate dosimetry.

5. REFERENCES

- [1]. Wagnières G., Braichotte D., Châtelain A., *Photodetection of early cancer in the upper aerodigestive tract and the bronchi using Photofrin II and colorectal adenocarcinoma with fluoresceinated monoclonal antibodies*, Proc. SPIE 1525, pp. 219-236 (1991)
- [2]. Monnier Ph., Savary M., Fontolliet Ch., *Photodetection and photodynamic therapy of early squamous cell carcinomas of the pharynx, oesophagus and tracheobronchial tree*, Lasers in Med. Sci. vol. 5, pp. 149-169 (1990)
- [3]. Wagnières G., Depeursinge Ch., Monnier Ph., *Photodetection of early cancer by laser induced fluorescence of a tumour - selective dye*, Proc. SPIE 1203, pp. 43-52 (1990)
- [4]. Braichotte D., Wagnières G., Monnier Ph., *Endoscopic tissue autofluorescence measurements in the upper aerodigestive tract and the bronchi*, Proc. SPIE 1525, pp. 212-218 (1991)
- [5]. Braichotte D., Wagnières G., Philippoz J.M., *Clinical LIF pharmacokinetic measurements with Photofrin II for optimizing the photodetection of early cancer*, proc. SPIE 1645, pp. 37-91 (1992)
- [6]. Bonnett R., White R.D., Winfield U.J., *Hydroporphyrins of the mesotetra (hydroxyphenyl) porphyrin series as tumour photosensitizers*, Biochem. J., vol. 261, pp. 277-280 (1989)
- [7]. Berenbaum M.C., Akande S.L., Bonnet R., *A new class of potent tumour photosensitizers with favourable selectivity*, Br.J. Cancer, vol. 54, pp. 717-725 (1986)
- [8]. Ris H.B., Altermatt H.J., Inderbitzi R., *Photodynamic therapy with chlorins for diffuse malignant mesothelioma*, Br. J. Cancer, vol. 64, pp. 1116-1120 (1991)
- [9]. Nicolau Silvia, Levai S., Sporea D., *Holographic method with optoelectronic interface in radiation dosimetry*, Anal. Univ. Buc., vol. 42, No. 2, pp. 83-90 (1993)
- [10]. Nicolau Silvia, Sporea D., Levai S., Vasiliu V., *Fast holographic interferometry with optoelectronic interface*, Optoelectronica, vol. 1, No. 4, pp. 45-48 (1993)
- [11]. Vasiliu V., Nicolau Silvia, Levai S., Sporea D., Scarlat F., *Integrated optics and some of its applications*, Optoelectronica, vol. 2, No. 1, pp. 49-53 (1994)
- [12]. Nicolau Silvia, Necsoiu Dana, Ristici Esofina, Ristici M., Levai S., Sporea D., Coles Evantya, Radu Mihaela, Scarlat F., *Spectroscopic and holographic studies for Photofrin II, microprocessor assisted clinical and physical localisation*, Optoelectronica, vol. 4, No. 2, pp. 42-44 (1996)
- [13]. Ungureanu-Coles Evantya, Nicolau Silvia, Ristici M., *On the photodynamic therapy of early cancer*, 1st Balkan Congress of Oncology, Athens, Greece, July 3-7 (1996)
- [14]. Nicolau Silvia, Nicolau I., Bârză I., Vasiliu V., Ungureanu-Coles Evantya, *Various experimental set-up for combined photodynamic therapy and hyperthermia in the oesophagus*, Rom. J. Optoelectronics, vol. 5, No. 2, pp. 197-202 (1997)
- [15]. Nicolau Silvia, Sporea D., Vasiliu V., *Computer modeling of laser light distribution in tissue for clinical applications*, Rom. J. Optoelectronics, vol. 5, No. 4, pp. 53-58 (1997).

AUTHOR INDEX

A

Acseste T.	91
Alexe M.	37
Anghel S.	108, 265
Antipa C.	265

B

Babin V.	103
Bălăsoiu B.	199
Băltăteanu N.	153
Barba N.A.	85
Beldiceanu M.	156
Bengulescu M.	91
Bivol V.V.	85, 177
Boerasu I.	37
Braic M.	195
Braic V.	195

C

Călian V.	139, 150, 153
Candea R.	192
Cantore C.	206
Cărmăzoiu A.	211
Cavaleru A.O.R.	192
Cengher D.	163
Chelarescu C.	262
Chelarescu D.	262
Chilibon I.	258
Chiriac H.	46, 49
Chumash V.	19
Cimpoca M.	163
Cimpoca V.	163
Ciuchita T.	265
Cojoc D.	219
Cojocaru I.	19
Coles E.U.	273
Copot R.	232
Coseac V.	123
Costache G.	252
Cotărlan C.	199
Cristescu C.P.	23

D

Degeratu V.	167
Dementiev I.V.	85
Dorogan V.	123
Drăgălina G.A.	85
Ducariu A.	131
Dumitru V.	71
Dyntu M.	42

E

Elflein W.	181
Elisa M.	58
Ersen S.	103

F

Facina M.	94
Forgaciu F.	80

G

Ghită R.	163
Giosanu D.	108
Goedgebuer J.P.	135, 181
Grabko D.Z.	33, 42
Grappe B.	131
Grattoni P.	219
Grigore M.	103
Grozescu I.	99
Guina M.	247

I

Iacobescu G.	64
Iliuță C.	232
Ioanid A.	147
Iorga L.	232
Irimia D.	99
Ispăsoiu C.	232
Ivan S.	167

J

Jackson D.A.	10, 241
Jianu D.	211
Jinga S.	52
Jitescu F.	160

K

Karavanskii V.	19
Kevorkian A.	23
Kiss A.	195

L

Lakatos E.	167
Levai St.	111, 115
Lozovan M.	46, 49
Lupascu A.	23

M

Mandache C.	91
Manu V.	94
Martinez C.G.	135
Medinschi M.	42
Medinskaya M.I.	33
Miclos S.	226, 230

Mincu N.	236
Mintea D.	115
Miyazawa S.	1
Mokhenache A.	10
Moldovan A.	103
Mollier P.	10, 135
Morosanu C.	71
Munteanu I.	226, 230
Mustaza D.	61

N

Nazarov M. V.	28
Nazarova T. A.	28
Neamtu J.	64
Nerino R.	219
Nicolae B.	111, 115
Nicolae D.	71
Nicolau S.	273
Nicolescu A.	265
Nicula T.	252
Niculescu V.I.R.	192
Novac O.	160

O

Olariu N.	163
Onose C.	52
Oprescu B.	255
Oros C.	163

P

Păcurar L.	55
Palistrant N.A.	33, 42
Pasat V.	19
Păun Ghe.	177
Păunescu G.	163
Perrone G.	144
Pettiti G.	219
Pintilie L.	37
Pîrcalaboiu D.	144
Podoleanu A.Gh.	241
Popescu I.M.	23, 131, 269
Popovici E.J.	55, 80
Porte H.	10, 135, 181
Pricop I.	236
Prisăcari A.M.	85, 177
Puscas N. N.	131, 144, 269
Pyshnaya N.B.	33

R

Radu C.	236
Radu S.	236
Rată D.	99
Rebigan R.	111, 115, 139
Rebigan S.N.	111, 115, 139

Rinza B. S.	135
Ristici M.	115, 273
Robea B.	226, 230
Robu M.	206
Robu S.V.	85
Rogojan R.	58
Rusu Fl. V.	46, 49
Rusu E.	42

S

Sanduloviciu M.	255
Sârbu S.	236
Sarpe-Tudoran C.	61, 64
Scarlat F.	94
Schiopu P.	167
Sergeev S.A.	173
Serghie M.	160
Shutov S.D.	173
Simăn I. I.	108
Smeu E.	269
Socaciu L.	139
Socaciu M.	61, 64
Stănculescu A.	67
Stănculescu F.	67
Stănescu C.	265
Sterian P.	58
Stoenescu G.	153
Stoica A.	211

T

Tănase, M.	71
Tomozeiu, N.	75
Tudoran, C. S.	64
Tugulea L.	71

U

Uncheselu C.	61
Ungureanu M.	91
Ursache M.	139, 150
Uşurelu M.	265

V

Vădan, M.	55
Vasilescu M.	80
Vieru, T.	123
Vlad L.A.	85
Vlădescu M.	247

W

Wacogne B.	10, 131
------------	---------

Z

Zisu T.	226, 230
Zoita C.N.	195